Exploring Thermal Photonics for Sustainability: From Selective Solar Absorbers to Terrestrial Radiative Cooling

Thesis by

Magel P. Su

In Partial Fulfillment of the Requirements for

the degree of

Doctor of Philosophy

CALIFORNIA INSTITUTE OF TECHNOLOGY

Pasadena, California

2024

(Defended May 2, 2024)

© 2024

Magel P. Su
ORCID: 0000-0003-4898-5024

ACKNOWLEDGEMENTS

I am immensely grateful for the guidance and support of numerous individuals who joined me on my experience through Caltech. Only with their company was this journey possible, and I am deeply thankful for all the time and friendship we shared together to make this experience everlasting.

First, I would like to thank my advisor Professor Harry Atwater. My journey at Caltech was difficult and tortuous, winding unknowingly on a path filled with obstacles. Harry's guidance, mixed with his unwavering support and optimism, gave me the strength to continue persevering past each challenge even at my lowest. His wisdom, insight, mentorship, and kindness were pivotal for shaping my growth and development throughout this time of my life. I would also like to thank my faculty members, Professor Katherine Faber, Professor Stevan Nadj-Perge, Professor Austin Minnich, and Professor Brent Fultz, who gave their time to serve on my candidacy/thesis committees and provided meaningful discussions about my work.

Next, I would like to thank all my peers, collaborators, and mentors at Caltech and beyond who gave me the encouragement, advice, and friendship I needed to succeed. In particular, I am grateful to Komron Shayegan, Parker Wray, Aisulu Aitbekova, Lucy Li, Aidan Fenwick, Phil Jahelka, Mike Kelzenberg, Matthew Salazar, Jared Sisler, Arun Nagpal, Lily Shiau, John Hylak, Maggie Potter, Sophia Cheng, Joeson Wong, Rebecca Glaudell, Yae Chan Lim, Gunnar Nelson, Himashi Andaraarachchi, Philip Hon, Zachery Iton, Benjamin Hatanpaa, Yuchun Sun, and Steve Lu for their integral support and friendship. I would also like to thank all the administrators and staff who contributed to my work, including Thomasine Murphy, Jonathan Gross, Kam Flowers, and Jennifer Blankenship for their infinite time, effort, and patience, and Matthew Hunt, Alex Wertheim, Nathan Lee, Lena Wolff, Kelly McKenzie, and Alireza Ghaffari for their invaluable discussions and insights.

Next, I would like to thank my closest friends who have been with me since the beginning. This journey would have been impossible to traverse without their company along the way. I would like to thank my Caltech friends Osmond Wen, Adriano Testa, Léo Borrel, and Sarah Rocha for their friendship every day at Caltech, my undergraduate friends Luis Castillo, Taylor Moon, and Dan Bruni for their continual love and care, and my oldest friends Jin Mo Park, Xusheng Zhao, and Kevin Xu for putting up with me through the decades. I would also like to thank Alison Xu for all her unending emotional support, her love, and her kindness in shaping my experience.

Next, I would like to thank my mentors who guided me outside of Caltech. In particular, I would like to thank Dr. Robin Fowler for her unending love, friendship, and mentorship for my personal growth. I would also like to thank Professor Steve Yalisove, Dr. Ben Torralva, Dr. Daniel Rumack, and Dr. Dorine Starace for showing me the fulfillment of pursuing science.

Finally, I would like to thank my family, my mom and dad and brother and sister-in-law and Marshal and Kiki and Kaitlyn, for their support and love through all of life's ups and downs. Without them, this journey would never have started.

Caltech has been an extraordinary experience and I am grateful for each and every person who walked the journey with me.

ABSTRACT

Photonic materials for thermal emission control have attracted much attention in sustainable technologies where energy and heat management are highly desirable. Controlling the frequency dependency of emissivity enables passive suppression or enhancement of thermal emission which can be used to exploit thermodynamically favorable conditions.

In Part I, we present the development of a selective solar absorber which suppresses thermal emission for efficient conversion of solar energy into thermal energy. Our absorber uses an ultrathin metal layer and an antireflective coating to suppress thermal emission and enhance solar absorption, respectively. Furthermore, we constructed a novel scalable photothermal reactor which utilizes the selective solar absorber for thermocatalytic processes. Thermochemical processes provide a sustainable alternative for fuel synthesis compared to traditional industrial methods, and catalyzed processes operate at reduced temperatures and pressures allowing them to be powered solely by direct solar thermal energy. Using sunlight, we synthesized C_6 – C_{24} carbon chain length olefins from ethylene gas with Ni-catalyzed ethylene oligomerization, demonstrating a vital step for direct CO_2 to sustainable aviation fuel synthesis.

In Part II, we present silicon oxide and silicon nitride bilayer laminate nanoparticle films as scalable efficient daytime terrestrial radiative coolers which couple enhanced thermal emission with the cold background of space. We show experimentally that laminate nanoparticle films deposited from a nonthermal plasma are well described by effective medium mixing models, and their fill fraction tunability enables them to spectrally match more efficiently to the atmospheric transmission window than conventional dense laminate thin films. During this process, we realized a need for directly measuring thermal emission in a controlled ambient to facilitate inter-comparisons between radiative cooling performances. In response, we constructed a new instrument for direct spectrally and angularly resolved radiative emission measurements, providing a new avenue to study the thermal emission behavior of photonic materials.

PUBLISHED CONTENT AND CONTRIBUTIONS

Wray, P. R., Su, M. P. & Atwater, H. A. (2020). Design of efficient radiative emission and daytime cooling structures with Si_3N_4 and SiO_2 nanoparticle laminate films. *Optics Express*, *28*(24), 35784-35794. DOI: 10.1364/OE.408845.

Contributions: Experimental design, thermodynamic modeling and calculations, data digitization, manuscript writing

Li, Z., Wray, P. R., Su, M. P., Tu, Q., Andaraarachchi, H. P., Jeong, Y. J., Atwater, H. A. & Kortshagen, U. R. (2020). Aluminum oxide nanoparticle films deposited from a nonthermal plasma: Synthesis, characterization, and crystallization. *ACS omega*, *5*(38), 24754-24761. DOI: 10.1021/acsomega.0c03353.

Contributions: Materials characterization, optical characterization, data analysis, manuscript writing

Tumkur, T. U., Sokhoyan, R., Su, M. P., Ceballos-Sanchez, A., Shirmanesh, G. K., Kim, Y., Atwater, H. A., Feigenbaum, E. & Elhadj, S. (2021). Toward high laser power beam manipulation with nanophotonic materials: evaluating thin film damage performance. *Optics Express*, *29*(5), 7261-7275. DOI: 10.1364/OE.413843.

Contributions: Materials fabrication, optical characterization, data analysis, manuscript writing

TABLE OF CONTENTS

Acknowledgements iii
Abstract v
Published Content and Contributions vi
Table of Contents vii
List of Illustrations x
List of Tables xxv
Chapter 1: Introduction 1
1.1 Motivation 1
1.2 Selective Solar Absorbers 3
1.3 Photothermal Reactors 4
1.4 Sustainable Aviation Fuels 6
1.5 Passive Daytime Terrestrial Radiative Coolers 7
1.6 Laminate Nanoparticle Films 9
1.7 Nonthermal Plasma Synthesis 11
1.8 Scope of this Thesis 14
Section I: Generating Sustainable Fuels from Sunlight 16
Chapter 2: Harnessing Solar Thermal Energy
With Selective Solar Absorbers 17
2.1 Introduction 17
2.2 Principles of Selective Solar Absorbers 18
2.2.1 Lower Limit Performance 21
2.2.2 Upper Limit Performance 23
2.3 Absorber Design and Optimization 27
2.3.1 ITO Absorber 28
2.3.2 PCWG Absorber 32
2.3.3 Metal AR Coated Absorber 34
2.4 Fabrication 37
2.5 Optical Characterization 39
2.6 Thermal Performance 42
2.7 Summary and Conclusion 43
Chapter 3: Designing a Solar Driven Photothermal Reactor 44
3.1 Introduction 44
3.2 Design Considerations 46
3.3 Reactor Design 48
3.4 Thermal Modeling 51
3.4.1 Model Setup 52
3.4.2 Construction Geometry 52
3.4.3 Materials Selection 53
3.4.4 ***Heat Transfer in Solids*** Interface 55
3.4.5 ***Surface-to-Surface Radiation*** Interface 55

3.4.6 Meshing 58
3.4.7 Results 59
3.4.8 Modeling an Industrial-Scale Reactor 63
3.5 Reactor Construction 64
3.6 Thermal Performance 66
3.7 Summary and Conclusion 69
Chapter 4: Solar Driven Ethylene Oligomerization 71
4.1 Introduction 71
4.2 Ethylene Oligomerization Reaction 73
4.2.1 Batch Operation:
Homogeneous Ni-Catalyzed Ethylene Oligomerization 73
4.2.2 Flow Operation:
Heterogeneous Ni-Catalyzed Ethylene Oligomerization 83
4.3 Summary and Conclusion 85
Section II: Passive Daytime Terrestrial Radiative Cooling 86
Chapter 5: Characterization of Al_2O_3 Nanoparticle Films
Deposited from a Nonthermal Plasma 87
5.1 Introduction 87
5.1.1 Abstract 88
5.2 Aluminum Oxide Nanoparticle Films
Deposited from a Nonthermal Plasma 89
5.3 Nanoparticle Synthesis 91
5.4 Nanoparticle Characterization 93
5.5 Synthesis of Amorphous Alumina Nanoparticles 95
5.6 Crystallization Behavior of Amorphous Alumina Nanoparticles 100
5.7 Summary and Conclusion 104
5.7 5.8 Supplemental Information 105
Chapter 6: Design of Daytime Radiative Cooling Structures
with Si_3N_4 and SiO_2 Nanoparticle Films 114
6.1 Introduction 114
6.1.1 Abstract 114
6.2 Laminate Nanoparticle Films for
Daytime Terrestrial Radiative Cooling 115
6.3 Principles of Daytime Terrestrial Radiative Cooling 117
6.4 Defining an Optimal Radiative Cooler 119
6.5 Radiative Cooling in SiO_2 and Si_3N_4
Laminate Nanoparticle Films 123
6.6 Summary and Conclusion 130
6.7 Supplemental Information 131
Chapter 7: Characterization of Si_3N_4 and SiO_2 Nanoparticle
Laminate Films for Daytime Radiative Cooling 150
7.1 Introduction 150
7.2 SiO_2 and Si_3N_4 Dense Laminate
Thin Film Radiative Coolers 153
7.3 Characterization of SiO_2 and Si_3N_4

Laminate Nanoparticle Films 162
7.4 Si_3N_4 Laminate Nanoparticle Film Radiative Coolers 173
7.5 Summary and Conclusion 177
Section III: Direct Spectrally and Angularly Resolved Radiative Emission Measurements 179
Chapter 8: A New Instrument for Spectrally and Angularly Resolved Radiative Emission Measurements of Radiative Cooling Structures 180
8.1 Introduction 180
8.2 Instrument Overview 181
8.2.1 Design Specifications 181
8.2.2 Design Considerations 188
8.3 Instrument Operating Procedure 190
8.3.1 Reference Sample Preparation 190
8.3.2 Alignment 191
8.3.3 Start Up 192
8.3.4 Measurement 193
8.3.5 Shut Down 194
8.4 Direct Radiative Emission Measurements 195
8.4.1 Preliminary Measurements 195
8.4.2 Si_3N_4 Laminate Nanoparticle Films 206
8.4.3 SiO_2 and Si_3N_4 Dense Laminate Thin Film 210
8.5 Summary and Conclusion 216
8.6 Supplemental Information 217
Chapter 9: Closing Remarks 220
9.1 Summary 220
9.2 Outlook 221
Bibliography 224

LIST OF ILLUSTRATIONS

Number *Page*

Figure 1.1. Projected annual greenhouse gas emissions based on the implementation of various mitigation technologies. Emissions reductions are shown comparing a conventional business-as-usual trend without further climate policies (green), use of abatement technologies (yellow) and use of carbon-negative technologies (blue). A red line shows the maximum greenhouse gas emissions allowed annually to keep global warming below 2 °C. 2

Figure 1.2. Average annual solar energy per day across the United States. 3

Figure 1.3. Flowchart showing the possible pathways for synthesizing sustainable fuels from sunlight. 5

Figure 1.4. Atmospheric transmission spectra at low humidity (Gemini Observatory) and average humidity (1976 U.S. Standard) showing the main atmospheric transparency window which exists from 8 – 14 μm. At low humidity, a second atmospheric transparency window exists from approximately 16 – 24 μm. 9

Figure 1.5. Schematic diagram showing a laminate nanoparticle film acting as a uniform index layer in the effective medium approximation size regime. Laminate nanoparticle films can be used to create graded index structures and compositionally graded multilayer stacks with effective optical properties different from their classical bulk thin film counterparts..... 11

Figure 1.6. Schematic diagrams showing the processes and interactions occurring in a nonthermal plasma. (a) Elementary processes in a nonthermal plasma which include acceleration of electrons in the electric field, ionization of gas atoms, creation of free electrons, and inelastic interactions; (b) Charging effect of nanoparticles and reactor walls due to free electrons in the nonthermal plasma. 12

Figure 1.7. Schematic diagrams showing the process of nanoparticle formation in a nonthermal plasma and laminate nanoparticle film deposition. (a) Initial nucleation of particles in the plasma due to condensation or chemical reaction between ions; (b) Nanoparticle agglomeration between nucleates forms larger particles which become negatively charged by free electrons, leading to continued growth through surface reactions with positive precursor ions in the

plasma; (c) Nanoparticle deposition onto a substrate forms a uniform laminate nanoparticle film. 13

Figure 2.1. Representative schematic of six major types of selective solar absorbers commonly found in literature. The designs include: (a) intrinsic absorbers; (b) AR coated semiconductor materials; (c) metal-dielectric multilayer stacks; (d) metal-dielectric composites known as cermets; (e) surface textured metals; (f) nanostructured photonic crystal designs..... 17

Figure 2.2. Comparison in the spectral centering between the AM1.5 solar spectrum and blackbody curves at various temperatures. The spectral center of the solar irradiance is approximately 0.5 μm and the blackbody curves are centered at approximately 8 μm (100 °C), 5 μm (300 °C), and 4 μm (500 °C). 19

Figure 2.3. (a) Comparison between the AM1.5 solar spectrum and the blackbody irradiance curve at 91 °C. Both curves have a total power of 1000 W/m^2. The emissivity for a perfectly absorbing surface is overlaid; (b) The net cooling power experienced by a perfectly absorbing surface as a function of temperature. Here dT is the difference between the ambient temperature (300 K) and the surface temperature. 22

Figure 2.4. (a) Comparison between the AM1.5 solar spectrum and the blackbody irradiance curve at 324 °C. The emissivity for an ideal selective solar absorber is overlaid; (b) The net cooling power experienced by an ideal selective solar absorber as a function of temperature. Here dT is the difference between the ambient temperature (300 K) and the surface temperature. 24

Figure 2.5. (a) Maximum theoretical temperature of a rectangular emissivity window as a function of the spectral size of the emissivity window. The emissivity window is bounded on the left at 0.3 μm; (b) The total absorbed solar power as a function of the emissivity spectral window size. 26

Figure 2.6. Schematic of an ITO-based selective solar absorber. 29

Figure 2.7. Complex refractive index of sputter deposited ITO from ellipsometry in the (a) visible and (b) infrared wavelength regime. 30

Figure 2.8. Calculated emissivity for a 500 nm ITO absorber overlaid with the AM1.5 solar spectrum and blackbody curves at 217 °C and 350 °C. The blackbody curves are at the absorber's maximum theoretical temperature under 1 sun and 3 sun intensity..... 32

Figure 2.9. (a) Model of a PCWG absorber with hole arrays; (b) Calculated emissivity for an optimized PCWG absorber overlaid with the AM1.5 solar spectrum and blackbody curves at 389 °C and 560

°C. The blackbody curves are at the absorber's maximum theoretical temperature under 1 sun and 3 sun intensity. 33

Figure 2.10. Schematic of a metal AR coated selective solar absorber. 34

Figure 2.11. Complex refractive index of PECVD deposited silicon nitride from ellipsometry in the (a) visible and (b) infrared wavelength regime. 35

Figure 2.12. Calculated emissivity for the highest performing silver AR coated absorber and gold AR coated absorber overlaid with the AM1.5 solar spectrum. 36

Figure 2.13. (a) Absorptivity of a gold AR coated absorber showing poor reflectivity in the infrared wavelength regime due to non-uniformity in the ultrathin gold layer; (b) SEM image showing the surface of the absorber. 38

Figure 2.14. (a) Schematic of an optimized gold AR coated selective solar absorber; (b) Image of a 4-inch diameter gold AR coated absorber. 39

Figure 2.15 (a) Emissivity of a gold AR coated absorber overlaid with the AM1.5 solar spectrum and blackbody curve at 249 °C, the maximum theoretical temperature of the absorber; (b) Angle-dependent emissivity of the absorber; (c) Electromagnetic mode profile versus film depth of the absorber. 41

Figure 2.16. Temperature versus time curve of a gold AR coated absorber in a low vacuum environment (1 mTorr) under 1 sun intensity. 43

Figure 3.1. Diagram showing the breakdown of existing photothermal reactors by their type, mode of operation, and heating source. 45

Figure 3.2 Schematic of a solar driven photothermal reactor comprised of a vacuum insulating layer, selective solar absorber, and thermocatalytic reaction layer. 49

Figure 3.3. Deconstructed CAD assembly of a photothermal reactor highlighting each active layer. (a) First layer showing thermocatalytic reaction layer constructed using a thin plate flange and a double-faced flange. An inlet port, outlet port, and thermocouple feedthrough are included in the double-faced flange; (b) Second layer showing the selective solar absorber and vacuum insulating layer constructed using a second thin plate flange and double-faced flange. A vacuum port and thermocouple feedthrough are included in the double-faced flange; (c) Fully constructed photothermal reactor with quartz

window flange enclosing the vacuum insulating layer; (d) Top view of photothermal reactor; (e) Side view cross-section of photothermal reactor. 50

Figure 3.4. (a) CAD assembly of photothermal reactor in batch mode setup. The thermocatalytic reaction layer is an isolated volume designed for batch reactions, and it is constructed using two thin plate flanges and a double-faced flange; (b) CAD assembly of photothermal reactor in flow mode setup. The thermocatalytic reaction layer is a single thick blank flange with a tube machined through the center. 51

Figure 3.5. Graph showing the effect of high temperatures and low pressures on air thermal conductivity. 55

Figure 3.6. Comparison between the measured emissivity of the gold AR coated selective solar absorber and the discretized emissivity used for the COMSOL model. 57

Figure 3.7. Photothermal reactor model built in COMSOL geometry with "normal" element size mesh for the (a) batch mode setup and (b) flow mode setup. 59

Figure 3.8. Temperature versus length profile of the batch mode photothermal reactor setup calculated from COMSOL thermal model. The temperature profiles are sampled along the surface of the selective solar absorber, the inside surface of the quartz window, and the top and bottom of the thermocatalytic reaction layer. Each plot shows the temperature profile of the reactor under different conditions: (a) I = 1000 W/m^2, Q = 0 $W/m^2/K$; (b) I = 1000 W/m^2, Q = 2 $W/m^2/K$; (c) I = 1000 W/m^2, Q = 4 $W/m^2/K$; (d) I = 3000 W/m^2, Q = 0 $W/m^2/K$; (e) I = 3000 W/m^2, Q = 2 $W/m^2/K$; (f) I = 3000 W/m^2, Q = 4 $W/m^2/K$. 61

Figure 3.9. Temperature versus length profile of the flow mode photothermal reactor setup calculated from COMSOL thermal model. The temperature profiles are sampled along the surface of the selective solar absorber, the inside surface of the quartz window, and the thermocatalytic reaction layer. Each plot shows the temperature profile of the reactor under different conditions: (a) I = 1000 W/m^2, Q = 0 $W/m^2/K$; (b) I = 1000 W/m^2, Q = 2 $W/m^2/K$; (c) I = 1000 W/m^2, Q = 4 $W/m^2/K$; (d) I = 3000 W/m^2, Q = 0 $W/m^2/K$; (e) I = 3000 W/m^2, Q = 2 $W/m^2/K$; (f) I = 3000 W/m^2, Q = 4 $W/m^2/K$. 62

Figure 3.10. (a) Temperature versus length/width profile of an industrial-scale photothermal reactor under various conditions calculated from COMSOL thermal model; (b) Spatial temperature profile under 1 sun intensity. 64

Figure 3.11. Fully constructed photothermal reactor in batch mode setup. Two quarter-turn valves with Quick Connect valves are attached. The other ports are sealed with plugs. Note that the selective solar absorber is not installed in (b). 65

Figure 3.12. (a) Photothermal reactor with insulation box. A transparent low-density polyethylene sheet is used to cover the opening of the box during operation; (b) Experimental setup of photothermal reactor in insulation box with ABET Sun 3000 Simulator. 66

Figure 3.13. Temperature versus time curve of the reactor under 1 sun and 3 sun illumination. The previously measured selective solar absorber temperature versus time curve under 1 sun is also shown..... 67

Figure 3.14. Comparison of temperature versus time in the flow mode photothermal reactor setup under argon gas flow versus no argon gas flow with 3 sun intensity over 10 hours. 68

Figure 4.1. Schematic showing the use of a solar driven photothermal reactor for converting ethylene to liquid hydrocarbon fuels using sunlight. A selective solar absorber is used to efficiently collect solar thermal energy in the visible wavelength regime while reducing thermal radiation loss in the infrared wavelength regime. 72

Figure 4.2. Homogeneous Ni-catalyzed ethylene oligomerization reaction. 74

Figure 4.3. GC-MS product analysis of Ni-SHOP catalyzed ethylene oligomerization in a Fisher-Porter tube at T = 75 °C, P = 1 bar, t = 11 hr, C = 4 mM, resulting in a hydrocarbon product distribution ranging from C_4 – C_{26}. 75

Figure 4.4. GC-MS product analysis of Ni-SHOP catalyzed ethylene oligomerization in a Fisher-Porter tube at T = 75 °C, P = 5 bar, t = 1 hr, C = 2 mM, resulting in a hydrocarbon product distribution ranging from C_4 – C_{34}. 76

Figure 4.5. Batch operation homogeneous Ni-catalyzed ethylene oligomerization reaction parameters. 77

Figure 4.6. Images of the photothermal reactor after a batch mode ethylene oligomerization reaction. (a) Liquid product dissolved in methanol; (b) Solid product left over on the bottom flange; (c) Solid product left over on the top flange. 78

Figure 4.7. Product analysis of the liquid filtrate collected after a Ni-SHOP catalyzed ethylene oligomerization in the photothermal reactor under dark conditions with T = 75 °C, P = 3.4 bar. (a) GC-MS product analysis showing a distribution of hydrocarbon products ranging from

$C_8 – C_{26}$; (b) ^{1}H NMR product analysis showing the presence of linear 1-alkene chains in the liquid filtrate. 79

Figure 4.8. (a) Image of the experimental setup with photothermal reactor under a solar simulator with heat tape for supplemental heat. The Ni-SHOP catalyzed ethylene oligomerization was operated at T = 75 °C, P = 3.4 bar; (b) Image of the liquid product dissolved in methanol; (c) GC-MS liquid product analysis showing a distribution of hydrocarbon products ranging from $C_6 – C_{24}$. 80

Figure 4.9. Results of the homogeneous Ni-catalyzed ethylene oligomerization reaction under 3 sun intensity in the batch mode photothermal reactor setup. (a) GC-MS liquid product analysis showing a distribution of hydrocarbon products ranging from $C_6 – C_{26}$; (b) GC-FID quantification of 1-alkene products from $C_8 – C_{18}$; (c) Temperature of the reactor over the course of the reaction. 82

Figure 4.10. Flow operation heterogeneous Ni-catalyzed ethylene oligomerization reaction parameters. 84

Figure 4.11. Results of the heterogeneous Ni-catalyzed ethylene oligomerization reaction under 3 sun intensity in the flow mode photothermal reactor setup. (a) Ethylene conversion efficiency over time showing an average of approximately 25% over a period of 3 hours; (b) Product selectivity over time showing a butene-to-hexene product ratio of approximately 9:1 after 3 hours. 84

Figure 5.1. Amorphous aluminum oxide nanoparticles synthesized from a nonthermal plasma which crystallize into γ, θ, and α phase alumina post-anneal. 89

Figure 5.2. Schematic of the two types of nonthermal plasma reactors used for AlO_x nanoparticle synthesis and film deposition. 91

Figure 5.3. Characterization of AlO_x nanoparticles synthesized from two types of reactors at p=3.8 Torr: (a) θ–2θ mode out-of-plane XRD patterns of the as-synthesized AlO_x nanoparticles from type A and type B reactors; (b) XPS survey scan of AlO_x nanoparticles from type A and type B reactors. (c) Typical FTIR spectra of AlO_x samples from type A and type B reactors, with major absorption peaks featuring Al−O, $-COO^-$, $-CH_3$, and −OH. 95

Figure 5.4. TEM images of AlO_x nanoparticles synthesized from type A and type B reactors at pressures of 3.8 Torr, 5.2 Torr and 7.5 Torr with mean sizes and standard deviations. 97

Figure 5.5. Cross-sectional SEM images of AlO_x nanoparticle laminate films synthesized from type A and type B reactors. A correction factor of 1/cos(38°) is applied in the y-axis to account for

the tilt of the setup with respect to the SEM Everhart-Thornley Detector (ETD). 98

Figure 5.6. Real and imaginary parts of the complex AlO_x nanoparticle films permittivity found in the type A reactor (a,b) and type B reactor (c,d), respectively. 99

Figure 5.7. XRD patterns of the post-synthesis annealed AlO_x nanoparticles from (a) type A and (b) type B reactors, with annealing temperature ranging from 400 ℃ to 1000 ℃ and annealing times of 18 h. 101

Figure 5.8. XRD patterns of the post-heated AlO_x nanoparticles from (a) type A and (b) type B. Both samples were annealed at 1100 ℃ for 18 h. The bottom columns in both graphs show the reference profile of γ-, θ-, and α-phase aluminum oxides. 102

Figure 5.9. (a) XRD pattern of type B AlO_x nanoparticles heated at 1100 ℃ for 18 h and 40h; TEM images of (b) AlO_x nanoparticles annealed at 1100 ℃ for 18 h and (c) AlO_x nanoparticles annealed at 1100 ℃ for 40 h. 103

Figure S5.1. XRD pattern from a standard LaB_6 sample taken using a Bruker D8 Discover 2D X-ray diffractometer. This pattern is used as a reference to correct for instrument broadening. 105

Figure S5.2. Atomic concentration in samples from type B reactor obtained by XPS with power varying from 5 W to 40 W. 105

Figure S5.3. XPS high resolution spectra of Al 2p peak, O 1s peak and C 1s peak for AlO_x nanoparticle samples from type A and type B reactors. The peak corresponding to adventitious carbon is shifted to 284.8 eV as a reference. 106

Figure S5.4. Size distributions corresponding to the TEM images in **Fig. 5.4a-f**. 107

Figure S5.5. Photograph showing AlO_x nanoparticles deposited from type A and type B reactors for same period of time. 107

Figure S5.6. Scherrer fittings of XRD patterns (λ = 1.54 Å) of AlO_x nanoparticles from type B reactor after heating at 1100 ˚C for 18 h and for 40 h. To obtain size estimates for the α-phase and θ-phase individually, we choose non-overlapping peaks from the two phases. For the α-phase, (113) peaks were fitted. For θ-phase, peaks around 30-34˚ and 44-50˚ were fitted. Instrumental broadening was accounted for by subtracting the FWHM of the nearest peak of the LaB_6 standard sample, **Fig. S5.1**. In the Scherrer equation, a shape factor of 0.89 was used. As the widths of α-phase peaks are close to

those of the LaB_6 standard sample indicating large crystallite sizes, a rough size estimate of >100 nm is quoted in the main text. 108

Figure S5.7. XRD patterns of samples from type B reactor for three nanoparticle sizes, obtained by varying the gas pressure, after annealing at 1100˚C for 18 hours. Only the smallest particles with about 6 nm size show the appearance of the α-phase..... 109

Figure 6.1. (a) Atmospheric transmission spectra at low humidity taken from the Gemini Observatory and at average humidity taken from the 1976 U.S. Standard; (b) blackbody spectra at various temperatures (300 K, 280 K, 260 K, and 240 K) overlaid on the atmospheric emission spectrum from 1976 U.S. Standard at 300 K; (c) radiative cooling power density versus operating temperature relationship for the four theoretically optimal radiative cooling spectral emission windows defined from (b), each is optimized to provide superior cooling power at a specific optimization temperature under ambient conditions (300 K). The solid lines show radiative cooling power (P_r) minus atmospheric heating (P_a) versus operating temperature for each of the optimal radiative coolers. Solar absorption percent is given by the horizontal dashed lines. Losses from conduction and convection for various non-radiative heat transfer coefficients (q), are marked with sloping dashed lines. The total net zero cooling power line is represented by a linear combination of the solar absorption line and non-radiative heat transfer coefficient line. 122

Figure 6.2. (a), (b) n_{eff} and k_{eff} for SiO_2 at various fill fractions with air as the matrix medium; (c) normalized k_{eff} for SiO_2 within atmospheric transmission window demonstrating spectral shifting as a function of fill fraction; (d), (e) n_{eff} and k_{eff} for Si_3N_4 at various fill fractions with air as the matrix medium; (f) normalized k_{eff} for Si_3N_4 within the atmospheric transmission window demonstrating spectral shifting as a function of fill fraction. 125

Figure 6.3. (a) Schematic of radiative cooler comprised of two layers of laminate nanoparticle films on a silver back reflector; (b) net radiative cooling power of all 32 optimal two-layer nanoparticle film, thin film, or nanoparticle and thin film composite structures of SiO_2 and Si_3N_4 operating at their optimization temperature calculated using the Bruggeman effective medium formula (v = 2); (c) net radiative cooling power of all 32 optimal two-layer nanoparticle film, thin film, or nanoparticle and thin film composite structures of SiO_2 and Si_3N_4 operating at their optimization temperature calculated using the Maxwell Garnett effective medium formula (v = 0); (d) net radiative cooling power versus optimization temperature for the optimal two-layer nanoparticle films calculated using different effective medium

theories. The nanoparticle film structure performance is compared to the two-layer thin film analog to demonstrate that superior radiative cooling power is predicted regardless of which effective medium formula is used. All figures assume an ambient temperature of 300 K and no conduction or convection losses (q = 0)..... 128

Figure 6.4. Comparison between various radiative structure performances from literature (solid) and proposed two-layer radiative cooling structures composed of SiO_2 and Si_3N_4 laminate nanoparticle films on silver back reflector (dashed). Each dashed curve represents a unique two-layer radiative cooler optimized for a different operating temperature. Literature curves are obtained through digitization of published emissivity data at normal incidence and it is assumed the emissivity is angle independent. This figure serves purely as a guide for visualizing the relative benefit of nanoparticle films in radiative cooling. 130

Figure S6.1. Spectral and angular resolved p-polarization (top) and s-polarization (bottom) emissivity profile for 2-layer laminate nanoparticle film radiative cooling structure optimized for 270 K at an ambient temperature of 300 K. Radiative cooling structure composed of Si_3N_4 (NP) on SiO_2 (NP) on Ag back reflector. 138

Figure S6.2. Spectral and angular resolved p-polarization (top) and s-polarization (bottom) emissivity profile for 2-layer laminate nanoparticle film radiative cooling structure optimized for 280 K at an ambient temperature of 300 K. Radiative cooling structure composed of SiO_2 (NP) on Si_3N_4 (NP) on Ag back reflector. 139

Figure S6.3. Spectral and angular resolved p-polarization (top) and s-polarization (bottom) emissivity profile for 2-layer laminate nanoparticle film radiative cooling structure optimized for 290 K at an ambient temperature of 300 K. Radiative cooling structure composed of SiO_2 (NP) on Si_3N_4 (NP) on Ag back reflector. 140

Figure S6.4. Spectral and angular resolved p-polarization (top) and s-polarization (bottom) emissivity profile for 2-layer laminate nanoparticle film radiative cooling structure optimized for 300 K at an ambient temperature of 300 K. Radiative cooling structure composed of SiO_2 (NP) on Si_3N_4 (NP) on Ag back reflector. 141

Figure S6.5. Spectral and angular resolved p-polarization (top) and s-polarization (bottom) emissivity profile for 2-layer dense solid thin film radiative cooling structure optimized for 270 K at an ambient temperature of 300 K. Radiative cooling structure composed of Si_3N_4 (Film) on SiO_2 (Film) on Ag back reflector. 142

Figure S6.6. Spectral and angular resolved p-polarization (top) and s-polarization (bottom) emissivity profile for 2-layer dense solid thin film radiative cooling structure optimized for 280 K at an ambient temperature of 300 K. Radiative cooling structure composed of Si_3N_4 (Film) on SiO_2 (Film) on Ag back reflector. 143

Figure S6.7. Spectral and angular resolved p-polarization (top) and s-polarization (bottom) emissivity profile for 2-layer dense solid thin film radiative cooling structure optimized for 290 K at an ambient temperature of 300 K. Radiative cooling structure composed of Si_3N_4 (Film) on SiO_2 (Film) on Ag back reflector. 144

Figure S6.8. Spectral and angular resolved p-polarization (top) and s-polarization (bottom) emissivity profile for 2-layer dense solid thin film radiative cooling structure optimized for 300 K at an ambient temperature of 300 K. Radiative cooling structure composed of Si_3N_4 (Film) on SiO_2 (Film) on Ag back reflector. 145

Figure S6.9. Digitized emissivity curve from a multilayer radiative cooler composed of seven alternating layers of HfO_2 and SiO_2. 146

Figure S6.10. Digitized emissivity curve from a 2-layer 2D photonic crystal of SiC and quartz. 147

Figure S6.11. Digitized emissivity curve from a polymer-coated fused silica mirror. 147

Figure S6.12. Digitized emissivity curve from a glass-polymer hybrid metamaterial. 148

Figure S6.13. Digitized emissivity curve from nanoparticle-based double layer cooling structure on a black substrate. 148

Figure S6.14. Digitized emissivity curve from nanoparticle-based double layer cooling structure on an aluminum substrate. 149

Figure 7.1. Schematic of the highest performing two-layer dense thin film radiative cooling structures composed of SiO_2 and Si_3N_4. The schematic also indicates the expected cooling power of each structure at 300 K. 151

Figure 7.2. Schematic of the highest performing two-layer nanoparticle film on dense thin film radiative cooling structures composed of SiO_2 and Si_3N_4. The schematic also indicates the expected cooling power of each structure at 300 K. 152

Figure 7.3. Schematic of the highest performing two-layer nanoparticle film radiative cooling structures composed of SiO_2 and Si_3N_4. The schematic also indicates the expected cooling power of each structure at 300 K. 152

Figure 7.4. Complex refractive index of sputter deposited silver from ellipsometry in the (a) visible and (b) infrared wavelength regime. 154

Figure 7.5. Complex refractive index of PECVD deposited SiO_2 from ellipsometry in the (a) visible and (b) infrared wavelength regime. 155

Figure 7.6. Complex refractive index of PECVD deposited Si_3N_4 from ellipsometry in the (a) visible and (b) infrared wavelength regime. 156

Figure 7.7. Comparison between the theoretical and measured emissivity (from ellipsometry) for the (a) 200 nm Si_3N_4 on 1200 nm SiO_2 structure and the (b) 700 nm SiO_2 on 800 nm Si_3N_4 158

Figure 7.8. Spectral emissivity of the 200 nm Si_3N_4 on 1200 nm SiO_2 structure in the (a) visible wavelength regime measured by UV-vis spectroscopy and in the (b) infrared wavelength regime measured by FT-IR spectroscopy. The theoretical spectral emissivity is also included to show the match between the theoretical and experimental results. Note that a CaF_2 beam splitter was used for the near-IR measurements, and a KBr beam splitter was used for the mid- and far-IR measurements. 160

Figure 7.9. Spectral emissivity of the 700 nm SiO_2 on 800 nm Si_3N_4 structure in the (a) visible wavelength regime measured by UV-vis spectroscopy and in the (b) infrared wavelength regime measured by FT-IR spectroscopy. The theoretical spectral emissivity is also included to show the match between the theoretical and experimental results. Note that a CaF_2 beam splitter was used for the near-IR measurements, and a KBr beam splitter was used for the mid- and far-IR measurements. 161

Figure 7.10. (a) Schematic of the nonthermal plasma reactor used to synthesize and deposit SiO_2 and Si_3N_4 nanoparticle films; (b) Image of the nonthermal plasma reactor. 163

Figure 7.11. TEM images of (a) SiO_2 nanoparticles and (b) Si_3N_4 nanoparticles synthesized from a nonthermal plasma reactor. 164

Figure 7.12. Laminate nanoparticle films of (a) SiO_2 and (b) Si_3N_4 deposited by nonthermal plasma synthesis onto gold coated substrates. The samples are approximately 1 cm wide and 4 cm long. 165

Figure 7.13. Cross-sectional SEM images of SiO_2 and Si_3N_4 nanoparticle laminate films synthesized from a nonthermal plasma reactor. The pass number refers to the number of times the substrate was moved across the deposition spray of the reactor. Note that a correction factor of 1/cos(38°) is applied in the y-axis to account for

the tilt of the setup with respect to the SEM Everhart-Thornley Detector (ETD). 166

Figure 7.14. FT-IR reflectivity of (a) SiO_2 and (b) Si_3N_4 nanoparticle laminate films synthesized from a nonthermal plasma reactor on a gold coated substrate. The pass number refers to the number of times the substrate was moved across the deposition spray of the reactor. 168

Figure 7.15. The complex refractive index of (a) SiO_2 nanoparticles and (b) Si_3N_4 nanoparticles synthesized in a nonthermal plasma reactor, extracted using ellipsometry. 170

Figure 7.16. The calculated spectral reflectivity of the (a) SiO_2 and (b) Si_3N_4 nanoparticle films from ray transfer matrix method and Bruggeman effective medium approximation using the nanoparticle complex refractive index extracted by ellipsometry. 172

Figure 7.17. Predicted radiative cooling power of a two-layer SiO_2 and Si_3N_4 laminate nanoparticle film radiative cooling structure with varying layer thickness and order. 173

Figure 7.18. Image of Si_3N_4 laminate nanoparticle film on silver substrate deposited from nonthermal plasma synthesis with 400 raster passes. The sample size is approximately 1 cm by 4 cm. 174

Figure 7.19. Cross-sectional SEM image of a Si_3N_4 nanoparticle laminate film synthesized from a nonthermal plasma reactor with 400 raster passes. Note that a correction factor of 1/cos(38°) is applied in the y-axis to account for the tilt of the setup with respect to the SEM Everhart-Thornley Detector (ETD). 175

Figure 7.20. FT-IR reflectivity of Si_3N_4 laminate nanoparticle films synthesized from a nonthermal plasma reactor with 400 raster passes on a (a) bare silver substrate and (b) silver with 5 nm SiO_2 passivation layer. The atmospheric transparency window is overlaid. 176

Figure 8.1. CAD schematic of the proposed instrument for simultaneous measurement of the direct radiative emission and surface temperature of a sample. The schematics shown include (a) solid schematic, (b) wireframe schematic, (c) solid schematic side view, and (d) solid schematic top view of the instrument. The instrument is a custom-design vacuum chamber with cryoshroud. 182

Figure 8.2. Schematic of the motorized rotary feedthrough. A sample stage (not shown here) can be mounted via the threaded end of the rotary shaft. 184

Figure 8.3. CAD schematic of the instrument sample stage. Combined with the rotary shaft, the sample stage enables xy-tilt adjustments and xz-translational adjustments. 185

Figure 8.4. Images of the instrument setup. 187

Figure 8.5. Characteristic cryoshroud cooling curve over time with LN_2, measured by a thermocouple attached to the surface of the cryoshroud. 193

Figure 8.6. Normalized radiative emissivity of Si_3N_4 laminate nanoparticle films at normal incidence and temperatures of 30, 40, and 50 °C. The nanoparticle films were synthesized from a nonthermal plasma reactor with 400 raster passes on (a) bare silver substrate and (b) silver with 5 nm SiO_2 passivation layer. 196

Figure 8.7. Comparison of the normalized radiative emissivity of Si_3N_4 laminate nanoparticle films, on either (a) bare silver substrate or (b) silver with 5 nm SiO_2 passivation layer, at normal incidence and temperatures of 30, 40, and 50 °C from two separate measurements made on different days. 198

Figure 8.8. Normalized spectrally and angularly resolved radiative emission of a Si_3N_4 laminate nanoparticle film on silver with 5 nm SiO_2 passivation layer from 0 – 75° with 2° angular resolution at a temperature of 50 °C. 199

Figure 8.9. Normalized average angularly resolved radiative emission from 8 – 14 μm of a Si_3N_4 laminate nanoparticle film on silver with 5 nm SiO_2 passivation layer from 0 – 75° with 2° angular resolution at a temperature of 50 °C. Note that a cos(θ) factor is applied to the result. The Cosine curve represents the radiative intensity of a perfectly Lambertian blackbody. 201

Figure 8.10. Normalized angularly resolved radiative emission at specific wavelengths of a Si_3N_4 laminate nanoparticle film on silver with 5 nm SiO_2 passivation layer from 0 – 75° with 2° angular resolution at a temperature of 50 °C. Note that a cos(θ) factor is applied to the result. The Cosine curve represents the radiative intensity of a perfectly Lambertian blackbody. 202

Figure 8.11. Normalized spectrally and angularly resolved radiative emission of a Si_3N_4 laminate nanoparticle film on silver with 5 nm SiO_2 passivation layer from 0 – 75° with 1° angular resolution at a temperature of 50 °C. 203

Figure 8.12. Normalized average angularly resolved radiative emission from 8 – 14 μm of a Si_3N_4 laminate nanoparticle film on silver with 5 nm SiO_2 passivation layer from 0 – 75° with 1° angular resolution at a temperature of 50 °C. Note that a cos(θ) factor is applied to the result. The Cosine curve represents the radiative intensity of a perfectly Lambertian blackbody. 204

Figure 8.13. Normalized angularly resolved radiative emission at specific wavelengths of a Si_3N_4 laminate nanoparticle film on silver with 5 nm SiO_2 passivation layer from 0 – 75° with 1° angular resolution at a temperature of 50 °C. Note that a cos(θ) factor is applied to the result. The Cosine curve represents the radiative intensity of a perfectly Lambertian blackbody. 205

Figure 8.14. Normalized spectrally and angularly resolved radiative emission of a Si_3N_4 laminate nanoparticle film on silver with 5 nm SiO_2 passivation layer from 0 – 75° with 1° angular resolution at temperatures of (a) 30 °C, (b) 40 °C, and (c) 50 °C. 208

Figure 8.15. Normalized angularly resolved radiative emission of a Si_3N_4 laminate nanoparticle film on silver with 5 nm SiO_2 passivation layer from 0 – 75° with 1° angular resolution at temperatures of (a) 30 °C, (b) 40 °C, and (c) 50 °C. Shown is the radiative emission at specific wavelengths as well as the average radiative emission from 8 – 12 μm. Note that a cos(θ) factor is applied to the result. The Cosine curve represents the radiative intensity of a perfectly Lambertian blackbody. 209

Figure 8.16. Normalized spectrally and angularly resolved radiative emission of a 200 nm Si_3N_4 / 1200 nm SiO_2 dense thin film radiative cooling structure on silver substrate from 0 – 75° with 1° angular resolution at temperatures of (a) 30 °C, (b) 40 °C, and (c) 50 °C. 211

Figure 8.17. Normalized angularly resolved radiative emission of a 200 nm Si_3N_4 / 1200 nm SiO_2 dense thin film radiative cooling structure on silver substrate from 0 – 75° with 1° angular resolution at temperatures of (a) 30 °C, (b) 40 °C, and (c) 50 °C. Shown is the radiative emission at specific wavelengths as well as the average radiative emission from 8 – 12 μm. Note that a cos(θ) factor is applied to the result. The Cosine curve represents the radiative intensity of a perfectly Lambertian blackbody. 212

Figure 8.18. Normalized spectrally and angularly resolved radiative emission of a 700 nm SiO_2 / 800 nm Si_3N_4 dense thin film radiative cooling structure on silver substrate from 0 – 75° with 1° angular resolution at temperatures of (a) 30 °C, (b) 40 °C, and (c) 50 °C. 213

Figure 8.19. Normalized angularly resolved radiative emission of a 700 nm SiO_2 / 800 nm Si_3N_4 dense thin film radiative cooling structure on silver substrate from 0 – 75° with 1° angular resolution at temperatures of (a) 30 °C, (b) 40 °C, and (c) 50 °C. Shown is the radiative emission at specific wavelengths as well as the average radiative emission from 8 – 12 μm. Note that a cos(θ) factor is applied to the result. The Cosine curve represents the radiative intensity of a perfectly Lambertian blackbody. 214

Figure S8.1. Normalized angularly resolved radiative emission of a Si_3N_4 laminate nanoparticle film on silver with 5 nm SiO_2 passivation layer from 0 – 75° with 1° angular resolution at temperatures of (a) 30 °C, (b) 40 °C, and (c) 50 °C. Shown is the radiative emission at specific wavelengths as well as the average radiative emission from 8 – 12 μm. The Cosine curve represents the radiative intensity of a perfectly Lambertian blackbody. 217

Figure S8.2. Normalized angularly resolved radiative emission of a 200 nm Si_3N_4 / 1200 nm SiO_2 dense thin film radiative cooling structure on silver substrate from 0 – 75° with 1° angular resolution at temperatures of (a) 30 °C, (b) 40 °C, and (c) 50 °C. Shown is the radiative emission at specific wavelengths as well as the average radiative emission from 8 – 12 μm. The Cosine curve represents the radiative intensity of a perfectly Lambertian blackbody. 218

Figure S8.3. Normalized angularly resolved radiative emission of a 700 nm SiO_2 / 800 nm Si_3N_4 dense thin film radiative cooling structure on silver substrate from 0 – 75° with 1° angular resolution at temperatures of (a) 30 °C, (b) 40 °C, and (c) 50 °C. Shown is the radiative emission at specific wavelengths as well as the average radiative emission from 8 – 12 μm. The Cosine curve represents the radiative intensity of a perfectly Lambertian blackbody. 219

LIST OF TABLES

Number *Page*

Table 2.1. Maximum theoretical temperature of an ITO absorber with varying thickness and substrate under 1 sun intensity. 31

Table 3.1. Materials properties assigned to domains in the COMSOL model for the photothermal reactor. 53

Table 3.2. Absorptivity values assigned to each spectral band for the materials assigned to boundaries in the COMSOL model for the photothermal reactor. 57

Table 3.3. Reflectivity values assigned to each spectral band for the materials assigned to boundaries in the COMSOL model for the photothermal reactor. 58

Table 5.1. Summary of synthesis parameters used in this study. 93

Table S5.1. Gaussian oscillator parameters used to reconstruct the permittivity of nanoparticles from type A reactor. Phonon resonance type (first column), amplitude (second column), spectral broadening (third column) and resonant frequency (fourth column) of the Gaussian oscillators used to calculate the AlO_x particle permittivity from Mueller matrix data. The fifth column gives the resonant frequency range expected from previous literature reports. Citations for the expected frequency range are in the sixth column. 110

Table S5.2. Gaussian oscillator parameters used to reconstruct the permittivity of nanoparticles from type B reactor. Phonon resonance type (first column), amplitude (second column), spectral broadening (third column) and resonant frequency (fourth column) of the Gaussian oscillators used to calculate the AlO_x particle permittivity from Mueller matrix data. The fifth column gives the resonant frequency range expected from previous literature reports. Citations for the expected frequency range are in the sixth column. 112

Table S6.1. Cooling power versus temperature for Si_3N_4 on SiO_2 (Film/Film) on Ag back reflector. 131

Table S6.2. Cooling power versus temperature for Si_3N_4 on SiO_2 (NP/Film) on Ag back reflector using the Bruggeman formula (v = 2). 131

Table S6.3. Cooling power versus temperature for Si_3N_4 on SiO_2 (Film/NP) on Ag back reflector using the Bruggeman formula (v = 2). 132

Table S6.4. Cooling power versus temperature for Si_3N_4 on SiO_2 (NP/NP) on Ag back reflector using the Bruggeman formula (v = 2). 132

Table S6.5. Cooling power versus temperature for SiO_2 on Si_3N_4 (Film/Film) on Ag back reflector. 132

Table S6.6. Cooling power versus temperature for SiO_2 on Si_3N_4 (NP/Film) on Ag back reflector using the Bruggeman formula (v = 2). 133

Table S6.7. Cooling power versus temperature for SiO_2 on Si_3N_4 (Film/NP) on Ag back reflector using the Bruggeman formula (v = 2). 133

Table S6.8. Cooling power versus temperature for SiO_2 on Si_3N_4 (NP/NP) on Ag back reflector using the Bruggeman formula (v = 2). 133

Table S6.9. Cooling power versus temperature for Si_3N_4 on SiO_2 (NP/Film) on Ag back reflector using Maxwell Garnett formula (v = 0). 134

Table S6.10. Cooling power versus temperature for Si_3N_4 on SiO_2 (Film/NP) on Ag back reflector using Maxwell Garnett formula (v = 0). 134

Table S6.11. Cooling power versus optimization temperature for Si_3N_4 on SiO_2 (NP/NP) on Ag back reflector using Maxwell Garnett formula (v = 0). 134

Table S6.12. Cooling power versus temperature for SiO_2 on Si_3N_4 (NP/Film) on Ag back reflector using Maxwell Garnett formula (v = 0). 135

Table S6.13. Cooling power versus temperature for SiO_2 on Si_3N_4 (Film/NP) on Ag back reflector using Maxwell Garnett formula (v = 0). 135

Table S6.14. Cooling power versus temperature for SiO_2 on Si_3N_4 (NP/NP) on Ag back reflector using Maxwell Garnett formula (v = 0). 135

Table S6.15. Cooling power versus temperature for SiO_2 on Si_3N_4 (NP/NP) on Ag back reflector using complementary Maxwell Garnett formula (v' = 0). 136

Table S6.16. Cooling power versus temperature for SiO_2 on Si_3N_4 (NP/NP) on Ag back reflector using a generalized formula (v = 1). 136

Table S6.17. Cooling power versus temperature for SiO_2 on Si_3N_4 (NP/NP) on Ag back reflector using Coherent Potential formula (v = 3). 136

Table S6.18. Cooling power at T = 270 K for Si_3N_4 on SiO_2 (NP/NP) on Ag back reflector using different effective medium formulas. 137

Table 8.1. Calculated terrestrial radiative cooling power of various radiative cooling structures from spectrally and angularly resolved direct radiative emission measurements..... 216

C h a p t e r 1

INTRODUCTION

1.1 Motivation

As the consumption of fossil fuels rises to meet rising energy demands, atmospheric carbon dioxide (CO_2) levels have also risen due to the increasing amounts of anthropogenic emissions being released into the atmosphere. In 2022 alone, it was estimated that 36.1 billion tons of CO_2 was released globally, a rise of approximately 1.5% over the previous year.[1] As CO_2 levels rise, the accompanying greenhouse gas effect has also given rise to the average global temperature, resulting in an estimated temperature rise of approximately 1 °C since pre-industrial revolution averages (1850 – 1900).[2,3] Furthermore, cascading effects such as ocean acidification have been observed due to the sequestration of atmospheric CO_2 in ocean water as carbonic acid, threatening many biological systems necessary to the delicate balance of the global ecological system.[4,5] In order to combat these worrying trends, the Paris Climate Accord in 2015 established 2 major goals: to limit the average global temperature rise to below the critical point of 2 °C within this century with efforts to limit the increase to 1.5 °C, and to aim for the global peaking of greenhouse gas emission through the pursuit of carbon-neutral and carbon-negative technologies.[6–8]

To meet these goals, much effort has been expended on exploring, implementing, and establishing carbon-free, carbon-neutral, and carbon-negative technologies across a wide range of industrial and commercial fields.[9] Carbon-free technologies do not emit CO_2 during operation such as renewable energy generation from sources like wind and solar. Carbon-neutral technologies produce CO_2 emissions but also offset CO_2 emissions elsewhere such that their overall contribution to CO_2 emission is net zero. Carbon-negative technologies actively remove more carbon than they produce during operation, and commonly refer to various carbon sequestration methods and technologies.[10–12] Projections on greenhouse gas

emissions in the future show that all of these technologies must soon be rapidly implemented in order to meet the Paris Climate Accord goals by the end of the century.[13]

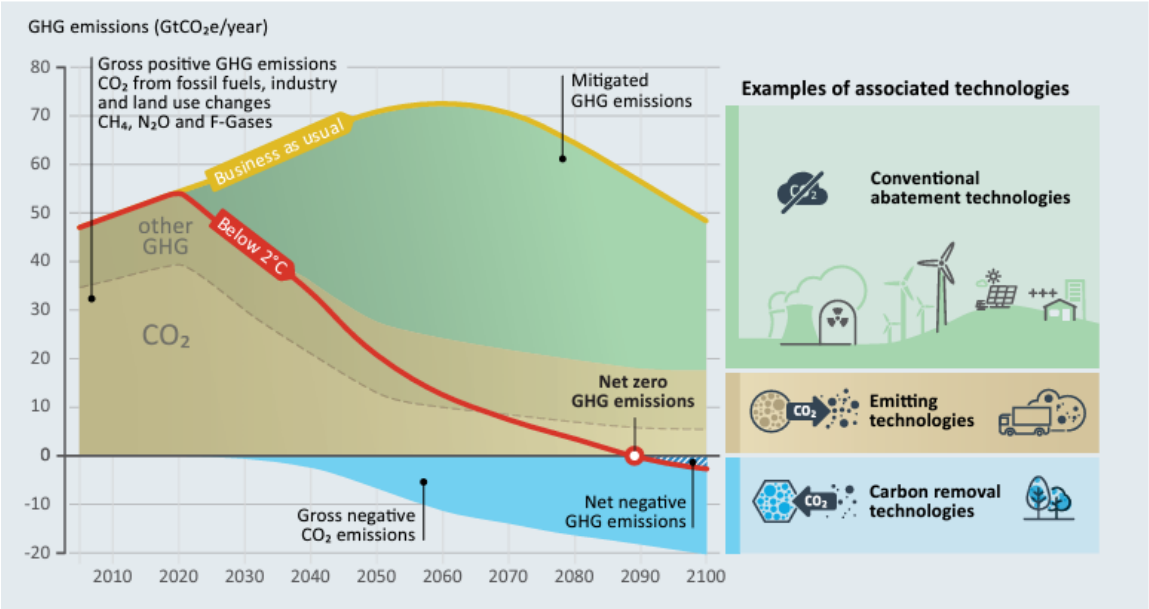

Figure 1.1. Projected annual greenhouse gas emissions based on the implementation of various mitigation technologies. Emissions reductions are shown comparing a conventional business-as-usual trend without further climate policies (green), use of abatement technologies (yellow) and use of carbon-negative technologies (blue). A red line shows the maximum greenhouse gas emissions allowed annually to keep global warming below 2 °C. Figure taken from [13].

Recent work has shown that the application of photonics towards sustainable technologies may be a creative pathway for further reduction of CO_2 emissions. Broadly defined, photonics is the study and manipulation of light and photons. Using photonics, infrared light in the form of radiative thermal emission can be manipulated. Here, two possible applications of photonics are discussed. One solution is to suppress thermal radiative emission and capture solar thermal energy to generate carbon-neutral sustainable fuels. Another solution is to enhance the re-emission of thermal radiation into space for passive terrestrial radiative cooling.

1.2 Selective Solar Absorbers

One source of energy which many other technologies have utilized is solar energy. A universally available source of terrestrial energy, the sun supplies an estimated 1000 W/m^2 peak power flux on the surface of the earth and an average annual of approximately 200 – 300 W/m^2 across the United States.[14,15] In total, it supplies an estimated 3×10^{15} kWh of energy every day. In context, in 2004, the global energy production was estimated at 3.6×10^{11} kWh, or 0.012% of the total solar energy budget.[16] The availability of solar energy makes it an ideal energy source for carbon-free and carbon-neutral technologies.

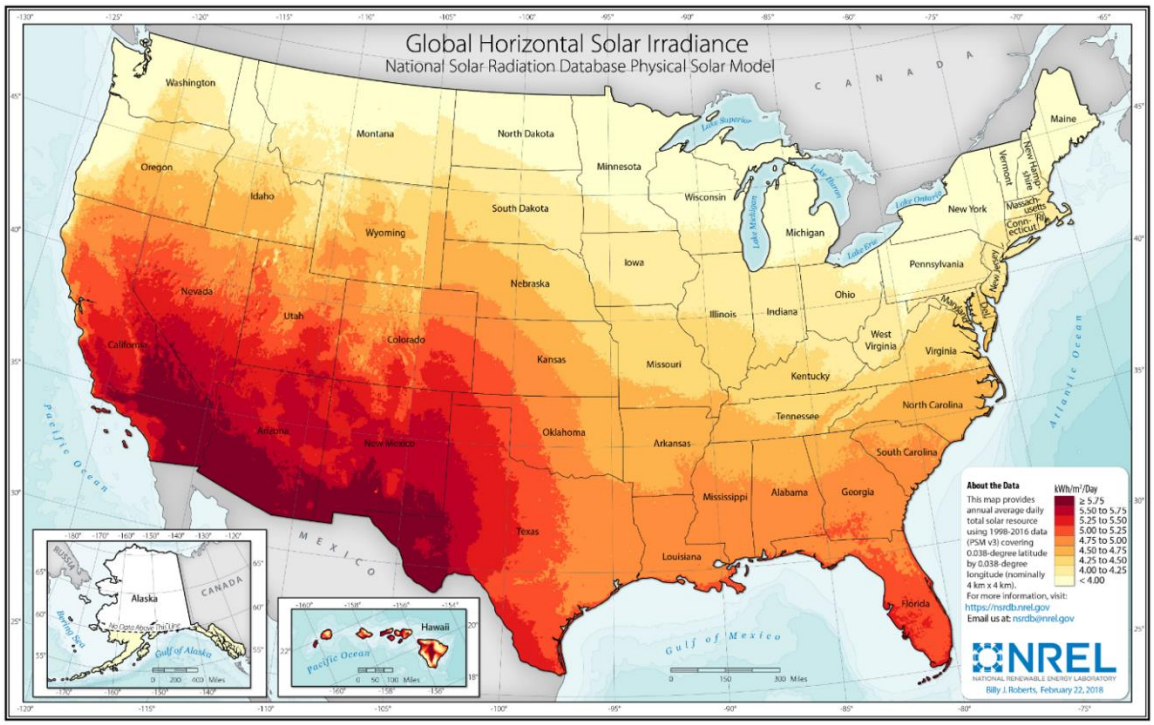

Figure 1.2. Average annual solar energy per day across the United States. Figure taken from [14].

While direct photon solar energy has been commercially available for decades already, the thermal energy of the sun can also be captured and directed in ways which utilize heat as a primary energy source. Methods for directing and collecting solar heat include using broadly absorbing black surfaces and solar concentrators; however, we can achieve much higher efficiencies than both of these methods using photonic structures known as selective solar

absorbers.[17,18] Unlike solar concentrators, which collect sunlight across a wide area, or black surfaces, which absorb at all wavelengths but lose significant energy to thermal re-radiation, a selective solar absorber can achieve high solar-thermal collection efficiencies by absorbing sunlight while suppressing infrared thermal radiation.[19] In other words, these structures have high absorptivity in the solar wavelength regime and low emissivity in the infrared wavelength regime, creating surfaces which can exceed the maximum temperature of black surfaces under the same sunlight intensity conditions.[18] Selective solar absorbers present an interesting photonics solution for capturing and harnessing solar thermal energy for carbon-neutral technology applications.

1.3 Photothermal Reactors

Once solar energy is captured and converted into thermal energy by a selective solar absorber, it can be coupled to a system to supply usable heat. Recently, selective solar absorbers have found uses in a number of sustainable applications including solar desalination and atmospheric water harvesting, wastewater treatment, solar thermophotovoltaic and hybrid thermophotovoltaic devices, solar thermoelectric generations, and photothermal chemistry.[20–26] While all of these applications aid in meeting the goals set forth by the Paris Climate Accord, solar driven photothermocatalytic chemistry in particular has generated recent widespread interest due to its potential impact as a sustainable technology.

By coupling a selective solar absorber to a thermochemical reactor, solar thermal heat can be transferred and used to drive chemical reactions at elevated temperatures. Furthermore, the inclusion of a catalyst decreases the minimum temperature required to drive reactions. Historically, unconcentrated sunlight (1000 W/m^2) has been considered too weak of an energy source to unlock the temperatures required to begin even the lowest temperature thermocatalytic reactions at around 75 – 100 °C.[27,28] As such, much of the previous work on solar driven thermochemistry has incorporated solar concentrators and focusing mirrors.[29,30] However, with the development of selective solar absorbers, radiative heat loss can be

reduced to the point where low temperature thermocatalytic reactions become thermodynamically available under unconcentrated sunlight conditions.

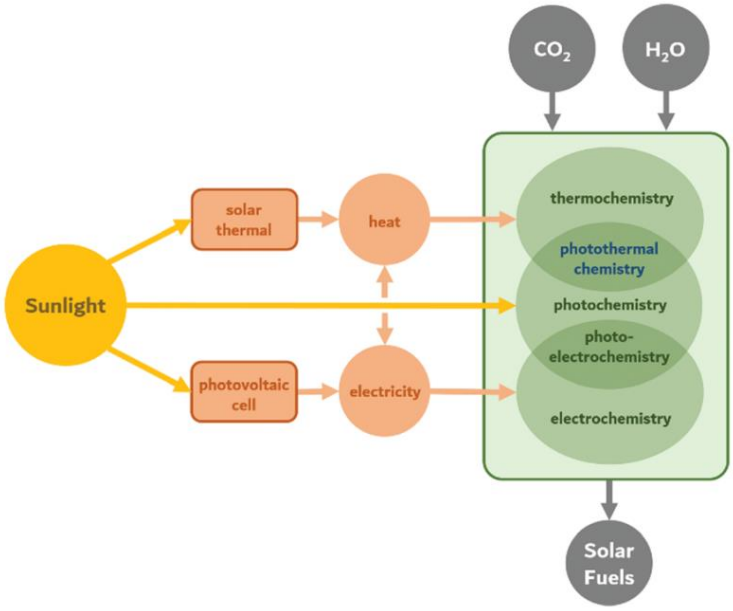

Figure 1.3. Flowchart showing the possible pathways for synthesizing sustainable fuels from sunlight. Figure taken from [31].

A solar driven photothermal reactor must be designed specifically to take advantage of a selective solar absorber. Specifically, the heat from the selective solar absorber must be efficiently transferred to the thermocatalytic site, while all other heat loss pathways are minimized. Sunlight must also be allowed to reach the selective solar absorber unimpaired. Thus, most solar driven photothermal reactors involve the use of a vacuum insulating layer around the selective solar absorber to reduce non-radiative heat loss to the surrounding environment, while the selective solar absorber itself reduces the radiative heat loss to the environment. Finally, the reactor itself is usually insulated as well to prevent further heat loss to the environment. If necessary, solar concentrators can also be coupled with a selective solar absorber to reach higher temperatures.

1.4 Sustainable Aviation Fuels

With the growing potential of solar driven photothermal chemistry, one area which has generated much widespread interest has been in the generation and synthesis of sustainable liquid fuels from sunlight. Sustainable fuels generally includes three types: biofuels or fuels made from waste resources, synthetic fuels, and recycled carbon fuels.[32–34] These fuels are important because they are zero or near zero net carbon emission emitters compared to conventional fossil fuels. Within sustainable fuels, solar driven photothermal chemistry has explored the synthesis of sustainable aviation fuels from CO_2 using sunlight.[34] There are several major impacts of this technology.

First, most carbon-free technologies such as solar energy primarily produce electrical energy. While electrical technology can replace many current existing systems such as combustion engine vehicles for electric vehicles, they cannot meet all current economic and industrial energy demands. This is most starkly highlighted in industries which require high energy density sources, namely the aviation, shipping, and transportation industry. For example, current aviation jet fuel has an energy density of approximately 43 MJ/kg, while state of the art lithium-ion batteries found in electric vehicles for electricity storage have an energy density of 0.72 MJ/kg, almost 100 times lower than jet fuel.[35] In these situations where electrical storage methods are insufficient, a viable solution is to produce sustainable aviation fuels instead.

Second, by using sunlight as the thermal energy for reduction of CO_2 to fuels, the fuel lifecycle is net carbon neutral. Net carbon negative can also be achieved by using this technology as an effective carbon sequestration method to store atmospheric CO_2 in liquid hydrocarbon form. Finally, the replacement of current fossil fuel aviation fuels with sustainable fuels means that global emissions from fossil fuel usage decreases. It is estimated that the aviation transportation industry contributes to approximately 2.4% of global anthropogenic CO_2 emissions, with 80% of those emissions emitted from long distance (>1500 km) flights with no alternative transportation options.[36] Sustainable aviation fuels are

a viable solution for preventing the disruption of these industries while still meeting the Paris Climate Accord goals this century.

Current work applying industrially relevant thermocatalytic reactions to sustainable solar powered methods has yielded many CO_2 reduction reactions with temperature requirements ranging from as low as 25 °C up to 500 °C, and products including formic acid, methane, carbon monoxide, methanol, hydrocarbons, and olefins.[37] Beyond CO_2 reduction, a reaction known as ethylene oligomerization may be an interesting candidate for solar driven thermocatalytic pathways. Ethylene oligomerization generates alkenes from ethylene gas:

$$nC_2H_4 \rightarrow C_{2n}H_{4n} \tag{1.1}$$

And can be a potential pathway for sustainable fuel generation. By coupling precursor ethylene gas produced from CO_2 reduction with a solar driven ethylene oligomerization process, then hydrogenating the product olefin to its corresponding paraffin, high molecular weight hydrocarbons can be directly synthesized from CO_2.[38] Therefore, the coupling of selective solar absorbers with photothermal reactors presents a multidisciplinary solution for accessing thermocatalytic pathways for sustainable fuel synthesis via sunlight. Furthermore, solar driven ethylene oligomerization can be a potential method for generating sustainable aviation fuels directly from CO_2.

1.5 Passive Daytime Terrestrial Radiative Coolers

An alternative application of photonics towards sustainable technologies aiming to reduce CO_2 emissions is in the development of passive daytime terrestrial radiative coolers. As a passive technology, radiative cooling aims to reduce emissions by reducing the current global energy usage spent on air conditioning and heat management. Also known as selective radiators, daytime radiative coolers are photonic structures designed to passively cool below the surrounding ambient temperature during the daytime by emitting infrared thermal radiation directly into space while reflecting incident sunlight.[39] Here, space acts as an unlimited heat sink with a background temperature of approximately 2.7 K. As such, these

structures have low absorptivity in the solar wavelength regime and high emissivity in the infrared wavelength regime. The low solar absorptivity prevents the structure from heating up due to solar thermal energy, while the high infrared emissivity acts as the primary cooling pathway for directing thermal energy away from the structure.[40,41] In other words, daytime radiative coolers are the opposite of selective solar absorbers; instead of enhancing solar absorptivity and reducing radiative heat loss, they reduce solar absorptivity and enhance radiative heat loss.

While these principles are sufficient for understanding radiative cooling, terrestrial radiative coolers also require that the atmosphere itself be a vital consideration in radiative cooling design.[39] Specifically, the terrestrial atmosphere, composed of nitrogen, oxygen, water vapor, and other gases, acts as a semi-transparent media which reduces the total infrared thermal radiation which can reach space from the surface of the earth.[42] Coincidentally, there exists an atmospheric transparency window from 8 – 14 μm which corresponds well with the 10 μm spectral peak of a blackbody at room temperature.[43,44] As such, a terrestrial radiative cooler is designed to take advantage of the atmospheric transparency window by maximizing its thermal infrared emission from 8 – 14 μm while minimizing infrared emission everywhere else. In doing so, the structure maximizes the total thermal radiation which reaches space while minimizing losses due to absorption in the atmosphere. Passive daytime terrestrial radiative coolers present an interesting photonics solution for reducing global active cooling energy costs.

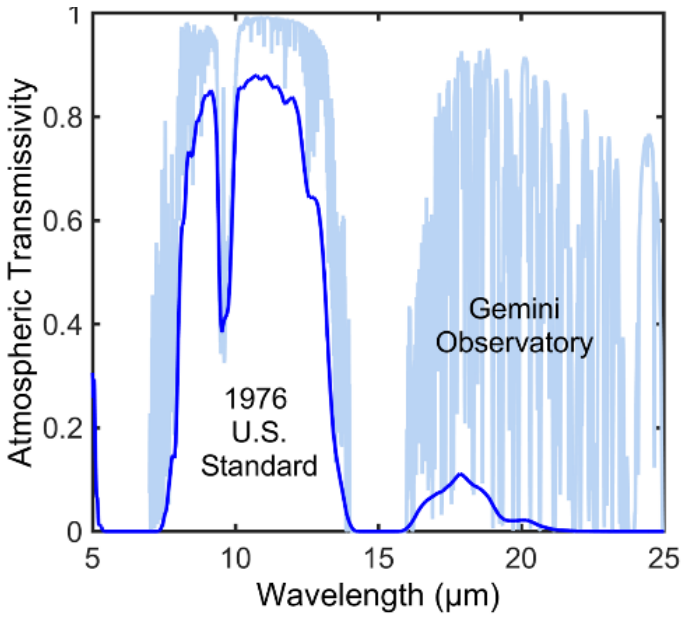

Figure 1.4. Atmospheric transmission spectra at low humidity (Gemini Observatory) and average humidity (1976 U.S. Standard) showing the main atmospheric transparency window which exists from 8 – 14 μm. At low humidity, a second atmospheric transparency window exists from approximately 16 – 24 μm. Data taken from [43].

1.6 Laminate Nanoparticle Films

Laminate nanoparticle films, or layered films composed of many nanoparticles packed in a random array on a substrate, present a potential photonic design for passive daytime terrestrial radiative coolers. In general, the optical response of dielectric and plasmonic nanoparticles depends on the relation between the nanoparticle size, the wavelength of incident light, and the refractive index of the nanoparticle material. In brief, the optical response of nanoparticles with sizes larger than the wavelength of light can be described by Mie resonance modes, nanoparticles with sizes on order of the wavelength of light by dipole scattering and diffraction, and nanoparticles with sizes much smaller than the wavelength of light by effective medium approximations.[45] When laminate nanoparticle films are composed of nanoparticles with sizes much smaller than the wavelength of light, effective medium approximations can be used to effectively design nanoparticle films as passive daytime terrestrial radiative coolers.

Effective medium approximations are methods for predicting the macroscopic properties of composite media without needing to consider the individual contributions from every constituent in the media and their local interactions with their neighbors.[46–48] In the case of laminate nanoparticle films, instead of calculating the individual contributions from each nanoparticle towards light scattering, an effective medium approximation is instead used to predict the macroscopic, or effective, optical properties of the entire nanoparticle film as if it were a homogeneous film.[49] This method works well for nanoparticle films because while they are inhomogeneous at the individual nanoparticle level, they can be assumed to be homogeneous at length scales much larger than the nanoparticle size. In other words, laminate nanoparticle films composed of nanoparticles much smaller than the wavelength of incident light can be described by effective medium approximations as a homogeneous film with effective optical properties describing their bulk behavior. In the case of radiative cooling, the nanoparticles are significantly smaller than the infrared wavelength length scale of 8 – 14 μm.

Using laminate nanoparticle films gives extra degrees of control over design factors such as the fill fraction or ratio of mixed nanoparticle materials in the film which can give rise to effective optical properties difficult to replicate using simple dense laminate thin films. This increased control in design can enable the creation of a wide variety of structures including uniform index layers, graded index structures, and compositionally graded multilayer stacks. By extending the extra degrees of control in laminate nanoparticle films towards the design of passive daytime terrestrial radiative coolers, they can be used to create structures which are better optimized for terrestrial radiative cooling than can be achieved by classical thin film multilayer designs.

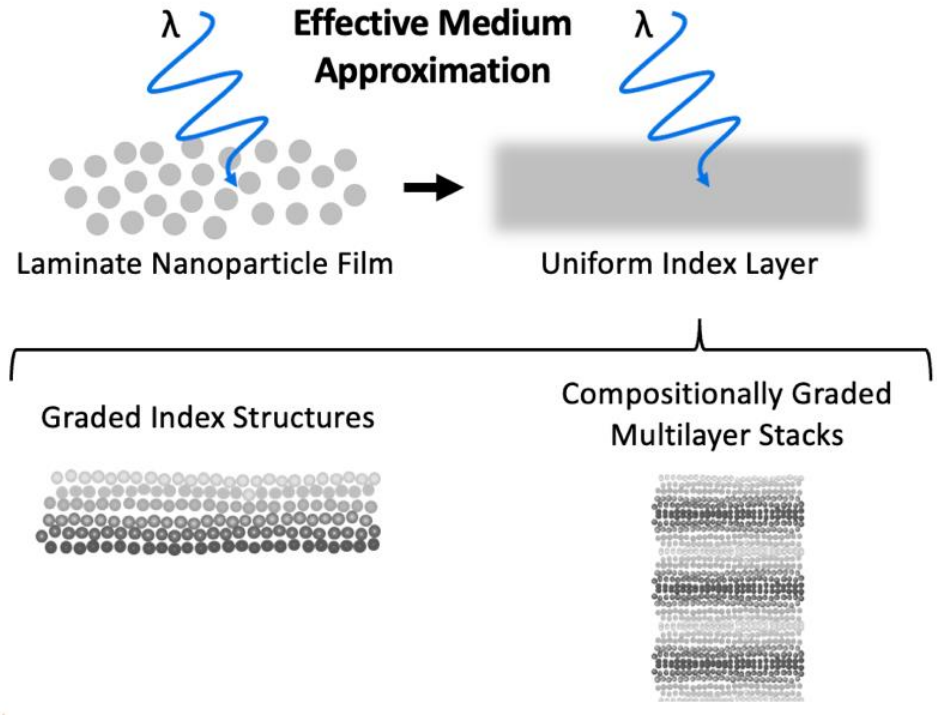

Figure 1.5. Schematic diagram showing a laminate nanoparticle film acting as a uniform index layer in the effective medium approximation size regime. Laminate nanoparticle films can be used to create graded index structures and compositionally graded multilayer stacks with effective optical properties different from their classical bulk thin film counterparts.

1.7 Nonthermal Plasma Synthesis

Laminate nanoparticle films can be produced from a synthesis method known as nonthermal plasma synthesis.[50,51] Nonthermal plasma synthesis is a technique which utilizes a plasma to nucleate and grow nanoparticles which can then be deposited uniformly as laminate nanoparticle films.

Briefly, nonthermal plasma synthesis of nanoparticles works by first applying a strong electric field to a gas. The electric field accelerates free electrons which cause a cascade of gas atom ionizations leading to more free electrons in an event known as electron avalanche. Over time, when the creation/recombination rates of ions/electrons are matched, a steady-state plasma is created. Here, the nonthermal property of the plasma refers to the fact that the

plasma is not at thermal equilibrium; the electrons are at significantly higher temperatures (11,000 – 55,000 K) compared to the gas ions (300 – 1200 K). In this steady state, the free electrons negatively charge the walls of the reactor and any larger species in the chamber. At this stage, nanoparticles are formed through a 3-step process. First, nucleation events create neutrally charged particle. Second, kinetics cause agglomeration of nucleated particles to form larger particles. Third, once the particles reach a size large enough to be charged by the free electrons in the plasma, the agglomeration phase ends, and particle growth continues through surface reactions with positive precursor ions in the plasma. As long as precursor gas is flowed through the plasma, the nanoparticles can continue growing in this phase. At this point, laminate nanoparticle films can be fabricated by stopping the precursor gas flow into the plasma and ejecting the nanoparticles onto a substrate.[52]

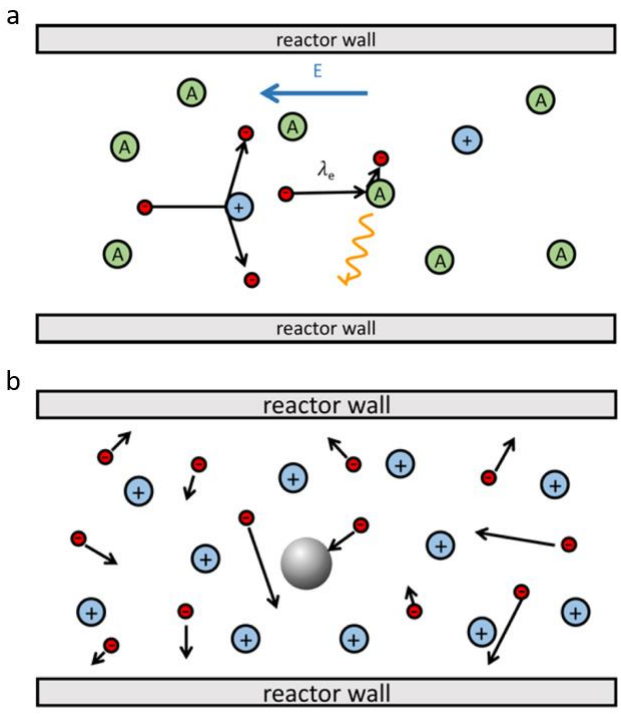

Figure 1.6. Schematic diagrams showing the processes and interactions occurring in a nonthermal plasma. (a) Elementary processes in a nonthermal plasma which include acceleration of electrons in the electric field, ionization of gas atoms, creation of free electrons, and inelastic interactions; (b) Charging effect of nanoparticles and reactor walls due to free electrons in the nonthermal plasma. Figure taken from [52].

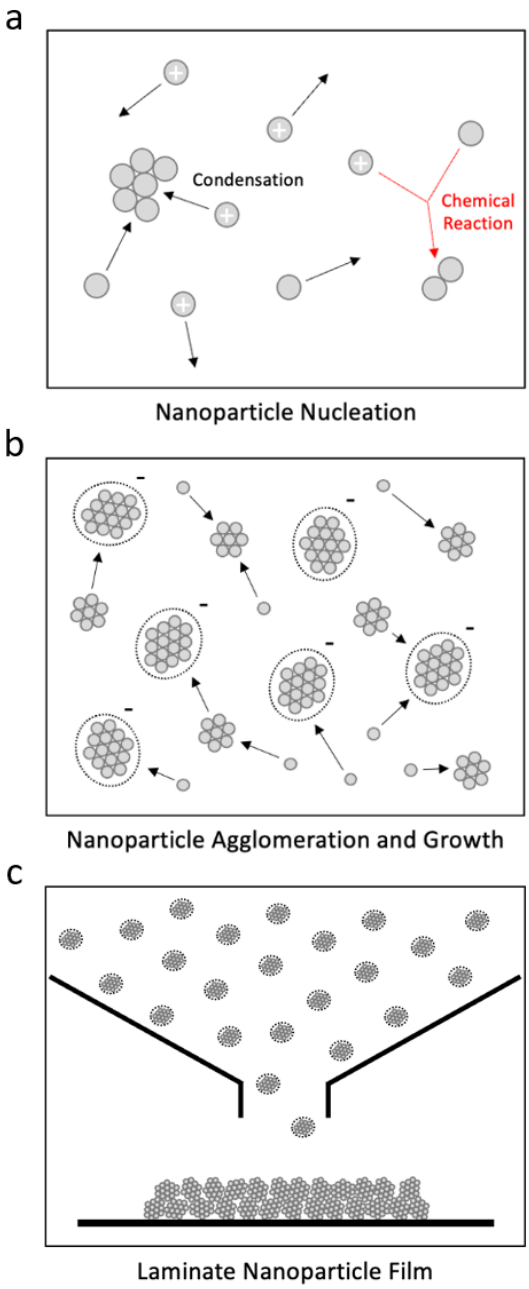

Figure 1.7. Schematic diagrams showing the process of nanoparticle formation in a nonthermal plasma and laminate nanoparticle film deposition. (a) Initial nucleation of particles in the plasma due to condensation or chemical reaction between ions; (b) Nanoparticle agglomeration between nucleates forms larger particles which become negatively charged by free electrons, leading to continued growth through surface reactions with positive precursor ions in the plasma; (c) Nanoparticle deposition onto a substrate forms a uniform laminate nanoparticle film.

Benefits of nonthermal plasma synthesis include its ability to produce extremely small nanoparticles ($r < 5$ nm), control nanoparticle size with narrow size distributions, produce high purity nanoparticles, produce nanoparticles of many different materials, and produce complex particles such as core/shell particles.[52] For the fabrication of laminate nanoparticle films, nonthermal plasma synthesis can be used to deposit films with uniform controlled thickness and fill fraction over wide areas. This technique provides a scalable method for fabricating large-scale laminate nanoparticle films as passive daytime terrestrial radiative coolers.

1.8 Scope of this Thesis

This thesis highlights the intersection between photonics and other fields to produce elegant multidisciplinary solutions for current sustainability challenges. Structured into three sections, this thesis investigates the application of photonics towards two different sustainable technologies as well as a new instrument for studying the thermal emission of photonic structures.

In Section I, we focus on the intersection between photonics and thermocatalysis to investigate and address challenges towards producing sustainable fuels from sunlight. Chapter 2 investigates the design of photonic structures as selective solar absorbers for collecting and converting solar energy into usable thermal energy. Chapter 3 discusses the design of a solar driven photothermal reactor which takes advantage of selective solar absorbers to drive thermocatalytic reactions. Chapter 4 presents the results of this multidisciplinary solution towards synthesizing sustainable fuels.

In Section II, we focus on the use of photonic nanoparticle films as radiative coolers to investigate and address challenges towards reducing global energy needs. Chapter 5 studies the physical and optical properties of laminate nanoparticle films. Chapter 6 investigates the advantages of laminate nanoparticle films for radiative cooling compared to current passive radiative cooling designs. Chapter 7 explores the fabrication and characterization of laminate nanoparticle films as effective radiative coolers.

In Section III, we report on a new instrument for studying the spectrally and angularly resolved radiative thermal emission of radiative cooling structures. Chapter 8 presents the design specifications, considerations, operational procedure, and results obtained from this instrument. This thesis aims to advance and explore our understanding and use of photonic solutions for tackling challenges found in current sustainable technologies.

SECTION I: GENERATING SUSTAINABLE FUELS FROM SUNLIGHT

Chapter 2

HARNESSING SOLAR THERMAL ENERGY WITH SELECTIVE SOLAR ABSORBERS

2.1 Introduction

As described in Chapter 1, selective solar absorbers have high absorptivity in the solar wavelength regime and low emissivity in the infrared wavelength regime, allowing them to capture solar thermal energy more efficiently than solar concentrators and black absorbers. Existing literature on selective solar absorbers have explored many ways for real materials and designs to mimic these ideal properties. Some of these representative designs include intrinsic absorbers with inherent favorable spectral emissivity, anti-reflective (AR) coatings on semiconductor materials, multilayer stacks of dielectric and metal layers, metal-dielectric composites, patterned microstructures on metals, and nanostructured photonic crystals.[18,53–59] Other designs have also explored nanoparticles or complex nanophotonic and metasurface structures to achieve elevated temperatures.[60–62]

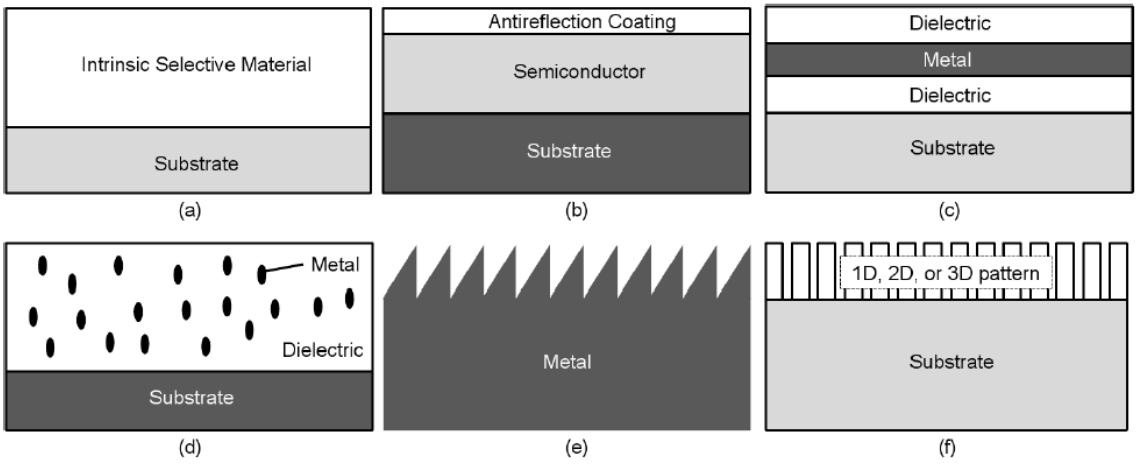

Figure 2.1. Representative schematic of six major types of selective solar absorbers commonly found in literature. The designs include: (a) intrinsic absorbers; (b) AR coated semiconductor materials; (c) metal-dielectric multilayer stacks; (d) metal-dielectric composites known as cermets; (e) surface textured metals; (f) nanostructured photonic crystal designs. Figure taken from [18].

In this chapter, we discuss the optimization procedure for designing efficient selective solar absorbers. We present work on three selective solar absorber designs: a transparent conducting oxide (TCO) absorber, a photonic crystal waveguide (PCWG) absorber, and a metal AR coated absorber. For each design, we report optimized design parameters and their maximum theoretical temperatures under 1 sun (1000 W/m^2) and 3 sun (3000 W/m^2) intensity. We also report their solar absorptivity and infrared emissivity. We discuss limitations pertaining to each design. Finally, we fabricate and report the optical characterization and thermal performance of the metal AR coated absorber under 1 sun intensity. Note that 1 standard sun intensity refers to the Reference Air Mass 1.5 Spectra (AM1.5) from the National Renewable Energy Laboratory (NREL).[15]

2.2 Principles of Selective Solar Absorbers

Selective solar absorbers work by absorbing light efficiently in the visible wavelength regime while having low absorptivity in the infrared wavelength regime. Due to Kirchhoff's Law of Thermal Radiation which states that a surface at thermal equilibrium must radiate the same amount of power that it absorbs, we can therefore define the emissivity of the surface at thermal equilibrium as equal to the absorptivity of the surface.[63] Thus, we can rephrase the first statement to state that selective solar absorbers work by having high emissivity in the visible wavelength regime while having low emissivity in the infrared wavelength regime. Due to the fact that the sun is approximately a blackbody at 5780 °C, which is spectrally centered far away from a room temperature blackbody at 300 °C, we can see that by splitting the emissivity of a surface into two regimes, one of high emissivity in the solar wavelength regime and one of low emissivity in the infrared wavelength regime, we can create an efficient selective solar absorber.

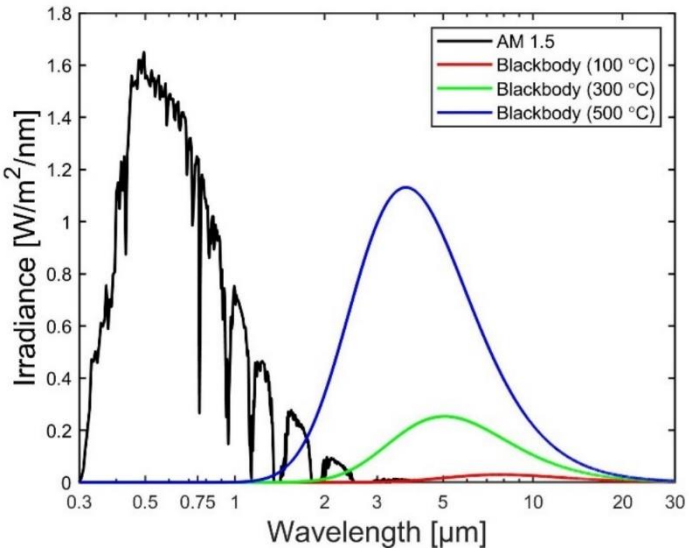

Figure 2.2. Comparison in the spectral centering between the AM1.5 solar spectrum and blackbody curves at various temperatures. The spectral center of the solar irradiance is approximately 0.5 μm and the blackbody curves are centered at approximately 8 μm (100 °C), 5 μm (300 °C), and 4 μm (500 °C).

In order to calculate the expected temperature of a selective solar absorber, we first write the power balance of the surface from the 1st Law of Thermodynamics:

$$P_{net} = P_{in} - P_{out} \tag{2.1}$$

$$P_{in} = P_{solar} \tag{2.2}$$

$$P_{out} = P_{rad} + P_{conv,cond} \tag{2.3}$$

$$\therefore P_{net} = P_{solar} - P_{rad} - P_{conv,cond} \tag{2.4}$$

As we can see from **Eq. 2.4**, the net power that the surface observes is the difference between the total solar energy gained by the surface and the total energy lost from the surface, either through radiative pathways or non-radiative pathways, namely convection and conduction. Thus, we can see mathematically that a selective solar absorber aims to maximize P_{solar} while minimizing P_{rad}.

Within **Eq. 2.4**, we can define the total solar energy absorbed by a surface as:

$$P_{solar} = A \int_0^{\infty} I_{AM1.5}(\lambda)\epsilon(\lambda)d\lambda \tag{2.5}$$

Where A is the area of the surface, $I_{AM1.5}(\lambda)$ is the AM1.5 solar spectrum incident on the surface, and $\varepsilon(\lambda)$ is the wavelength-dependent emissivity of the surface. Here, we note that for **Eq. 2.5**, we only integrate across the wavelength because we treat the incident solar radiation as a plane wave. As such, for a surface facing the sun at normal incidence, we use only the normal incidence emissivity (and for incident sunlight at other angles, we use the corresponding emissivity at that angle).

Next, the energy radiated by the surface via blackbody radiative emission can be defined as:

$$P_{rad} = 2\pi A \int_0^{\frac{\pi}{2}} \int_0^{\infty} I_B(\lambda, T)\epsilon(\lambda, \theta) \sin\theta \cos\theta \, d\lambda d\theta \tag{2.6}$$

Where $I_B(\lambda,T)$ is the blackbody spectral irradiance at temperature T of the surface and $\varepsilon(\lambda,\theta)$ is the wavelength and angle-dependent emissivity of the surface. Note here that **Eq. 2.6** integrates over the entire hemispherical radiative emission from the surface. This is because radiative thermal emission radiates in all directions away from the surface. Also, $I_B(\lambda,T)$ is defined explicitly by Planck's Law as:

$$I_B(\lambda, T) = \frac{2hc^2}{\lambda^5} \frac{1}{e^{\frac{hc}{\lambda k_B T}} - 1} \tag{2.7}$$

Where h is Planck's constant, k_B is the Boltzmann constant, and c is the speed of light. For surfaces whose emissivity is constant across all wavelengths, Stefan-Boltzmann Law can instead be used to simplify P_{rad}:

$$P_{rad} = A\epsilon\sigma T^4 \tag{2.8}$$

Where σ is the Stefan-Boltzmann Constant. Finally, we approximate the non-radiative heat loss component as a simple linear relationship:

$$P_{conv,cond} = QA(\mathrm{T} - T_a) \tag{2.9}$$

Where T_a is the ambient temperature surrounding the surface, and Q is the non-radiative heat loss coefficient. Q is a representative value which encompasses all of the effects of non-radiative loss into a single variable for simplicity. Note that when calculating the maximum theoretical temperature of a surface, we ignore all non-radiative effects (Q = 0 $W/m^2/K$). From these equations, we now find by substituting **Eq. 2.5 – 2.9** into **Eq. 2.4** the following generalized relationship with respect to temperature:

$$P_{net}(T) = P_{sun} - P_{rad}(T^4) - P_{conv,cond}(T) \tag{2.10}$$

Thus, we can see from **Eq. 2.10** that the radiative emission has a significant impact on the maximum theoretical temperature that a surface can reach. From these equations, we can now calculate the maximum temperature of a surface given its emissivity. By setting P_{net} = 0 W/m^2 and solving for T, which is encompassed in **Eq. 2.6** and **Eq. 2.9**, we find the equilibrium temperature at which the total absorbed power of sunlight equals the total power lost through radiative and non-radiative loss. In sections 2.2.1 and 2.2.2, we observe several consequences of these equations.

2.2.1 Lower Limit Performance

Here, we find the maximum theoretical temperature of a perfectly absorbing black surface. A perfectly absorbing blackbody is also a perfectly emitting blackbody due to Kirchhoff's Law of Thermal Radiation, thus ε(λ,θ) = 1 for all wavelengths and angles. When calculating the theoretical maximum temperature of a surface, we ignore all non-radiative effects. Using **Eq. 2.5**, we find that the overall solar power flux is approximately 1000 W/m^2, which matches our expectation that the integral of the AM1.5 solar spectrum returns 1 sun intensity. Setting P_{net} = 0 in **Eq. 2.4**, we now solve for the temperature which corresponds to a

blackbody that radiates with a power of 1000 W/m^2. Thus, we find that the corresponding blackbody temperature is approximately 91 °C.

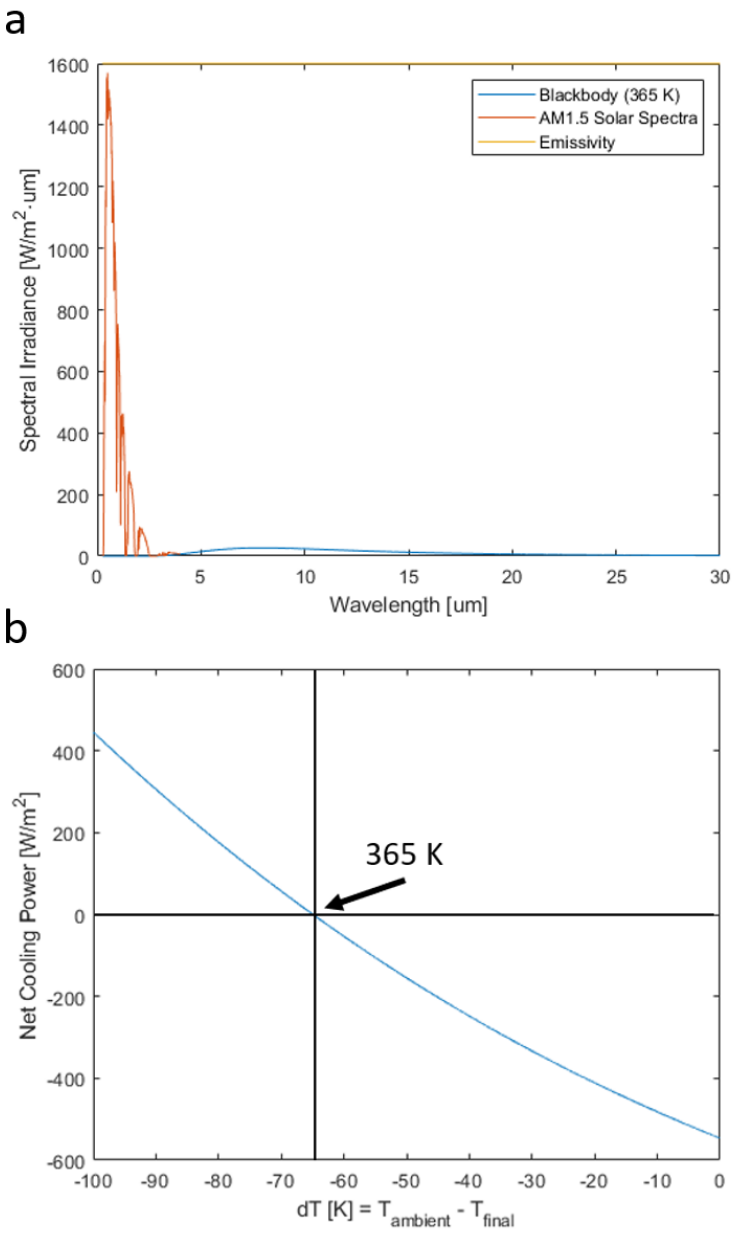

Figure 2.3. (a) Comparison between the AM1.5 solar spectrum and the blackbody irradiance curve at 91 °C. Both curves have a total power of 1000 W/m^2. The emissivity for a perfectly absorbing surface is overlaid; (b) The net cooling power experienced by a perfectly absorbing surface as a function of temperature. Here dT is the difference between the ambient temperature (300 K) and the surface temperature.

From this result, we can see that any applications which require temperatures higher than 91 °C will require either solar concentrators or selective solar absorbers to achieve their temperature requirements. While solar concentrators can also achieve high temperatures, their implementation generally requires more complexity, bulk, and space than selective solar absorbers.[17] Furthermore, we can take this temperature as the practical lower limit for selective solar absorber performance since any absorber which has a maximum temperature below 91 °C can essentially be replaced by a simple black surface.

2.2.2 Upper Limit Performance

Here, we calculate an upper limit on performance for a selective solar absorber. We begin by studying a surface with an emissivity which is 1 across the entire solar wavelength regime and 0 everywhere else, also known generally as an ideal selective solar absorber. In other words, this surface has an emissivity window which can be represented by a rectangular function:

$$\epsilon(\lambda) = \begin{cases} 1, & \text{if } 0.3\ \mu\text{m} \leq \lambda \leq 4\mu\text{m} \\ 0, & else \end{cases} \tag{2.11}$$

Performing the same calculation outlined in the previous sub-section, we find that the maximum theoretical temperature of this structure is approximately 324 °C.

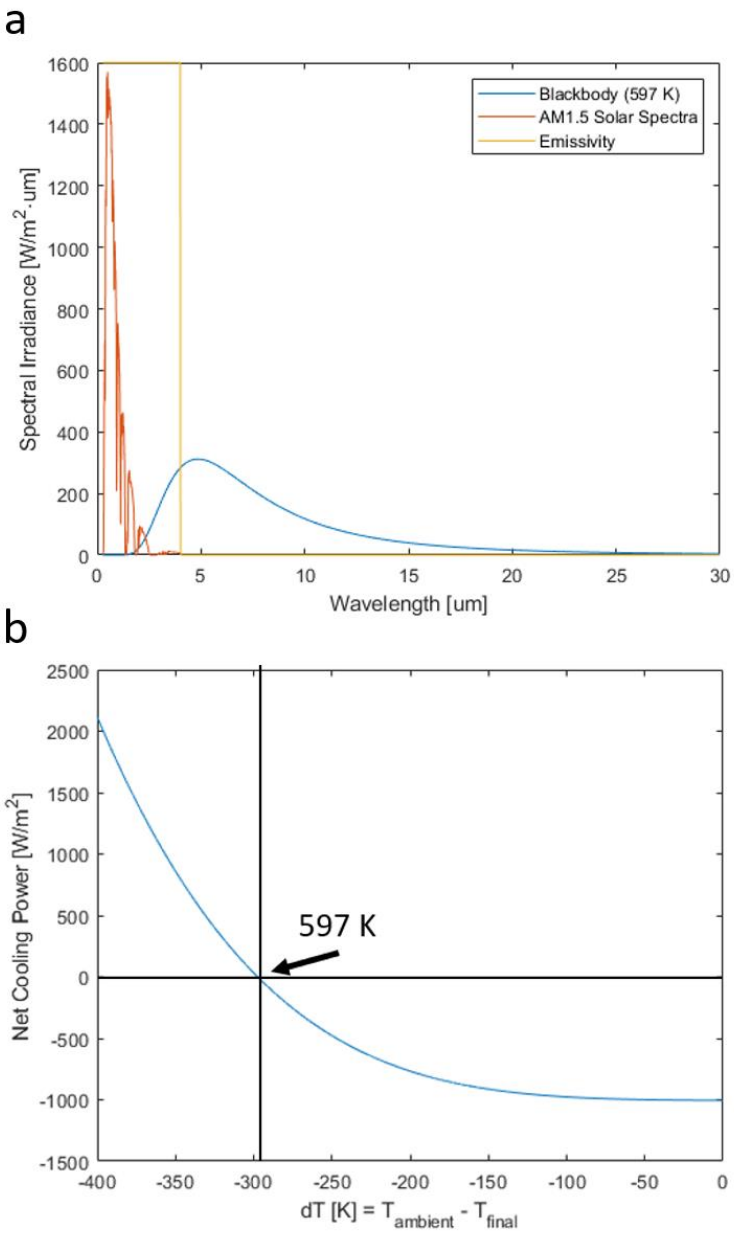

Figure 2.4. (a) Comparison between the AM1.5 solar spectrum and the blackbody irradiance curve at 324 °C. The emissivity for an ideal selective solar absorber is overlaid; (b) The net cooling power experienced by an ideal selective solar absorber as a function of temperature. Here dT is the difference between the ambient temperature (300 K) and the surface temperature.

Furthermore, we can increase the temperature by moving the right boundary of the rectangular function to even shorter wavelengths. When we reduce this emissivity window, we see that the maximum theoretical temperature rapidly rises: this is because the integral of the tail of the blackbody curve at short wavelengths must match the total absorbed solar power flux. However, the practical trade-off for this increase in temperature is loss in heating rate: as the emissivity window becomes smaller, the rate of heating of the surface also decreases due to the decrease in total absorbed solar power flux.

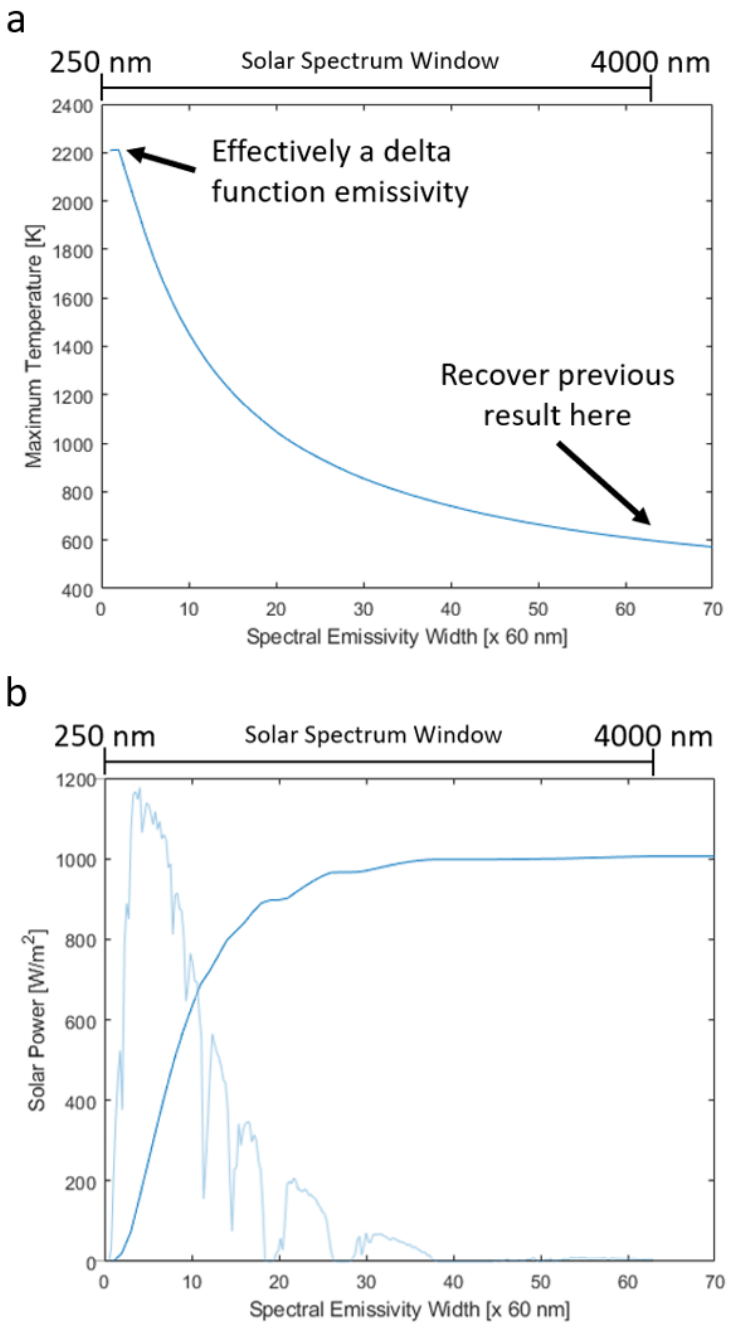

Figure 2.5 (a) Maximum theoretical temperature of a rectangular emissivity window as a function of the spectral size of the emissivity window. The emissivity window is bounded on the left at 0.3 μm; (b) The total absorbed solar power as a function of the emissivity spectral window size.

From this result, we find an effective upper limit on selective solar absorber performance. It is also important to note that once non-radiative effects are considered, the maximum theoretical temperature will reduce further; thus, a broad unitary emissivity window which covers most of the solar wavelength regime will generally reach a higher temperature in practice than a narrow window, especially given diurnal time constraints.

2.3 Absorber Design and Optimization

Here, we outline our procedure for designing and optimizing selective solar absorbers:

1. We begin the design stage by qualitatively selecting appropriate materials which have optical properties that may yield a favorable emissivity curve.
2. Once the candidate materials are chosen, we fabricate the individual material layers and optically characterize the bulk material properties by extracting their complex refractive index using visible and infrared ellipsometry.
3. Using the extracted complex refractive index, we apply ray transfer-matrix method to calculate the reflectivity, transmissivity, and absorptivity/emissivity of any multilayer stack comprised of those materials.[64]
4. Using the calculated emissivity, we calculate the maximum theoretical temperature of the design using the procedure outlined in Section 2.2.
5. We perform a parametric sweep of the design space, usually the layer thickness and order, and report the design with the highest temperature performance.

Using this procedure, we study and report on 3 unique designs:

1. Indium tin oxide (ITO) absorber
2. Photonic crystal waveguide (PCWG) absorber
3. Metal AR coated absorber

2.3.1 ITO Absorber

The first design we present is a transparent conducting oxide (TCO) layer on an absorbing substrate. TCOs are materials which possess both transparent and conducting properties due to the fact that their carrier density and mobility lie in-between values commonly found for metals and semiconductors. This results in a material which is transparent in the visible wavelength regime, but reflective in the infrared wavelength regime.[65]

To explain this phenomenon, we first note that reflectivity can be understood in conducting materials to be the result of carriers in a material oscillating at the frequency of the incident light, producing a plasma oscillation. As the frequency of the light increases, the carriers become unable to keep up with this increase in electromagnetic frequency, and the light instead transmits through the material without reflection. The maximum frequency at which these plasma oscillations occur is known as the plasma frequency of the material, and is defined as:

$$\omega_p = \frac{ne^2}{\epsilon_0 m} \tag{2.12}$$

Where n is the carrier concentration, m is the electron rest mass, and ε_0 is the vacuum permittivity. We can also re-write this as the plasma wavelength of the material:

$$\lambda_p = \frac{2\pi c}{e}\sqrt{\frac{\epsilon_0 m}{n}} \tag{2.13}$$

Where c is the speed of light. Thus, from **Eq. 2.13**, we can see that as the carrier concentration increases, λ_p decreases; this means that for most metals which have high carrier concentrations and high conductivity, their plasma wavelength is located near the ultraviolet wavelength regime, resulting in a material which is highly reflective in the visible wavelength regime. Alternatively, insulating materials which have low carrier concentrations and low conductivity have long plasma wavelengths resulting in their transparent nature. In TCOs, since their conductivity lies between metals and semiconductors, they possess a

plasma wavelength in the near or mid-IR wavelength regime while being transparent in the visible wavelength regime. This results in a material that has both transparent and conducting properties.[65]

To take advantage of this, we propose a selective solar absorber comprised of an ITO layer on an absorbing substrate, either silicon or germanium. The reason we chose ITO is because ITO is the most widely used commercial transparent conducting oxide. A silver back reflector was added to prevent loss of solar energy through the back of the absorber.

Figure 2.6. Schematic of an ITO-based selective solar absorber.

Following the procedure outlined at the beginning of Section 2.3, once the ITO design was selected, ITO layers were fabricated for characterization. The 75 nm ITO layers were deposited by sputter deposition with 0.4 sccm O_2 and 20 sccm Ar gas flow onto a silicon substrate. After deposition, the material was characterized by visible and infrared ellipsometry. A Drude-Lorentz oscillator model was used for the ellipsometry model for ITO. Fitting the ellipsometry data, we found that the carrier concentration for the ITO was 3.47×10^{20} cm^3 with a corresponding plasma wavelength of 1.79 μm.

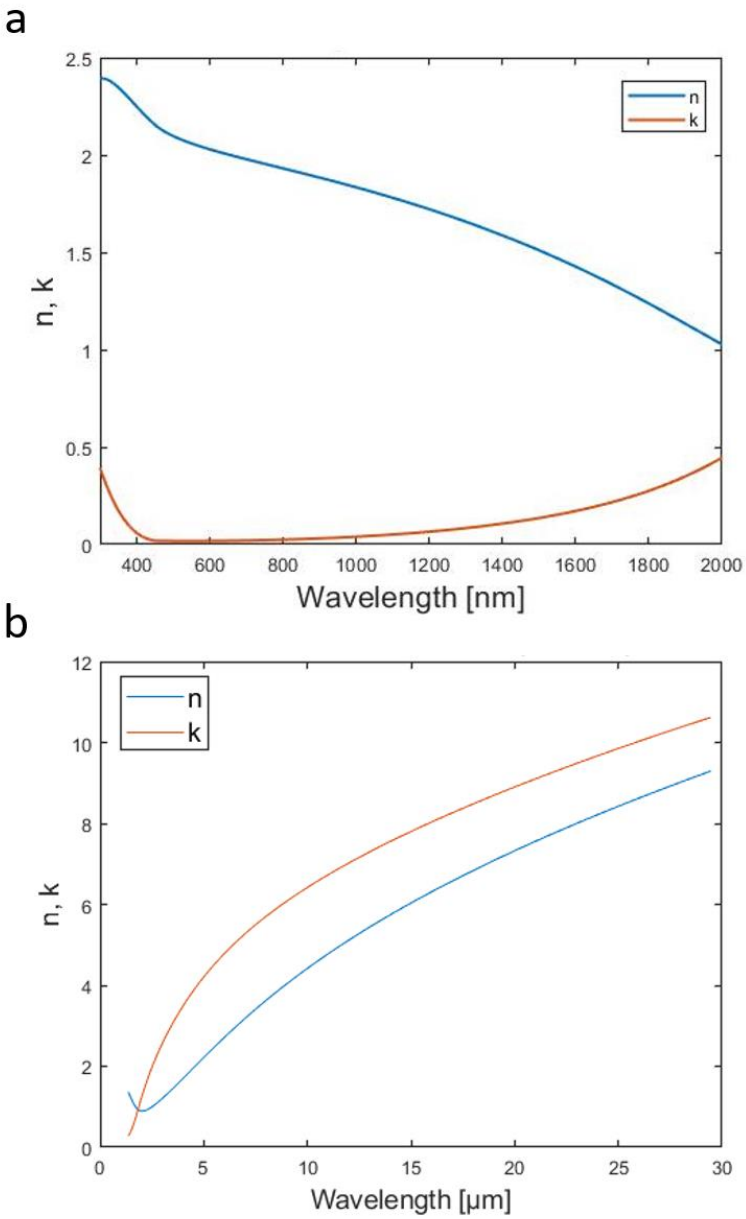

Figure 2.7. Complex refractive index of sputter deposited ITO from ellipsometry in the (a) visible and (b) infrared wavelength regime.

Using the complex refractive index of ITO in **Fig. 2.7**, we calculated the corresponding reflectivity, transmissivity, and absorptivity of the multilayer design presented in **Fig. 2.6** using ray transfer matrix method.[64] We observe that the ITO layer gives high transmissivity in the solar wavelength regime and high reflectivity in the infrared wavelength regime as

expected for a TCO material. Using the emissivity calculated from ray transfer matrix method, we calculate the maximum theoretical temperature of each structure with the procedure outlined in Section 2.2. For this specific design, we swept the ITO thickness parameter space on both a silicon and germanium substrate and reported the maximum temperatures and optimal parameters for this design.

Table 2.1. Maximum theoretical temperature of an ITO absorber with varying thickness and substrate under 1 sun intensity.

ITO Thickness [nm]	Si Substrate: Max Temp [°C]	Ge Substrate: Max Temp [°C]
25	102.6	108.6
100	146.8	154.1
200	177.8	183.1
300	200.4	204.3
400	212.0	213.7
600	218.0	216.9
800	219.6	218.0
1000	220.2	219.6

From the optimization results, we find that increasing ITO thickness past 500 nm results in diminishing returns for the increase in the maximum temperature. We also find that at thicker ITO layers, the Si substrate outperforms the Ge substrate. As such, we recommend the following design parameters: 500 nm ITO layer with carrier concentration 3.47×10^{20} cm^3 on a 500 μm silicon substrate with a silver back reflector. The calculated maximum temperature of this ITO absorber is approximately 217 °C and 350 °C under 1 sun and 3 sun intensity, respectively. The absorber has a solar absorptivity of 81.8% and an infrared emissivity of 25.0% at 217 °C. Note that we report the infrared emissivity at a specific temperature because the blackbody irradiance curve shifts spectrally with respect to temperature.

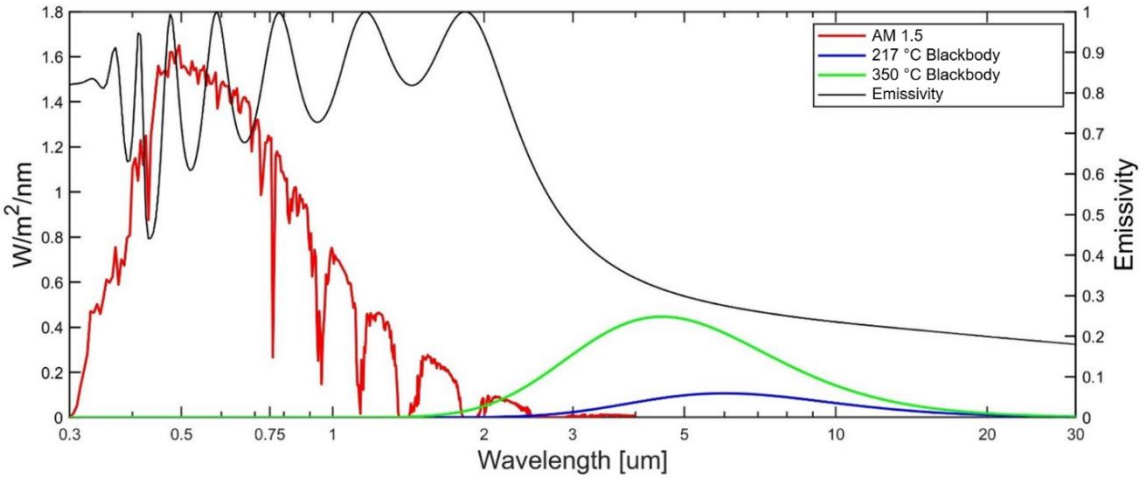

Figure 2.8. Calculated emissivity for a 500 nm ITO absorber overlaid with the AM1.5 solar spectrum and blackbody curves at 217 °C and 350 °C. The blackbody curves are at the absorber's maximum theoretical temperature under 1 sun and 3 sun intensity.

2.3.2 PCWG Absorber

The second design we present is a photonic crystal waveguide (PCWG) based selective solar absorber. A photonic crystal is a nanostructure capable of manipulating electromagnetic waves due to its structured periodicity. Here, the photonic crystal is designed as an infrared photon (thermal) concentrator, directing and trapping infrared radiation along its waveguide mode. The proposed PCWG design utilizes periodic hole arrays in a germanium layer. Germanium was chosen due to its high refractive index, absorption coefficient stability in the visible wavelength regime, and its very low loss infrared properties. The design was optimized by iterating the layer thickness, hole-to-hole pitch, hole radius, and material refractive index. Note that the design and optimization of the photonic crystal waveguide is not a part of the scope of this thesis and was performed by another student.

Here we report the following parameters for an optimized PCWG absorber: 3.1 μm germanium layer with real(n) = 1.5, 0.775 μm hole radius, 3.1 μm pitch. The absorptivity of the PCWG design was extracted, and following the procedure outlined in Section 2.2, the maximum theoretical temperature was calculated. The calculated maximum temperature of this selective solar absorber design is approximately 389 °C and 560 °C under 1 sun and 3

sun intensity, respectively. The PCWG absorber has a solar absorptivity of 51.1% and an infrared emissivity of 4.7% at 389 °C.

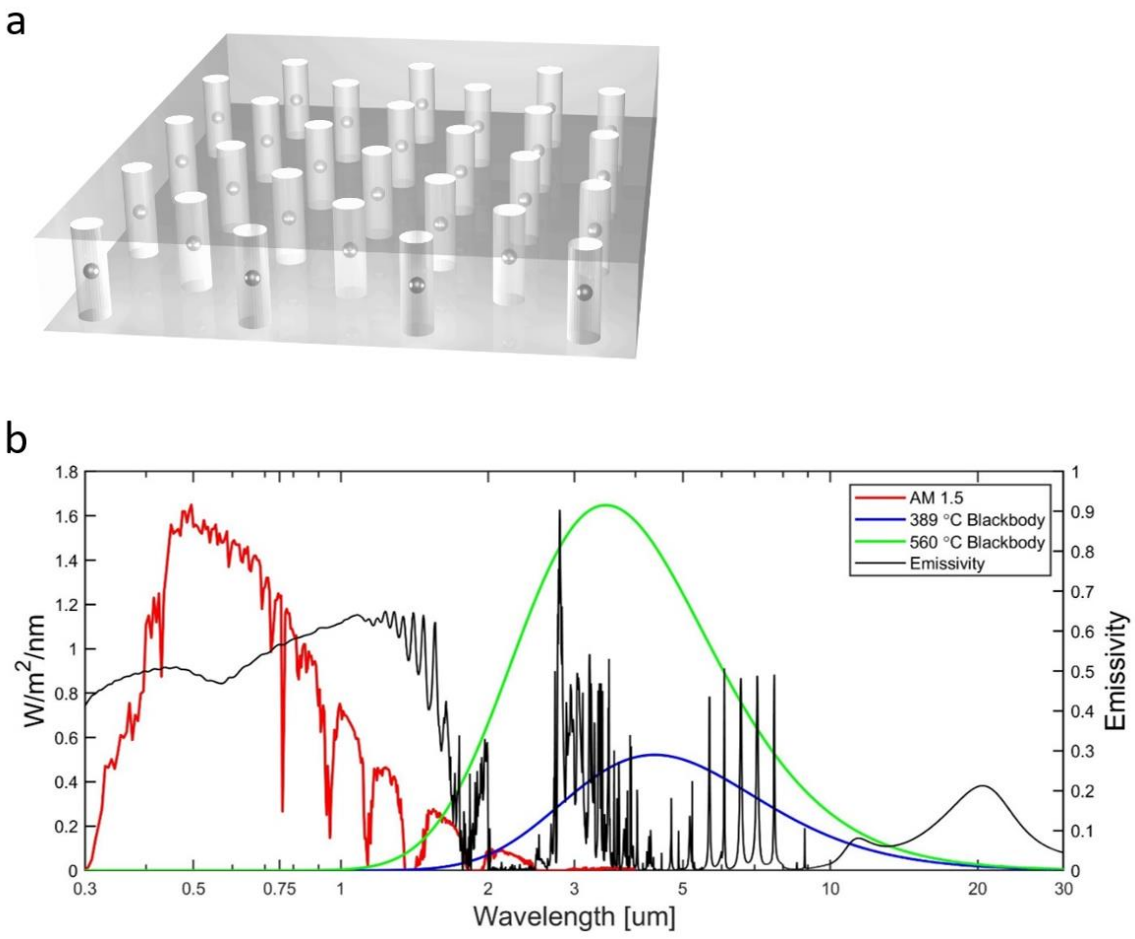

Figure 2.9. (a) Model of a PCWG absorber with hole arrays; (b) Calculated emissivity for an optimized PCWG absorber overlaid with the AM1.5 solar spectrum and blackbody curves at 389 °C and 560 °C. The blackbody curves are at the absorber's maximum theoretical temperature under 1 sun and 3 sun intensity.

We can see that even though the solar absorption in the PCWG absorber is lower than the ITO absorber, the maximum theoretical temperature is higher because the radiative thermal power is significantly lower. As a consequence of **Eq. 2.10**, the decrease in radiative power contributes more greatly to the maximum temperature than the increase in solar absorption.

2.3.3 Metal AR Coated Absorber

The third design we present is a multilayer structure comprised of a coupled metal layer and AR coating on an absorbing substrate. Here, we use both an AR coating and an optically thin transparent layer of metal to increase the absorptivity of the substrate layer in the solar wavelength regime and decrease the emissivity of the surface in the infrared wavelength regime, respectively. The metal layer must be sufficiently thin such that it is transparent to visible light but remain highly reflective to infrared radiation. Furthermore, if we layer the metal layer on the AR coating, we can potentially create a metal-dielectric interface which acts as a plasmonic waveguide that suppresses outgoing infrared thermal radiation by confining it along the metal-dielectric interface.

For materials selection, we chose silicon or germanium as the substrate. For the AR coating, we chose silicon nitride due to its well-known commercial use as an anti-reflective coating.[66] For the optically transparent metal layer, we chose gold and silver due to their stability and their favorable plasma wavelength compared to other metals such as aluminum. A silver back reflector was added to prevent loss of solar energy through the back of the absorber.

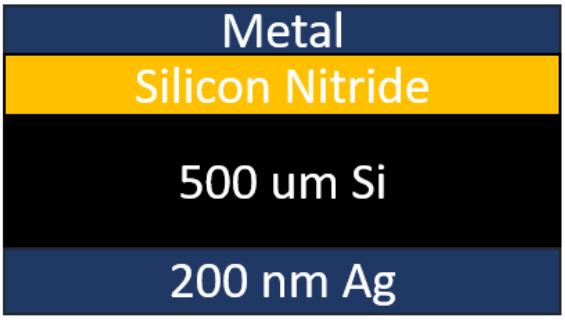

Figure 2.10. Schematic of a metal AR coated selective solar absorber.

Once the materials were selected, we deposited individual layers of silicon nitride, gold, and silver. The 50 nm gold and silver layers were deposited by electron beam evaporation on silicon, and 50 nm silicon nitride was deposited by plasma-enhanced chemical vapor deposition (PECVD) at 200 °C on silicon. After deposition, the layers were measured in

visible and infrared ellipsometry and fitted using the J.A. Woollam library oscillator models for each specific material. From the ellipsometry results, we confirmed that electron beam deposited gold and silver complex refractive index was extremely well-matched with literature values. The PECVD deposited silicon nitride complex refractive index is shown in **Fig. 2.11**.

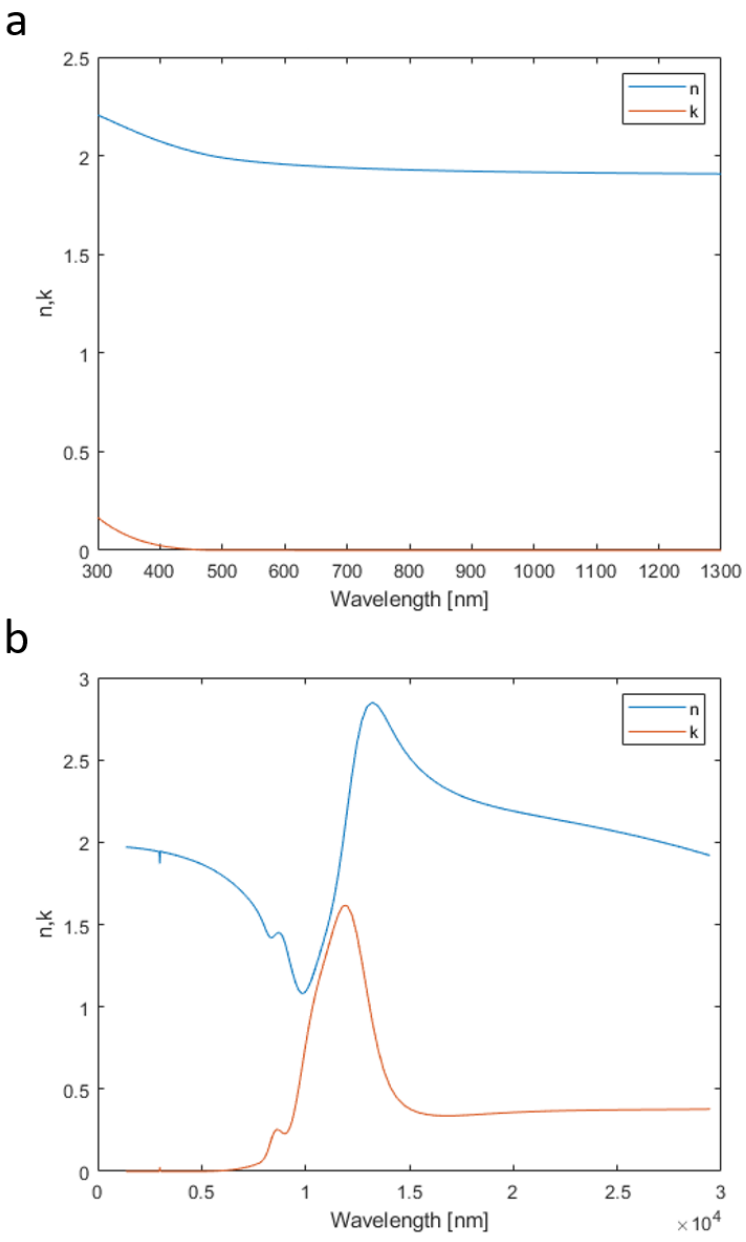

Figure 2.11. Complex refractive index of PECVD deposited silicon nitride from ellipsometry in the (a) visible and (b) infrared wavelength regime.

Applying the bulk material complex refractive index results to the schematic presented in **Fig. 2.10**, we use ray transfer matrix method to calculate the reflectivity, transmissivity, and absorptivity of the multilayer structure.[64] For this design, we swept the substrate material (Si, Ge), metal material (Au, Ag), metal thickness, silicon nitride thickness, and metal-silicon nitride layer order. From the emissivity, we calculate the maximum theoretical temperature and report the design parameters for the highest temperature absorber.

We report the design parameters for the highest performing silver and highest performing gold AR coated absorbers: 10 nm silver layer on 70 nm silicon nitride layer on a silicon substrate with silver back reflector, and a 13 nm gold layer on 70 nm silicon nitride layer on a silicon substrate with silver back reflector. The maximum theoretical temperature of each selective solar absorber design was: 448 °C and 614 °C under 1 sun and 3 sun intensity for the silver structure, and 428 °C and 611 °C under 1 sun and 3 sun intensity for the gold structure. The silver AR coated absorber has an average solar absorptivity of 46.1% and an infrared emissivity of 3.0% at 448 °C, while the gold AR coated absorber has an average solar absorptivity of 47.4% and an infrared emissivity of 3.5% at 428 °C.

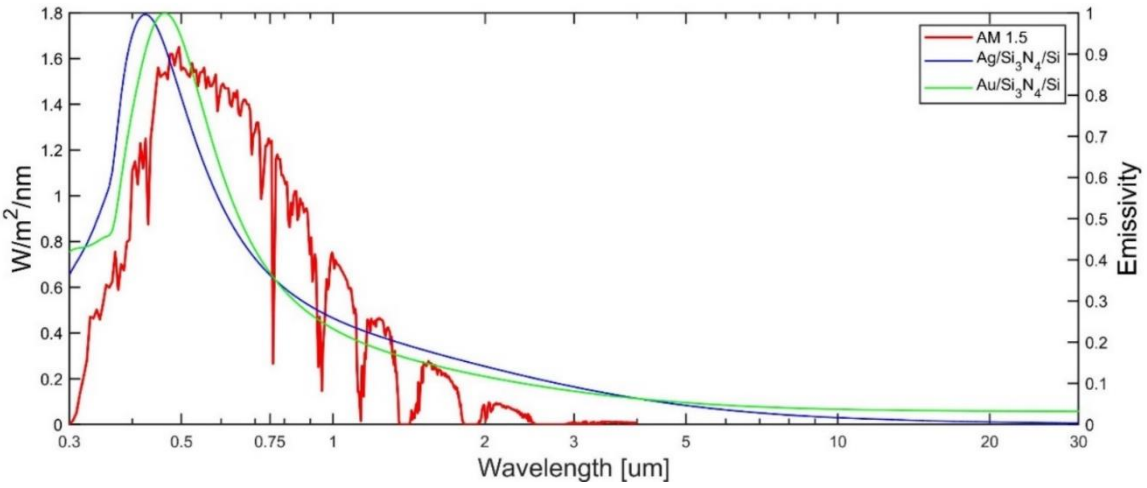

Figure 2.12. Calculated emissivity for the highest performing silver AR coated absorber and gold AR coated absorber overlaid with the AM1.5 solar spectrum.

As we can see, the metal AR coated absorber has a similar solar absorptivity compared to the PCWG absorber while also having an even lower infrared reflectivity. As a result, this structure has the highest maximum theoretical temperature of the three designs that we studied.

2.4 Fabrication

For full scale selective solar absorber fabrication and testing, we chose to move forward with the gold AR coated absorber. This is because the gold AR coated absorber is the least complex to fabrication and most scalable for industrial applications: the ITO carrier concentration in the ITO absorber could not be consistently controlled between deposition runs, and the PCWG absorber was inherently difficult to fabricate. Furthermore, the gold AR coated absorber had the highest predicted temperature performance. Between the gold and silver AR coated absorber, gold was chosen due to its stability in air compared to silver which tarnishes to silver oxide.

For the fabrication process, 70 nm of silicon nitride was deposited by PECVD on a silicon substrate, then 13 nm of gold was deposited by electron beam evaporation. Electron beam evaporation was also used to deposit a 200 nm silver back reflector on the reverse side of the selective solar absorber.

During initial fabrication, it was discovered that ultrathin layers (< 20 nm) of gold could not be deposited uniformly without a wetting layer.[67–70] When gold is deposited, it initially forms islands on the surface, which then coalesce as more material is deposited until all of the islands are connected as a uniform surface. For thicknesses under 20 nm, the gold layer forms only a non-uniform disconnected layer which greatly reduces its reflectivity in the infrared wavelength regime. We observed this phenomenon both indirectly and directly. When the

emissivity of the selective solar absorber was measured, the reflectivity in the infrared wavelength regime was significantly lower expected. This was corroborated by scanning electron microscopy (SEM) images showing gold non-uniformity on the surface of the selective solar absorber.

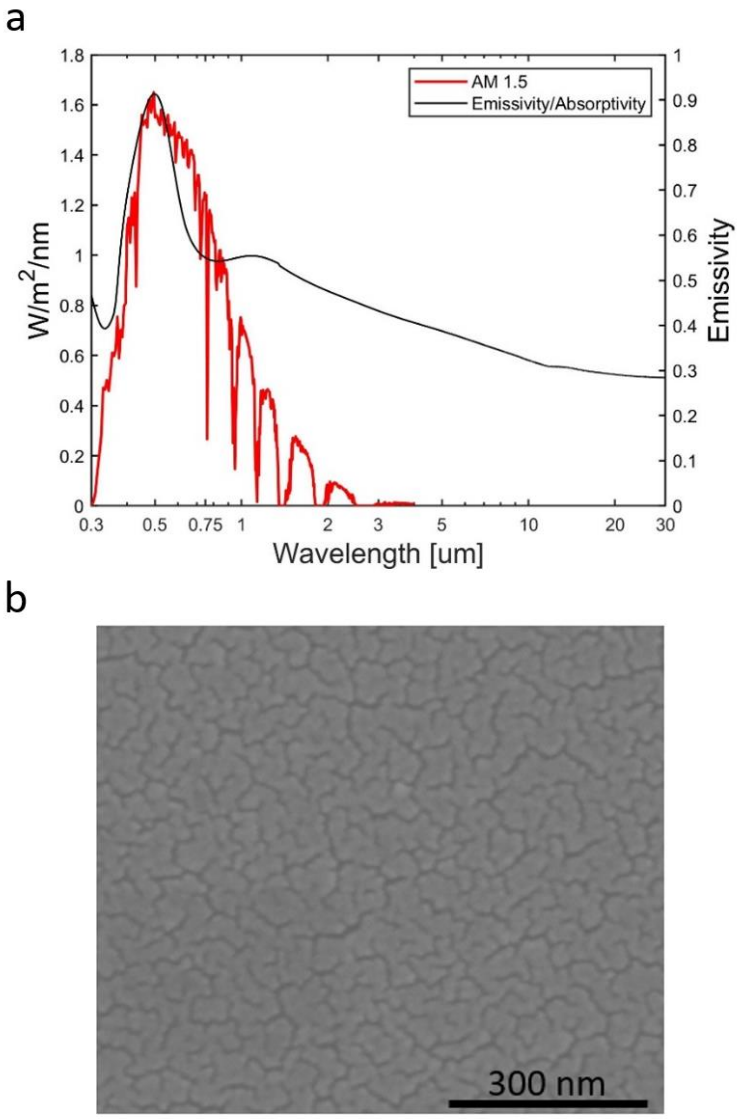

Figure 2.13. (a) Absorptivity of a gold AR coated absorber showing poor reflectivity in the infrared wavelength regime due to non-uniformity in the ultrathin gold layer; (b) SEM image showing the surface of the absorber.

To resolve this issue, a 1 nm germanium layer was added as a wetting layer underneath the gold layer. This resolved the issue as confirmed in both visible and infrared ellipsometry and SEM. We also confirmed using ray transfer matrix method that a 1 nm germanium layer had no effect on the emissivity of the multilayer stack. Thus, the final gold AR coated absorber design is a multilayer stack comprised from top to bottom with 13 nm gold, 1 nm germanium, 70 nm silicon nitride, 500 μm silicon, and 200 nm silver back reflector.

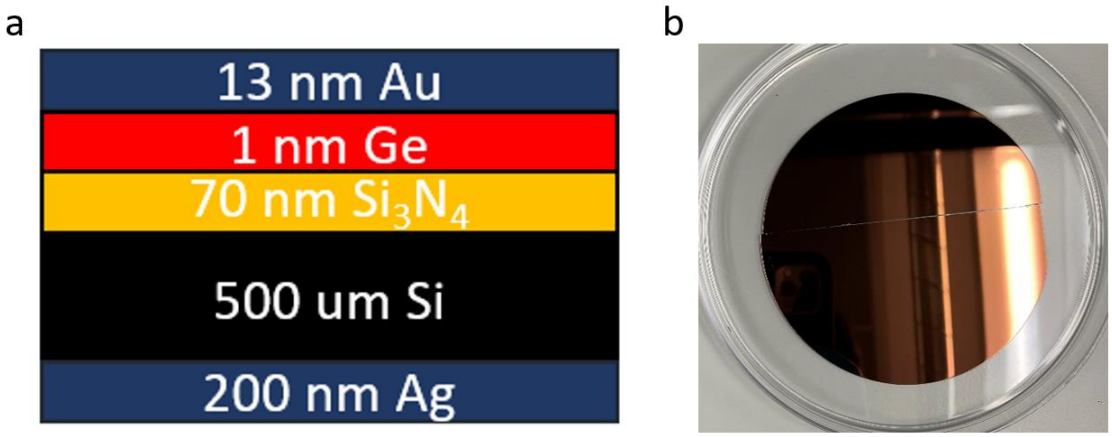

Figure 2.14. (a) Schematic of an optimized gold AR coated selective solar absorber; (b) Image of a 4-inch diameter gold AR coated absorber.

2.5 Optical Characterization

Visible and infrared ellipsometry was used to characterize the selective solar absorber. The complete ellipsometry model was constructed from the individual materials models previously used to fit each material during the optimization process. For the ellipsometry model, all of the oscillator models for each layer and thickness were fit simultaneously. Ray transfer matrix method was used to calculate the emissivity, and the emissivity was used to calculate the maximum theoretical temperature.

From the ellipsometry results, we report the thickness of each layer: 11.5 nm gold, 0.7 nm germanium, and 67.9 nm silicon nitride. This matches well with our optimized structure

design parameters. From the emissivity, we recalculated the maximum temperature of the absorber: 249 °C and 416 °C under 1 sun and 3 sun intensity, respectively. We attribute this temperature decrease from the optimized absorber to the fact that the ultrathin layer of gold is not perfectly smooth. As such, we see a sizable increase in the infrared emissivity from 3.5% to 11.7% for the fabricated absorber compared to the theoretical absorber. The solar absorptivity increased slightly from 47.4% to 49.2%.

Finally, we also observe the angle-dependent emissivity. This is interesting because a wide range angle of absorption allows for better solar absorption as the sun moves across the sky. We also calculate the electromagnetic field mode profile of the absorber with the electric and magnetic field intensities plotted versus structure depth with an incident 500 nm plane wave.

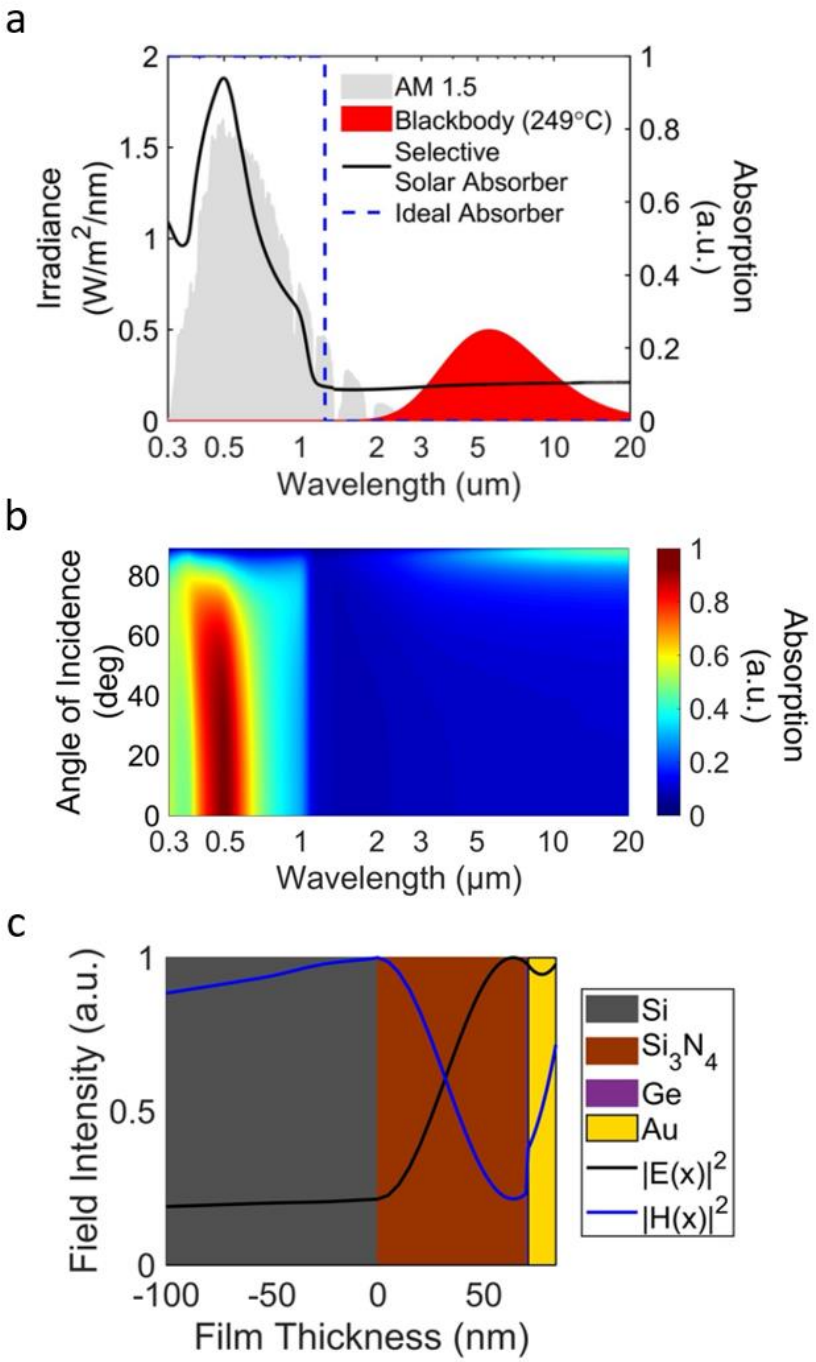

Figure 2.15 (a) Emissivity of a gold AR coated absorber overlaid with the AM1.5 solar spectrum and blackbody curve at 249 °C, the maximum theoretical temperature of the absorber; (b) Angle-dependent emissivity of the absorber; (c) Electromagnetic mode profile versus film depth of the absorber.

2.6 Thermal Performance

To measure the thermal performance of the gold AR coated absorber, we placed the absorber inside a vacuum chamber with a quartz window. The structure was balanced on a thin bare wire type K thermocouple with thermal paste for increased adhesion and thermal conductivity between the thermocouple junction and absorber. A vacuum level of approximately 1 mTorr (1.3×10^{-6} Bar) was generated with a rough pump to reduce non-radiative heat loss. Solar radiation was introduced with an ABET Sun 3000 Simulator. The solar irradiance was independently measured with a ThorLabs power meter. Under a solar intensity of 1000 W/m^2, the absorber measured a peak temperature of 121 °C over a period of 120 minutes.

Finally, we fit for the non-radiative heat loss coefficient Q to better understand how much heat is lost to the environment. By using **Eq. 2.9** in the power balance equation, we calculate Q such that the calculated temperature matches the experimentally measured temperature. Taking the area of the absorber into account and the fact that environmental heat loss pathways conduct through both the top and bottom surfaces of the absorber, we find a final Q = 1.8 W/m^2/K for this vacuum environment.

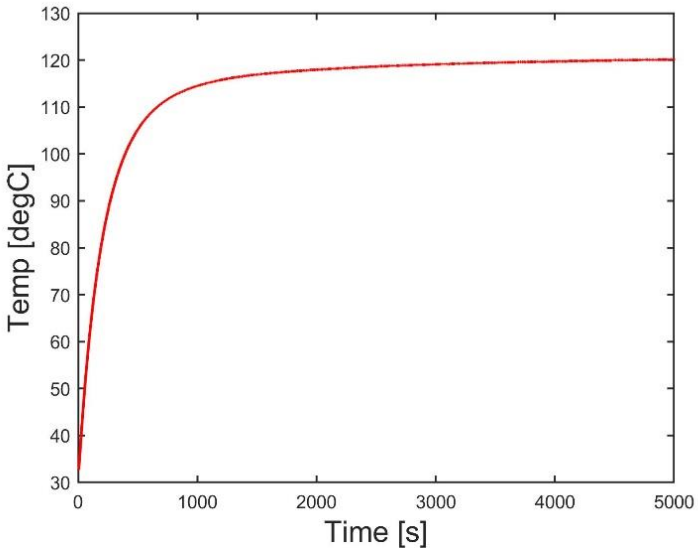

Figure 2.16. Temperature versus time curve of a gold AR coated absorber in a low vacuum environment (1 mTorr) under 1 sun intensity.

2.7 Summary and Conclusion

In this chapter, we discussed the working principles of a selective solar absorber as well as current designs existing in literature. We proposed and optimized three types of selective solar absorbers: an ITO absorber, a PCWG absorber, and a gold AR coated absorber. We reported optimized absorbers achieving maximum theoretical temperatures of 217 °C, 389 °C, and 428 °C under 1 sun intensity for each absorber. At 1 sun, the solar absorptivity for each absorber was 81.8%, 51.1%, and 47.4%, and the infrared emissivity was 25.0%, 4.7%, and 3.5% at maximum temperature. We fabricated and characterized the gold AR coated absorber and measured a solar absorptivity of 49.2% and an infrared reflectivity of 11.7%. Finally, we measured a thermal performance of 121 °C under 1 sun intensity and fitted an environmental non-radiative heat loss coefficient of Q = 1.8 $W/m^2/K$.

Chapter 3

DESIGNING A SOLAR DRIVEN PHOTOTHERMAL REACTOR

3.1 Introduction

As stated in Chapter 1, while selective solar absorbers have found use in a wide range of thermal applications, synthesis of sustainable aviation fuels via sunlight has gained widespread interest for its high potential impact on the aviation, transportation, and shipping industries. In order to utilize a selective solar absorber, it must be coupled to a system capable of efficiently transferring heat to the desired application. Thus, a number of solar driven reactors have been demonstrated for this purpose. Interestingly, most literature currently concerns the development and improvement of catalysts to increase the efficiency and selectivity of products as opposed to solar driven reactor engineering design.[71] This is because product yield from solar driven thermocatalysis tends to be lower compared to industrial heating methods. Also, solar driven reactor design is most relevant primarily among photothermal reactors. This is because unlike conventional thermochemical reactors, photothermal reactors require light during operation, and are therefore best adapted to utilizing sunlight and a selective solar absorber.

By studying current photothermal reactor designs for sustainable fuel synthesis, we find that reactor designs can be categorized by their mode of operation, their heating source, and their type. The mode of operation is divided into batch process reactors and continuous or flow process reactors. Heating sources include both radiative (light) and external (non-radiative) heating. Finally, the types of reactors include fixed bed reactors and structured reactors.

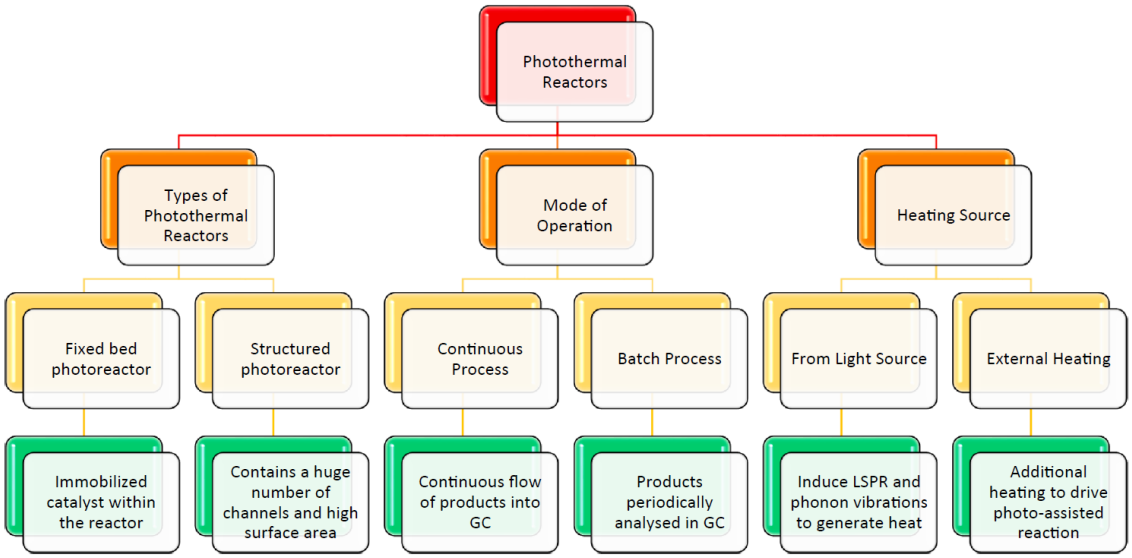

Figure 3.1. Diagram showing the breakdown of existing photothermal reactors by their type, mode of operation, and heating source. Figure taken from [71].

Most current photothermal reactors operate from between 1 – 10 sun intensity (1 – 10 kW/m^2) with reactor volumes ranging from as low as 1.5 mL up to 550 mL, with operational temperatures ranging from 100 – 350 °C; reported conversion efficiencies of CO_2 to C_{2+} products range from approximately 9% up to 35% in these reactors.[71–84] We note here that there also exists industrial scale thermochemical reactors which use solar concentrators to reach extremely high sun intensities (10 – 100 kW/m^2) such as the Ivanpah Solar Electric Generating System in California and the Solar Thermal Advanced Reactor System by Pacific Northwest National Laboratory.[85,86] However, we will focus primarily on reactor designs which can operate under little to no sun concentration (1 – 3 kW/m^2) for the scope of this thesis because solar concentration can always be used to supplement thermal performance afterwards. Given the current literature on solar driven photothermal reactors, many areas of improvement can be explored including the solar thermal efficiency, scalability, and product yield.

In this chapter, we discuss the design considerations for a solar driven photothermal reactor which utilizes a selective solar absorber as its primary heating source. From the

considerations, we propose a planar scalable reactor design with a selective solar absorber capable of operating in both batch and flow mode. We present work on modeling the geometry and thermal performance of our design using SolidWorks computer-aided design (CAD) and COMSOL Multiphysics with an in-depth discussion on the thermal modeling process and results.[87,88] Following the modeling, we construct a working lab-scale photothermal reactor and measure the thermal performance under experimental operating conditions and calculate its thermal efficiency.

3.2 Design Considerations

We propose several factors to consider when designing a solar driven photothermal reactor. These include the mode of operation, the minimum operational requirements, the thermal efficiency the selective solar absorber, the long-term chemical and mechanical stability, and the ease of construction, usability, and scalability.

1. The mode of operation can depend on several factors including the desired reaction, product yield, and product quantification method:

   First, batch mode reactors are loaded with reactant and catalyst, and the products are measured after a certain amount of time. Alternatively, flow mode reactors continually flow reactant through the reactor and quantify the product generation in real time. In this case, flow mode reactors are more desirable because they give better product quantification compared to batch mode reactors.

   Second, batch mode reactors generally achieve higher conversion efficiencies compared to flow reactors, especially for reactions which have longer reaction times. In this case, batch mode reactors may be advantageous because solar thermal may not be able to reach temperatures comparable with other heating methods; the decrease in temperature naturally increases the reaction time due to kinetics.

   Third, batch mode reactors may be able to reach higher peak temperatures compared to flow mode reactors. This is because flowing reactant will naturally act as a cooling

mechanism for removing heat from the reactor through convective/conduction. This can be counteracted by either pre-heating the reactants or lowering the flow rate. Thus, it is possible that batch mode reactors are better suited for longer reactions requiring higher temperatures, while flow mode reactors are better suited for faster reactions with lower temperature requirements. For C_{2+} product generation, we may expect batch mode reactors to generate longer hydrocarbon chains, while flow mode reactors generate more total product over time albeit with shorter hydrocarbon chains.

2. The minimum operational requirements of the reactor are defined by the reaction requirements. In other words, the reactor must be able to operate at the minimum operating temperature and pressure of the desired reaction. In general, because product generation is more favorable at higher temperatures and pressures due to Le Chatelier's principle, we want to design the reactor to operate at the highest possible temperature and pressure. In practice, the reactor must simply operate at the peak temperature of the selective solar absorber because the major limitation to reactor operation is the available solar thermal energy.

3. The reactor must efficiently couple with the selective solar absorber such that heat is funneled from the absorber to the catalyst/reaction, and all other heat loss pathways are minimized. Furthermore, the reactor must allow the selective solar absorber to access as much sunlight as possible. In general, meeting these requirements involves utilizing a vacuum insulating layer around the selective solar absorber and a transparent window. The vacuum insulating layer reduces convective/conductive heat loss, and the transparent window allows sunlight through. To summarize, the selective solar absorber is responsible for minimizing the radiative heat loss, and the photothermal reactor is responsible for minimizing the non-radiative heat loss.

4. Consideration must be given towards the chemical and mechanical stability of the reactor. Since we do not want the reactor itself to affect the reactivity of the reaction, chemically inert materials should be used. Furthermore, as an extension of point #2, fatigue

from cycling of thermal and mechanical stress can occur over time. Chosen material should be rated appropriately.

5. Finally, the ease of construction, usability, and scalable can all be important factors favoring one design over another. In particular, the potential for scalability of a photothermal reactor up to industrial levels can be considered a major design advantage for real-world applications.

3.3 Reactor Design

Based on all of the previously listed photothermal reactor design considerations, we designed a planar photothermal reactor from top to bottom with three active layers: a vacuum insulating layer, a selective solar absorbing layer, and a thermocatalytic reaction layer. As previously stated, the vacuum insulating layer reduces the convective and conductive heat loss from the selective solar absorber to the surrounding environment and encourages conductive heat flow downwards towards the thermocatalytic reaction layer. We use a transparent quartz window to enclose the vacuum layer and allow incident sunlight to reach the selective solar absorber. We use the gold AR coated absorber as our selective solar absorber. Below the selective solar absorber, we use a stainless-steel plate to separate the absorber and the thermocatalytic reaction layer. Another stainless-steel plate encloses and isolates the thermocatalytic reaction layer. The overall design is planar so that it scales linearly in area with total collected solar irradiance; increasing the length and width of the reactor does not change the overall thermodynamics of the reactor.

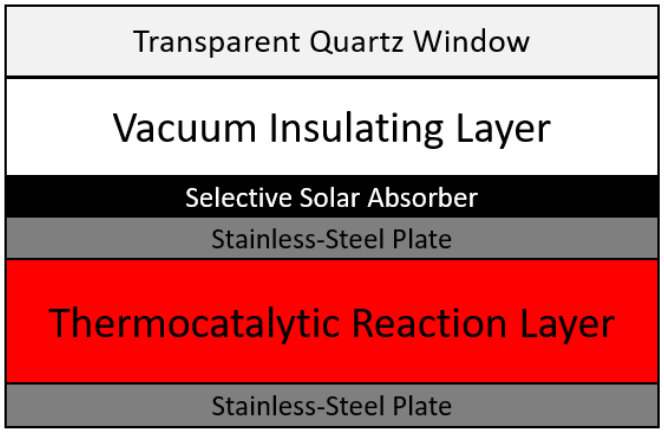

Figure 3.2 Schematic of a solar driven photothermal reactor comprised of a vacuum insulating layer, selective solar absorber, and thermocatalytic reaction layer.

For the actual construction of a working lab-scale photothermal reactor, we decided to use a multilayer stack of stainless-steel 6-inch diameter ConFlat (CF) flanges. In other words, we constructed the schematic shown in **Fig. 3.2** using a quartz window flange, a double-faced flange, a thin plate flange, a second double-faced flange, and a second thin plate flange. We chose CF flanges because of their off-the-shelf availability, modularity, vacuum pressure rating, and overall mechanical strength. Furthermore, the stainless steel allows us to machine ports directly into the double-sided flanges for direct attachment of adapters, hoses, and valves with vacuum tightness. For the thermocatalytic reaction layer, we include a reaction inlet port, product outflow port, and thermocouple feedthrough port. In the vacuum insulating layer, we include a vacuum port and a thermocouple feedthrough port. The selective solar absorber is adhered directly to the surface of the thin plate flange using thermally conductive paste. **Fig. 3.3** shows a CAD assembly of the deconstructed photothermal reactor. The CAD assembly uses 3D STP files of flanges imported from VacuCAD, a free library of CAD models for vacuum components provided by Kurt J. Lesker Company.

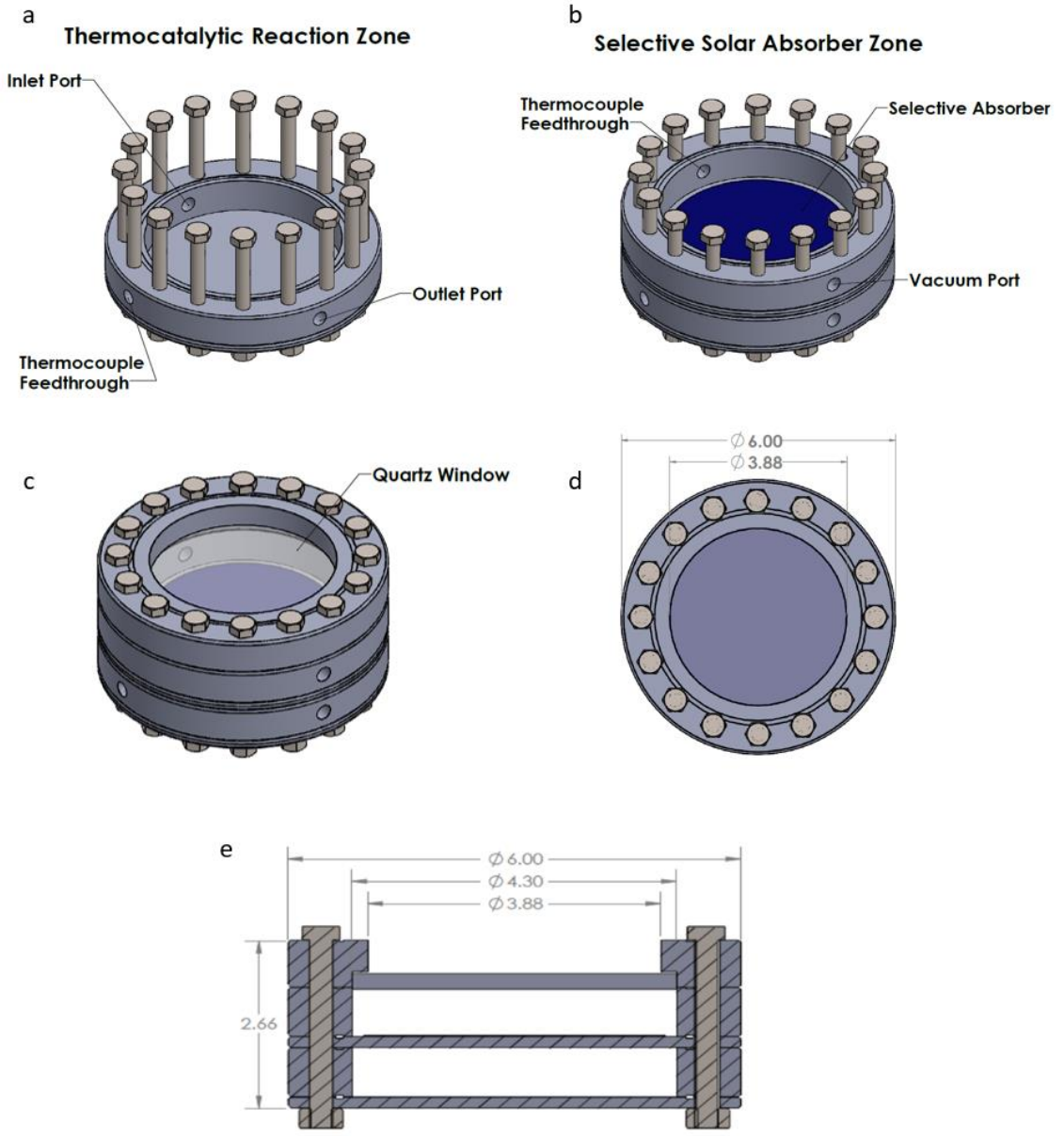

Figure 3.3. Deconstructed CAD assembly of a photothermal reactor highlighting each active layer. (a) First layer showing thermocatalytic reaction layer constructed using a thin plate flange and a double-faced flange. An inlet port, outlet port, and thermocouple feedthrough are included in the double-faced flange; (b) Second layer showing the selective solar absorber and vacuum insulating layer constructed using a second thin plate flange and double-faced flange. A vacuum port and thermocouple feedthrough are included in the double-faced flange; (c) Fully constructed photothermal reactor with quartz window flange enclosing the vacuum insulating layer; (d) Top view of photothermal reactor; (e) Side view cross-section of photothermal reactor.

Due to the modular nature of the design, the thermocatalytic reaction layer can be set up for both batch mode and flow mode operation. In **Fig. 3.3**, the reactor is set up in batch mode operation. In batch mode setup, the thermocatalytic reaction layer is a large, isolated volume composed of a thin plate flange, a double-faced flange, and another thin plate flange. However, we can set up the reactor in flow mode operation by replacing the thermocatalytic reaction layer with a single thick blank flange instead. By machining a tube through the center of the thick blank flange, we can flow reactant continuously through the reactor. Thus, for the flow mode setup, the reactor multilayer stack is instead constructed from a quartz window flange, a double-faced flange, and a thick blank flange. **Fig. 3.4** shows CAD assemblies of the photothermal reactor in both batch mode setup and flow mode setup.

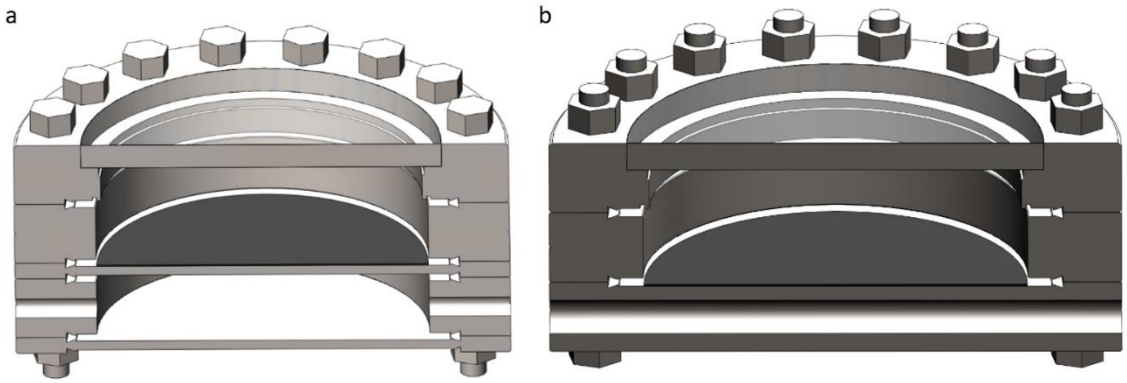

Figure 3.4. (a) CAD assembly of photothermal reactor in batch mode setup. The thermocatalytic reaction layer is an isolated volume designed for batch reactions, and it is constructed using two thin plate flanges and a double-faced flange; (b) CAD assembly of photothermal reactor in flow mode setup. The thermocatalytic reaction layer is a single thick blank flange with a tube machined through the center.

3.4 Thermal Modeling

To understand and predict the thermal performance of the reactor, we use COMSOL Multiphysics with finite element analysis for thermal modeling.[87] We model both the batch mode setup and the flow mode setup. This section covers the modeling procedure step-by-step in detail, then reports the results.

3.4.1 Model Setup

Using the model wizard, we set up a 3D time-independent study with the *Heat Transfer in Solids* and *Surface-to-Surface Radiation* physics interfaces, and the *Heat Transfer with Surface-to-Surface Radiation* multiphysics interface.

3.4.2 Construction Geometry

We re-construct the reactor geometries in **Fig. 3.4** in the COMSOL geometry construction interface. The goal of re-constructing the geometry is to simplify/remove unnecessary features as much as possible to increase the model efficiency. As such, we model all the flanges as simple cylinders, either hollow or solid. All dimensions are rounded from the commercial specification sheets for each component.

1. Thin plate flanges are cylinders with h = 0.175 in, r = 3 in.
2. Double-faced flanges are hollow cylinders with h = 0.75 in, r_{inner} = 2 in, and r_{outer} = 3 in.
3. Thick blank flanges are cylinders with h = 0.78 in, r = 3 in. For the flow mode setup, we remove through the center of the flange a cylindrical domain with h = 6 in, r = 0.1875 with axis parallel to the flat face of the flange.
4. The quartz window is constructed from a hollow cylinder representing the stainless-steel flange and a solid cylinder representing the quartz. The stainless-steel flange has h = 0.78 in, r_{inner} = 2 in, r_{outer} = 3 in, and the quartz window itself has h = 0.25 in, r = 2 in.
5. We must add domains representing each empty region within the reactor that we wish to include as part of the heat transfer modeling. Thus, we add a cylinder representing the vacuum domain and a cylinder representing the domain within the thermocatalytic reaction layer. For the batch mode setup, our vacuum domain has h = 1.28 in, r = 2 in, and our air domain has h = 0.75 in, r = 2 in. For the flow mode setup, our vacuum domain is the same, but our air domain is instead a long cylinder with h = 6 in, r = 0.1875 in. It is minor, but important to note here that

we perform a Collapse Face operation on the cylinder. This is because we are placing a cylindrical rod sideways inside another cylinder (thick blank flange), so a sliver of face will be exposed at the ends of the rod due to the side curvature of the thick blank flange.

3.4.3 Materials Selection

Once the reactor geometry is constructed, we assign the necessary materials properties to all domains and boundaries as required by the selected physics interfaces. For the *Heat Transfer in Solids* interface, we must assign the density ρ, thermal conductivity k, and heat capacity at constant pressure C_p to all domains. For the *Surface-to-Surface Radiation* interface, we must assign the reflectivity, transmissivity, and absorptivity to all boundaries. The following section discusses the domain assignments while the boundary assignments will be discussed in Section 3.4.5.

For the domain assignments, we assign stainless steel, quartz glass, vacuum, and nitrogen to the appropriate domains in the model. Nitrogen was used to represent the thermocatalytic reaction layer domain. **Table 3.1** shows the materials property values for all materials assigned in the model.

Table 3.1. Materials properties assigned to domains in the COMSOL model for the photothermal reactor.

Material	ρ [kg/m^3]	k [W/m/K]	C_p [J/kg/K]
304L Stainless Steel [a]	8000	15	500
Quartz Glass [b]	2210	1.4	730
Nitrogen [b]	ρ(T,P)	k(T)	C_p(T)
Vacuum	1.5×10^{-6} [c]	0.01 [c]	1000 [d]

[a] Property manually input from literature [89–92]
[b] Properties from built-in COMSOL materials library [87]
[c] Property manually calculated and input
[d] Property manually input from literature [93]

For the vacuum properties, we manually calculated the density and the thermal conductivity of dry air at 1 mTorr and 25 °C. To calculate the density, we used the ideal gas law for dry air:

$$\rho_{air} = \frac{P}{R_{air}T} \tag{3.1}$$

Where P is the pressure, R_{air} is the dry air specific gas constant, and T is the temperature. For the thermal conductivity, we used the following empirical relationship:

$$k(P,T) = \frac{k_0}{\left(1 + \frac{CT}{Pd}\right)} \tag{3.2}$$

Where K_0 is the thermal conductivity of air at 1 atm, P is the pressure, T is the temperature, d is the characteristic length, and C is an empirical constant equal to 7.6×10^{-5} (m•K)/N.[94] **Fig. 3.5** shows the empirical relationship between air thermal conductivity and pressure at various temperatures above 25 °C and pressures below 1 atm. From this relationship, we used a value of 0.01 W/m/K for the vacuum thermal conductivity as a safe upper limit for modeling, even though **Fig. 3.5** suggests that at 1 mTorr (1.3×10^{-6} Bar), the thermal conductivity should be much lower than 0.01 W/m/K.

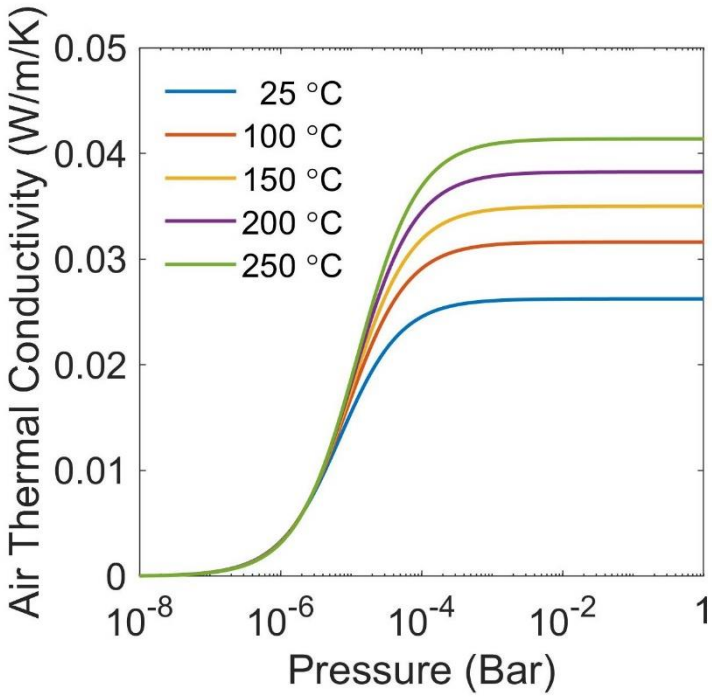

Figure 3.5. Graph showing the effect of high temperatures and low pressures on air thermal conductivity. Calculated from [94].

3.4.4 ***Heat Transfer in Solids*** *Interface*

Here, we set the modeling conditions, boundary conditions, and other parameters for the heat transfer interface. We set the ambient temperature to 300 K. We assign a heat flux boundary to all external surfaces of the model to represent convective and conductive heat loss from the reactor to the environment. The heat flux relationship used in COMSOL is the same non-radiative heat loss relationship as **Eq. 2.9**.

3.4.5 ***Surface-to-Surface Radiation*** *Interface*

Here, we set the radiative modeling settings, introduce the radiative sunlight source, and assign the reflectivity, transmissivity, and absorptivity properties for all boundaries. For the radiative modeling settings, we used ray shooting method with a resolution of 16.

For the sunlight source, we use a plane wave with a direction vector normal to the surface of the reactor. The source temperature is 5780 K, and the source heat flux is 1000 W/m^2 and 3000 W/m^2 for 1 sun and 3 sun intensity, respectively.

To assign the optical properties of each material, we use Semitransparent Surfaces which allow us to manually define the reflectivity, transmissivity, and absorptivity of each surface. It is important to note here that at the time of this work, COMSOL limited the number of user-defined spectral bands allowed for defining wavelength-dependent radiative properties. In other words, the exact emissivity of the selective solar absorber could not be imported directly into COMSOL and as a result, the emissivity had to be discretized and averaged over a limited number of spectral bands. In order to solve this issue, we wrote an algorithm which attempted to optimally subdivide the selective solar absorber emissivity into discrete spectral bands with an average emissivity within each spectral band such that the discretized emissivity would give very similar results to the original emissivity when used to calculate the maximum theoretical temperature. Therefore, **Fig. 3.6** compares the original emissivity of the gold AR coated absorber and the discretized emissivity used for COMSOL modeling the selective solar absorber. **Table 3.2** and **Table 3.3** report the absorptivity and reflectivity values assigned for each material at each defined spectral band in COMSOL. The transmissivity of the material at each spectral band is then 1 – A – R.

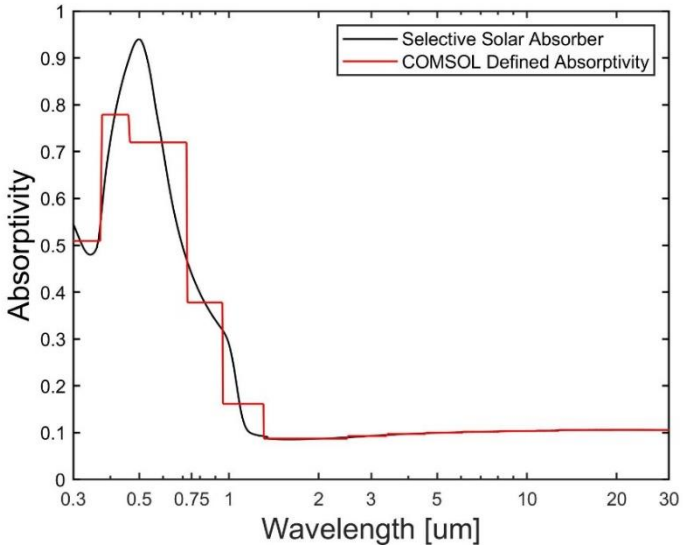

Figure 3.6. Comparison between the measured emissivity of the gold AR coated selective solar absorber and the discretized emissivity used for the COMSOL model.

Table 3.2. Absorptivity values assigned to each spectral band for the materials assigned to boundaries in the COMSOL model for the photothermal reactor.

Spectral Band [μm – μm]	Selective Solar Absorber	Stainless Steel	Quartz Glass
0.300 – 0.375	0.5092	0.075	0.05
0.375 – 0.465	0.7790	0.075	0.05
0.465 – 0.725	0.7197	0.075	0.05
0.725 – 0.955	0.3780	0.075	0.05
0.955 – 1.310	0.1613	0.075	0.05
1.310 – 2.505	0.0873	0.075	0.05
2.505 – 3.390	0.0927	0.075	0.525
3.390 – 4.580	0.0972	0.075	1
4.580 – 6.095	0.1001	0.075	1
6.095 – 8.080	0.1021	0.075	1
8.080 – 10.780	0.1033	0.075	1
10.780 – 12.810	0.1043	0.075	1
12.810 – 19.345	0.1057	0.075	1
19.345 – 24.695	0.1059	0.075	1
24.695 – ∞	0.1057	0.075	1

Table 3.3. Reflectivity values assigned to each spectral band for the materials assigned to boundaries in the COMSOL model for the photothermal reactor.

Spectral Band [μm – μm]	Selective Solar Absorber	Stainless Steel	Quartz Glass
0.300 – 0.375	0.4908	0.925	0
0.375 – 0.465	0.2210	0.925	0
0.465 – 0.725	0.2803	0.925	0
0.725 – 0.955	0.6220	0.925	0
0.955 – 1.310	0.8387	0.925	0
1.310 – 2.505	0.9127	0.925	0
2.505 – 3.390	0.9073	0.925	0
3.390 – 4.580	0.9028	0.925	0
4.580 – 6.095	0.8999	0.925	0
6.095 – 8.080	0.8979	0.925	0
8.080 – 10.780	0.8967	0.925	0
10.780 – 12.810	0.8957	0.925	0
12.810 – 19.345	0.8943	0.925	0
19.345 – 24.695	0.8941	0.925	0
24.695 – ∞	0.8943	0.925	0

For the boundary assignments, we assigned the selective solar absorber properties to the top surface of the thermocatalytic reactor layer domain, quartz glass properties to the top and bottom surface of the quartz window domain, and stainless-steel properties to all other boundaries in the model.

3.4.6 Meshing

We used a physics-controlled mesh with “normal” element size for the model mesh. We note here that for this model, using any mesh element “coarser” or finer all produced results within approximately 0.5 – 1 °C of the “normal” element size mesh results.

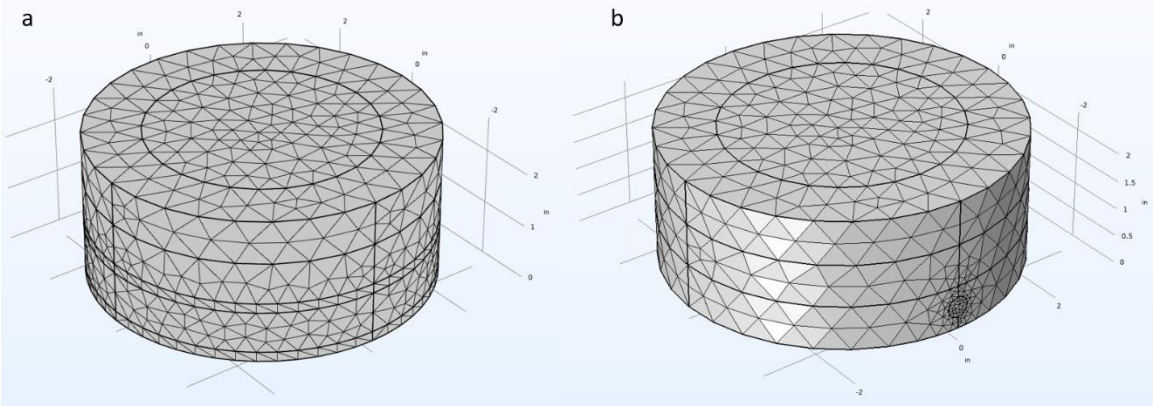

Figure 3.7. Photothermal reactor model built in COMSOL geometry with “normal” element size mesh for the (a) batch mode setup and (b) flow mode setup.

3.4.7 Results

We report the COMSOL thermal modeling results of the photothermal reactor. For both the batch mode setup and the flow mode setup, we report temperature versus length profiles along the thermocatalytic reaction layer, the surface of the selective solar absorber, and the inside surface of the quartz window. The profile along the absorber shows the highest temperature in the reactor, the profile along the thermocatalytic reaction layer shows the temperatures that the reaction/catalyst can access, and the profile along the quartz window shows a measure of the effectiveness of the vacuum insulating layer. For both reactor setups, we report the temperature profiles at 1 sun and 3 sun intensity and heat fluxes of Q = 0, 2, and 4 $W/m^2/K$.

From the COMSOL results, we can see that the maximum theoretical temperature with no non-radiative environmental heat loss is approximately 85 – 90 °C and 160 – 180 °C for 1 sun and 3 sun intensity. We observe a large temperature difference between the selective solar absorber and the quartz window showing that the vacuum insulating layer is working as intended. Both the batch mode and flow mode setup achieve similar temperatures under the same operating conditions. The reason the maximum theoretical temperature of the reactor is lower than that of the selective solar absorber is because the reactor surfaces also emit thermal radiation; in other words, solar energy collects across a 4-inch diameter circular

area, but thermal radiation emits from the entire cylindrical area of the reactor. As such, we expect that we increase the reactor area, the maximum theoretical temperature of the reactor approaches that of the selective solar absorber as the edge effects of the reactor disappear. Finally, we observe that a non-radiative heat flux of 4 $W/m^2/K$ results in a large decrease in temperature. This suggests that the photothermal reactor itself will also need to be thermally insulated from the environment for best performance.

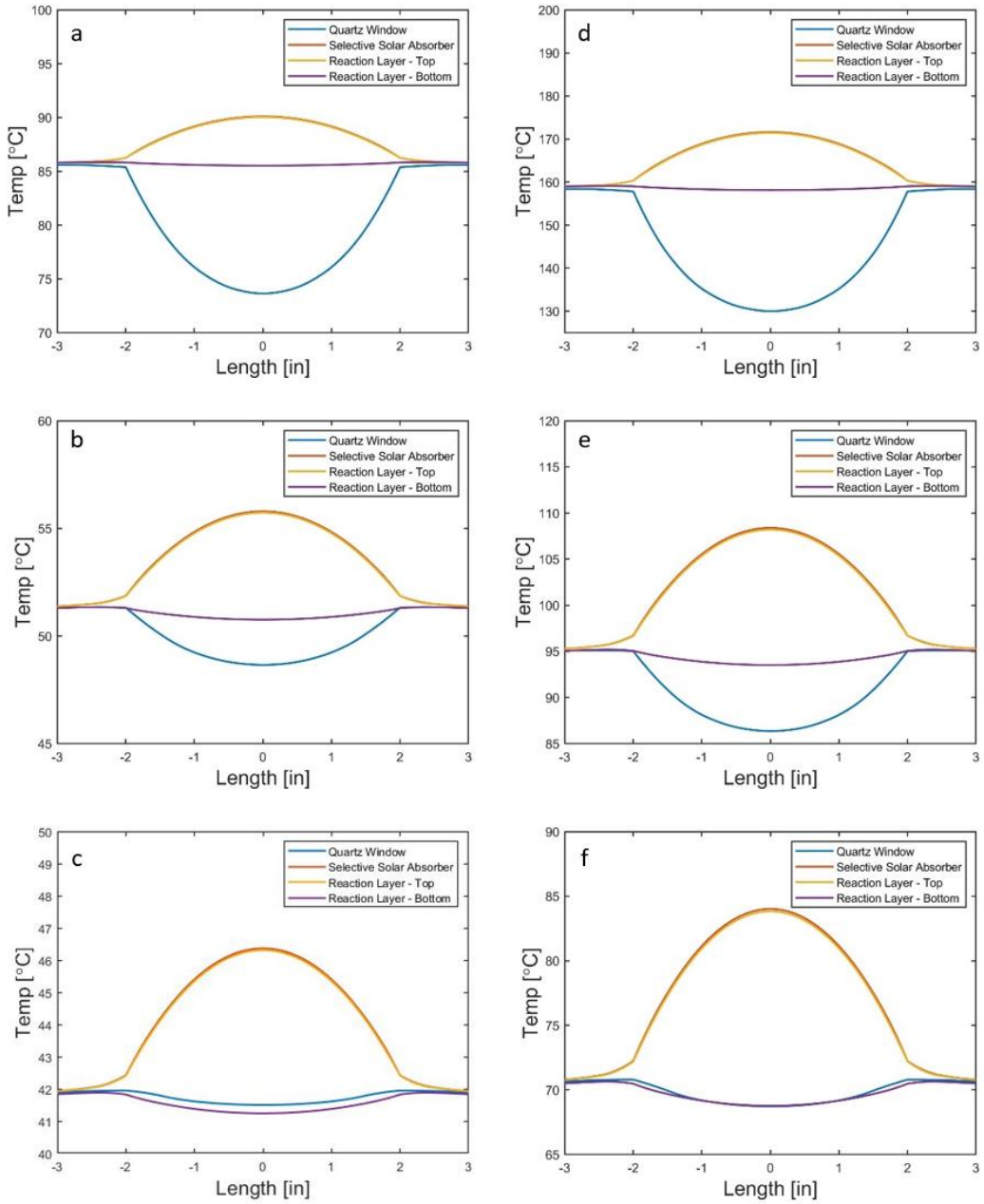

Figure 3.8. Temperature versus length profile of the batch mode photothermal reactor setup calculated from COMSOL thermal model. The temperature profiles are sampled along the surface of the selective solar absorber, the inside surface of the quartz window, and the top and bottom of the thermocatalytic reaction layer. Each plot shows the temperature profile of the reactor under different conditions: (a) I = 1000 W/m^2, Q = 0 W/m^2/K; (b) I = 1000 W/m^2, Q = 2 W/m^2/K; (c) I = 1000 W/m^2, Q = 4 W/m^2/K; (d) I = 3000 W/m^2, Q = 0 W/m^2/K; (e) I = 3000 W/m^2, Q = 2 W/m^2/K; (f) I = 3000 W/m^2, Q = 4 W/m^2/K.

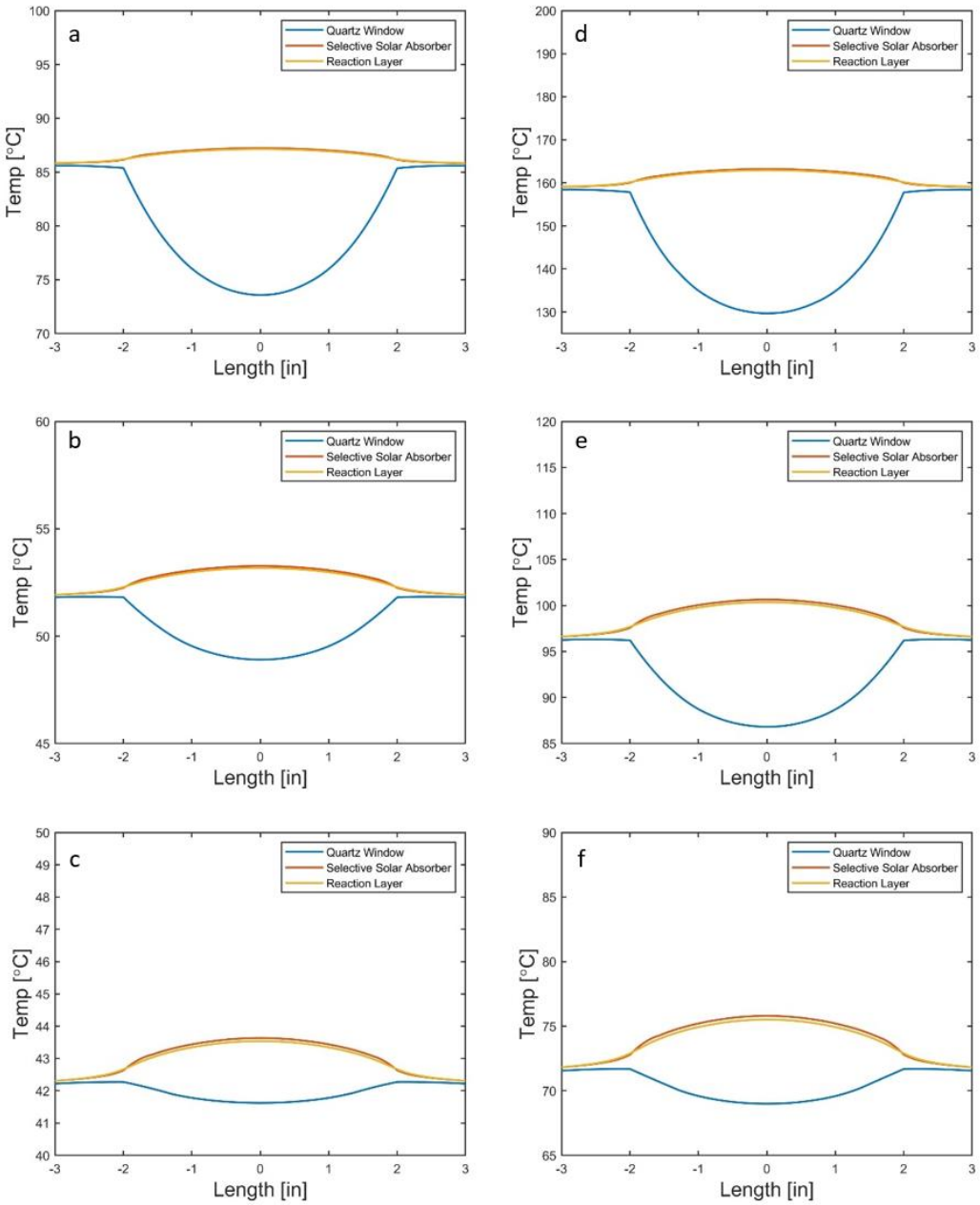

Figure 3.9. Temperature versus length profile of the flow mode photothermal reactor setup calculated from COMSOL thermal model. The temperature profiles are sampled along the surface of the selective solar absorber, the inside surface of the quartz window, and the thermocatalytic reaction layer. Each plot shows the temperature profile of the reactor under different conditions: (a) I = 1000 W/m^2, Q = 0 W/m^2/K; (b) I = 1000 W/m^2, Q = 2 W/m^2/K; (c) I = 1000 W/m^2, Q = 4 W/m^2/K; (d) I = 3000 W/m^2, Q = 0 W/m^2/K; (e) I = 3000 W/m^2, Q = 2 W/m^2/K; (f) I = 3000 W/m^2, Q = 4 W/m^2/K.

3.4.8 Modeling an Industrial-Scale Reactor

To demonstrate the scalability for the photothermal reactor, we modeled an industrial-scale rectangular reactor. To ensure consistency in the thermal modeling process, the industrial-scale reactor was modeled by simply scaling up the COMSOL geometry with no changes to the underlying physics. The length and width were increased to match that of the LONGi Hi-MO 5 solar panel which has dimensions of 2256 mm by 1133 mm.[95] We chose to replicate the LONGi solar panel size because it is representative of the current sizes of commercially available thin films and thin film devices. From the COMSOL results, we see that the industrial-scale photothermal reactor reaches a maximum theoretical temperature of 120 °C and 210 °C under 1 sun and 3 sun intensity. Operating under a typical ambient environment with Q = 6 $W/m^2/K$, the reactor reaches 75 °C and 150 °C under 1 sun and 3 sun intensity. The temperature profile is fairly uniform across the length and width of the reactor. As expected, as the reactor area increases, the temperature rises because the edge effects diminish.

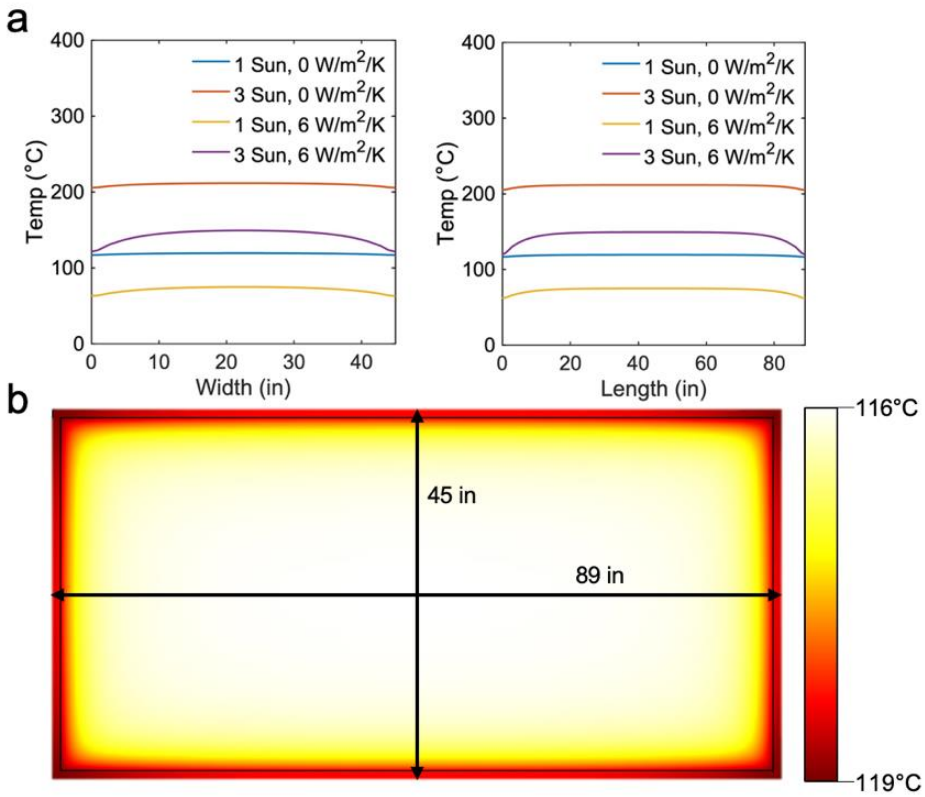

Figure 3.10. (a) Temperature versus length/width profile of an industrial-scale photothermal reactor under various conditions calculated from COMSOL thermal model; (b) Spatial temperature profile under 1 sun intensity.

3.5 Reactor Construction

The working lab-scale photothermal reactor was constructed using off-the-shelf 6-inch CF flange components. For the ports, 1/8-inch female NPT threads were machined into the sides of the double-sided flanges as described in **Fig. 3.3**. For the batch mode setup, two quarter-turn valves were installed to seal the inlet and outlet flow ports during operation. For the flow mode setup, 1/8-inch NPT to stainless steel tube fitting adapters were used to connect the reactor to the inlet and outlet lines. A 0.25-inch hole was drilled through the center of a thick blank flange for the flow mode setup. For the vacuum insulating layer, a 1/8-inch NPT to KF adapter was used to connect a rough pump to the reactor. The gold AR coated absorber was

adhered to the surface of the reactor using thermally conductive paste. **Fig. 3.11** shows the fully constructed photothermal reactor.

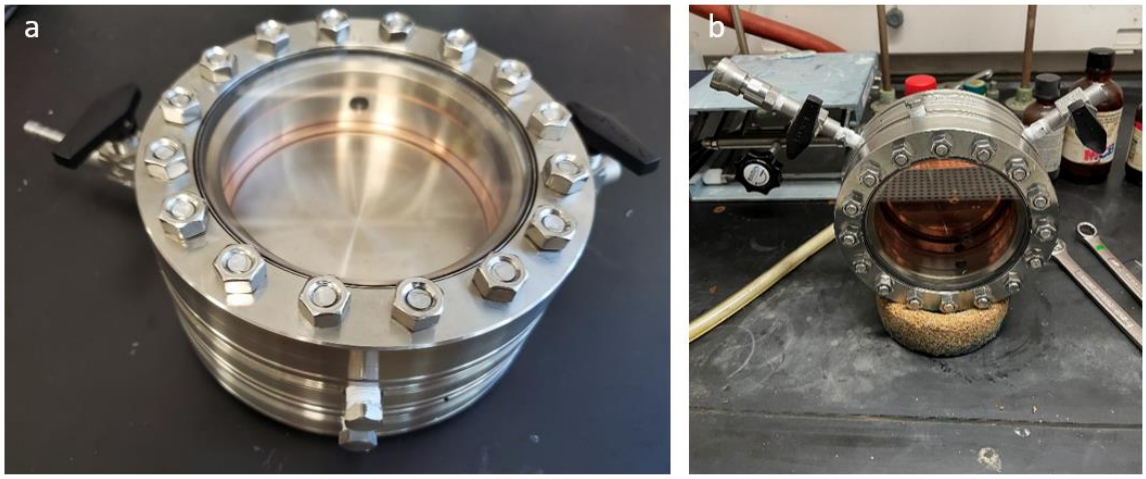

Figure 3.11. Fully constructed photothermal reactor in batch mode setup. Two quarter-turn valves with Quick Connect valves are attached. The other ports are sealed with plugs. Note that the selective solar absorber is not installed in (b).

In order to insulate the reactor from the environment as suggested from the COMSOL thermal modeling, we constructed an insulation box comprised of a 1-inch polystyrene layer, radiative reflective shields, and fiberglass insulation. A transparent ultrathin low-density polyethylene sheet was used to cover the open of the box while allowing sunlight in. **Fig. 3.12** shows the photothermal reactor inside the insulation box.

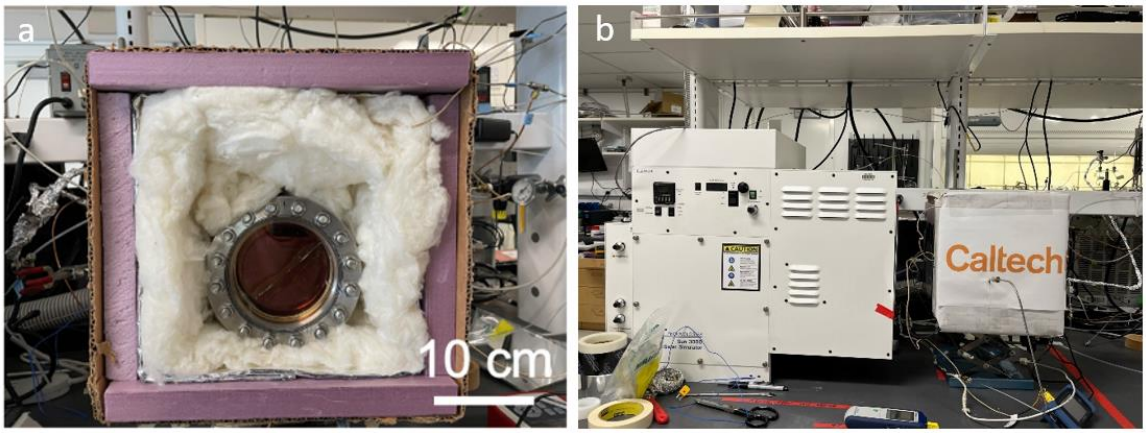

Figure 3.12. (a) Photothermal reactor with insulation box. A transparent low-density polyethylene sheet is used to cover the opening of the box during operation; (b) Experimental setup of photothermal reactor in insulation box with ABET Sun 3000 Simulator.

3.6 Thermal Performance

First, we measured the thermal performance of the photothermal reactor under 1 sun and 3 sun intensity. For the measurements, the photothermal reactor was placed inside the insulation box and a thermocouple was connected through the thermocouple feedthrough port into the thermocatalytic reaction layer. We used an ABET Sun 3000 Simulator to generate the solar irradiance, and the power flux was independently measured with a ThorLabs power meter. Measurements were made over 48 hours to observe the steady-state temperature. The photothermal reactor reached a steady-state temperature of approximately 55 °C under 1 sun intensity and approximately 120 °C under 3 sun intensity. We also re-measured the selective solar absorber performance under these conditions and observed a steady-state temperature of approximately 130 °C with Q = 1.6 $W/m^2/K$ for the vacuum insulation.

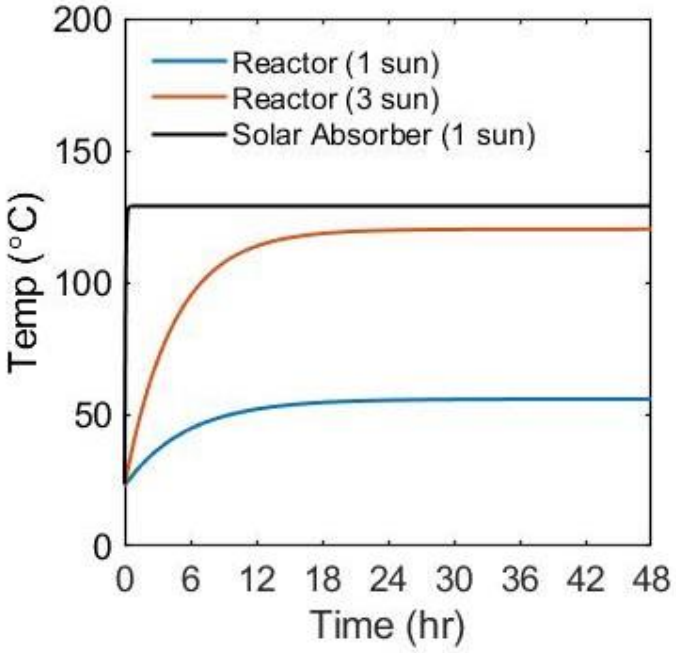

Figure 3.13. Temperature versus time curve of the reactor under 1 sun and 3 sun illumination. The previously measured selective solar absorber temperature versus time curve under 1 sun is also shown.

We also measured the effect of gas flow on the flow mode photothermal reactor setup. For this measurement, we flowed argon gas at 5 sccm and compared the temperature rise with no argon gas flow. **Fig. 3.14** compares the photothermal reactor temperature under 3 sun intensity with and without argon gas flow over a 10-hour period, showing little to no effect.

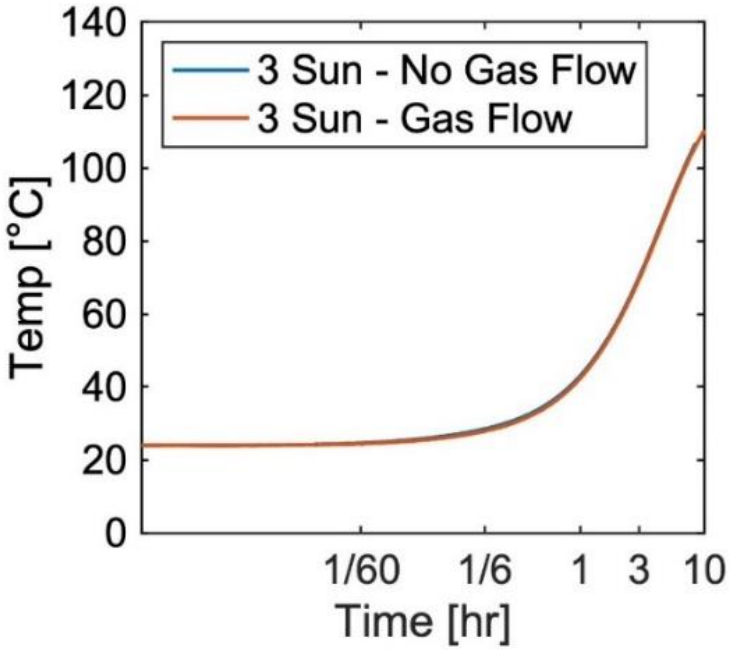

Figure 3.14. Comparison of temperature versus time in the flow mode photothermal reactor setup under argon gas flow versus no argon gas flow with 3 sun intensity over 10 hours.

From the temperature results, we used our COMSOL model to characterize the thermal performance of the insulation box. To do so, we fit the non-radiative heat flux Q in our COMSOL model such that the calculated temperature of the thermocatalytic reaction layer matches our experimental temperature measurements. In other words, we find the Q for our COMSOL model which best returns the temperature closest to 120 °C at 3 sun intensity. This value of Q is then the representative heat flux through the insulation box. From COMSOL, we find that the insulation box has an approximate heat flux of 1.15 W/m^2/K.

Finally, we calculated the thermal efficiency per unit area of our reactor operating at these conditions. We define the thermal efficiency as:

$$\eta_{thermal} = \frac{P_{in}}{P_{total}} = 1 - \frac{P_{out}}{P_{total}} \tag{3.3}$$

Where P_{out} is the energy that escapes and does not contribute towards heating the reactor and P_{total} is the total solar energy available. We calculate P_{out} as the sum of all heat loss contributions:

$$P_{out} = P_{reflect} + P_{rad} + P_{conv,cond} \tag{3.4}$$

Where $P_{reflect}$ is the solar energy reflected by the selective solar absorber, P_{rad} is the power radiated by the absorber, and $P_{conv,cond}$ is the power lost from the photothermal reactor through non-radiative heat flux. Since the total solar power is the sum of the reflective and absorptive power from the absorber:

$$P_{AM1.5} = P_{solar} + P_{reflect} \tag{3.5}$$

We can substitute **Eq. 3.5** and **Eq. 3.4** into **Eq. 3.3** to find the thermal efficiency:

$$\eta_{thermal} = \frac{P_{solar} - P_{rad}(T) - P_{conv,cond}(Q, T_{amb})}{P_{AM1.5}} \tag{3.6}$$

Where T is the operating temperature, T_{amb} is the ambient temperature, and P_{solar}, P_{rad}, and $P_{conv,cond}$ are defined by **Eq. 2.5**, **Eq. 2.6**, and **Eq. 2.9**, respectively. We can see qualitatively that **Eq. 3.6** represents the total solar power absorbed minus the power lost to radiative and non-radiative heat flux divided by the total available solar power. Using $P_{AM1.5}$ = 3000 W/m^2, Q = 1.15 W/m^2/K, T = 120 °C, and T_{amb} = 25 °C, we calculate a thermal efficiency per unit area of 40.4% for the photothermal reactor.

3.7 Summary and Conclusion

In this chapter, we presented a multilayer solar driven photothermal reactor comprised of a vacuum insulating layer, a selective solar absorber, and a thermocatalytic reaction layer. The reactor is capable of operating using both a batch mode and flow mode setup. We presented in detail the thermal modeling that was performed in COMSOL Multiphysics and reported on the maximum achievable temperatures of our design using a gold AR coated selective solar absorber: 85 – 90 °C and 160 – 180 °C for 1 sun and 3 sun intensity. We also showed

thermal modeling results for a potential industry-scale photothermal reactor with an active area of 2.5 m^2 capable of reaching uniform temperatures up to 120 ℃ and 210 ℃ under 1 sun and 3 sun intensity. Experimentally, we constructed a working lab-scale photothermal reactor along with an insulation box. Under 1 sun and 3 sun intensity, we measured steady-state temperatures of 55 ℃ and 120 ℃. We showed that in the flow mode setup, the gas flow had little to no effect on the temperature of the reactor. Finally, we used COMSOL to determine that the heat flux through the insulation box was approximately 1.15 $W/m^2/K$ and calculated a thermal efficiency of 40.4% for the reactor.

Chapter 4

SOLAR DRIVEN ETHYLENE OLIGOMERIZATION

4.1 Introduction

As stated in Chapter 1, sustainable aviation fuel synthesis via photothermal chemistry has generated much widespread interest due to its necessity in the aviation, shipping, and transportation industries. Currently, the two main commercial types of aviation fuels are Jet A and Jet A-1, with Jet A used in the United States and Jet A-1 used globally. Both fuels are kerosene fuels processed from petroleum and composed primarily of alkanes (linear, branched, and cyclic) with carbon chain lengths ranging from C_6 – C_{16}.[96,97] Interestingly, jet fuel is defined not by its chemical composition but by its performance specifications. Its physical properties include a minimum flash point of 38 °C, boiling point range of 170 – 300 °C, autoignition temperature of 210 °C, and specific energy density of 43 MJ/kg; the primary difference between the two fuels is their freezing points, which is -40 °C for Jet A and -47 °C for Jet A-1.[96,98–100]

Currently, a sustainable alternative for Jet A/A-1 is a synthetic fuel known as Fischer-Tropsch Synthetic Paraffinic Kerosene (FT-SPK). This fuel is produced by first pyrolyzing biomass into syngas, then using the Fischer-Tropsch reaction to form liquid hydrocarbon fuels.[101–103] The main drawback of using a solar-driven photothermal reactor for this process is that both the pyrolysis and Fischer-Tropsch reactions are energy intensive and usually require operating temperatures ranging from 150 – 300 °C, above what is commonly achievable with little to no sunlight concentration.[102,104–108]

Due to this limitation, ethylene oligomerization has generated interest for its potential as an alternative pathway for synthesizing sustainable fuels. In this process, ethylene gas is oligomerized to form alkene chains which are hydrogenated afterwards to form alkanes.[109] The ethylene gas can be sourced from alcohol dehydrogenation of ethanol or direct electrochemical reduction of CO_2.[110–113] The main benefit of this process is that nickel-based

catalyst driven ethylene oligomerization can be operated at temperatures as low as 50 – 120 °C.[114,115] Another benefit is that this process allows for the direct synthesis of liquid hydrocarbon fuels from CO_2 without biomass as an intermediate product.

In this chapter, we use the solar driven photothermal reactor with gold AR coated absorber reported in Chapters 2 – 3 to run two different Ni-catalyzed ethylene oligomerization reactions for conversion of ethylene to liquid hydrocarbon fuels under sunlight. We test a homogeneous Ni-catalyzed reaction in batch operation with the batch mode setup, and a different heterogeneous Ni-catalyzed reaction in flow operation with the flow mode setup. Afterwards, we report the performance of both ethylene oligomerization reactions in the photothermal reactor, including the product distribution and conversion efficiency.

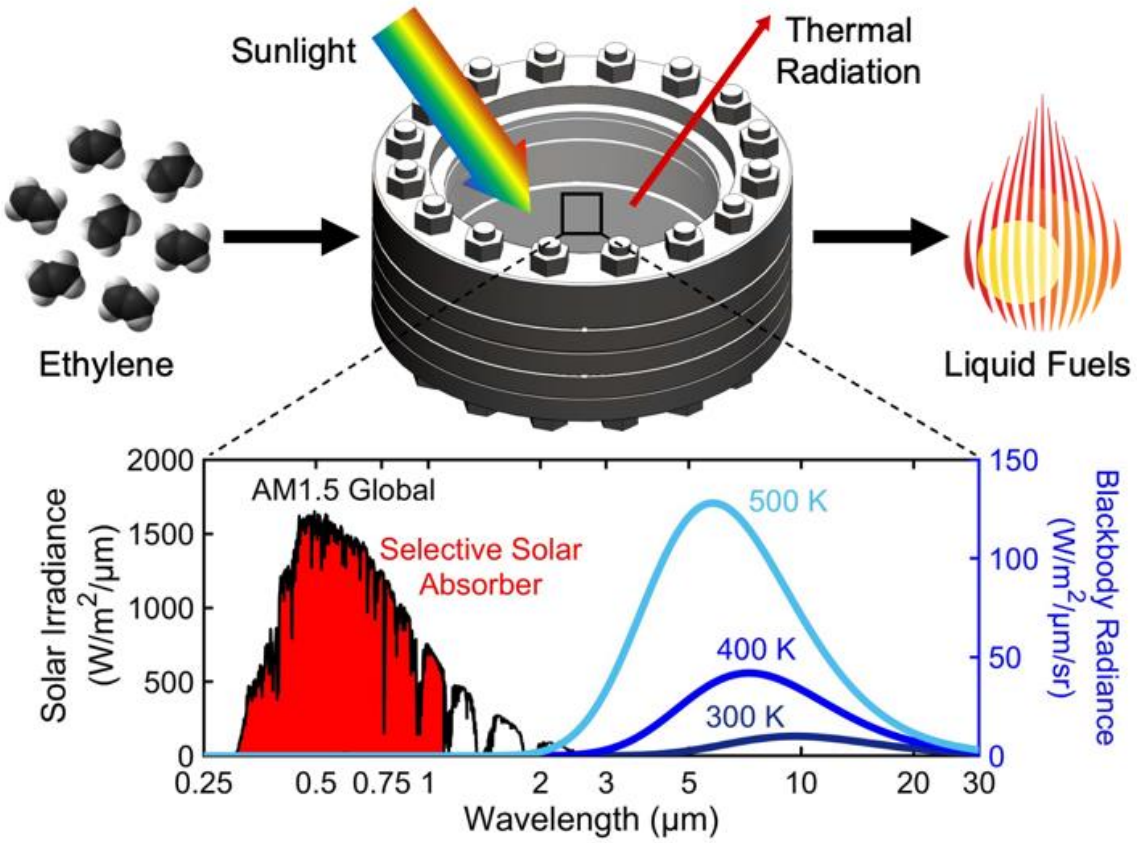

Figure 4.1. Schematic showing the use of a solar driven photothermal reactor for converting ethylene to liquid hydrocarbon fuels using sunlight. A selective solar absorber is used to efficiently collect solar thermal energy in the visible wavelength regime while reducing thermal radiation loss in the infrared wavelength regime.

4.2 Ethylene Oligomerization Reaction

The ethylene oligomerization reaction describes the polymerization of ethylene into longer carbon chain alkenes:

$$nC_2H_4 \rightarrow C_{2n}H_{4n} \tag{4.1}$$

The goal of using this reaction is to produce hydrocarbon chains with a length ranging from $C_6 - C_{16}$ which can be hydrogenated afterwards to produce alkanes for sustainable aviation fuels. A Ni catalyst is used to drive the reaction at temperatures which are more accessible by solar thermal heating.[114] Results from Chapter 3 reported that our photothermal reactor can achieve temperatures up to 120 °C under 3 sun (3000 W/m^2) intensity with the use of a gold AR coated selective solar absorber; thus, this is the maximum operating temperature at which we can run this reaction. Since our reactor can operate in both batch mode and flow mode, we selected two different Ni-catalyzed ethylene oligomerization reactions, one for each operating mode.

4.2.1 Batch Operation: Homogeneous Ni-Catalyzed Ethylene Oligomerization

For the batch mode setup, we selected a known homogeneous Ni-catalyzed ethylene oligomerization reaction.[116,117] The catalyst used in this reaction was a Shell higher olefin process (SHOP) Ni-catalyst supported by a phosphine-enolate (P,O) ligand. To use the Ni-SHOP catalyst, it was dissolved with Ni(COD)2 in toluene.

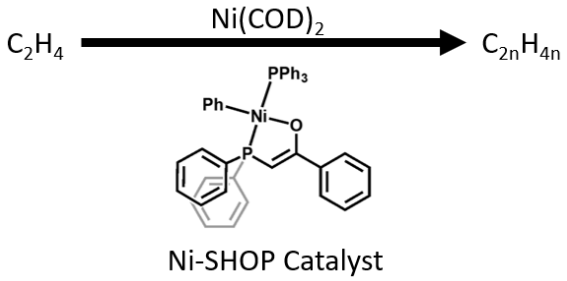

Figure 4.2. Homogeneous Ni-catalyzed ethylene oligomerization reaction.

Initial work on this reaction tested the catalyst activity and performance at different temperatures, pressures, reaction times, and catalyst concentrations. Catalyst activity was tested in a typical thermochemical Fisher-Porter tube and products were analyzed via gas chromatography/mass spectrometry (GC-MS). Testing showed that the Ni-SHOP catalyst was active for pressures as low as 1 – 5 bar and temperatures as low as 75 °C.

Testing at a pressure of 1 bar and temperature of 75 °C showed no olefin generation when 2 mM of catalyst was present. However, increasing the catalyst concentration to 4 mM and increasing the reaction time to 11 hours showed product generation with carbon chain lengths ranging from C_4 – C_{26}.

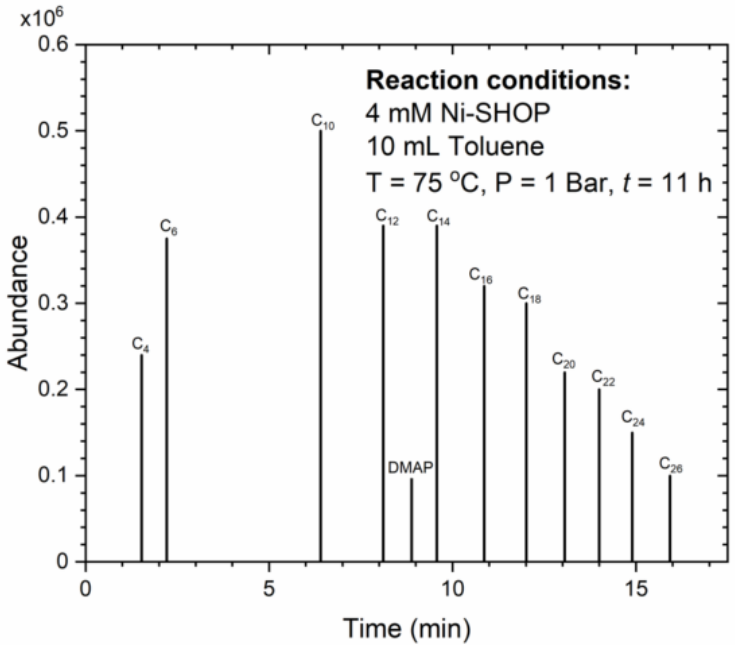

Figure 4.3. GC-MS product analysis of Ni-SHOP catalyzed ethylene oligomerization in a Fisher-Porter tube at T = 75 °C, P = 1 bar, t = 11 hr, C = 4 mM, resulting in a hydrocarbon product distribution ranging from C_4 – C_{26}.

Further experiments showed that increasing the pressure to 5 bar resulted in an even wider range of products with carbon chain lengths ranging from C_4 – C_{34} to be synthesized, even when the reaction time was decreased from 11 hours to 1 hour and the catalyst concentration was decreased from 4 mM to 2 mM. These experiments suggest an optimal operating condition of P = 5 bar and T = 75 °C for the Ni-SHOP catalyzed ethylene oligomerization reaction.

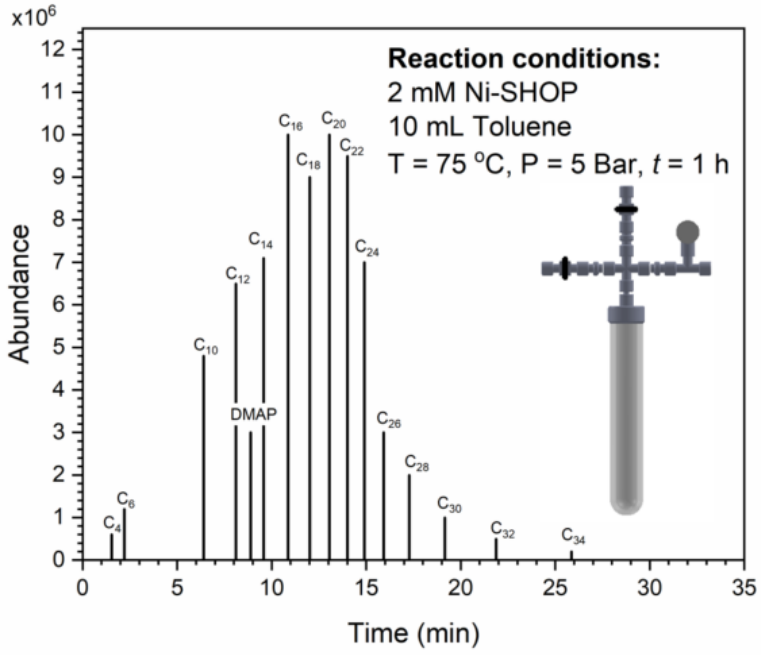

Figure 4.4. GC-MS product analysis of Ni-SHOP catalyzed ethylene oligomerization in a Fisher-Porter tube at T = 75 °C, P = 5 bar, t = 1 hr, C = 2 mM, resulting in a hydrocarbon product distribution ranging from C_4 – C_{34}.

For ethylene oligomerization inside the photothermal reactor, the reactor was set up in batch mode as described in **Fig. 3.4a**. A Quick Connect valve, a quarter-turn valve, and a thermocouple were attached to the thermocatalytic reaction layer. Due to the high sensitivity of the Ni-SHOP catalyst to air, the catalyst was prepared in a nitrogen glove box. For the catalyst preparation, Ni-SHOP catalyst (4 µmol) and $Ni(COD)_2$ (16 µmol) was dissolved in 7.5 mL of toluene. Before loading the catalyst into the reactor, the reactor was purged in the glove box transfer chamber with nitrogen at 1 atm for 24 hours. After 24 hours, the reactor was transferred into the glove box and the catalyst was loaded into the thermocatalytic reaction layer using a syringe through the quarter-turn valve. Once the catalyst was loaded, the quarter-turn valve was closed, and the reactor was removed from the glove box. Next, ethylene gas was loaded into the thermocatalytic reaction layer using the Quick Connect valve up to a total pressure of 50 psi (3.4 atm). As a result, the total gas loaded into the reactor was 1 atm nitrogen and 2.4 atm ethylene gas. Finally, the photothermal reactor was heated up to 75 °C and the reaction was left for 3 hours. **Fig. 4.5** shows the batch operation reaction

parameters for the homogeneous Ni-catalyzed ethylene oligomerization reaction in the photothermal reactor.

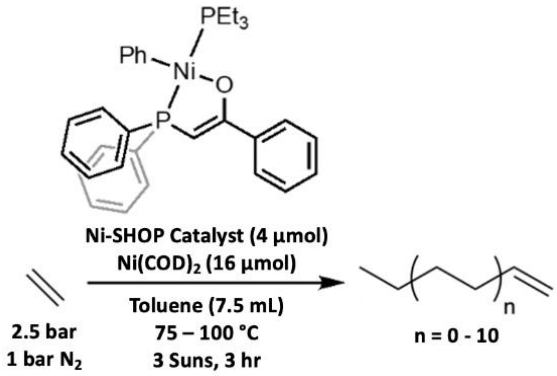

Figure 4.5. Batch operation homogeneous Ni-catalyzed ethylene oligomerization reaction parameters.

The first experiment was performed under dark conditions. In other words, the thermal energy was provided by a furnace instead of solar illumination. For the first experiment, a furnace was set to 75 °C, and once the photothermal reactor was prepared as described previously, it was placed inside the furnace for 3 hours. After 3 hours, the reactor was taken out and the quarter-turn valve was opened, releasing the remaining ethylene pressure and stopping the reaction by deactivating the catalyst with exposure to air. Once the reactor was cooled to room temperature, the liquid filtrate was collected in a vial and the solid product was collected by filtration. **Fig. 4.6** shows images of the liquid and solid product leftover after the reaction.

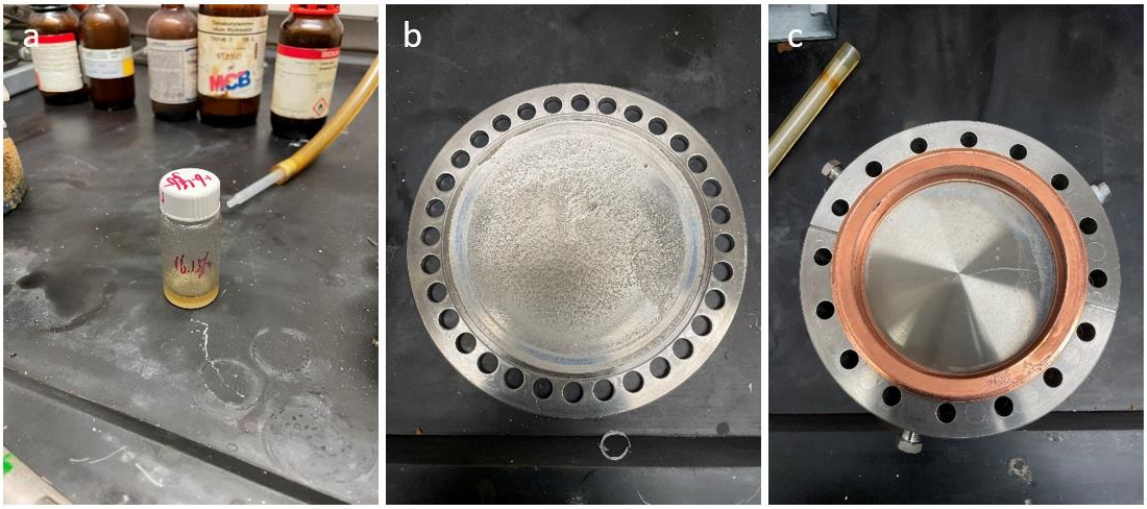

Figure 4.6. Images of the photothermal reactor after a batch mode ethylene oligomerization reaction. (a) Liquid product dissolved in methanol; (b) Solid product left over on the bottom flange; (c) Solid product left over on the top flange.

The liquid filtrate was analyzed by GC-MS and proton nuclear magnetic resonance (^{1}H NMR). The GC-MS results showed product generation of carbon chain lengths ranging from C_8 – C_{26}. The ^{1}H NMR suggested the liquid filtrate was comprised primarily of linear 1-alkene chains as opposed to branched or cyclic alkenes. Afterwards, both the liquid and solid product were filtered, dried, and massed. The liquid product yield was 230 mg, and the solid product yield was 66 mg. The total ethylene charged was 442 mg, so the estimated ethylene conversion efficiency was approximately 67%.

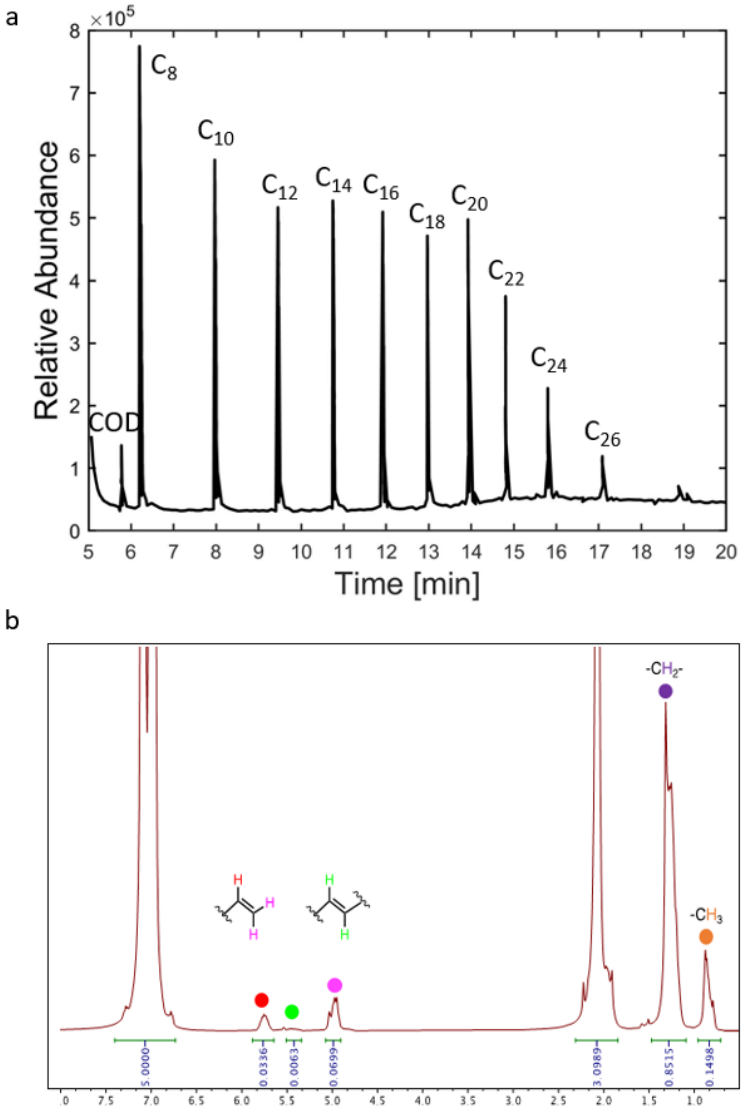

Figure 4.7. Product analysis of the liquid filtrate collected after a Ni-SHOP catalyzed ethylene oligomerization in the photothermal reactor under dark conditions with T = 75 °C, P = 3.4 bar. (a) GC-MS product analysis showing a distribution of hydrocarbon products ranging from C_8 – C_{26}; (b) ^{1}H NMR product analysis showing the presence of linear 1-alkene chains in the liquid filtrate.

A second experiment was performed using solar illumination and supplemental heat from heat tape. In this experiment, setup was prepared as described in the first experiment. The main difference was that the reactor was placed under an ABET 2000 Solar Simulator at 1 sun intensity and wrapped in heat tape as opposed to being placed in a furnace. Also, a rough

pump was connected to the vacuum insulating layer and pumped down to 1 mTorr. The heat tape enabled the reactor to reach 75 °C in several minutes, and once the reactor was at 75 °C, the reaction was left for 3 hours. After 3 hours, the reaction was stopped, and the liquid filtrate was analyzed by GC-MS. The GC-MS results showed product generation of 1-alkenes ranging from $C_6 – C_{24}$, similar to the first experiment performed in the furnace.

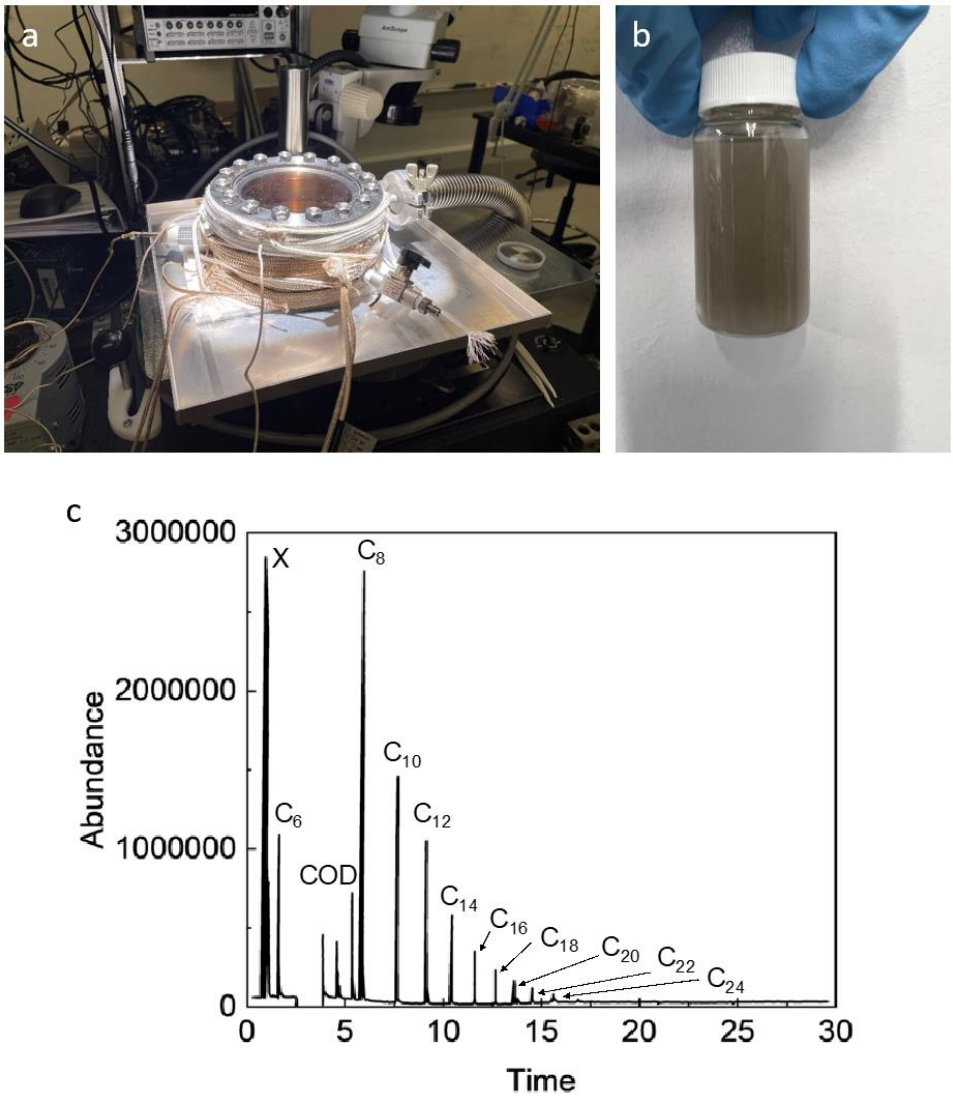

Figure 4.8. (a) Image of the experimental setup with photothermal reactor under a solar simulator with heat tape for supplemental heat. The Ni-SHOP catalyzed ethylene oligomerization was operated at T = 75 °C, P = 3.4 bar; (b) Image of the liquid product dissolved in methanol; (c) GC-MS liquid product analysis showing a distribution of hydrocarbon products ranging from $C_6 – C_{24}$.

Lastly, a fully solar driven homogeneous Ni-catalyzed ethylene oligomerization reaction was performed. Once again, the photothermal reactor was prepared as described in the first experiment. The difference in this experiment was that the photothermal reactor was placed into the insulation box and set up in front of an ABET Sun 3000 Simulator under 3 sun intensity (see **Fig. 3.12**). After setup, the reactor was allowed to reach 75 °C over a period of approximately 3 hours. Once the reactor was at 75 °C, the reaction was left for another 3 hours. We note here that the reactor temperature continued to rise to 100 °C over the course of the reaction. In other words, the reactor was left under 3 sun intensity for 6 total hours, with 3 hours below 75 °C and 3 hours above 75 °C. After 3 hours above 75 °C, the reaction was stopped, and the liquid filtrate was analyzed by GC-MS. Furthermore, GC with flame ionization detection (GC-FID) was used to quantify the soluble products in the $C_8 – C_{18}$ range using commercially available authentic samples. Finally, the solid product was filtered, dried, and massed.

The GC-MS results once again showed product generation of 1-alkenes ranging from $C_6 – C_{26}$, replicating the previous experimental results. The GC-FID results showed that the 1-alkene product yield peaked at C_{10} and steadily decreased from C_{10} to C_{18}. Using the GC-FID results, we calculated a conversion efficiency from ethylene to $C_8 – C_{18}$ 1-alkenes of 12.2%. Finally, the solid product yield was 27.8 mg, resulting in a total ethylene conversion efficiency of approximately 18.5%.

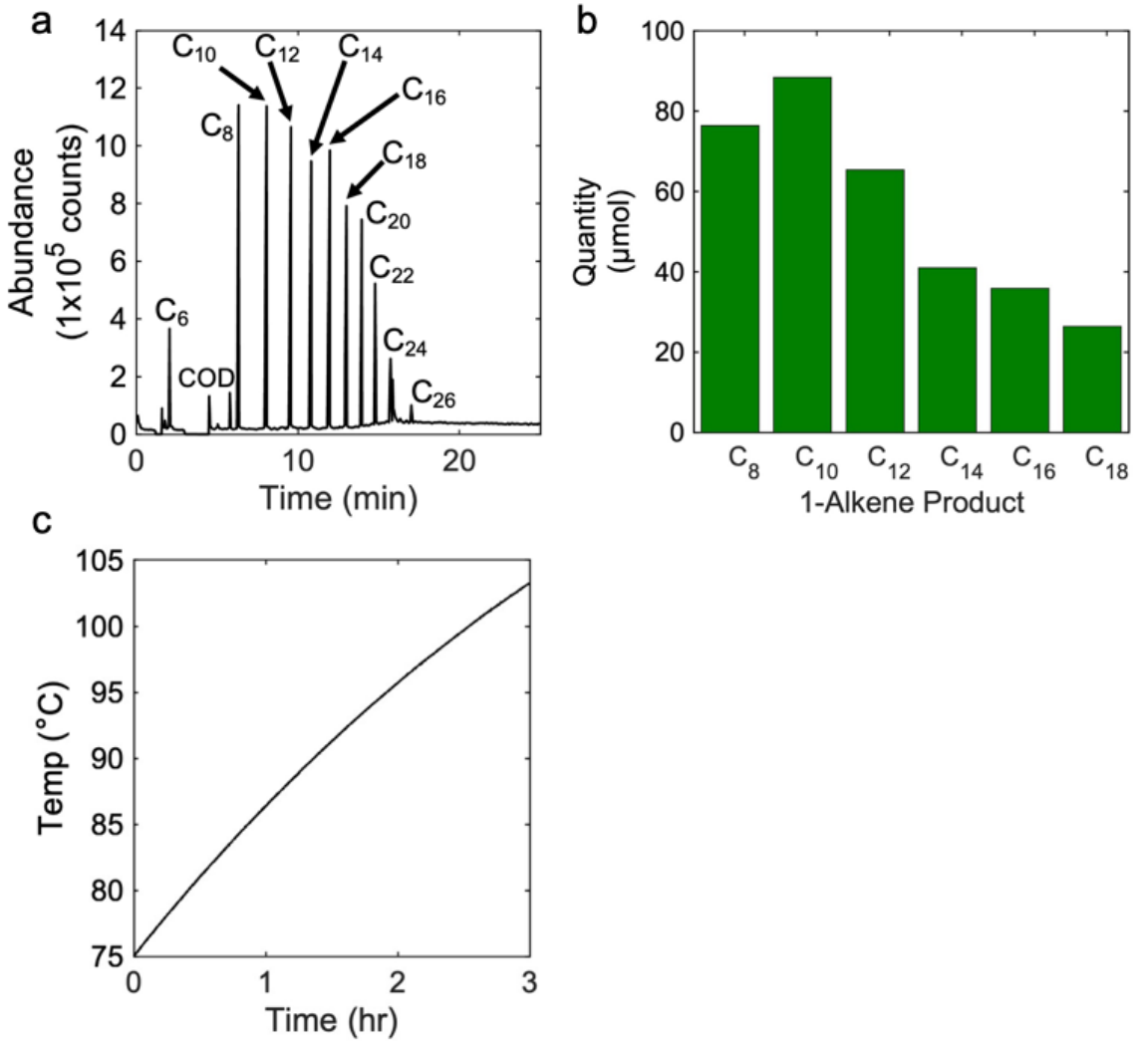

Figure 4.9. Results of the homogeneous Ni-catalyzed ethylene oligomerization reaction under 3 sun intensity in the batch mode photothermal reactor setup. (a) GC-MS liquid product analysis showing a distribution of hydrocarbon products ranging from C_6 – C_{26}; (b) GC-FID quantification of 1-alkene products from C_8 – C_{18}; (c) Temperature of the reactor over the course of the reaction.

From the results reported in this section, we see that the homogeneous Ni-catalyzed ethylene oligomerization reaction can consistently produce 1-alkenes with carbon chain lengths ranging from C_6 – C_{26} under 3 sun intensity. Furthermore, the generation of solid product suggests that even longer 1-alkene chains or branched/cross-linked hydrocarbons were produced in the process. The primary limitation of this reaction is the propensity for the Ni-

SHOP catalyst to be deactivated by air; multiple experiments were aborted or resulted in no product generation when the photothermal reactor leaked due to improper closing. As such, while this catalyst can be used in a batch mode reaction with pure ethylene and nitrogen, it is much more difficult to incorporate in a flow mode reaction, especially if the reactant ethylene gas comes directly as effluent from an electrochemical cell. In other words, the practical usage of this catalyst requires purifying the ethylene stream before flowing into the photothermal reactor, increasing the complexity of the system.

4.2.2 Flow Operation: Heterogeneous Ni-Catalyzed Ethylene Oligomerization

For the flow mode setup, we selected a heterogeneous Ni-catalyzed ethylene oligomerization reaction.[118] The catalyst used in this reaction was a nickel-impregnated silica-alumina catalyst with 4 wt. % Ni (Ni/SIRAL-30) prepared using a previously published procedure.[118] In short, the catalyst was prepared by first adding SIRAL-30 to an aqueous solution of nickel (II) nitrate hexahydrate and stirred for 3 hours, then dried at 80 °C overnight, then calcined at 550 °C in air for 5 hours with a 1 °C/min ramp rate, then sieved below 180 μm grain size. SIRAL-30 is a silica-alumina with an Al_2O_3 to SiO_2 weight percent ratio of 70 to 20 from SASOL.

For ethylene oligomerization inside the photothermal reactor, the reactor was set up in flow mode as described in **Fig. 3.4b**. Stainless steel tubing for continuous gas inflow/outflow was attached to both ends of the thermocatalytic reaction layer using 1/8-inch NPT to tube fitting adapters. A thermocouple was also attached to the thermocatalytic reaction layer. Before the reaction, the catalyst was first loaded into the center of the reactor by hand, then pretreated *in-situ* at 300 °C while flowing argon at 40 sccm using heat tape wrapped around the reactor. After pretreatment, the heat tape was removed and the reactor was cooled to room temperature, then placed into the insulation box and set up in front of an ABET Sun 3000 Simulator under 3 sun intensity (see **Fig. 3.12**). Once the reactor reached a temperature of 120 °C under solar illumination, ethylene gas was flowed at 5 sccm and the pressure was increased to 4 bar. **Fig. 4.10** shows the flow operation reaction parameters for the heterogeneous Ni-catalyzed ethylene oligomerization reaction in the photothermal reactor.

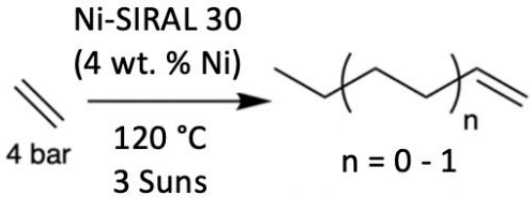

Figure 4.10. Flow operation heterogeneous Ni-catalyzed ethylene oligomerization reaction parameters.

Outflowing gas was sampled and quantified continuously by an Agilent GC (7890A) with Molsieve 5A and Hayesep columns. Products were detected using a thermal conductivity detector and flame ionization detector equipped with a methanizer (Jetanizer by Activated Research Company), and quantitative analysis was based on calibration with five different gas standards. Under these reaction conditions, the GC results showed primarily butene (C_4) and hexene (C_6) production with an average ethylene conversion efficiency of 25%. Butenes were the primary product observed with a selectivity of 90%.

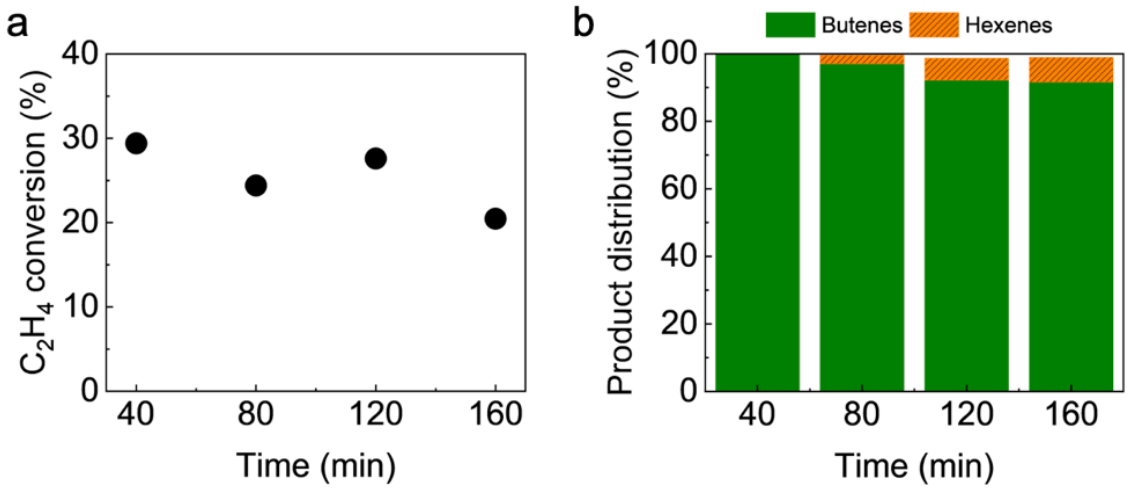

Figure 4.11. Results of the heterogeneous Ni-catalyzed ethylene oligomerization reaction under 3 sun intensity in the flow mode photothermal reactor setup. (a) Ethylene conversion efficiency over time showing an average of approximately 25% over a period of 3 hours; (b) Product selectivity over time showing a butene-to-hexene product ratio of approximately 9:1 after 3 hours.

From the results reported in this section, we see that the heterogeneous Ni-catalyzed ethylene oligomerization produces 1-alkenes with $C_4 – C_6$ carbon chain lengths under 3 sun intensity. Unlike the homogeneous Ni-catalyzed ethylene oligomerization, we do not observe any products that are longer than C_6 which is a limitation of this reaction. This is somewhat expected due to the general concept that batch mode reactions can generate longer hydrocarbon chains compared to flow mode reactions because of the increased reaction time. However, major benefits of using this catalyst/reaction are that it is not as easily deactivated by air, it can be used in a flow operation for continuous product generation, and it is less labor intensive to set up compared to the batch mode setup.

4.3 Summary and Conclusion

In this chapter, we demonstrated two different Ni-catalyzed ethylene oligomerization reactions for the conversion of ethylene to 1-alkenes with carbon chain lengths ranging from $C_6 – C_{26}$ using our photothermal reactor and selective solar absorber. In the first reaction, we reported work on a homogeneous Ni-catalyzed ethylene oligomerization using a Ni-SHOP catalyst in batch mode to produce a wide distribution of liquid hydrocarbons. Three separate experiments differing primarily in heating source (furnace, heating tape and sunlight, and sunlight) were reported with consistent generation of products with carbon chain lengths ranging from $C_6 – C_{26}$ for all of them. ^{1}H NMR was used to confirm 1-alkene generation, and GC-FID was used to quantify $C_8 – C_{18}$ products. In all cases, solid product leftover in the reactor was also observed. Under pure solar thermal energy, we reported an overall ethylene conversion efficiency of 18.5% (12.2% from liquid product, 6.3% from solid product). In the second reaction, we reported work on a heterogeneous Ni-catalyzed ethylene oligomerization using a Ni/SIRAL-30 catalyst in flow mode to continuously produce butenes and hexenes. In these experiments, we reported an ethylene conversion efficiency of 25% and a butene-to-hexene product selectivity of 9:1. This chapter concludes Section I: Generating Sustainable Fuels from Sunlight.

SECTION II: PASSIVE DAYTIME TERRESTRIAL RADIATIVE COOLING

Chapter 5

CHARACTERIZATION OF AL_2O_3 NANOPARTICLE FILMS DEPOSITED FROM A NONTHERMAL PLASMA

5.1 Introduction

As described in Chapter 1, nonthermal plasma synthesis can be used to fabricate uniform laminate nanoparticle films for passive daytime terrestrial radiative cooling applications. Before using nanoparticle films to design radiative coolers, they are first characterized using a collection of materials and optical characterization techniques to better understand their physical and optical properties. The materials characterization techniques commonly employed to study these nanoparticle films include transmission electron microscopy (TEM), scanning electron microscopy (SEM), energy dispersive spectroscopy (EDS), atomic force microscopy (AFM), and profilometry. The optical characterization techniques include ultraviolet-visible spectroscopy (UV-vis), Fourier-transform infrared spectroscopy (FT-IR), and visible and infrared ellipsometry. It is primarily the use of ellipsometry which allows the extraction of the effective complex refractive index of the nanoparticle films as a homogeneous bulk film. In general, especially when working in the infrared wavelength regime, effective medium approximations can be a fair method for understanding and characterizing the effective optical properties of nanoparticle films.[45] Due to the nature of ellipsometry as an indirect measurement technique, the other characterization techniques are needed to inform the ellipsometry models used to characterize these films.

In this chapter, we present work on characterizing and understanding the materials and optical properties of alumina nanoparticle films deposited from a nonthermal plasma. This chapter serves as a detailed introduction into laminate nanoparticle films from nonthermal plasma synthesis, using previous work done on alumina nanoparticle films as a representative introduction. As such, it serves to demonstrate the different characterization methods that we used to study laminate nanoparticle films. It reports characteristic physical and optical

properties which can be expected from these films. Finally, it provides an overview of the nonthermal plasma synthesis method used to deposit these films.

5.1.1 Abstract

Aluminum oxide, both in amorphous and crystalline forms, is a widely used inorganic ceramic material due to its chemical and structural properties. In this work, we synthesized amorphous aluminum oxide nanoparticles using a capacitively coupled nonthermal plasma utilizing trimethylaluminum and oxygen as precursors and studied their crystallization and phase transformation behavior through post-synthetic annealing. The use of two reactor geometries resulted in amorphous aluminum oxide nanoparticles with similar compositions but different sizes. Size tuning of these nanoparticles was achieved by varying the reactor pressure to produce amorphous aluminum oxide nanoparticles ranging from 6 nm to 22 nm. During post-synthetic annealing, amorphous nanoparticles began to crystallize at 800 °C, forming crystalline θ and γ phase alumina. Their phase transformation behavior was found to be size dependent in that small 6 nm amorphous particles transformed to form phase pure α-Al_2O_3 at 1100 °C, while large 11 nm particles remained in the θ and γ phases. This phenomenon is attributed to the fast rate of densification and neck formation in small amorphous aluminum oxide particles.

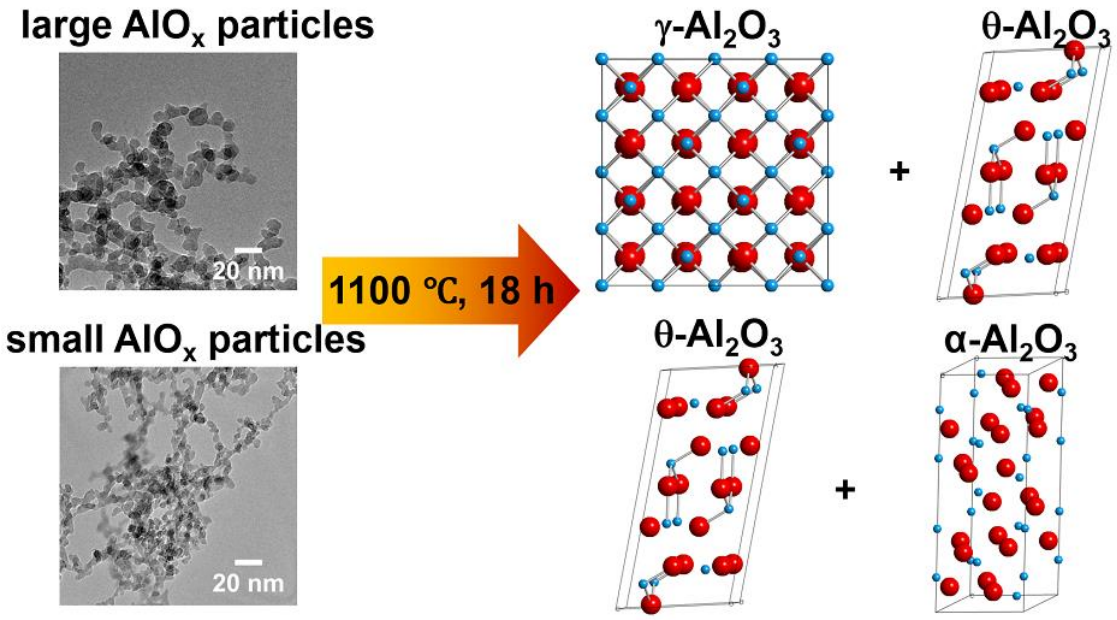

Figure 5.1. Amorphous aluminum oxide nanoparticles synthesized from a nonthermal plasma which crystallize into γ, θ, and α phase alumina post-anneal.

5.2 Aluminum Oxide Nanoparticle Films Deposited from a Nonthermal Plasma

Aluminum oxide (Al_2O_3), commonly known as alumina, is one of the most widely used inorganic ceramic materials due to its superior thermal, chemical, and structural properties. Alumina can exist in both amorphous and crystalline forms. Amorphous alumina is considered to be an excellent candidate for anodic materials, gate insulators in transistors, protective coatings, and catalysts.[119–123] Various methods have been employed to synthesize amorphous alumina nanoparticles, which include sol-gel processing[124,125], solution combustion[126–130], precipitation[131–133], ultrasonic treatment of porous anodic alumina membranes[134], energetic pulsed laser ablation[135], and tragacanth gel synthesis.[136]

The structure of amorphous alumina has been studied extensively and found to be comprised of a network of AlO_4 tetrahedra, AlO_5 polyhedra, and small fractions of AlO_6 octahedra.[137–142] Solid-state ^{27}Al nuclear magnetic resonance (NMR) studies revealed that the existence of a significant fraction of AlO_5 polyhedra, where Al^{3+} ions are penta-coordinated with oxygen ions, creates disorder and hinders the crystallization and growth of crystalline alumina

phases.[143] Thus, high temperatures (~800 °C) are required for the transformation of amorphous to crystalline alumina nanoparticles.[144] This process involves a structural rearrangement reaction converting AlO_5 polyhedra into AlO_4 and AlO_6.

Phase transformation of amorphous to crystalline alumina nanoparticles can greatly depend on several parameters such as synthetic route, heating rate, grain size, and chemical composition. Crystalline alumina can exist in various metastable crystalline phases (χ, η, δ, κ, θ, γ, ρ)[145–147] and corundum or α-alumina is identified as the most thermodynamically stable phase in bulk form. The typical phase transformation sequence in crystalline alumina can be depicted as $\gamma \rightarrow \delta \rightarrow \theta \rightarrow \alpha$-$Al_2O_3$.[144] The transformation of γ-Al_2O_3 (density ρ = 3.56 g/cm^{-3}) to α-Al_2O_3 (ρ = 3.98 g/cm^{-3}) is accompanied by a volume reduction of about 10% and proceeds through a meta-phase of θ-Al_2O_3.[148] Typically, the final transformation to α-Al_2O_3 requires higher annealing temperature around 1100 °C.[144] With superior hardness, low friction, unique heat transfer properties, and excellent wear resistance, α-Al_2O_3 plays a critical role in the production of advanced ceramic materials and as a core and filler material for nanocomposites.[149–151] γ-Al_2O_3 nanoparticles themselves also exhibit excellent catalytic properties due to their surface acidity and high surface area.[152]

In this work, we synthesized amorphous alumina nanoparticles by a nonthermal plasma approach and studied their crystallization and phase transformation behavior during post-synthetic annealing. Nonthermal plasma synthesis has shown the potential to produce a variety of nanoparticles with high purity and narrow size distributions, and the library of nanoparticle materials has been expanded from group-IV semiconductors to metal oxides and metal sulfides.[51,153–158] Furthermore, nanoparticles made by this method can be directly deposited into particle films with densities ranging from 20% to 60%.[159,160] The as-deposited aluminum oxide nanoparticles are annealed at 600 – 1100 °C for the investigation of their phase transformation behavior.

5.3 Nanoparticle Synthesis

For the synthesis of amorphous alumina (AlO_x) nanoparticles via nonthermal plasma, trimethylaluminum (TMA) and oxygen (O_2) gas were used as precursors, with argon as the carrier gas. We considered the following chemical equation to control appropriate flow rates:

$$2\,Al(CH_3)_3 + 12\,O_2 \rightarrow Al_2O_3 + 6\,CO_2 + 9\,H_2O \tag{5.1}$$

Based on the stoichiometric molar ratio of TMA and oxygen (TMA:O_2 = 1:6), over six times more oxygen than TMA should be fed for complete oxidation of TMA to Al_2O_3 and other reaction products (CO_2 and H_2O). We chose an excess oxygen flow rate of 6 standard cubic centimeters per minute (sccm) compared with a TMA flow rate of 0.2 sccm.

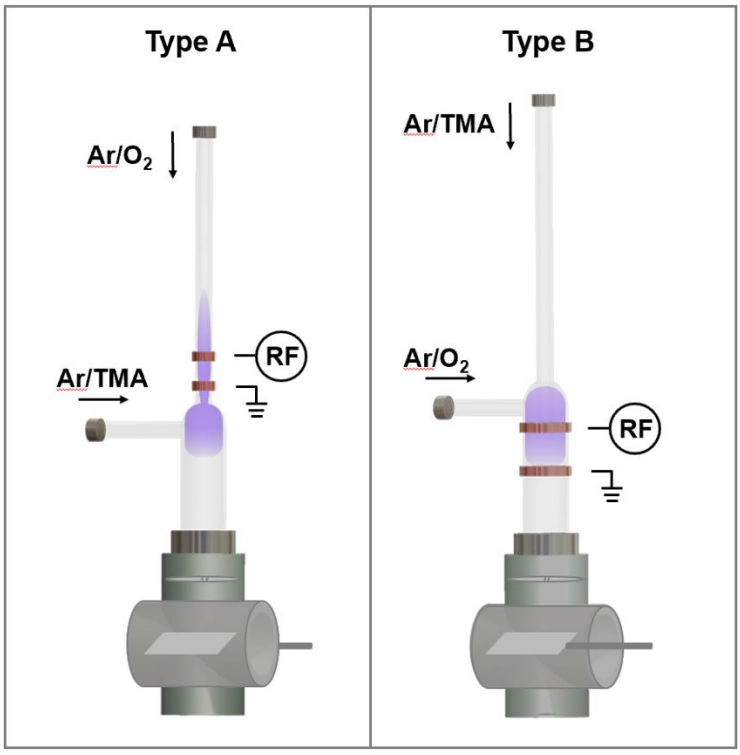

Figure 5.2. Schematic of the two types of nonthermal plasma reactors used for AlO_x nanoparticle synthesis and film deposition.

A schematic of the two types of reactors used in this work is shown in **Fig. 5.2**. AlO_x nanoparticles were synthesized in a nonthermal, low pressure flow-through reactor equipped with a 13.56 MHz radio-frequency (RF) capacitively-coupled plasma source similar to that used in [153][154]. Because two precursors can spontaneously react with each other to produce uncontrolled products[161], we injected both precursor species separately into the plasma for dissociation to occur in the plasma zone. There are two strategies that have been demonstrated before for the successful synthesis of metal oxide nanoparticles.[154,155] In the first method, denoted as type A, O_2 diluted in Ar gas was injected from the top inlet of the reactor and flowed through the region where RF power was applied. Meanwhile, 0.2 sccm of TMA vapor with 6 sccm of Ar gas were injected from a sidearm tube into the downstream region of the Ar/O_2 plasma. In this afterglow zone, AlO_x nanoparticles nucleated and grew. In the second method, denoted as type B, the TMA vapor diluted in Ar was injected through an inlet tube that extended into the main reactor chamber, while O_2 gas diluted with Ar gas was passed through a sidearm tube and into the space around the upper injection tube. The ring electrodes were placed such that plasma initiated about 1 cm above the end of the top injection tube and the discharge extended downstream of the tube end in order to dissociate TMA and O_2 precursors individually before they mix in the main reactor chamber. As-synthesized AlO_x nanoparticles in both configurations were collected on silicon wafers through a slit-shaped orifice where supersonic nanoparticle impaction produced a curtain of nanoparticles traveling at high speeds.[159] For each type of reactor, three pressure conditions were studied by using three different orifice sizes (0.3, 0.4, 0.5 mm × 8 mm) while keeping the gas flow rates constant.

For optical characterization, nanoparticle films were deposited by using the 0.5 mm × 8 mm orifice and passing a piece of Si wafer carrying a 300 nm Au film below the orifice with 240 raster passes. The gas flow rates and upstream and downstream pressures are summarized in **Table 5.1**.

Table 5.1. Summary of synthesis parameters used in this study.

	Gas	Flow rate [sccm]	P_{up} [Torr]	P_{down} [Torr]
Type A	O_2 diluted in Ar (O_2/Ar)	6 (O_2) / 60 (Ar)	3.8	0.42
	TMA vapor with Ar (TMA/Ar)	0.2 (TMA) / 6 (Ar)		
Type B	O_2 diluted in Ar (O_2/Ar)	6 (O_2) / 60 (Ar)	3.8	0.47
	TMA vapor with Ar (TMA/Ar)	0.2 (TMA) / 6 (Ar)		

5.4 Nanoparticle Characterization

X-ray diffraction (XRD) was performed with a Bruker D8 Discover 2D X-ray diffractometer equipped with a Co Kα radiation point source. Instrument broadening was obtained by measuring a standard LaB_6 crystal powder sample with the same scanning parameters (**Fig. S5.1**). For XRD analysis, aluminum oxide nanoparticles were directly deposited onto Si wafers to form a pile of powder. The XRD patterns were converted to the wavelength of a Cu source (λ=1.54 Å) for data analysis.

TEM images were taken from a Tecnai T12 microscope with an accelerating voltage of 120 kV. Nanoparticles were either directly deposited from the gas phase or drop-cast in a methanol dispersion on holey carbon TEM grids for imaging.

Fourier-transform infrared spectroscopy (FTIR) was performed with a Bruker ALPHA FT-IR spectrometer using the attenuated total reflection (ATR) module in a nitrogen-filled glovebox. AlO_x nanoparticles were dispersed in methanol and drop-cast onto the ATR crystal. Nanoparticles were allowed to dry before taking measurements.

X-ray photoelectron spectroscopy (XPS) was performed with a PHI Versa Probe III XPS and UPS system. For XPS analysis, aluminum oxide nanoparticles were deposited onto Si wafers with 30 raster passes to form a film.

Nanoparticle laminate film thicknesses were measured empirically by cross-sectioning the nanoparticle laminate films with a Ga focused ion beam (Ga-FIB) and imaging with a scanning electron microscope (FEI Nova 600 NanoLab DualBeam) at a 52° tilt. The cross-sectioning was performed in two steps: a regular cross-section (30 kV, 1 nA) approximately 2 µm in width was cut first followed by a cleaning cross-section (30 kV, 30 pA). The thickness of the cross-sections were measured with ImageJ with a correction factor of 1/cos(38°) in the y-axis to account for the tilt.

To analyze the film optical properties, the first four columns of the angle- and wavelength-resolved Mueller matrix were measured in reflection mode. Mueller matrix measurements were performed using an IR-VASE Mark II ellipsometer with an AutoRetarder from the J.A. Woollam Company. The configuration was polarizer-sample-compensator-analyzer (PSCA). The measurement spectral range extended from 250 to 5000 cm^{-1} with a resolution of 7.7 cm^{-1}. The angular range was 40 to 70 degrees from the surface normal, with an angular resolution of 5 degrees. Data was averaged over 400 measurements - five days of continuous measurement per sample under ambient conditions. Once the samples were measured, an oscillator model of the film permittivity was constructed using the software WVASE32 from J.A. Woollam. Model parameters such as film thickness and particle fill fraction were initialized based on the empirical measurement averages and constrained by three times the measurement standard deviations. Initial values for the particle oscillator model were taken from literature. All model parameters were simultaneously fitted using the full angle and wavelength-resolved Mueller matrix data.

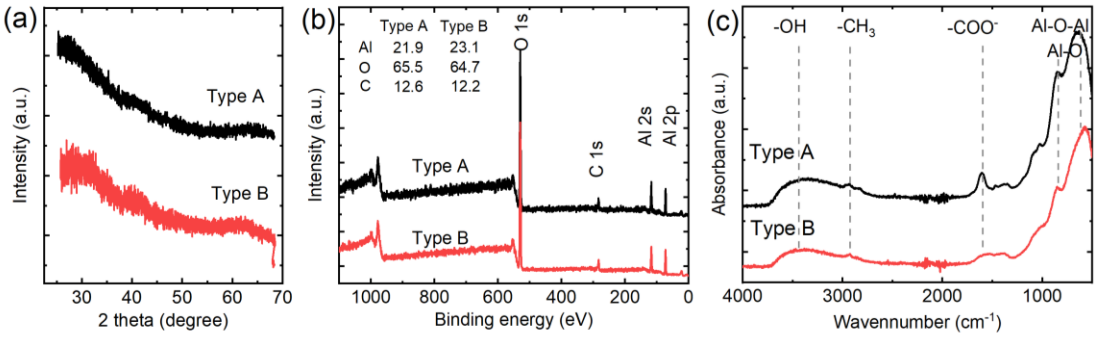

Figure 5.3. Characterization of AlO_x nanoparticles synthesized from two types of reactors at p=3.8 Torr: (a) θ–2θ mode out-of-plane XRD patterns of the as-synthesized AlO_x nanoparticles from type A and type B reactors; (b) XPS survey scan of AlO_x nanoparticles from type A and type B reactors. (c) Typical FTIR spectra of AlO_x samples from type A and type B reactors, with major absorption peaks featuring Al−O, $-COO^-$, $-CH_3$, and −OH.

Amorphous alumina (AlO_x) nanoparticles were synthesized using the two reactor geometries shown in **Fig. 5.2**. **Fig. 5.3a** shows the XRD spectra of as-synthesized AlO_x nanoparticle samples from both type A and B reactors at p = 3.8 Torr. The absence of definitive peaks in XRD suggests that as-synthesized AlO_x nanoparticles are amorphous. As shown in a previous study, amorphous alumina nanoparticles are thermodynamically more stable with the lowest surface energy compared to θ- and α phase polymorphs at large surface areas.[162]

XPS and FTIR measurements were performed to evaluate the surface and atomic composition of AlO_x nanoparticles from both reactor configurations (**Fig. 5.3b and 5.3c**). For both samples, XPS survey shows main peaks corresponding to O 1s, C 1s, and Al 2p at 530, 284, and 73 eV respectively, which confirms the elemental composition in AlO_x nanoparticles. Carbon incorporation (5 – 10 at%) is commonly observed when TMA is used as the aluminum source due to strong Al−C bonds.[163–165] The carbon content can be partly due to contamination in air, as samples are shortly exposed to air during the transfer, but can also originate from the methyl groups in TMA. Atomic percentage ratios of Al to O are around 1:3 for both A and B type reactor samples, with carbon percentages around 10%–

15%. The atomic ratios are in general not affected by the plasma power used for synthesis (**Fig. S5.2**). The high-resolution XPS spectra were analyzed to gain some insight into the composition of both types of AlO_x nanoparticle samples (**Fig. S5.3**). The binding energy of Al 2p peak at ~74.6 eV corresponds to Al−O bonding in alumina.[166,167] The O 1s peak at ~531.5 eV can be resolved into two individual peaks representing O^{2-} and OH^-.[167–169] FTIR spectra for samples from both reactor types reveal absorption bands related to hydroxyl (−OH), alkyl (C−H), (C−O), and aluminum species (Al−O and Al−O−Al). The peak around ~670 cm^{-1} and the shoulder which is located around ~860 cm^{-1} correspond to the Al–O stretching vibrations in five-fold coordinated AlO_5 and four-fold coordinated AlO_4, respectively. Features from AlO_6 stretching vibrations could also be present, which according to the literature lie in the 400–650 cm^{-1} spectral range and overlap with Al–O stretching vibrations and oscillations in AlO_4 and AlO_5.[163,170,171]

The average sizes of the AlO_x nanoparticles were determined using TEM. At p = 3.8 Torr, the average sizes of AlO_x nanoparticles from type A and type B reactors are 11 ± 3 nm and 6 ± 1 nm, respectively. Size tuning of AlO_x nanoparticles can be achieved by varying the reactor pressure which changes the particle residence time in the plasma. TEM images of as-synthesized AlO_x nanoparticles from type A and B reactors under three sets of reactor pressures are shown in **Fig. 5.4**. At each pressure, the type B reactor produces smaller particles than the type A reactor. For both reactor configurations, the mean particle size increases with increasing pressure. At 3.8 and 5.2 Torr, AlO_x nanoparticles from both reactors are aggregated but nearly spherical in shape and have relatively narrow size distributions (**Fig. S5.4**). At the relatively high pressure of 7.5 Torr, AlO_x nanoparticles exhibit a bimodal size distribution with both small and large irregular nanoparticles present.

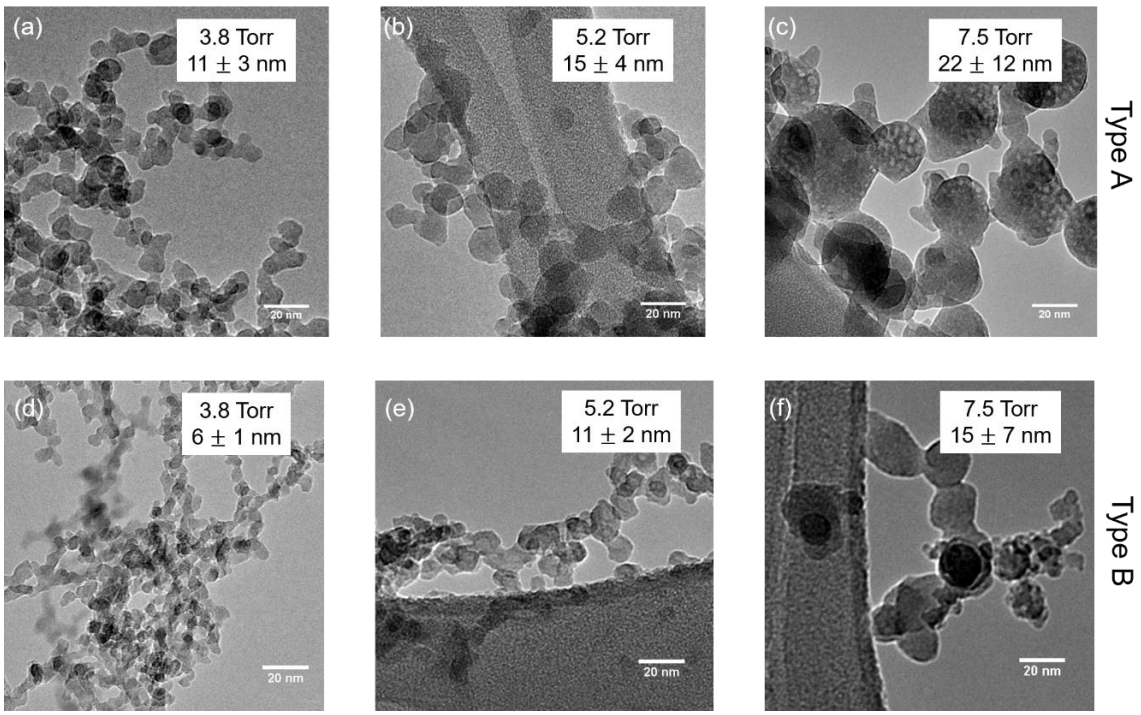

Figure 5.4. TEM images of AlO_x nanoparticles synthesized from type A and type B reactors at pressures of 3.8 Torr, 5.2 Torr and 7.5 Torr with mean sizes and standard deviations.

We estimated the process yield of each type of reactor setup by measuring the weight of the AlO_x nanoparticle powders collected at p = 3.8 Torr for 10 minutes. With a fixed substrate position, samples collected from both types of reactor setups were piles of white powders (**Fig. S5.5**). The sample weights from type A and B reactor are 3.2 mg and 7.0 mg, respectively, which corresponds to yields of 19.2 mg/hour and 42.0 mg/hour. The current production rates are limited by the TMA and oxygen flow rates due to safety considerations.

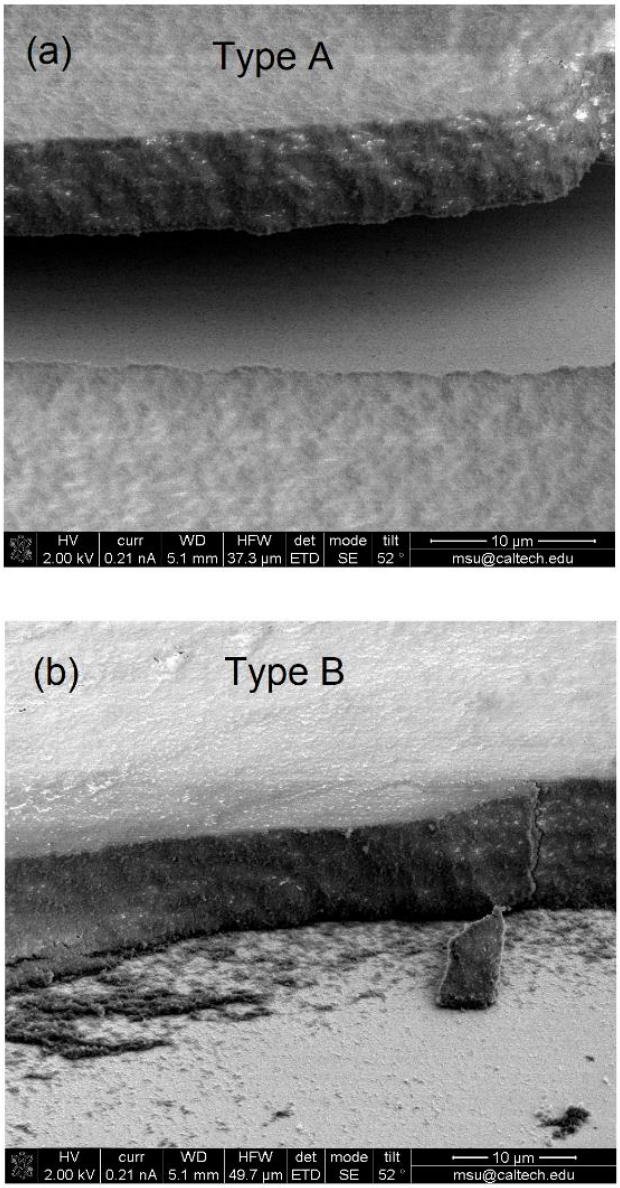

Figure 5.5. Cross-sectional SEM images of AlO_x nanoparticle laminate films synthesized from type A and type B reactors. A correction factor of 1/cos(38°) is applied in the y-axis to account for the tilt of the setup with respect to the SEM Everhart-Thornley Detector (ETD).

We deposited AlO_x nanoparticle films by rastering the substrate beneath the orifice to study the optical properties of AlO_x nanoparticles. The films were deposited with 240 raster passes and examined by SEM and Mueller matrix measurements. The thickness of the AlO_x

nanoparticle laminate films was measured to be 7.1 ± 1.1 μm for the type A and 9.1± 0.9 μm for the type B reactor films. Characteristic cross-sectional SEM images of the nanoparticle laminate films are shown in **Fig. 5.5**.

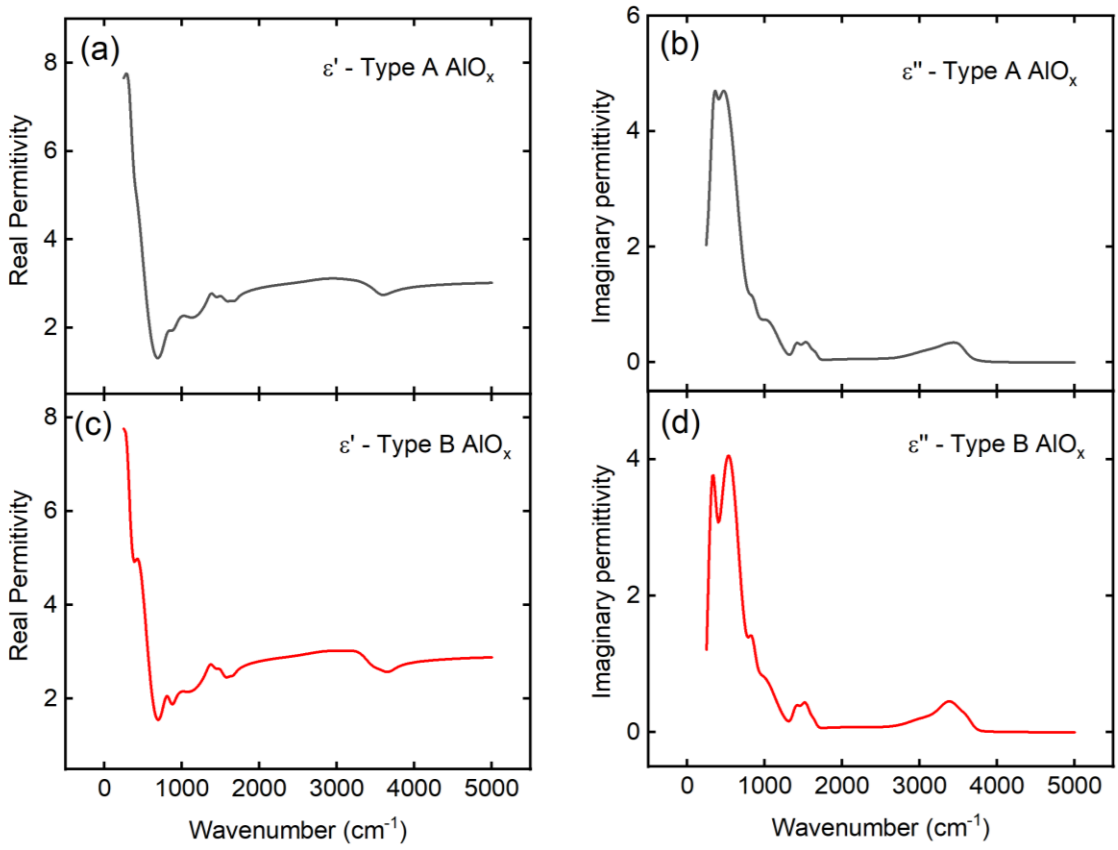

Figure 5.6. Real and imaginary parts of the complex AlO_x nanoparticle films permittivity found in the type A reactor (a,b) and type B reactor (c,d), respectively.

Mueller matrix measurements, which allow for characterization of anisotropic-depolarizing samples, including cross-polarization, were performed to extract the effective (homogenized) complex permittivity of the type A and B reactor particle films as well as the complex permittivity of the corresponding AlO_x nanoparticles. In both type A and B films, no polarization conversion from p-polarized to s-polarized or vice versa was present. The Mueller matrix data showed only noise for elements mm_{13}, mm_{31}, mm_{22}, mm_{23}, mm_{32}, mm_{41},

and mm_{42}. Furthermore, $mm_{12} = mm_{21}$. This block diagonal structure of the Mueller matrix indicates that the samples can be treated as macroscopically isotropic.[172–174] Therefore, the film effective permittivity can be represented by a wavelength dependent scalar. The nanoparticle films were best homogenized using the Bruggeman mixing formula, which has been shown to consistently produce an effective permittivity to accurately model nanoparticle films, including anisotropic-depolarizing effects.[175–180] Maxwell-Garnett and linear mixing formulas were also explored, but less accurately modeled the measured data. The permittivity of the individual nanoparticles was modeled using Gaussian oscillators, to represent amorphous phonon resonances, while satisfying the Kramers-Kronig relations. For type A, a sample thickness of 7.75 μm and a particle fill fraction of 22.3% and, for type B, and a thickness of 9.23 μm and fill fraction of 19.4% provided the best fit to the optical interference patterns in a nearly lossless region of the amorphous alumina film between 4000 – 6250 cm^{-1}. Further detail about Bruggeman homogenization and the corresponding Gaussian oscillator model, including tables for the oscillator parameters, can be found in **Section 5.8**. **Fig. 5.6** shows the reconstructed imaginary part of the particle permittivity. Strong oscillators in the 300–700 cm^{-1} spectral range correspond to AlO_4, AlO_5 and AlO_6 stretching vibrational modes. These values corroborate our results from FTIR as well as literature.[163,170,171,178] Similar to our findings from XPS and FTIR, the reconstructed permittivity shows that the particles from both types of reactors have similar chemical composition. The depolarization constant for type A and B reactor films was 0.261 ± 0.005 and 0.407 ± 0.006, respectively. This indicates predominantly scattering of spherical like inclusions post deposition. All of the above characterizations reveal that particles from type A and type B reactors have similar compositions but different sizes.

5.6 Crystallization Behavior of Amorphous Alumina Nanoparticles

In a nonthermal plasma, crystallization of nanoparticles can occur through the recombination of electrons and ions on the nanoparticle surfaces.[181,182] Here, the as-produced AlO_x nanoparticles have amorphous structures, indicating that particle heating from the nonthermal plasma is not sufficient to induce crystallization. Post-synthetic annealing of

amorphous alumina nanoparticles was explored to induce crystallization and subsequent phase transformation of crystalline alumina nanoparticles.

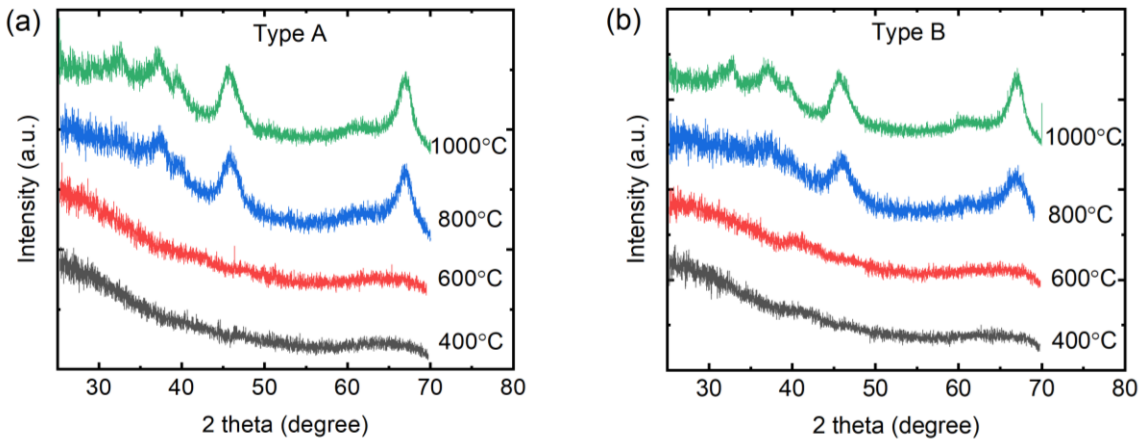

Figure 5.7. XRD patterns of the post-synthesis annealed AlO_x nanoparticles from (a) type A and (b) type B reactors, with annealing temperature ranging from 400 °C to 1000 °C and annealing times of 18 h.

To study the crystallization and phase transformation behavior of amorphous AlO_x nanoparticles, a pile of AlO_x nanoparticles was collected and annealed in a Thermo Scientific Lindberg Blue furnace at temperatures of 400–1100 °C in the atmosphere. The typical temperature ramp rate was ~50 °C/min. Since the properties of small AlO_x nanoparticles are of primary interest, we explored the crystallization behavior of samples synthesized at 3.8 Torr from type A and B reactors, respectively. Phase transformation of amorphous alumina typically proceeds through the amorphous-to-γ and γ-to-α phase transitions[183,184], or with an additional transition to the θ-phase between the transformation from the γ- to α- phase[185], before reaching the thermodynamically stable α-phase. Our observations reveal that AlO_x nanoparticles from both types of reactors begin to crystallize at 800 °C producing a mixture of θ- and γ-phases, as shown in **Fig. 5.7a and 5.7b**. The crystallization temperature is consistent with that from the literature.[127,162]

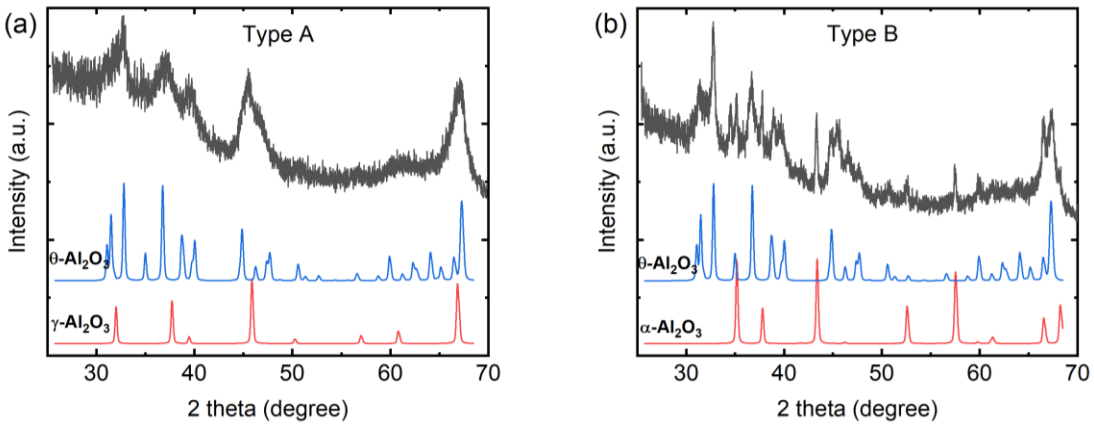

Figure 5.8. XRD patterns of the post-heated AlO_x nanoparticles from (a) type A and (b) type B. Both samples were annealed at 1100 °C for 18 h. The bottom columns in both graphs show the reference profile of γ-, θ-, and α-phase aluminum oxides.

As the annealing temperature increased up to 1100 °C, we observed that AlO_x nanoparticles from type A and B reactors form different crystalline phases (**Fig. 5.8**). The larger AlO_x nanoparticles from the type A reactor form a mixture of θ- and γ-phase at 1100 °C whereas the smaller AlO_x nanoparticles from the type B reactor form a mixture of θ- and α-phases. Time of post-synthetic annealing also affects phase transformation of the type B AlO_x nanoparticles. When the annealing time increased up to 40 h, type B AlO_x nanoparticles form phase pure α-Al_2O_3 nanocrystals (**Fig. 5.9**).

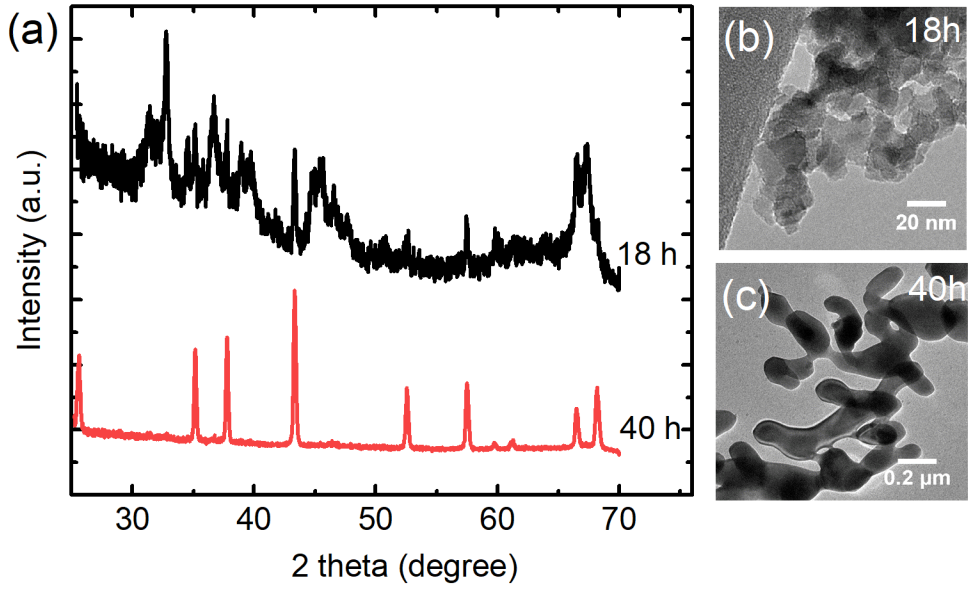

Figure 5.9. (a) XRD pattern of type B AlO_x nanoparticles heated at 1100 °C for 18 h and 40h; TEM images of (b) AlO_x nanoparticles annealed at 1100 °C for 18 h and (c) AlO_x nanoparticles annealed at 1100 °C for 40 h.

This transformation is also accompanied with a significant crystal growth. Mean crystallite sizes of crystalline alumina particles after 18 h annealing were estimated using Scherrer fittings. 18 h annealing of ~6 nm AlO_x nanoparticles at 1100 °C resulted in a mixture of ~30 nm θ-Al_2O_3 and >100 nm α-Al_2O_3 particles (**Fig. S5.6**). Phase pure α-Al_2O_3 particles obtained after 40 h are also estimated to be larger than 100 nm. The crystalline sizes are also confirmed by TEM images (**Fig. 5.9b and 5.9c**). It is interesting to observe that the larger AlO_x nanoparticles from the type A reactor never form α-Al_2O_3 phase even with longer annealing times.

As AlO_x nanoparticles from both types of reactors have similar composition, we postulated that the difference in their phase transformation behavior is likely due to their different as-synthesized particle sizes. To test this assumption, we investigated the phase transformation behavior of the large AlO_x particles with mean sizes around 11 and 15 nm synthesized in the type B reactor with higher reactor pressures. XRD patterns taken after 18 h of annealing time reveal that smaller ~6 nm AlO_x nanoparticles form α-phase Al_2O_3 along with θ-Al_2O_3, while

larger ~11 and ~15 nm AlO_x nanoparticles only forms θ-Al_2O_3 and do not exhibit any α-phase features (**Fig. S5.7**). These observations support our assumption that smaller size AlO_x nanoparticles have a higher tendency to transform to α-phase after annealing.

It has been pointed out that necking and densification of particles starts to occur when annealing amorphous AlO_x nanoparticles, forming nanoporous structures before crystallization.[162,186,187] It is likely that during the annealing, the rate of densification and neck formation is faster in smaller particles compared to larger particles, as the neck growth is dominated by mass transport and is thus enhanced in smaller size particles.[188] The fact that densification can be promoted by decrease of particle sizes has also been observed in other nanoparticle systems.[189] After neck growth, the big, interconnected structures tend to transform to α-phase Al_2O_3 as temperature further increases, as it is the thermodynamically stable phase for bulk Al_2O_3.

5.7 Summary and Conclusion

Amorphous alumina nanoparticles with average sizes ranging from 6 nm to 22 nm were successfully synthesized using a nonthermal plasma approach with two different reactor geometries with typical yields of 19 mg/hour and 42 mg/hour, respectively. Infrared Mueller matrix measurements indicated the optical properties of the nanoparticle film could be modeled by a homogenized effective refractive index. The homogenized refractive index of the particle film was shown to be accurately represented using the Bruggeman effective medium model. Based on this model, particle fill fractions were estimated to be around 20% for both type A and type B reactors. Furthermore, the refractive index of the amorphous alumina nanoparticles was modeled using Gaussian oscillators, showing clear AlO_4, AlO_5, AlO_6, and Al−OH spectral peaks, matching reports in literature. Post-thermal annealing of both AlO_x particles led to crystallization, forming a mixture of θ- and γ phases at 800 °C. While small AlO_x nanoparticles with average diameters of ~ 6 nm were transformed into phase pure α-Al_2O_3 upon annealing at 1100 °C, larger AlO_x nanoparticles never formed α-Al_2O_3.

5.8 Supplemental Information

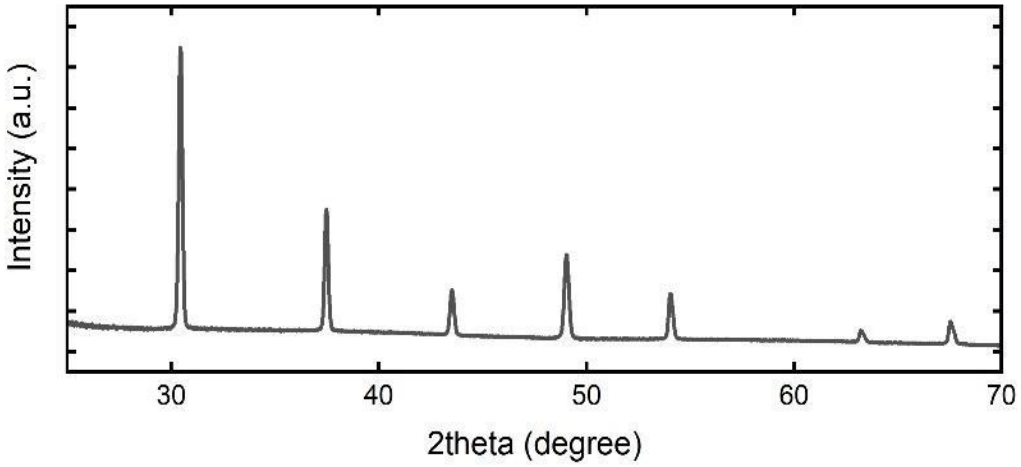

Figure S5.1. XRD pattern from a standard LaB_6 sample taken using a Bruker D8 Discover 2D X-ray diffractometer. This pattern is used as a reference to correct for instrument broadening.

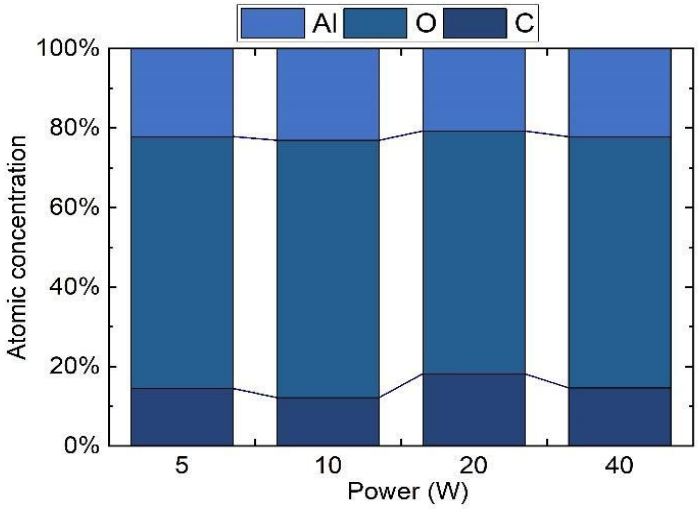

Figure S5.2. Atomic concentration in samples from type B reactor obtained by XPS with power varying from 5 W to 40 W.

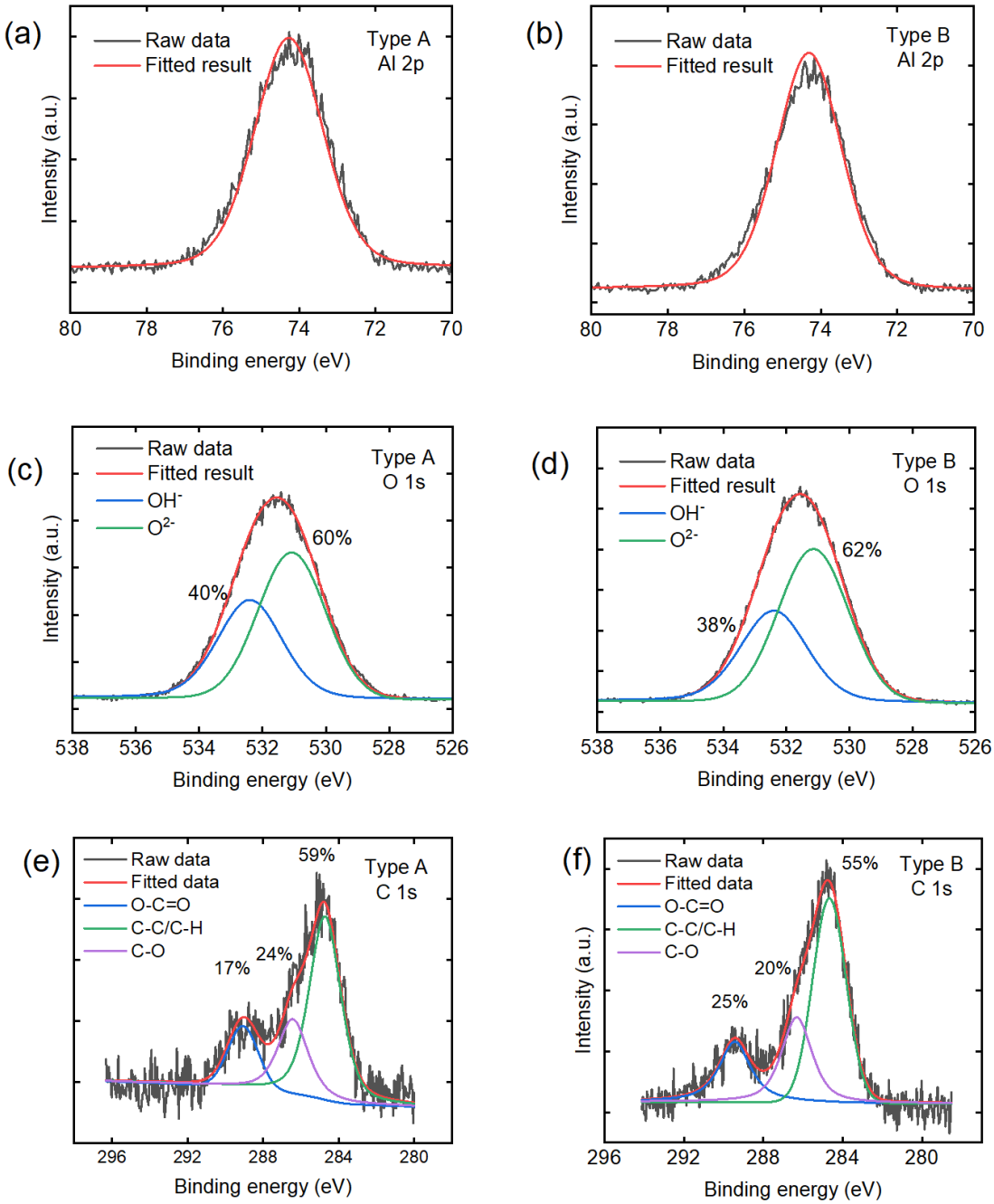

Figure S5.3. XPS high resolution spectra of Al 2p peak, O 1s peak and C 1s peak for AlO_x nanoparticle samples from type A and type B reactors. The peak corresponding to adventitious carbon is shifted to 284.8 eV as a reference.

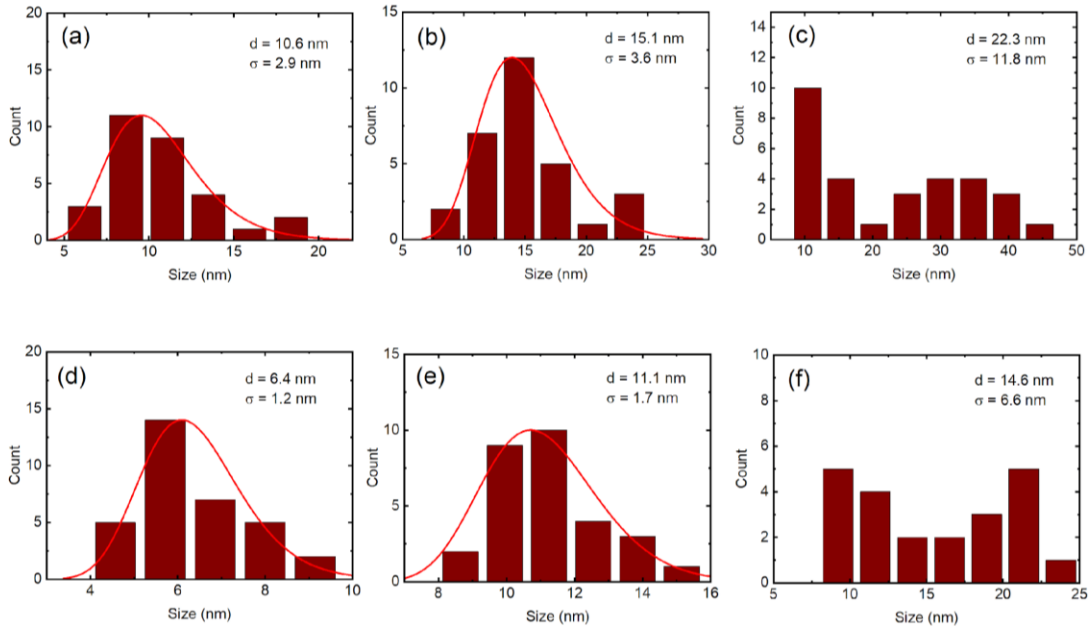

Figure S5.4. Size distributions corresponding to the TEM images in **Fig. 5.4a-f**.

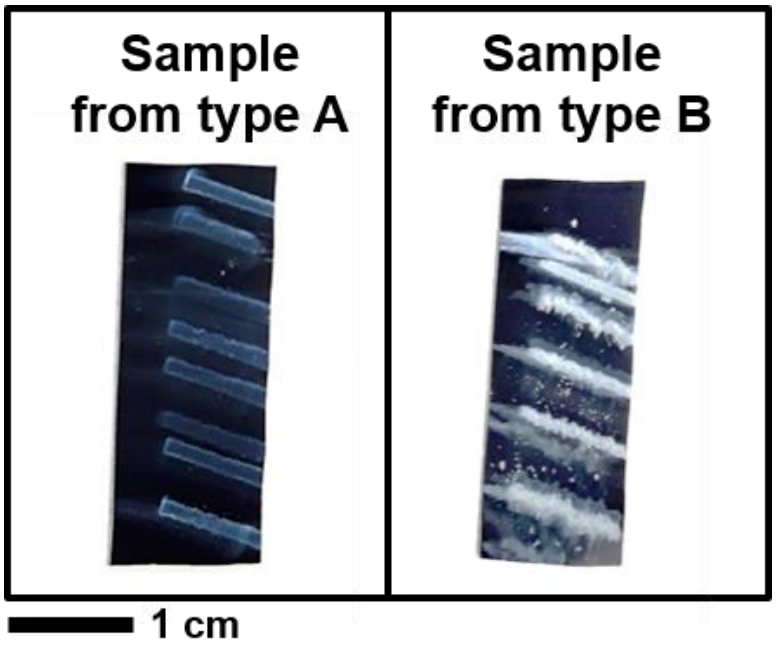

Figure S5.5. Photograph showing AlO_x nanoparticles deposited from type A and type B reactors for same period of time.

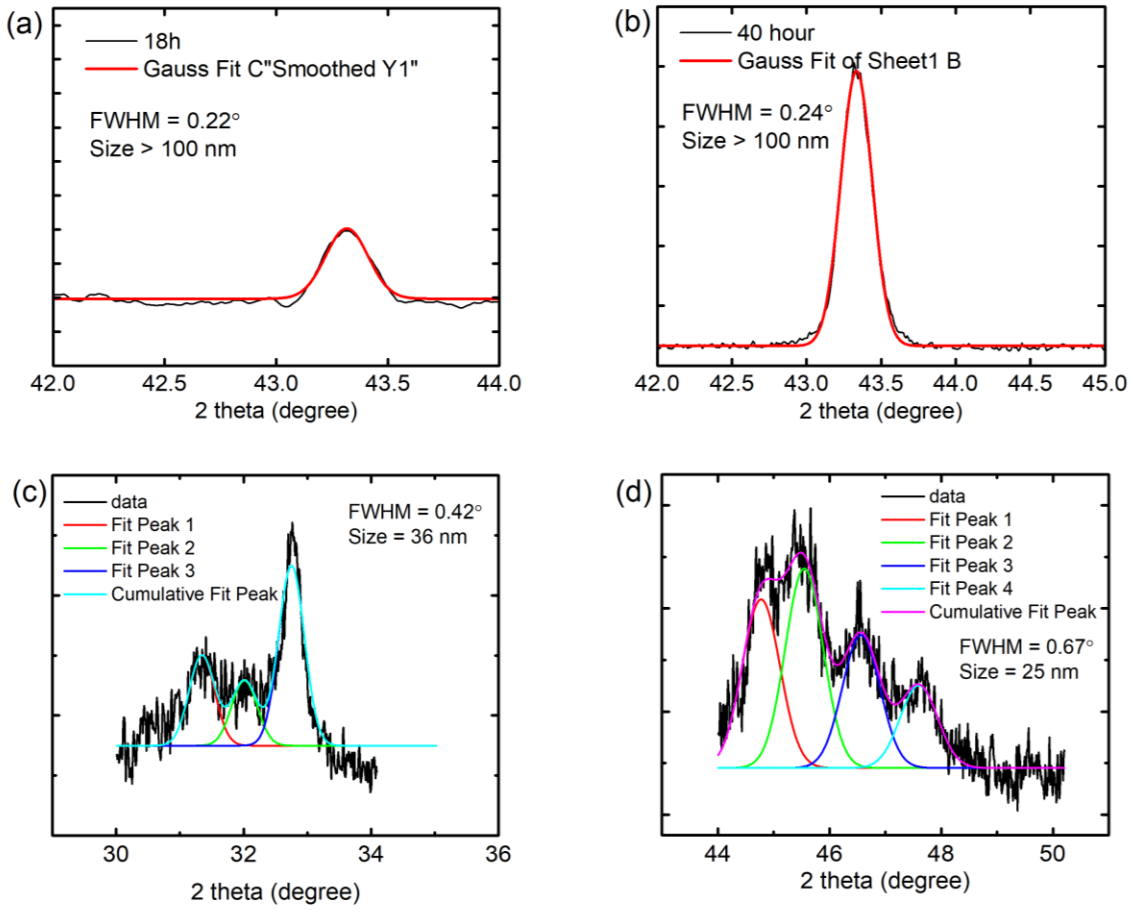

Figure S5.6. Scherrer fittings of XRD patterns (λ = 1.54 Å) of AlO_x nanoparticles from type B reactor after heating at 1100 ˚C for 18 h and for 40 h. To obtain size estimates for the α-phase and θ-phase individually, we choose non-overlapping peaks from the two phases. For the α-phase, (113) peaks were fitted. For θ-phase, peaks around 30-34˚ and 44-50˚ were fitted. Instrumental broadening was accounted for by subtracting the FWHM of the nearest peak of the LaB_6 standard sample, **Fig. S5.1**. In the Scherrer equation, a shape factor of 0.89 was used. As the widths of α-phase peaks are close to those of the LaB_6 standard sample indicating large crystallite sizes, a rough size estimate of >100 nm is quoted in the main text.

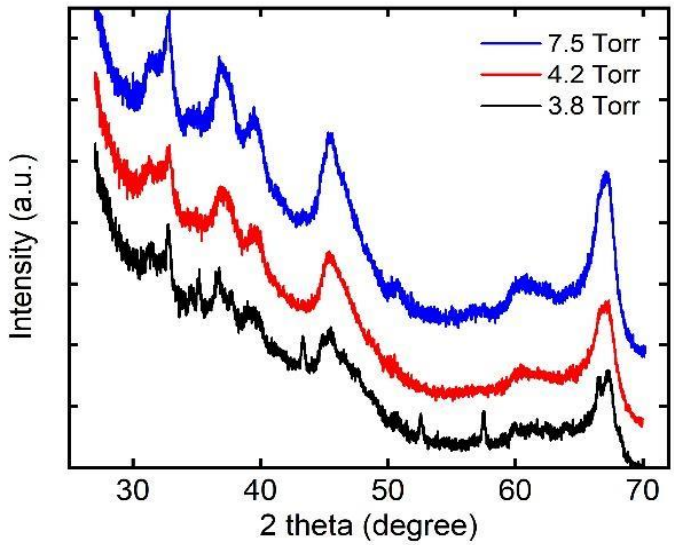

Figure S5.7. XRD patterns of samples from type B reactor for three nanoparticle sizes, obtained by varying the gas pressure, after annealing at 1100˚C for 18 hours. Only the smallest particles with about 6 nm size show the appearance of the α-phase.

Permittivity Modeling of Amorphous Aluminum Oxide Nanoparticle Films

The film's homogenized permittivity (ε_{eff}) can be represented by a wavelength dependent scalar. We model (ε_{eff}) using the Bruggeman mixing formula:

$$f_{AlO_x}\frac{\varepsilon_{AlO_x}-\varepsilon_{eff}}{\varepsilon_{eff}+k\left(\varepsilon_{AlOx}-\varepsilon_{eff}\right)}+\left(1-f_{AlO_x}\right)\frac{\varepsilon_{air}-\varepsilon_{eff}}{\varepsilon_{eff}+k\left(\varepsilon_{air}-\varepsilon_{eff}\right)}=0 \qquad (S5.1)$$

Where ε_{AlOx} and ε_{air} are the permittivity of the nanoparticles and air, respectively; f_{AlOx} (22.3 ± 0.33% for type A and 19.4 ± 0.11% for type B) volume fill fraction of the AlO_x nanoparticles; and k (0.261 ± 0.005 for type A and 0.407 ± 0.006 for type B) is the depolarizing factor 1. ε_{AlOx} is modeled as:

$$\frac{\varepsilon_{AlO_x}(E)}{\varepsilon_o}=\varepsilon_\infty+\varepsilon_{pole1}+\varepsilon_{pole2}+\sum_{n=1}^{11}\varepsilon_{Gauss_n}(E) \qquad (S5.2)$$

Where ε_0 is the permittivity of free space and ε_∞ (3.09 ± 0.01 for type A and 2.97 ± 0.02 for type B) is the infinite frequency permittivity. The complex part of the Gaussian oscillators:

$$\left(\varepsilon_{Gauss_n} = \varepsilon_{1n}(E) + i\varepsilon_{2n}(E)\right) \qquad (S5.3)$$

are given by:

$$\varepsilon_{2n}(E) = A_n e^{-\left(\frac{E-E_n}{\sigma_n}\right)^2} - A_n e^{-\left(\frac{E+E_n}{\sigma_n}\right)^2}, \sigma_n = \frac{Br_n}{2\sqrt{\ln(2)}}, \qquad (S5.4)$$

where Br_n is the full-width at half-maximum, which accounts for spectral broadening. The real part of the permittivity is given by the Kramers-Kronig relation:

$$\varepsilon_{1n}(E) = \frac{2}{\pi} P \int_0^\infty \frac{\xi \varepsilon_{2n}(\xi)}{\xi^2 - E^2} d\xi\,, \qquad (S5.5)$$

where P is the principle value. **Table S1** and **Table S2** give the fit parameters of the Gaussian oscillators for the amorphous Al_2O_3 nanoparticle films from type A and type B reactors, respectively.

Table S5.1. Gaussian oscillator parameters used to reconstruct the permittivity of nanoparticles from type A reactor. Phonon resonance type (first column), amplitude (second column), spectral broadening (third column) and resonant frequency (fourth column) of the Gaussian oscillators used to calculate the AlO_x particle permittivity from Mueller matrix data. The fifth column gives the resonant frequency range expected from previous literature reports. Citations for the expected frequency range are in the sixth column.

Type A	*Gaussian Oscillator Fit*			*Literature Values*	
Vibration	*Amplitude*	*Broadening [cm^{-1}]*	*Frequency [cm^{-1}]*	*Frequency [cm^{-1}]*	*Ref.*
AlO_6, AlO_4 Deformations	1.0340	83.221	344.27	322−326	163,171
AlO_6 stretching	4.6977	408.32	475.78	482−491	171
AlO_4 stretching	0.3357	107.70	851.46	902−880	170,171,178
Al−OH sym/asym	0.6933	341.47	1027.5	1072−1160	171,190
H_2O deformations/ vibrations	0.22815	92.908	1410.6	1375	171
H−O−H bend	0.31668	159.19	1535.8	1600	178
$-COO^-$	0.0783	74.000	1655.8	1300−1850	163
	0.05905	1700.8	2355.7		
Al−OH stretching	0.19133	618.98	3207.7	3250−3600	163,178
O−H stretching	0.20091	278.01	3429.0	3400-3600	163,171,190
Al−OH stretching	0.0719	162.00	3523.7	3250−3600	163,178

Table S5.2. Gaussian oscillator parameters used to reconstruct the permittivity of nanoparticles from type B reactor. Phonon resonance type (first column), amplitude (second column), spectral broadening (third column) and resonant frequency (fourth column) of the Gaussian oscillators used to calculate the AlO_x particle permittivity from Mueller matrix data. The fifth column gives the resonant frequency range expected from previous literature reports. Citations for the expected frequency range are in the sixth column.

Type B	*Gaussian Oscillator Fit*			*Literature Values*	
Vibration	*Amplitude*	*Broadening [cm^{-1}]*	*Frequency [cm^{-1}]*	*Frequency [cm^{-1}]*	*Ref.*
AlO_6, AlO_4 Deformations	2.5049	109.52	318.72	322−326	[163,171]
AlO_6 stretching	4.0194	320.53	531.22	482−491	[171]
AlO_4 stretching	0.4802	100.47	837.05	902−880	[170,171,178]
Al−OH sym/asym	0.78315	397.17	966.53	1072−1160	[171,190]
H_2O deformations/vibrations	0.26118	98.502	1403.0	1375	[171]
H−O−H bend	0.37889	140.14	1520.6	1600	[178]
$-COO^-$	0.0780	74.000	1635.8	1300−1850	[163]
	0.0759	1883.7	2237.9		
Al−OH stretching	0.1738	559.78	3129.3	3250−3600	[163,178]
O−H stretching	0.3324	304.69	3406.2	3400-3600	[163,171,190]
Al−OH stretching	0.1019	162.53	3607.7	3250−3600	[163,178]

Chapter 6

DESIGN OF DAYTIME RADIATIVE COOLING STRUCTURES WITH SI_3N_4 AND SIO_2 NANOPARTICLE FILMS

6.1 Introduction

In Chapter 5, laminate nanoparticle films and nonthermal plasma synthesis were introduced using previous work on alumina nanoparticle films. While the previous chapter focused on alumina nanoparticles, nonthermal plasma synthesis can also be used to deposit nanoparticle films from materials such as silica and silicon nitride.[50,52] Consequently, the use of nanoparticle films with different materials can be naturally extended towards radiative cooling applications, as suggested in Chapter 1 which proposed laminate nanoparticle films as a photonic design for passive terrestrial radiative coolers.

In this chapter, we present work on the design of efficient passive terrestrial daytime radiative coolers using silica and silicon nitride laminate nanoparticle films. We introduce the principles for designing terrestrial daytime radiative coolers and use a generalized effective medium theory to design two-layer nanoparticle structures comprised of silica and silicon nitride. We report their expected cooling performance, and we compare their performance with the performances of other radiative cooling structures report in literature using a standardized method.

6.1.1 Abstract

Research on radiative cooling has attracted recent widespread interest owing to the potential for low-cost passive structures to enable large-scale thermal energy management. Using a generalized effective medium theory, we theoretically show that two-layer films comprised of SiO_2 and Si_3N_4 nanoparticle layers on an Ag back reflector exhibit superior radiative cooling compared to single-layer or two-layer dense solid films and can outperform other reported designs. The performance enhancement is a result of the ability

to tune the nanoparticle fill fraction, which improves the spectral match between emissivity of this structure and the atmospheric transmission window. We also propose a standardized method for comparing the performance of radiative cooling structures reported by the research community.

6.2 Laminate Nanoparticle Films for Daytime Terrestrial Radiative Cooling

Approximately forty percent of the world population lives in consistently hot regions, many of which have homes lacking air conditioning.[191–193] Rising standards of living and growing demand for improved public health and comfortable living conditions is projected to lead to a 450% increase in air conditioning from 2010 to 2050 worldwide, representing one of the largest contributors to worldwide energy consumption.[194–196] Furthermore, current air conditioning systems account for almost 700 million metric tons of CO_2-equivalent emissions per year.[192] Seventy-four percent of these emissions are from electricity generation and approximately nineteen percent from refrigerant based hydrochlorofluorocarbons (HCFCs) which have a disproportionately large global warming impact relative to their mass.[192] These predictions highlight the importance of developing improved sustainable and environmentally friendly cooling technologies. Furthermore, a low cost and easily implemented passive cooling technology can promote early adoption in developing countries, reduce overall energy use, and lower greenhouse gas emissions.

Cooling by radiative heat transfer from a terrestrial ambient to the cold ambient of space is a passive, sustainable solid-state technique to provide cooling without the need for external power or additional operating costs. Photonic structures which are both highly reflective in the solar spectrum (below 2.5 μm) and highly emissive in the infrared atmospheric transmission window (8 – 14 μm) can suppress solar heating and remove heat through infrared (IR) radiation to cool throughout the diurnal cycle. Radiative cooling structures are particularly applicable in regions with low humidity, where the atmosphere is most transparent, such as Mexico, northern and southern Africa, the Middle East, Australia, India, parts of North and South America, and areas of northern Asia.[192,197] The primary requirement of a radiative cooler is to provide enough cooling power at a specified

temperature to more than offset its own parasitic heating, thus providing net cooling, and is constrained by the limited bandwidth of the infrared atmospheric transmission window and stringent reflectivity requirements in the solar spectrum. Recent designs for daytime radiative cooling structures to improve cooling performance include structures with glass nanoparticles embedded into a polymer film, layered thin films on back reflectors, and complex lithographically patterned structures such as many-layered nanoarrays.[198–209] Other passive cooling techniques – such as earth to air heat exchangers, evaporative coolers, and nocturnal convective coolers – focus on removing heat through a heat sink (ground, water, or air respectively), but suffer from high initial costs, continual operating costs, and/or external power requirements.[210,211]

Films composed of Rayleigh scattering nanoparticles can provide simple photonic designs for improving daytime cooling performance and are amenable to scalable manufacturing.[50,51] By tuning the nanoparticle fill fraction, air-material composites of this type can provide broadband impedance matching to free space and the ability to spectrally tune absorption resonances by changing the local (Lorentz) field.[46,179,212] Conversely, layered structures synthesized by thin film deposition can enable improved impedance matching to free space and resonance shifts through either graded index stacks, periodic layered structures, or intricate patterning.[213–216] For graded index and periodic structures, impedance matching is limited by the minimum practically achievable refractive index in the low index layers and the number of layers in the stack.[213] Furthermore, graded index and periodic layered structures are constrained by the limited portfolio of materials that can be used to achieve the stringent broadband reflection and emission requirements of a daytime radiative cooler.[40] Use of patterned subwavelength-scale resonant or wavelength-scale diffractive photonic structures represents another approach to tune photonic properties but is limited by fabrication complexity for large-area low-cost structures.[40] In this paper, we theoretically show that nanoparticle films can circumvent the impedance matching and materials limits which constrain layered structures. Two-layer nanoparticle films can achieve radiative cooling performance comparable to or greater than others reported to date, based solely on tuning nanoparticle fill fraction and film thickness.

Using a generalized effective medium theory, we show that simple two-layer nanoparticle films composed of separate layers of SiO_2 and Si_3N_4 particles on a silver back reflector can outperform all dense solid laminate thin films and provide a cooling performance superior to those reported previously.[198–202] Using consistent solar, atmospheric, convective/conductive, and ambient temperature conditions across comparisons, we find that the radiative cooling performance of two-layer nanoparticle film designs exceeds many reports of radiative cooling designs in literature by up to 20 W/m^2 and 25 W/m^2 at operating temperatures of 290 K and 280 K respectively. Furthermore, optimized two-layer nanoparticle film designs have higher cooling power than optimized dense solid laminate thin films, regardless of which structure or composition is chosen. These results support the idea that random nanoparticle laminate films could provide a feasible alternative to dense solid thin film or patterned designs, provided scalable synthesis techniques can be identified. In this regard, plasma synthesis or ball milling could be considered as possible scalable deposition methods.[50,217]

6.3 Principles of Daytime Terrestrial Radiative Cooling

Radiative cooling structures are designed to selectively emit radiation within the atmospheric transmission window, reflect the solar spectrum, and minimize conductive or convective heating losses. Formally this is expressed as a power balance:

$$P_{net} = P_r - P_a - P_{sun} - P_{other} \tag{6.1}$$

where P_{net} is the net power leaving the structure, P_r is the thermal power the structure emits, P_a is the thermal power emitted from the atmosphere that is absorbed by the radiative cooler, P_{sun} is the solar power absorbed by the radiative cooler, and P_{other} accounts for heating due to conduction or convection. To cool below room temperature, the structure must reflect the solar spectrum to prevent heat buildup and emit within the atmospheric transmission window to radiate its heat into outer space. The cooling power of a radiative cooler is defined by the amount of thermal radiation it emits per unit time and can be expressed as:

$$P_r(T) = 2\pi A \int_0^{\frac{\pi}{2}} \int_0^{\infty} I_B(\lambda, T_r) e_r(\lambda, \theta) \sin\theta \cos\theta \, d\lambda d\theta \tag{6.2}$$

where A is the structure area, e_r is the emissivity of the radiative cooler and I_B is the blackbody spectral radiance of the radiative cooler:

$$I_B(\lambda, T) = \frac{2hc^2}{\lambda^5} \frac{1}{e^{\frac{hc}{\lambda k_B T}} - 1}, \tag{6.3}$$

where T_r is the structure's temperature and λ is the emission wavelength.

Under thermodynamic equilibrium, emissivity and absorptivity can be interchanged based on Kirchhoff's law of radiation. Heating of the structure by absorbed atmospheric radiation is expressed as:

$$P_a(T) = 2\pi A \int_0^{\frac{\pi}{2}} \int_0^{\infty} I_B(\lambda, T_a) e_r(\lambda, \theta) e_a(\lambda, \theta, \alpha) \sin\theta \cos\theta \, d\lambda d\theta \tag{6.4}$$

where e_a is the emissivity of the atmosphere, $I_B(\lambda, T_a)$ is the blackbody spectral radiance of the atmosphere at ambient temperature T_a, and α is a variable encapsulating the conditions relating to the composition of the atmosphere.[218] The power absorption from direct solar radiation can be expressed as:

$$P_{sun} = A \int_0^{\infty} I_{solar} e_r d\lambda \tag{6.5}$$

where I_{solar} is the AM1.5 solar spectrum. Finally, heating due to conduction and convection can be collectively expressed as:

$$P_{other} = qA(T_a - T_r) \tag{6.6}$$

where T_a is the ambient temperature, T_r is the temperature of the radiative cooler, and q is the non-radiative heat coefficient from conductive and convective heat transfer through the air and surfaces in contact with the radiative cooler.

Eq. 6.1–6.6 outline three important facts for radiative cooling structure design. First, the criterion for an optimal cooling structure should be defined by its cooling power at a given operating temperature. This is because as the structure cools below the ambient temperature, the optimal spectral window to achieve maximum cooling power becomes a subset of the atmospheric window. Second, the performance limit for a cooling structure is fundamentally limited by the atmospheric emission spectrum. Third, to achieve net cooling performance, solar absorption and other forms of parasitic heating must be below a critical threshold.

6.4 Defining an Optimal Radiative Cooler

There are three important factors to consider when designing a daytime radiative cooling structure, which can be inferred from **Eq. 6.1–6.6**. First, the criterion for defining an optimal radiative cooling structure should be to maximize the structure's net cooling power at a desired target operating temperature, called the "optimization temperature". Second, the performance of a radiative cooling structure is fundamentally limited by the atmospheric emission spectrum. As such, the atmospheric emission spectrum of the target operating environment needs to be carefully considered. Third, to achieve cooling below ambient temperature, solar absorption and other forms of parasitic heating must be kept below a critical threshold.

We can define the theoretical spectral emission of an optimal radiative cooling structure as

$$e_r(\lambda, T_r, T_a, \theta, \alpha) = \begin{cases} 1, & I_B(\lambda, T_r) > I_B(\lambda, T_a) e_a(\lambda, \theta, \alpha) \\ 0, & else \end{cases} \tag{6.7}$$

where e_r is the emissivity of the structure, e_a is the emissivity of the atmosphere, λ is the free space wavelength, T_r is the structure's temperature, T_a is the ambient temperature, θ is

the angle of emission, and α is a variable encapsulating the conditions relating to the composition of the atmosphere.[218] I_B is defined as the blackbody spectral radiance

$$I_B = \frac{2hc^2}{\lambda^5} \frac{1}{e^{\frac{hc}{\lambda k_B T}} - 1} \tag{6.8}$$

where h is Plank's constant, k_B is the Boltzmann constant, and c is the speed of light. **Eq. 6.7** shows that the theoretical optimal cooling performance is a function of the temperature of the radiative cooling structure, ambient temperature, emission angle, and atmospheric composition.

In regard to choosing the appropriate atmospheric emission spectrum, **Fig. 6.1a** shows the atmospheric transmission windows from the Gemini Observatory (low humidity level) and from the 1976 United States Standard (average humidity level).[43] The spectra at the Gemini Observatory represents near ideal conditions where a radiative cooler with high emissivity in both the first (8 – 14 μm) and second (16 – 24 μm) atmospheric transmission windows could achieve the highest possible cooling power. However, it is shown in **Fig. 6.1a** that while two atmospheric transmission windows exist at very low humidity levels, the prevalence of water molecules in the atmosphere greatly diminishes the contribution of the second atmospheric transmission window towards radiative cooling for most areas of the world.[219] Consequently, practical radiative coolers in terrestrial applications should optimize emission only in the first atmospheric transmission window and over all angles. The 1976 United States Standard atmospheric emission spectrum was modeled using LOWTRAN7, an open-source software comparable to MODTRAN.[220–222] **Fig. 6.1b** shows the 1976 United States Standard atmospheric emission spectra at 300 K with blackbodies of 300 K, 280 K, 260 K, and 240 K overlaid in the background.[219] From **Fig. 6.1b**, we see that the optimal emission window as described in **Eq. 6.7** for achieving maximum cooling power is denoted by the area of each blackbody that is not overlapped by the atmospheric emittance. This demonstrates the dependence of the optimal spectral emission window on the operating temperature. **Fig. 6.1c** illustrates the radiative cooling power (P_r) to operating temperature relationship for ideal radiative coolers as defined by **Eq. 6.7**. Each solid curve

is the radiative cooling power based on spectral emission windows optimized for 300 K, 280 K, 260 K, and 240 K blackbodies minus the atmospheric heating (P_a), at an ambient temperature of 300 K. From the solid curves in **Fig. 6.1c**, we see that each optimal spectral emission window achieves a superior cooling power compared to its peers when operating at or near its optimization temperature. The dashed horizontal lines show the net-zero power curves ($P_{net} = 0$) for different percentages of solar absorption (P_{sun}). From these dashed lines, we find that radiative cooling while operating below the ambient temperature of 300 K is effectively impossible if parasitic solar absorption is higher than 10%. The dashed sloped lines show $P_{net} = 0$ when considering different non-radiative heat transfer coefficients (q), which account for convective and conductive heat transfer (P_{other}). The overall $P_{net} = 0$ line is determined by a linear combination of the solar absorption and non-radiative heat transfer effects.

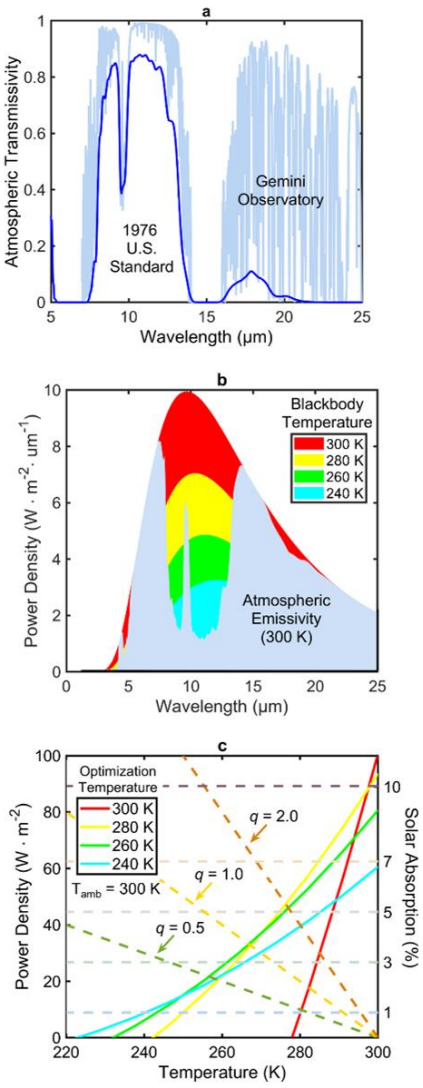

Figure 6.1. (a) Atmospheric transmission spectra at low humidity taken from the Gemini Observatory and at average humidity taken from the 1976 U.S. Standard; (b) blackbody spectra at various temperatures (300 K, 280 K, 260 K, and 240 K) overlaid on the atmospheric emission spectrum from 1976 U.S. Standard at 300 K; (c) radiative cooling power density versus operating temperature relationship for the four theoretically optimal radiative cooling spectral emission windows defined from (b), each is optimized to provide superior cooling power at a specific optimization temperature under ambient conditions (300 K). The solid lines show radiative cooling power (P_r) minus atmospheric heating (P_a) versus operating temperature for each of the optimal radiative coolers. Solar absorption percent is given by the horizontal dashed lines. Losses from conduction and convection for various non-radiative heat transfer coefficients (q), are marked with sloping dashed lines. The total net zero cooling power line is represented by a linear combination of the solar absorption line and non-radiative heat transfer coefficient line.

6.5 Radiative Cooling in SiO_2 and Si_3N_4 Laminate Nanoparticle Films

Using a generalized effective medium theory, we design different radiative cooling structures comprised of separate layers of SiO_2 and Si_3N_4 nanoparticle films with air as the matrix medium. We find that two-layer nanoparticle films always outperform dense solid laminate thin films and are sufficient to achieve cooling performances greater than or similar to previously reported structures.[198–202] In our designs, SiO_2 and Si_3N_4 were chosen as the emissive materials because of their strongly peaked absorption within the atmospheric transmission window. Specifically, in-phase and out-of-phase stretching of the Si–O bond is responsible for the strong absorption peak in SiO_2 from 8 – 10 μm, and Si–N bond stretching is responsible for the broad absorption peak in Si_3N_4 from 9 – 15 μm.[223–226] In both cases the absorption coefficient for wavelengths between 0.25 – 5 μm can be made negligibly small. The generalized effective medium permittivity, considering a single type of inclusion, is given by:

$$\frac{\varepsilon_{eff} - \varepsilon_e}{2\varepsilon_e + \varepsilon_{eff} + \nu\left(\varepsilon_{eff} - \varepsilon_e\right)} = f\frac{\varepsilon_i - \varepsilon_e}{2\varepsilon_e + \varepsilon_i + \nu\left(\varepsilon_{eff} - \varepsilon_e\right)} \tag{6.9}$$

where ε_e is the host permittivity (free space in this case), ε_i is the inclusion permittivity (SiO_2 or Si_3N_4), f is the inclusion fill fraction, ε_{eff} is the resulting effective permittivity, and ν is a continuous variable which encapsulates how the inclusion responds to the internal field. Using this framework, the Maxwell Garnett (MG) formula is recovered at $\nu = 0$, Bruggeman at $\nu = 2$, and Coherent Potential (CP) at $\nu = 3$.[48] Therefore, this generalized formula spans a set of effective medium theories and values of ν between the common theories can be viewed as a hybrid response in the internal field. For each structure designed, we span ν to compare the structure's cooling performance under each effective medium formula and hybrid parameters. As a representative example **Fig. 6.2a–e** show the real (n) and complex (k) refractive index for bulk SiO_2 and Si_3N_4 as well as the effective n_{eff} and k_{eff} for laminate nanoparticle films of SiO_2 or Si_3N_4 as a function of fill fraction under the Bruggeman formula.[48,227] **Fig. 6.2a–b** and **Fig. 6.2d–e** show that by tuning the nanoparticle fill fraction, we can reduce impedance mismatch between the nanoparticle

film and free space. We can also spectrally shift the location of maximum k_{eff} of the material composite as a result of coupling between phonons and the internal field.[46,179,212] **Fig. 6.2c and Fig. 6.2f** emphasize the effect of spectral shifting by normalizing the amplitude of k_{eff} for SiO_2 and Si_3N_4 laminate nanoparticle films within the atmospheric transmission window, respectively. Both increased impedance matching and spectral absorption resonance shifting are found to be consistent features no matter the choice of v. We note that SiO_2 and Si_3N_4 nanoparticles with diameters of 50 nm or less satisfy the condition of Rayleigh scattering throughout the visible and IR wavelength regime.[45] Under this condition, the effective medium theory given by **Eq. 6.9** is valid.[46,49,176,179,212,228–230] Synthesis of nanoparticle films composed of nanoparticles of this size and smaller, and with sufficiently narrow size distributions and high uniformity, can be done via both dusty plasma synthesis and ball milling.[153,217,231–233] We set a 60% fill fraction as a realistic upper limit due to the theoretical limit of random sphere packing (62 – 64%).[234,235]

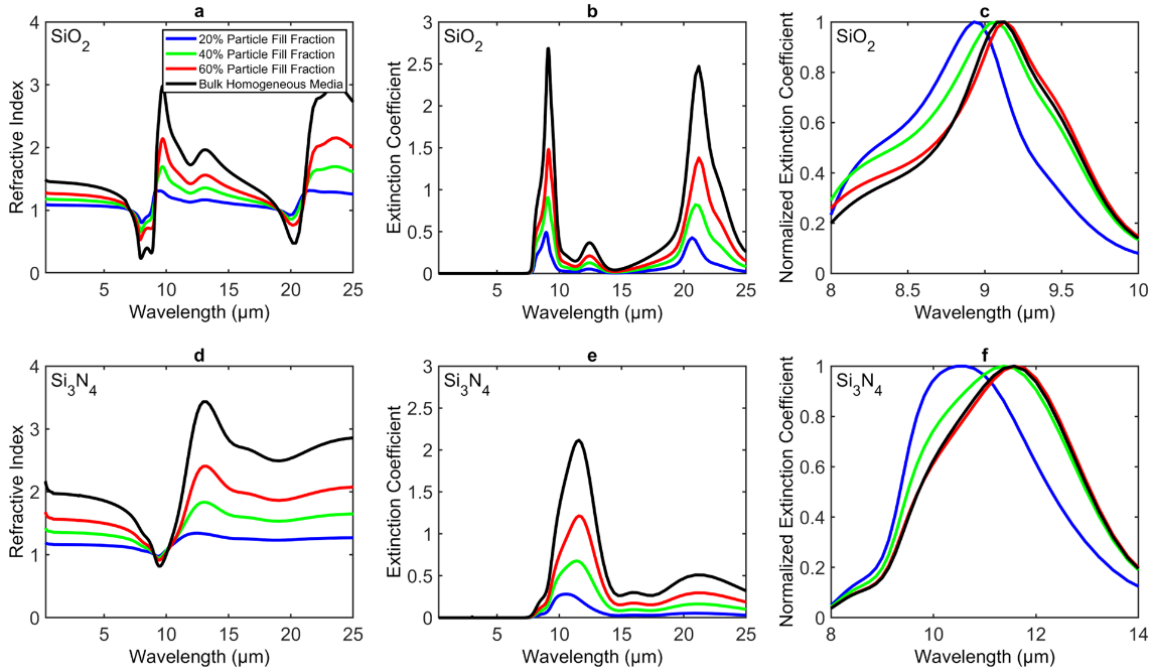

Figure 6.2. (a), (b) n_{eff} and k_{eff} for SiO_2 at various fill fractions with air as the matrix medium; (c) normalized k_{eff} for SiO_2 within atmospheric transmission window demonstrating spectral shifting as a function of fill fraction; (d), (e) n_{eff} and k_{eff} for Si_3N_4 at various fill fractions with air as the matrix medium; (f) normalized k_{eff} for Si_3N_4 within the atmospheric transmission window demonstrating spectral shifting as a function of fill fraction.

We also study the limits an effective permittivity for a random particle film can be, which is determined from the Hashin-Shtrikman (HK) bounds:

$$\varepsilon_{MG} \leq \varepsilon_{eff} \leq \varepsilon_{MG-Comp} \tag{6.10}$$

where the lower limit is given by the MG formula and the upper limit by the MG formula of the complementary structure in which the host and medium materials are transposed. Thus, **Eq. 6.10** gives an estimate on the permittivity extrema we may encounter for nanoparticle laminate films, and **Eq. 6.9** provides the framework to model the behavior of these films under an entire class of effective medium theories within the HK bounds. From this framework, we can compare two-layer SiO_2 and Si_3N_4 laminate nanoparticle films to dense solid thin film equivalents.

Using transfer matrix calculations, we determine each structure's wavelength, angle, and polarization-resolved absorption/emission profile, then calculate its net radiative cooling power (P_{net}) as a function of operating temperature.[64,236] Optimal designs for each temperature regime were found by systematically varying each laminate nanoparticle layer thickness, fill fraction, material orientation (alternating the material of the top and bottom layers), and film type (laminate nanoparticle film or dense solid thin film) for all permutations of two-layer structures of SiO_2 and Si_3N_4 on an Ag back reflector. As such, a total of 32 two-layer radiative cooling structures were optimized. At each of four optimization temperature (300 K, 290 K, 280 K, 270 K), we optimized eight unique two-layer structures on a silver back reflector based on material order (SiO_2 on Si_3N_4 or Si_3N_4 on SiO_2) and film type (two thin film layers, thin film on laminate nanoparticle film, laminate nanoparticle film on thin film, and two laminate nanoparticle films). **Fig. 6.3a** shows an example schematic of a radiative cooling structure comprised of two layers of laminate nanoparticle films on a silver back reflector. The specific design parameters (layer thickness, fill fraction) and radiative cooling powers for all 32 optimized radiative cooling structures can be found in Tables (S1)–(S18).

Fig. 6.3b shows the radiative cooling power of each of the 32 optimized two-layer radiative cooling structures under the Bruggeman mixing rule ($v = 2$). Each structure is shown at the operating temperature where their spectra has been optimized to give the most cooling power (optimization temperature). We assume an ambient of 300 K and account for solar absorption. No conduction or convection losses ($q = 0$) are shown as they would be common to each structure and are not an aspect of the photonic design. From **Fig. 6.3b**, we see that optimized two-layer laminate nanoparticle films on a silver back reflector outperform optimized two-layer dense solid thin films at all optimization temperatures. The best performing two-layer laminate nanoparticle film structures show a 40% to 120% increase in radiative cooling power compared to the best performing two-layer dense solid thin film structures. The laminate nanoparticle films also demonstrate cooling at 270 K, which is unachievable in a dense solid thin film structure. **Fig. 6.3c** shows the radiative cooling power of each of 32 optimized two-layer radiative cooling structures under the

Maxwell Garnett mixing rule. From **Fig. 6.3c**, we see that optimized two-layer laminate nanoparticle films on silver back reflector are still predicted to outperform optimized two-layer dense solid thin films at all target temperatures, with increases of 30% and 109% in radiative cooling power when using the Maxwell Garnett mixing rule. Using the design parameters for the best performing two-layer laminate nanoparticle film and its two-layer thin film analog at each optimization temperature, we show in **Fig. 6.3d** the radiative cooling power of the laminate nanoparticle films when calculated using different effective medium formulas (v = 0, 1, 2, 3). Results from the HK bounds and the optimal thin film design are also plotted. From **Fig. 6.3d** we see that laminate nanoparticle films have higher predicted radiative cooling powers than two-layer thin film structures of the same material at all operating temperatures regardless of the effective medium theory used. In all cases, the AM1.5 solar spectrum was used, and the atmospheric transmittance data was taken from the 1976 U.S. Standard using LOWTRAN7[43,220,237], integrated over angle and wavelength for both polarizations, and the ambient temperature was 300 K. Non-radiative heat losses were not considered since these losses would be common since film thicknesses are negligible for heat capacitance, the losses can be and often are controlled by the design of an external box, and are not inherent to the photonic aspects of the design. This does not detract from the comparison. The angular, spectral, and polarization-resolved emissivity profiles for all two-layer laminate nanoparticle film structures as calculated by both Bruggeman and Maxwell Garnett effective medium formulas can be found in **Fig. S6.1–S6.8**.

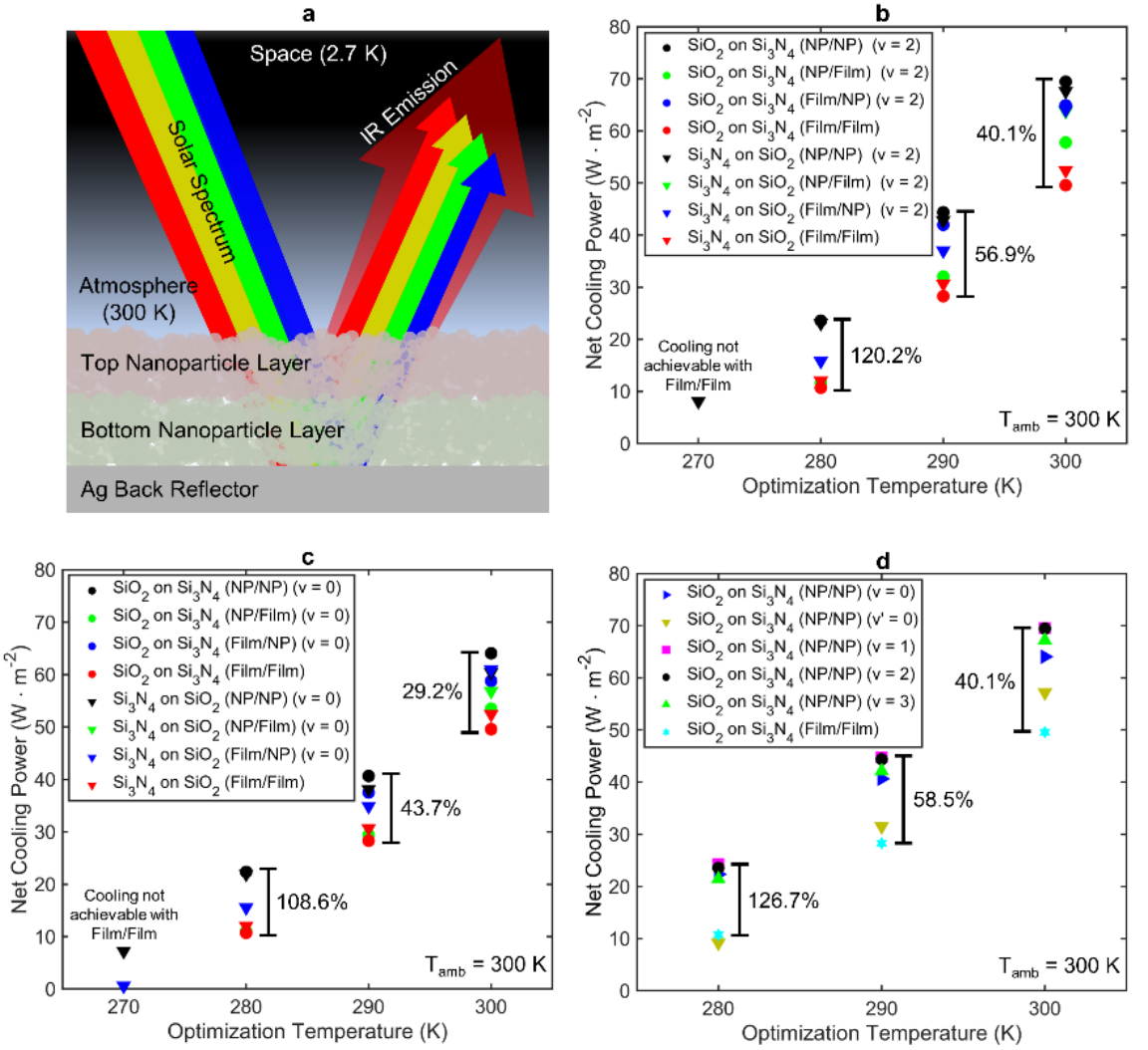

Figure 6.3. (a) Schematic of radiative cooler comprised of two layers of laminate nanoparticle films on a silver back reflector; (b) net radiative cooling power of all 32 optimal two-layer nanoparticle film, thin film, or nanoparticle and thin film composite structures of SiO_2 and Si_3N_4 operating at their optimization temperature calculated using the Bruggeman effective medium formula (v = 2); (c) net radiative cooling power of all 32 optimal two-layer nanoparticle film, thin film, or nanoparticle and thin film composite structures of SiO_2 and Si_3N_4 operating at their optimization temperature calculated using the Maxwell Garnett effective medium formula (v = 0); (d) net radiative cooling power versus optimization temperature for the optimal two-layer nanoparticle films calculated using different effective medium theories. The nanoparticle film structure performance is compared to the two-layer thin film analog to demonstrate that superior radiative cooling power is predicted regardless of which effective medium formula is used. All figures assume an ambient temperature of 300 K and no conduction or convection losses (q = 0).

Fig. 6.4 compares the cooling performance of the optimal two-layer laminate nanoparticle films from **Fig. 6.3a** under the Bruggeman mixing rule to structures that have been previously reported.[198–201,208] In order to provide a direct comparison, absorptivity/emissivity curves from previous reports are digitized and the radiative cooling performance is compared using the same AM1.5 solar spectrum and atmospheric absorption spectrum (the 1976 U.S. Standard).[43] Furthermore, all calculations use an ambient of 300 K, and no non-radiative heat losses were considered. Therefore, the results should be interpreted as the relative average performance based on United States standards. Since multiple papers only report emissivity curves at normal incidence, all calculations assume the structure emits as a Lambertian surface.[198–201,208] We then perform the angular integration found in **Eq. 6.2–6.4** under this assumption, allowing us to account for the angular dependence of the 1976 U.S. Standard atmospheric spectra. While the lack of angular information will alter the achievable cooling power, applying the approximation of Lambertian emittance allows for a consistent comparison between curves. Non-radiative heat losses were not considered since these losses are or can be controlled by the design of an external box and are not inherent to the photonic aspects of the design. Solar absorption is considered since it is part of the photonic design for daytime cooling. The results suggest that laminate nanoparticle film structures can provide cooling performance superior to other reported radiative cooling structures at temperatures below a 300 K ambient, many of which are achieved only through complex photonic designs.

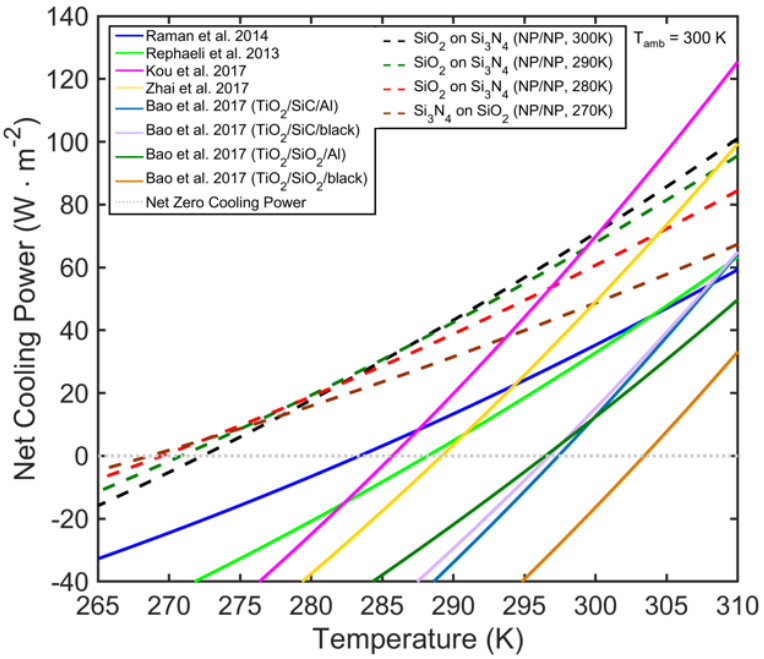

Figure 6.4. Comparison between various radiative structure performances from literature (solid) and proposed two-layer radiative cooling structures composed of SiO_2 and Si_3N_4 laminate nanoparticle films on silver back reflector (dashed). Each dashed curve represents a unique two-layer radiative cooler optimized for a different operating temperature. Literature curves are obtained through digitization of published emissivity data at normal incidence and it is assumed the emissivity is angle independent. This figure serves purely as a guide for visualizing the relative benefit of nanoparticle films in radiative cooling.

6.6 Summary and Conclusion

We have demonstrated that SiO_2 and Si_3N_4 two-layer nanoparticle laminate films can give rise to radiative cooling powers that are higher than the best dense solid thin film laminate designs using the same materials. This result is robust with respect to the effective medium theory employed for optimization. Furthermore, we show that simple two-layer nanoparticle structures are sufficient to achieve cooling performances exceeding that of previously reported designs. Cooling performance improvements ranging from 20 W/m^2 to 25 W/m^2 over previously reported designs are possible with two-layer laminate nanoparticle films at operating temperatures of 290 K and 280 K respectively, and two-layer laminate nanoparticle films remain competitive with previously reported designs at

300 K. This work suggests that nanoparticle laminate films are a promising component for future simple, scalable, and effective daytime radiative cooling structures.

6.7 Supplemental Information

Tables of cooling power versus temperature for 2-layer radiative cooling structure design parameters:

Table S6.1. Cooling power versus temperature for Si_3N_4 on SiO_2 (Film/Film) on Ag back reflector.

T (K)	P (W/m^2)	Si_3N_4 Thickness (nm)	SiO_2 Thickness (nm)
300	52.39	200	1200
290	30.65	100	1300
280	12.02	100	1100
270	-1.57	600	25

Table S6.2. Cooling power versus temperature for Si_3N_4 on SiO_2 (NP/Film) on Ag back reflector using the Bruggeman formula (v = 2).

T (K)	P (W/m^2)	Si_3N_4 Thickness (nm)	Si_3N_4 Fill Fraction (%)	SiO_2 Thickness (nm)
300	63.76	3000	25	200
290	41.25	2750	25	0
280	22.83	2500	25	0
270	8.01	2500	20	0

Table S6.3. Cooling power versus temperature for Si_3N_4 on SiO_2 (Film/NP) on Ag back reflector using the Bruggeman formula (v = 2).

T (K)	P (W/m^2)	Si_3N_4 Thickness (nm)	SiO_2 Thickness (nm)	SiO_2 Fill Fraction (%)
300	64.00	200	2500	20
290	37.01	100	2250	30
280	15.82	100	2000	25
270	-0.09	100	1700	20

Table S6.4. Cooling power versus temperature for Si_3N_4 on SiO_2 (NP/NP) on Ag back reflector using the Bruggeman formula (v = 2).

T (K)	P (W/m^2)	Si_3N_4 Thickness (nm)	Si_3N_4 Fill Fraction (%)	SiO_2 Thickness (nm)	SiO_2 Fill Fraction (%)
300	67.60	1100	35	1800	25
290	42.79	1600	25	1400	20
280	23.10	2500	25	50	20
270	8.10	2500	20	25	20

Table S6.5. Cooling power versus temperature for SiO_2 on Si_3N_4 (Film/Film) on Ag back reflector.

T (K)	P (W/m^2)	SiO_2 Thickness (nm)	Si_3N_4 Thickness (nm)
300	49.57	700	800
290	28.28	800	600
280	10.71	700	600
270	-1.64	0	600

Table S6.6. Cooling power versus temperature for SiO_2 on Si_3N_4 (NP/Film) on Ag back reflector using the Bruggeman formula (v = 2).

T (K)	P (W/m^2)	SiO_2 Thickness (nm)	SiO_2 Fill Fraction (%)	Si_3N_4 Thickness (nm)
300	57.78	1700	35	900
290	32.05	1600	35	800
280	11.64	1400	25	700
270	-1.64	0	-	600

Table S6.7. Cooling power versus temperature for SiO_2 on Si_3N_4 (Film/NP) on Ag back reflector using the Bruggeman formula (v = 2).

T (K)	P (W/m^2)	SiO_2 Thickness (nm)	Si_3N_4 Thickness (nm)	Si_3N_4 Fill Fraction (%)
300	64.91	50	2750	30
290	41.97	25	2750	25
280	22.83	0	2500	25
270	8.01	0	2500	20

Table S6.8. Cooling power versus temperature for SiO_2 on Si_3N_4 (NP/NP) on Ag back reflector using the Bruggeman formula (v = 2).

T (K)	P (W/m^2)	SiO_2 Thickness (nm)	SiO_2 Fill Fraction (%)	Si_3N_4 Thickness (nm)	Si_3N_4 Fill Fraction (%)
300	69.43	900	20	2250	35
290	44.38	700	20	2250	30
280	23.58	200	20	2500	25
270	8.01	0	-	2500	20

Table S6.9. Cooling power versus temperature for Si_3N_4 on SiO_2 (NP/Film) on Ag back reflector using Maxwell Garnett formula (v = 0).

T (K)	P (W/m^2)	Si_3N_4 Thickness (nm)	Si_3N_4 Fill Fraction (%)	SiO_2 Thickness (nm)
300	56.82	3000	25	200
290	37.89	2750	25	0
280	21.33	2500	25	0
270	8.38	2500	20	0

Table S6.10. Cooling power versus temperature for Si_3N_4 on SiO_2 (Film/NP) on Ag back reflector using Maxwell Garnett formula (v = 0).

T (K)	P (W/m^2)	Si_3N_4 Thickness (nm)	SiO_2 Thickness (nm)	SiO_2 Fill Fraction (%)
300	60.94	200	2500	20
290	34.88	100	2250	30
280	15.54	100	2000	25
270	0.59	100	1700	20

Table S6.11. Cooling power versus optimization temperature for Si_3N_4 on SiO_2 (NP/NP) on Ag back reflector using Maxwell Garnett formula (v = 0).

T (K)	P (W/m^2)	Si_3N_4 Thickness (nm)	Si_3N_4 Fill Fraction (%)	SiO_2 Thickness (nm)	SiO_2 Fill Fraction (%)
300	60.41	1100	35	1800	25
290	38.12	1600	25	1400	20
280	21.95	2500	25	50	20
270	7.22	2500	20	25	20

Table S6.12. Cooling power versus temperature for SiO_2 on Si_3N_4 (NP/Film) on Ag back reflector using Maxwell Garnett formula (v = 0).

T (K)	P (W/m^2)	SiO_2 Thickness (nm)	SiO_2 Fill Fraction (%)	Si_3N_4 Thickness (nm)
300	53.47	1700	35	900
290	29.39	1600	35	800
280	10.99	1400	25	700
270	-1.64	0	-	600

Table S6.13. Cooling power versus temperature for SiO_2 on Si_3N_4 (Film/NP) on Ag back reflector using Maxwell Garnett formula (v = 0).

T (K)	P (W/m^2)	SiO_2 Thickness (nm)	Si_3N_4 Thickness (nm)	Si_3N_4 Fill Fraction (%)
300	58.78	50	2750	30
290	37.49	25	2750	25
280	21.33	0	2500	25
270	6.99	0	2500	20

Table S6.14. Cooling power versus temperature for SiO_2 on Si_3N_4 (NP/NP) on Ag back reflector using Maxwell Garnett formula (v = 0).

T (K)	P (W/m^2)	SiO_2 Thickness (nm)	SiO_2 Fill Fraction (%)	Si_3N_4 Thickness (nm)	Si_3N_4 Fill Fraction (%)
300	64.05	900	20	2250	35
290	40.64	700	20	2250	30
280	22.34	200	20	2500	25
270	6.99	0	-	2500	20

Table S6.15. Cooling power versus temperature for SiO_2 on Si_3N_4 (NP/NP) on Ag back reflector using complementary Maxwell Garnett formula ($v' = 0$).

T (K)	P (W/m^2)	SiO_2 Thickness (nm)	SiO_2 Fill Fraction (%)	Si_3N_4 Thickness (nm)	Si_3N_4 Fill Fraction (%)
300	57.17	900	20	2250	35
290	31.51	700	20	2250	30
280	9.18	200	20	2500	25

Table S6.16. Cooling power versus temperature for SiO_2 on Si_3N_4 (NP/NP) on Ag back reflector using a generalized formula ($v = 1$).

T (K)	P (W/m^2)	SiO_2 Thickness (nm)	SiO_2 Fill Fraction (%)	Si_3N_4 Thickness (nm)	Si_3N_4 Fill Fraction (%)
300	69.55	900	20	2250	35
290	44.81	700	20	2250	30
280	24.28	200	20	2500	25

Table S6.17. Cooling power versus temperature for SiO_2 on Si_3N_4 (NP/NP) on Ag back reflector using Coherent Potential formula ($v = 3$).

T (K)	P (W/m^2)	SiO_2 Thickness (nm)	SiO_2 Fill Fraction (%)	Si_3N_4 Thickness (nm)	Si_3N_4 Fill Fraction (%)
300	67.18	900	20	2250	35
290	42.11	700	20	2250	30
280	21.42	200	20	2500	25

Table S6.18. Cooling power at T = 270 K for Si_3N_4 on SiO_2 (NP/NP) on Ag back reflector using different effective medium formulas.

v	P (W/m^2)	Si_3N_4 Thickness (nm)	Si_3N_4 Fill Fraction (%)	SiO_2 Thickness (nm)	SiO_2 Fill Fraction (%)
0	7.22	2500	20	25	20
0 (complement)	-5.45	2500	20	25	20
1	8.35	2500	20	25	20
3	6.86	2500	20	25	20

Spectral, angular, and polarization resolved emissivity profile of 2-layer radiative cooling structures:

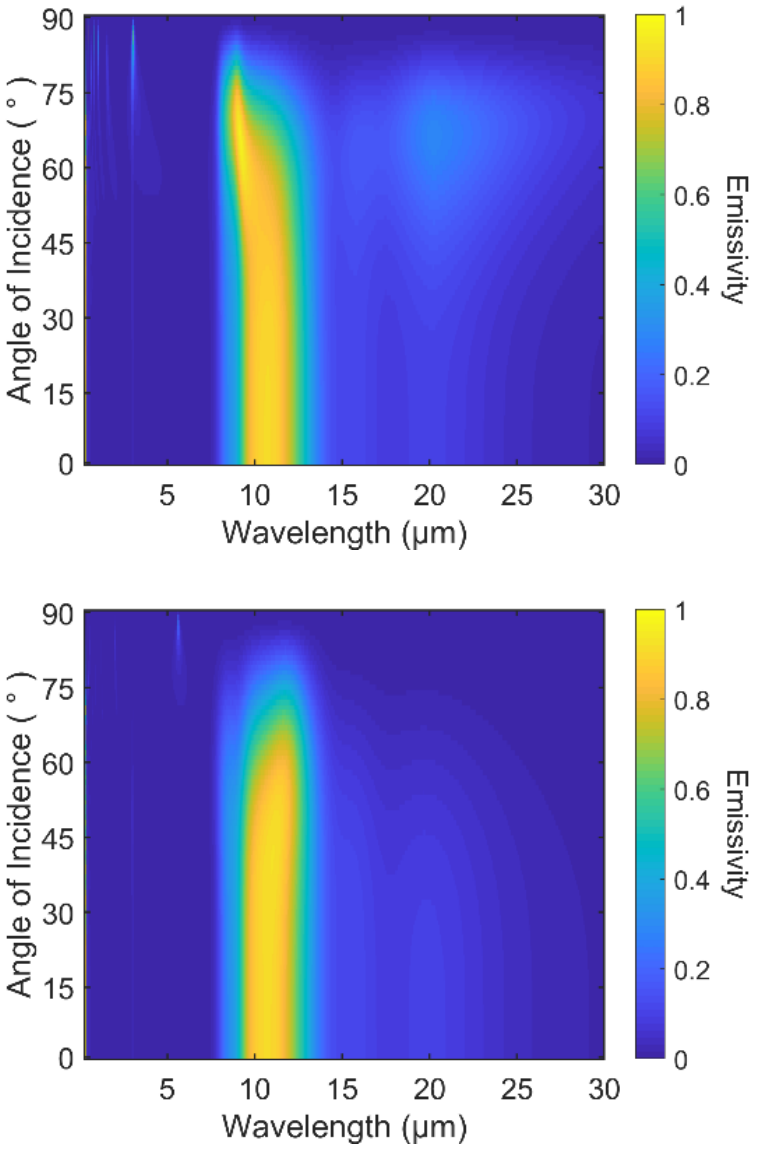

Figure S6.1. Spectral and angular resolved p-polarization (top) and s-polarization (bottom) emissivity profile for 2-layer laminate nanoparticle film radiative cooling structure optimized for 270 K at an ambient temperature of 300 K. Radiative cooling structure composed of Si_3N_4 (NP) on SiO_2 (NP) on Ag back reflector.

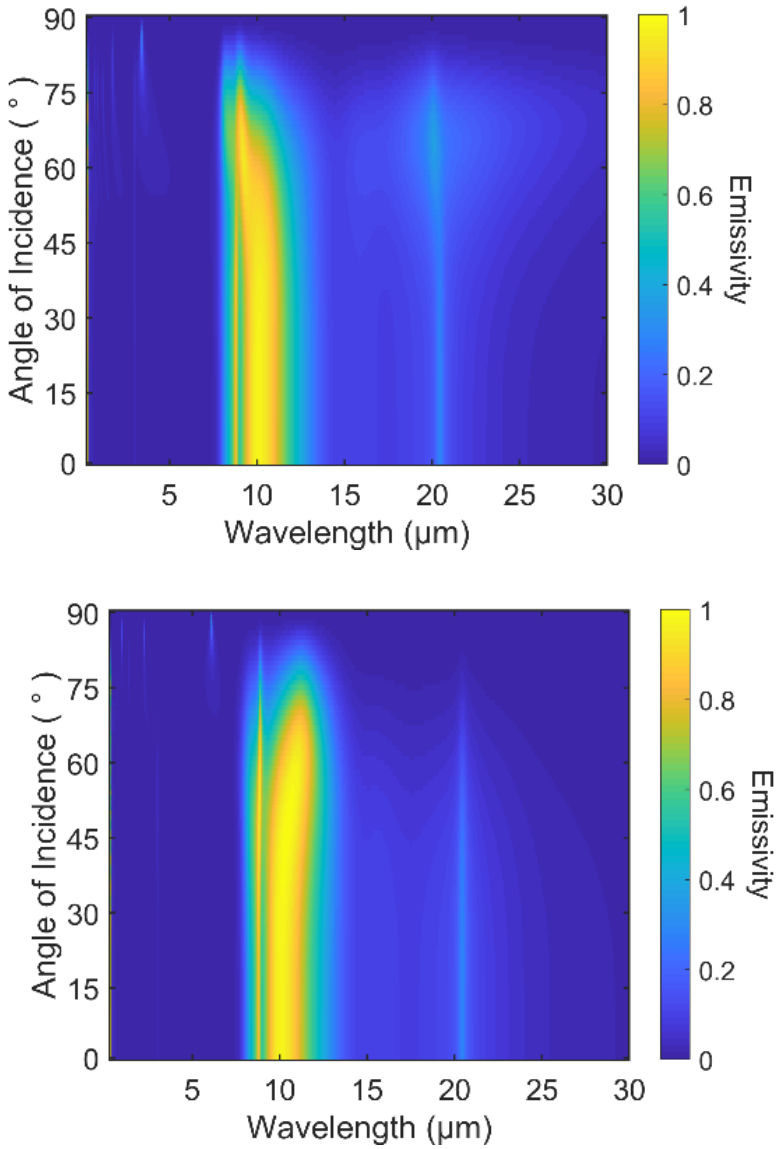

Figure S6.2. Spectral and angular resolved p-polarization (top) and s-polarization (bottom) emissivity profile for 2-layer laminate nanoparticle film radiative cooling structure optimized for 280 K at an ambient temperature of 300 K. Radiative cooling structure composed of SiO_2 (NP) on Si_3N_4 (NP) on Ag back reflector.

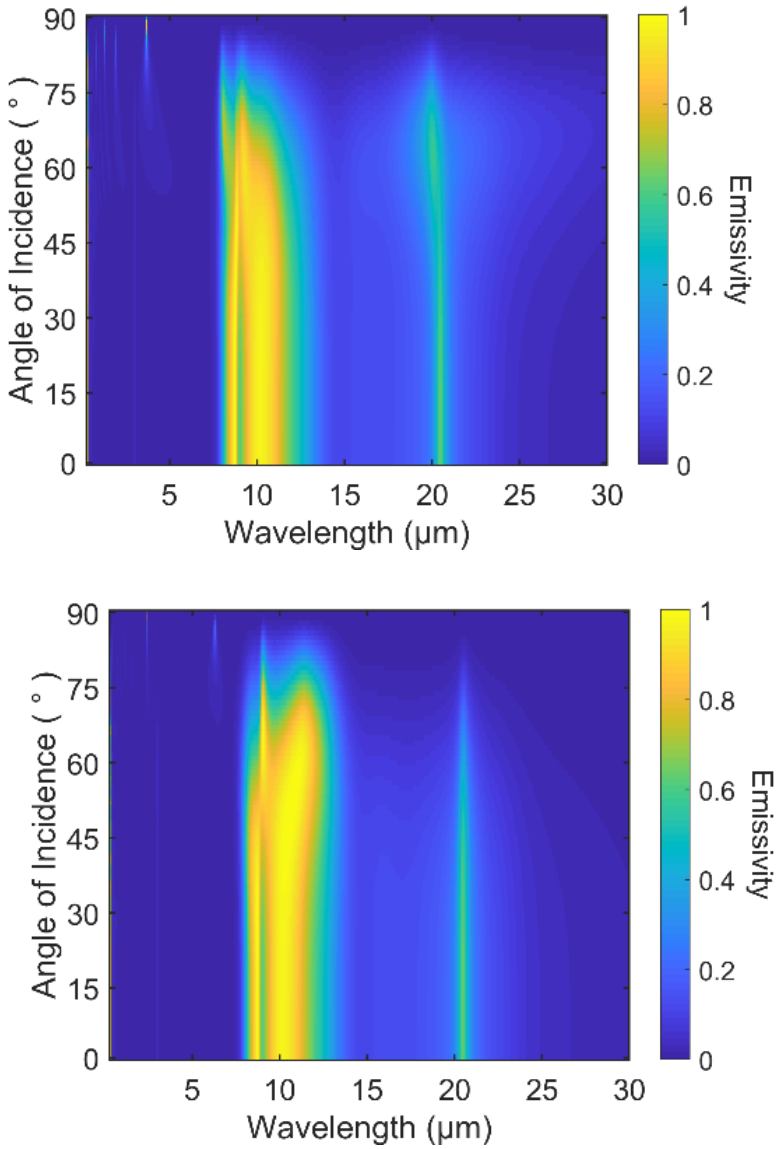

Figure S6.3. Spectral and angular resolved p-polarization (top) and s-polarization (bottom) emissivity profile for 2-layer laminate nanoparticle film radiative cooling structure optimized for 290 K at an ambient temperature of 300 K. Radiative cooling structure composed of SiO_2 (NP) on Si_3N_4 (NP) on Ag back reflector.

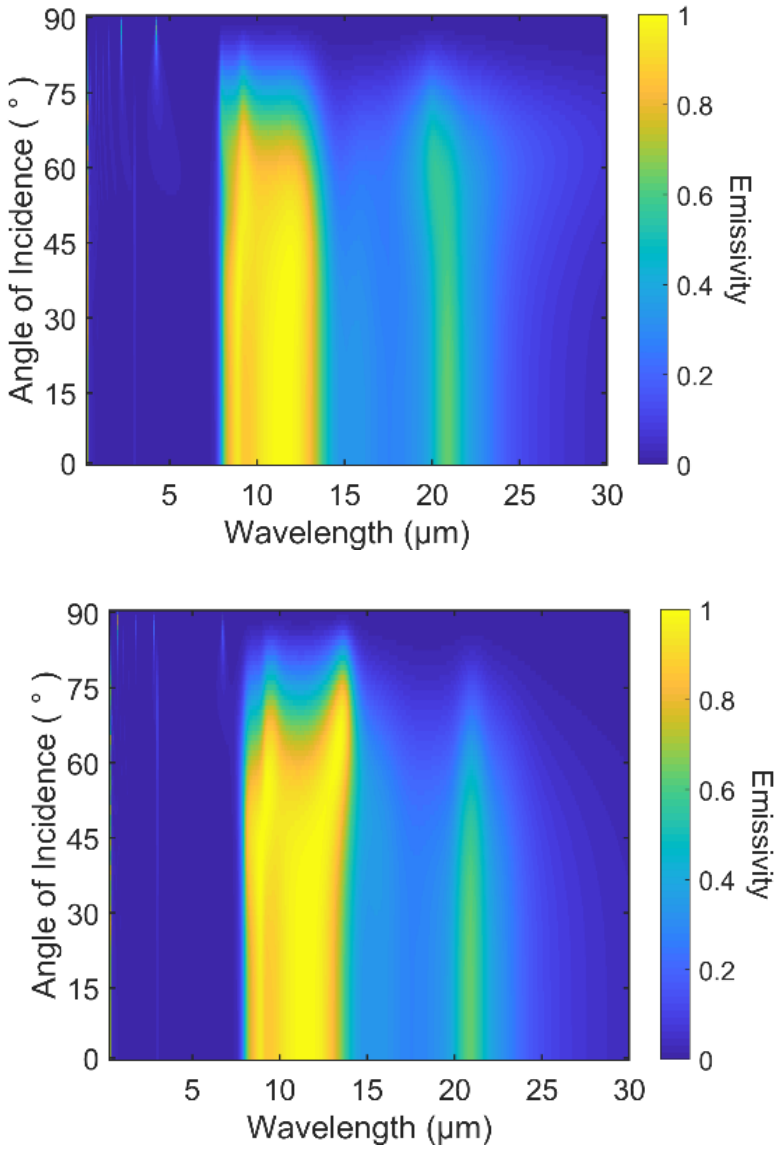

Figure S6.4. Spectral and angular resolved p-polarization (top) and s-polarization (bottom) emissivity profile for 2-layer laminate nanoparticle film radiative cooling structure optimized for 300 K at an ambient temperature of 300 K. Radiative cooling structure composed of SiO_2 (NP) on Si_3N_4 (NP) on Ag back reflector.

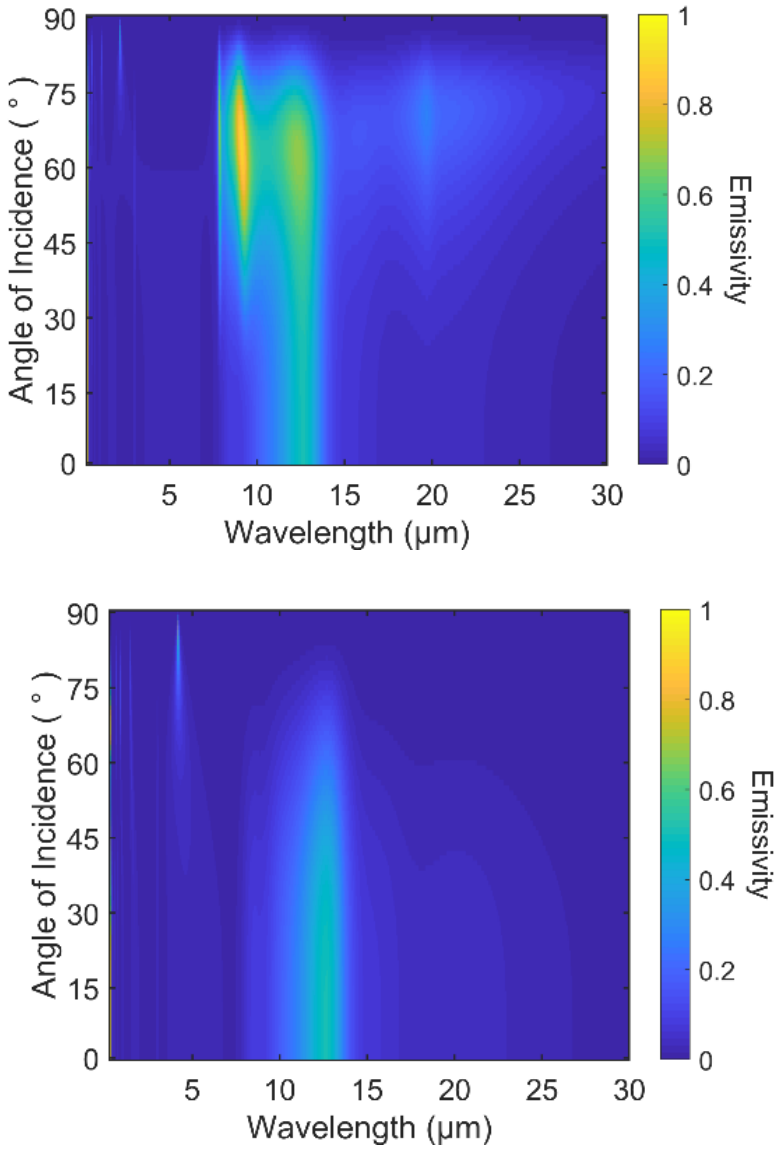

Figure S6.5. Spectral and angular resolved p-polarization (top) and s-polarization (bottom) emissivity profile for 2-layer dense solid thin film radiative cooling structure optimized for 270 K at an ambient temperature of 300 K. Radiative cooling structure composed of Si_3N_4 (Film) on SiO_2 (Film) on Ag back reflector.

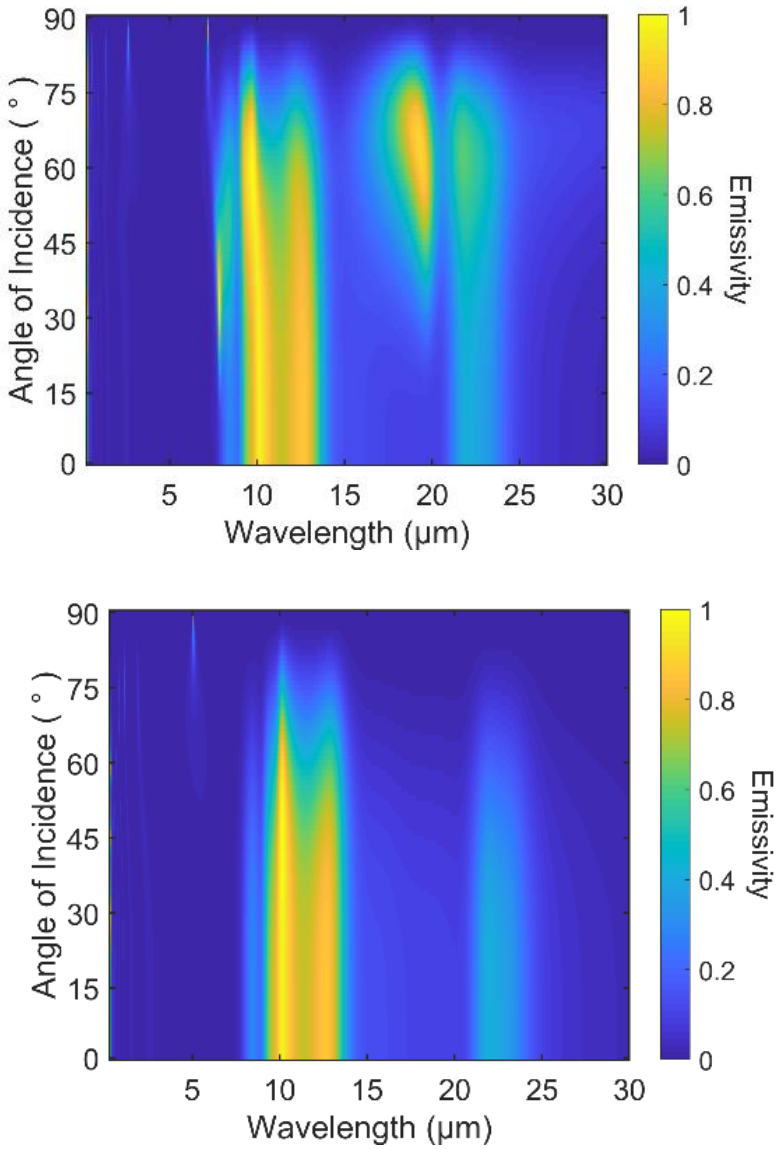

Figure S6.6. Spectral and angular resolved p-polarization (top) and s-polarization (bottom) emissivity profile for 2-layer dense solid thin film radiative cooling structure optimized for 280 K at an ambient temperature of 300 K. Radiative cooling structure composed of Si_3N_4 (Film) on SiO_2 (Film) on Ag back reflector.

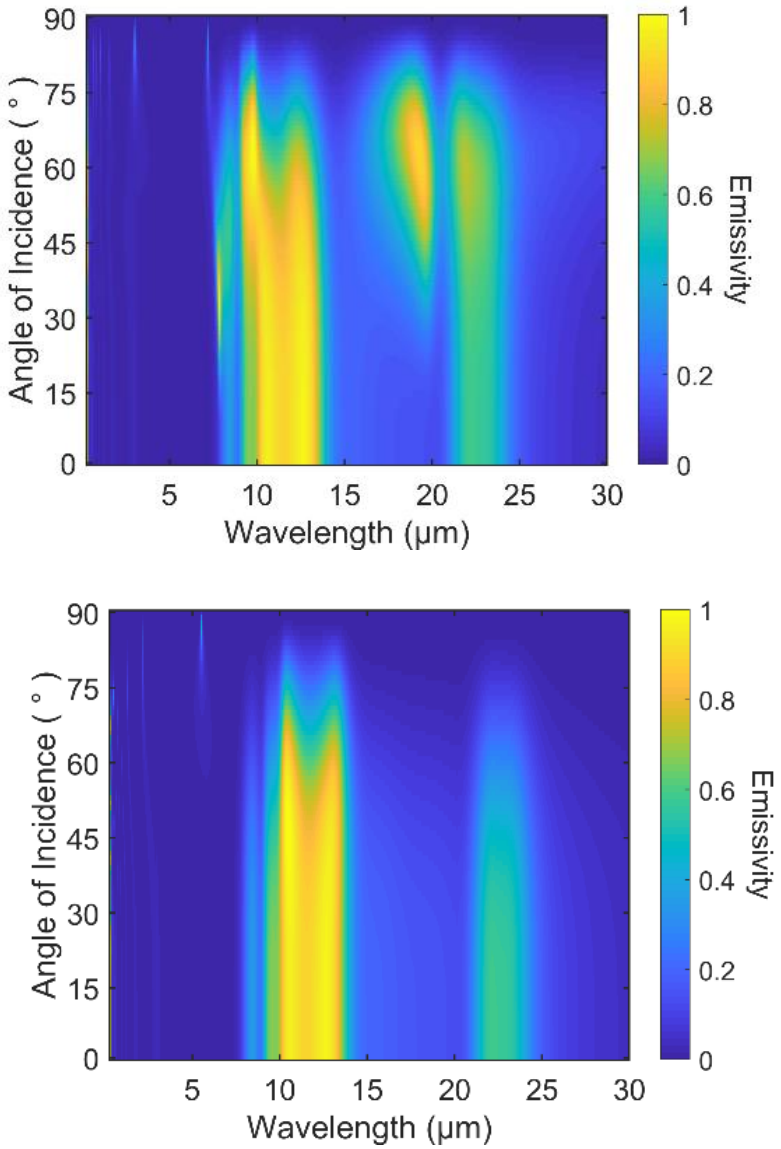

Figure S6.7. Spectral and angular resolved p-polarization (top) and s-polarization (bottom) emissivity profile for 2-layer dense solid thin film radiative cooling structure optimized for 290 K at an ambient temperature of 300 K. Radiative cooling structure composed of Si_3N_4 (Film) on SiO_2 (Film) on Ag back reflector.

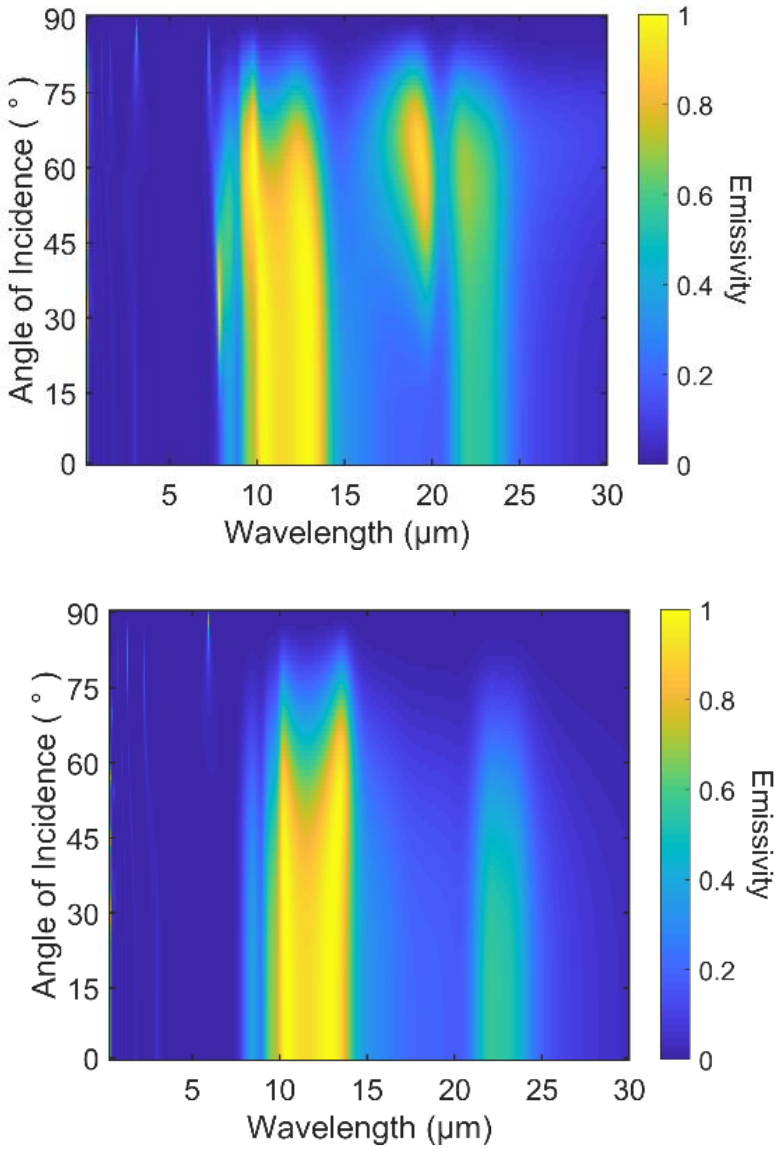

Figure S6.8. Spectral and angular resolved p-polarization (top) and s-polarization (bottom) emissivity profile for 2-layer dense solid thin film radiative cooling structure optimized for 300 K at an ambient temperature of 300 K. Radiative cooling structure composed of Si_3N_4 (Film) on SiO_2 (Film) on Ag back reflector.

Numerical emissivity data from various reports in literature:

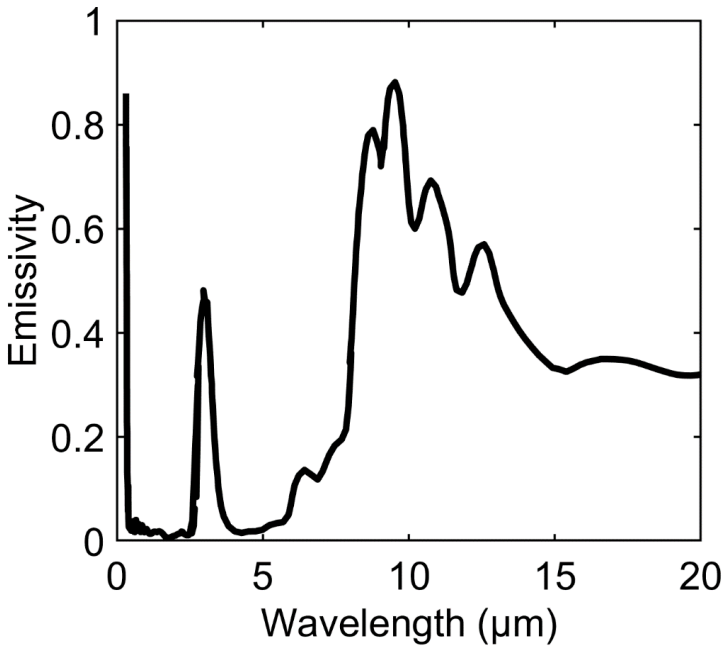

Figure S6.9. Digitized emissivity curve from a multilayer radiative cooler composed of seven alternating layers of HfO2 and SiO2. Data from [200].

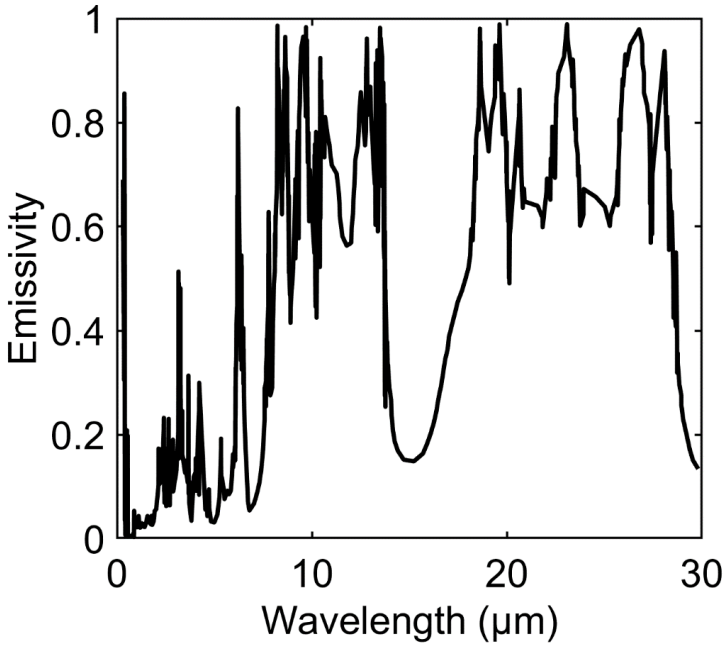

Figure S6.10. Digitized emissivity curve from a 2-layer 2D photonic crystal of SiC and quartz. Data from [201].

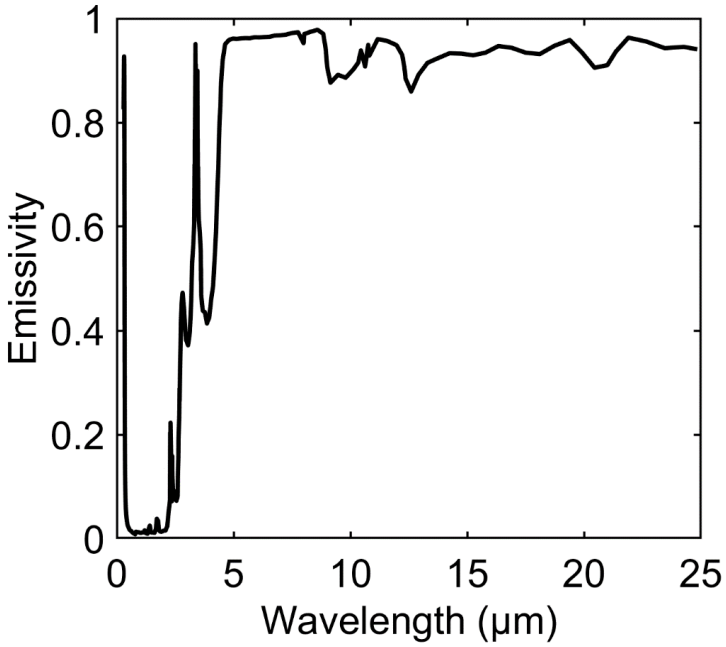

Figure S6.11. Digitized emissivity curve from a polymer-coated fused silica mirror. Data from [199].

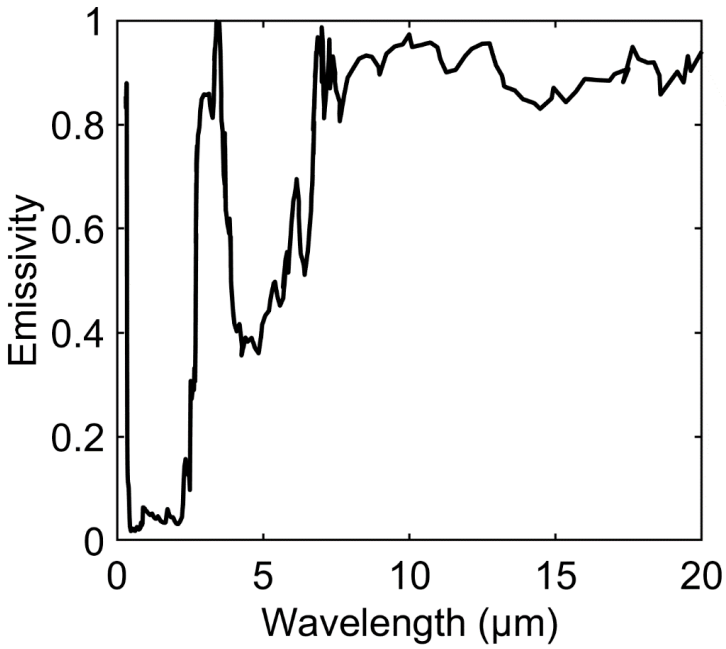

Figure S6.12. Digitized emissivity curve from a glass-polymer hybrid metamaterial. Data from [198].

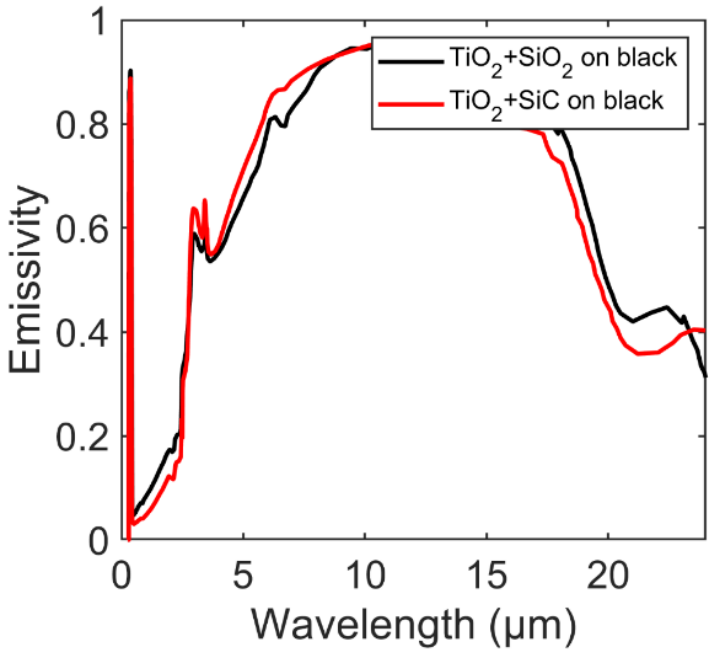

Figure S6.13. Digitized emissivity curve from nanoparticle-based double layer cooling structure on a black substrate. Data from [208].

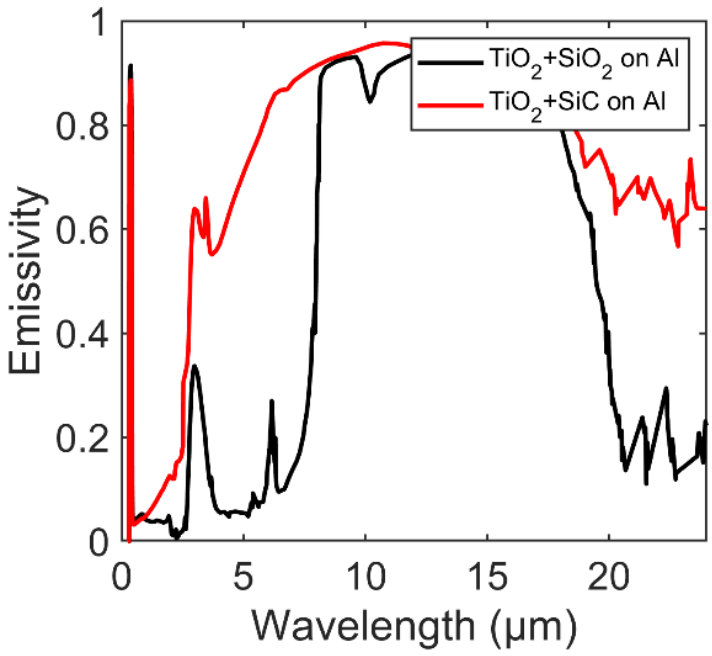

Figure S6.14. Digitized emissivity curve from nanoparticle-based double layer cooling structure on an aluminum substrate. Data from [208].

Chapter 7

CHARACTERIZATION OF SI_3N_4 AND SIO_2 NANOPARTICLE LAMINATE FILMS FOR DAYTIME RADIATIVE COOLING

7.1 Introduction

The previous two chapters introduced the use of laminate nanoparticle films as photonic structures for passive daytime terrestrial radiative cooling applications. Chapter 5 showed work on the characterization of alumina nanoparticle films deposited from a nonthermal plasma, and Chapter 6 reported on optimized radiative cooling structures comprised of nanoparticle films of SiO_2 and Si_3N_4 with cooling powers comparable to the best reports in literature at the time.

Chapter 5 demonstrated the use of a variety of characterization techniques for characterizing the materials and optical properties of the nanoparticle films. Importantly, it showed that laminate nanoparticle films deposited from nonthermal plasmas optically behaved like a macroscopically isotropic homogeneous film in the infrared wavelength regime as expected from theory. It also showed that the Bruggeman effective medium approximation was the appropriate mixing method for modeling the effective optical properties of these films.

Chapter 6 demonstrated that changing the fill fraction of the nanoparticle films could be used to spectrally shift the effective absorption peaks of the films in the mid-infrared to better match the atmospheric transmission window. This effect was present regardless of the effective medium approximation used. As a consequence of this extra tunability, laminate nanoparticle films were shown to always outperform their classical dense laminate thin film analogs. Finally, Chapter 6 also reported the optimal design parameters for sets of two-layer SiO_2 and Si_3N_4 film structures composed of either dense thin films or nanoparticle films for maximum radiative cooling power.

In this chapter, we build on the discoveries of the previous two chapters by reporting work on the fabrication and characterization of radiative cooling structures composed of laminate nanoparticle films deposited from a nonthermal plasma. We also fabricate and characterize several dense laminate thin film structures to experimentally compare the radiative cooling performance of laminate nanoparticle films and dense laminate thin films directly. From the optical characterization of the laminate nanoparticle films, we re-optimize our original radiative cooling designs and fabricate new laminate nanoparticle film radiative cooling structures.

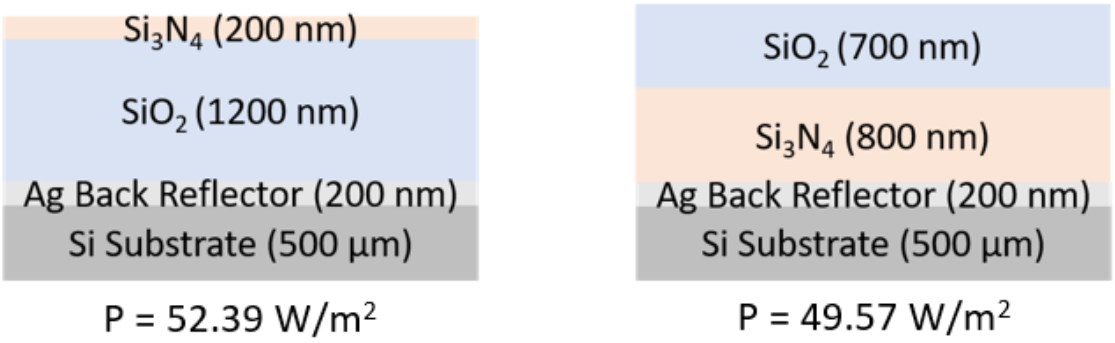

Figure 7.1. Schematic of the highest performing two-layer dense thin film radiative cooling structures composed of SiO_2 and Si_3N_4. The schematic also indicates the expected cooling power of each structure at 300 K.

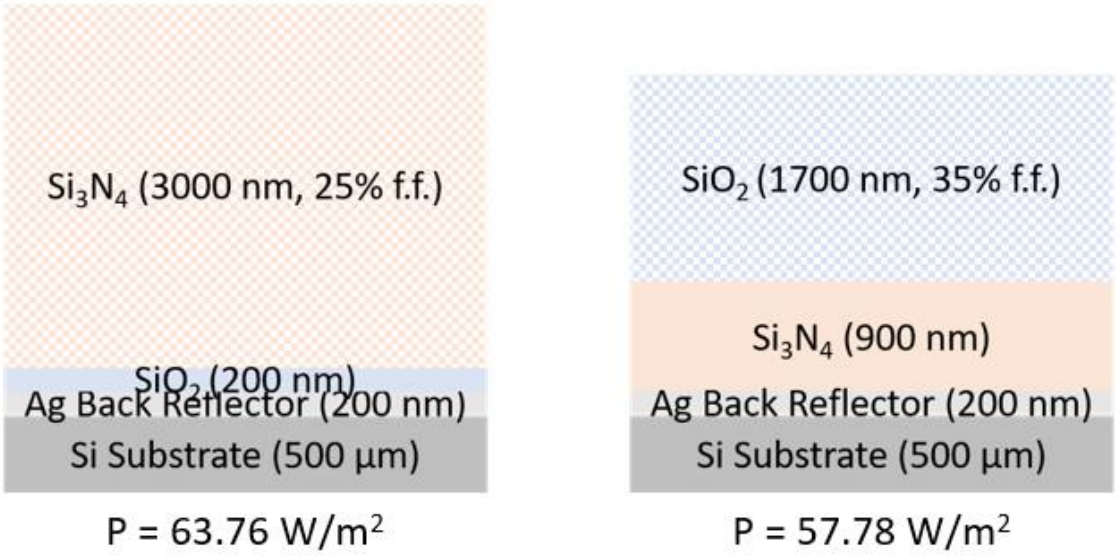

Figure 7.2. Schematic of the highest performing two-layer nanoparticle film on dense thin film radiative cooling structures composed of SiO_2 and Si_3N_4. The schematic also indicates the expected cooling power of each structure at 300 K.

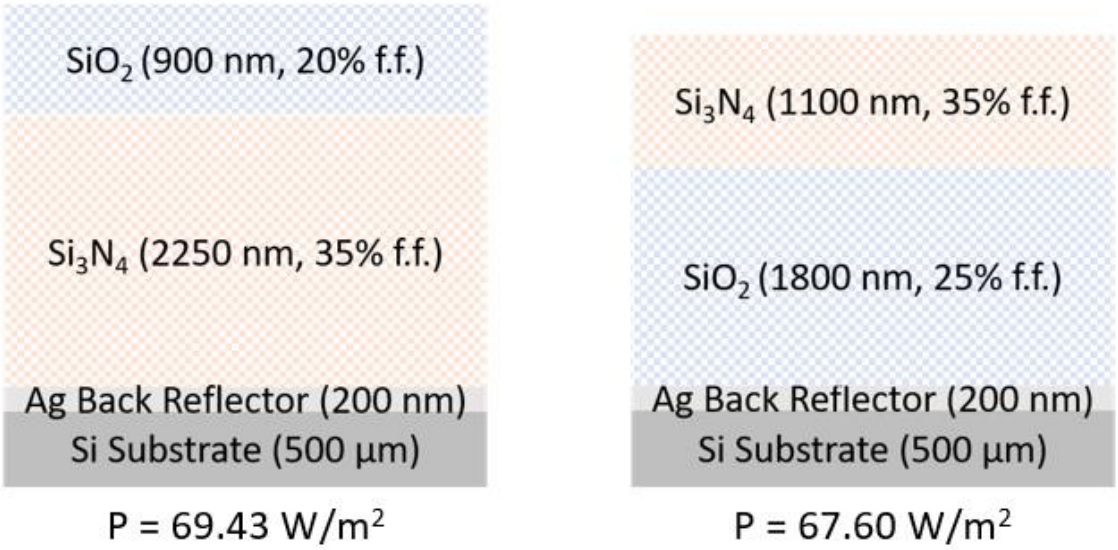

Figure 7.3. Schematic of the highest performing two-layer nanoparticle film radiative cooling structures composed of SiO_2 and Si_3N_4. The schematic also indicates the expected cooling power of each structure at 300 K.

7.2 SiO_2 and Si_3N_4 Dense Laminate Thin Film Radiative Coolers

Chapter 6 reported the optimal design parameters for every set of two-layer radiative cooling structures composed of SiO_2 and Si_3N_4, using either dense thin films or nanoparticle films. **Fig. 7.1-7.3** shows the schematics of 6 of the optimized radiative cooling structures. The structures shown are optimized for maximum cooling power at 300 K, and they are composed of either two dense thin films, one dense thin film and one nanoparticle film, or two nanoparticle films. Note that the designs which involve a dense thin film on top of a nanoparticle film are excluded.

In order to both validate the optimization results presented in Chapter 6 as well as compare the radiative cooling power performance between dense laminate thin film and laminate nanoparticle film radiative cooling structures, we began by fabricating the 2 two-layer dense thin film structures shown in **Fig. 7.1**.

To fabricate the 2 two-layer dense thin film structures, we deposited a 10 nm Ti adhesion layer and then a 200 nm Ag back reflector layer on silicon wafers using sputter deposition. Then, the SiO_2 and Si_3N_4 layers were deposited by plasma-enhanced chemical vapor deposition (PECVD) in the order and with the thicknesses indicated in **Fig. 7.1**.

Before fabricating the full structures shown in **Fig. 7.1**, we used ellipsometry to test each deposition process and ensure the optical quality of each deposited material layer matched expectations. To do this, sample layers for each material were deposited individually first on a silicon substrate and then characterized using visible and infrared ellipsometry. The ellipsometry results were fitted using the J.A. Woollam library oscillator models for Ag, SiO_2, and Si_3N_4, and the complex refractive index of each material was extracted from the ellipsometry fits. **Fig. 7.4-7.6** show the extracted complex refractive index of the Ag, SiO_2, and Si_3N_4 material layers deposited by either sputter deposition (Ag) or PECVD (SiO_2, Si_3N_4). From the ellipsometry results, we found that the Ag, SiO_2, and Si_3N_4 materials matched well with expected results for each material from literature. After each individual

deposition process was tested and the optical qualities of the deposited materials characterized, we fabricated the two-layer dense thin film structures.

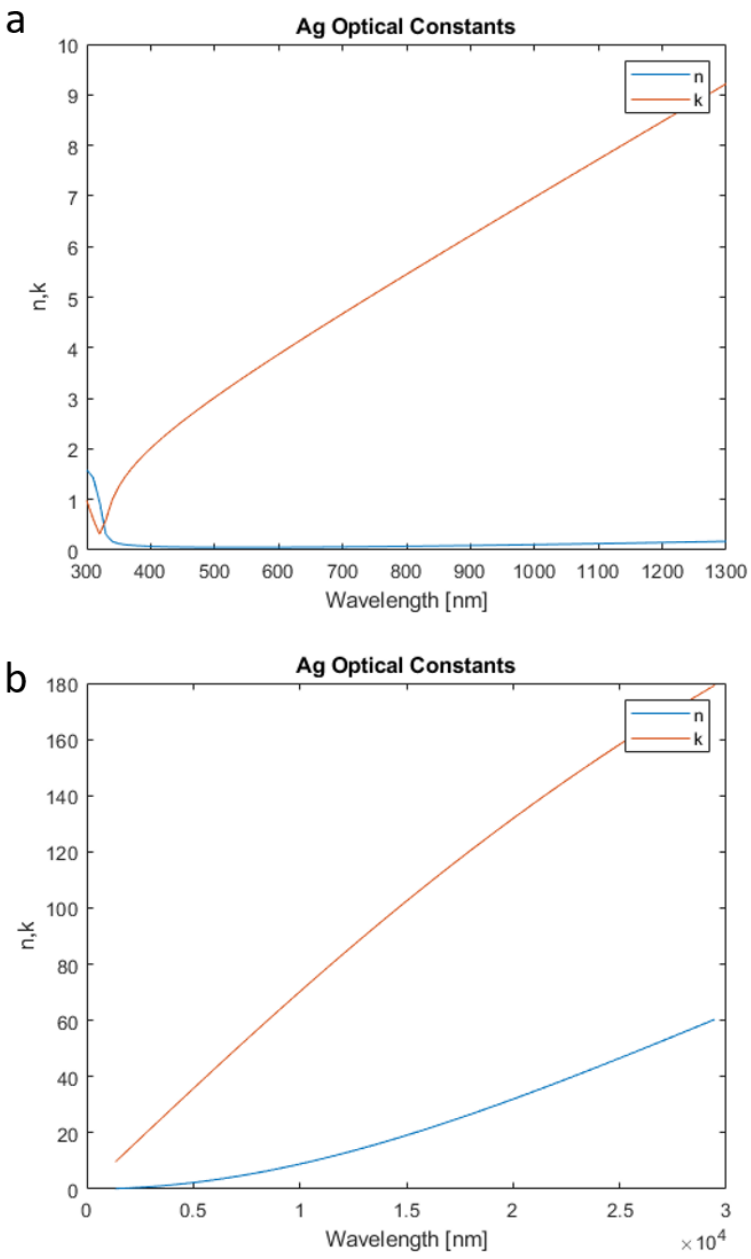

Figure 7.4. Complex refractive index of sputter deposited silver from ellipsometry in the (a) visible and (b) infrared wavelength regime.

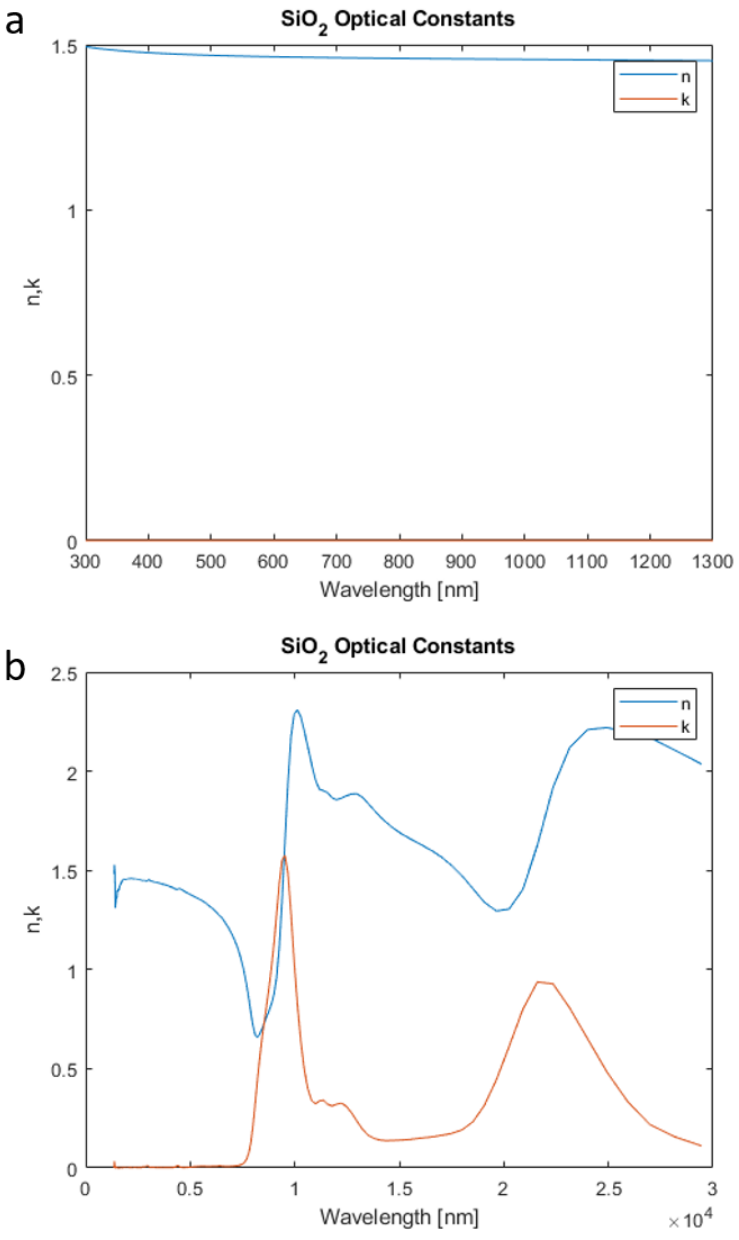

Figure 7.5. Complex refractive index of PECVD deposited SiO_2 from ellipsometry in the (a) visible and (b) infrared wavelength regime.

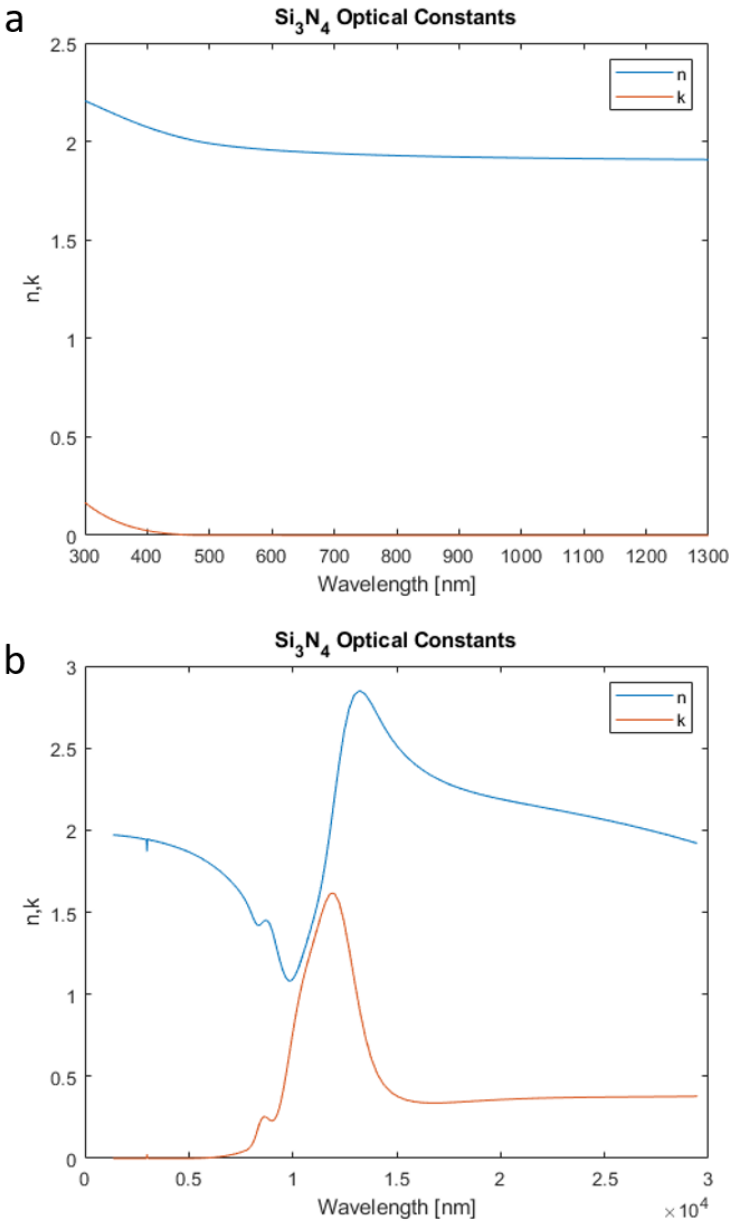

Figure 7.6. Complex refractive index of PECVD deposited Si_3N_4 from ellipsometry in the (a) visible and (b) infrared wavelength regime.

After the full two-layer thin film structures were fabricated using sputter deposition and PECVD, visible and infrared ellipsometry were used again to characterize the optical quality of the entire structure. In this case, the ellipsometry model was constructed using the

previously extracted complex refractive index and materials models for each individual material. Then, for the fitting process, all of the oscillator models for each layer and the thickness were fit simultaneously. Once the new complex refractive index and thicknesses were extracted, ray transfer matrix method was used to calculate the expected spectral absorptivity response of the structure.

From the ellipsometry results, we measured a thickness of 194 nm Si_3N_4 on 1208 nm SiO_2 for the first structure (200 nm Si_3N_4 on 1200 nm SiO_2), and a thickness of 736 nm SiO_2 and 791 nm Si_3N_4 for the second structure (700 nm SiO_2 on 800 nm Si_3N_4). Using the extracted complex refractive index of the structures and ray transfer matrix method, we calculated the absorptivity of the structures, which is shown in **Fig. 7.7**. We also compared the experimental absorptivity of the structures to the expected theoretical absorptivity of the optimized structures. From **Fig. 7.7**, we can see that our experimental structures have a spectral absorptivity which matches well with the theoretical absorptivity that we expected from the optimized structures. This suggests that these experimental structures should perform relatively well as radiative coolers as predicted from our theoretical results.

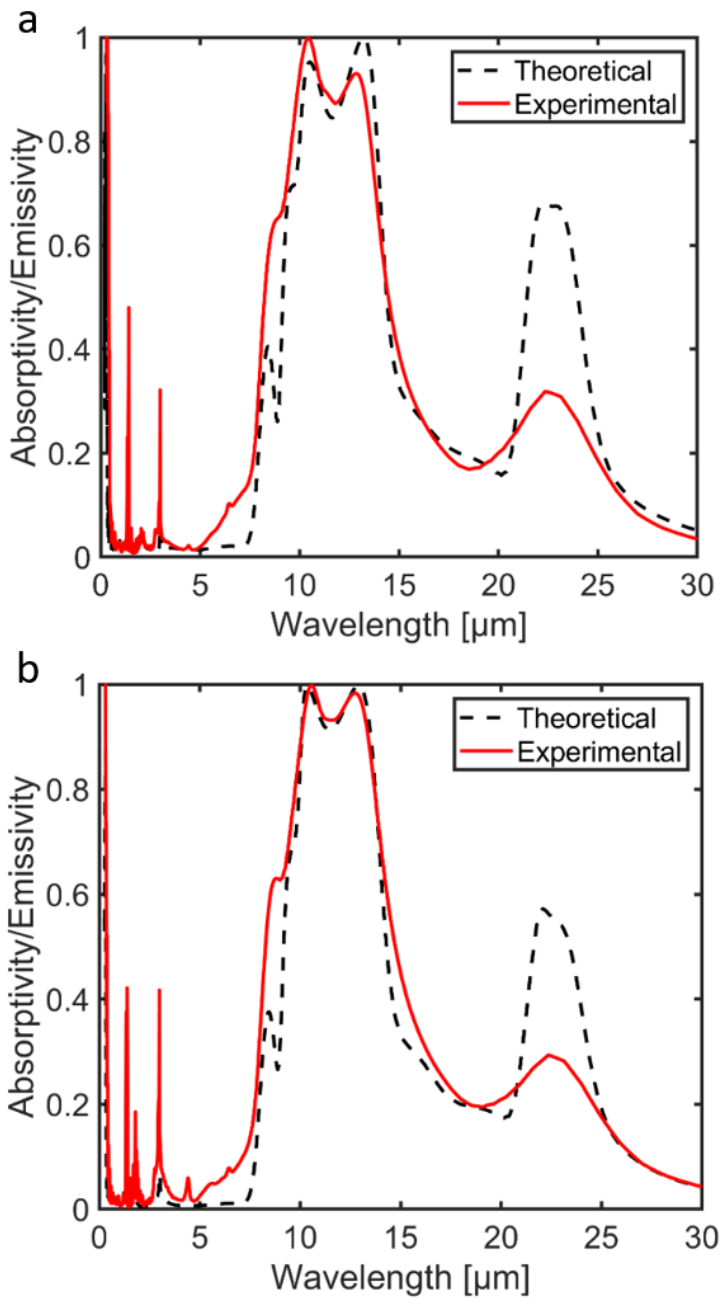

Figure 7.7. Comparison between the theoretical and measured emissivity (from ellipsometry) for the (a) 200 nm Si_3N_4 on 1200 nm SiO_2 structure and the (b) 700 nm SiO_2 on 800 nm Si_3N_4.

We also used UV-vis and FT-IR spectroscopy to characterize the optical properties of the structures directly. Here, we used UV-vis spectroscopy to measure the reflectivity of the

structures in the solar wavelength regime, and FT-IR spectroscopy to measure the radiative emissivity in the mid-infrared wavelength regime. **Fig. 7.8-7.9** shows the absorptivity/emissivity of the 2 two-layer thin film structures in the visible and infrared wavelength regime measured by UV-vis and FT-IR spectroscopy. Once again, we also compared these experimental results with the expected theoretical absorptivity of the optimized structures.

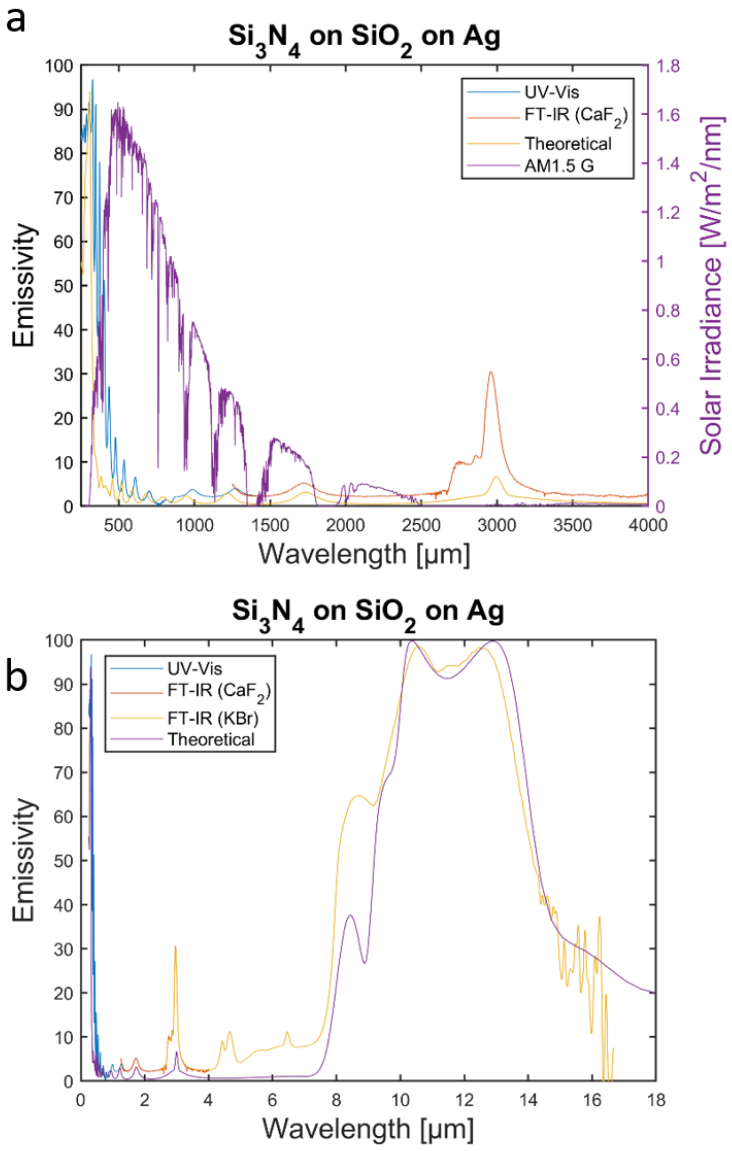

Figure 7.8. Spectral emissivity of the 200 nm Si_3N_4 on 1200 nm SiO_2 structure in the (a) visible wavelength regime measured by UV-vis spectroscopy and in the (b) infrared wavelength regime measured by FT-IR spectroscopy. The theoretical spectral emissivity is also included to show the match between the theoretical and experimental results. Note that a CaF_2 beam splitter was used for the near-IR measurements, and a KBr beam splitter was used for the mid- and far-IR measurements.

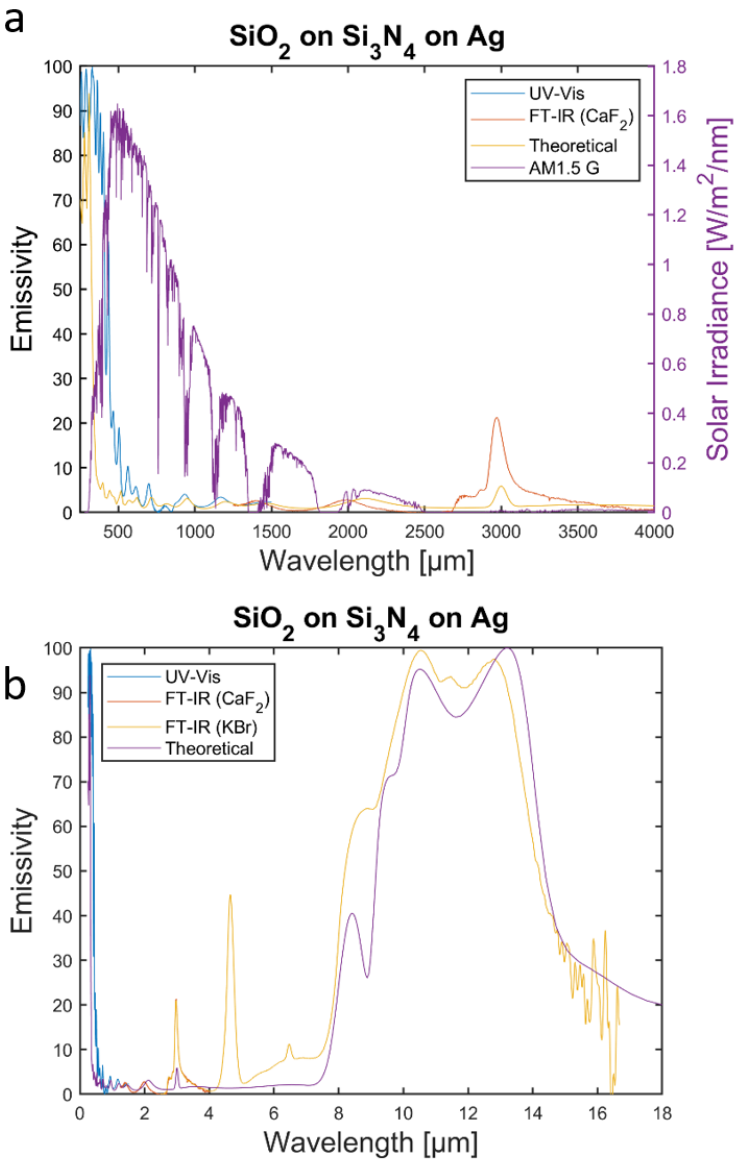

Figure 7.9. Spectral emissivity of the 700 nm SiO_2 on 800 nm Si_3N_4 structure in the (a) visible wavelength regime measured by UV-vis spectroscopy and in the (b) infrared wavelength regime measured by FT-IR spectroscopy. The theoretical spectral emissivity is also included to show the match between the theoretical and experimental results. Note that a CaF_2 beam splitter was used for the near-IR measurements, and a KBr beam splitter was used for the mid- and far-IR measurements.

From the results shown in **Fig. 7.7-7.9**, we observed that the fabricated two-layer dense thin film structures had measured spectral emissivity responses very similar to the theoretical

spectral emissivity expected from the optimized structures in **Fig. 7.1**. This suggests that these films should perform relatively well as radiative coolers as expected from the optimization process, and that the fabrication process that we used to fabricate these films is a sufficient and consistent method for fabricating these 2 two-layer dense thin film radiative cooling structures.

7.3 Characterization of SiO_2 and Si_3N_4 Laminate Nanoparticle Films

After fabricating and characterizing the 2 two-layer dense thin film radiative cooling structures shown in **Fig. 7.1**, we moved towards fabricating the laminate nanoparticle film structures shown in **Fig. 7.2-7.3**. Similar to the process used in Section 7.2, we first deposited and characterized individual laminate nanoparticle films of SiO_2 and Si_3N_4 from nonthermal plasma synthesis to measure the individual film optical qualities. To deposit the nanoparticle films, precursor gas was flowed through the reactor to form nanoparticles in the plasma. Then, the nanoparticles were spray deposited onto a substrate which was moved back and forth to control the size and overall thickness of the film. The SiO_2 deposition parameters were 50 W, 5 sccm O_2, 30 sccm Ar, 1 sccm SiH_4, and the Si_3N_4 deposition parameters were 50 W, 50 sccm N_2, 30 sccm Ar, 1 sccm SiH_4. **Fig. 7.10** shows the nonthermal plasma reactor which was used to deposit the nanoparticle films.

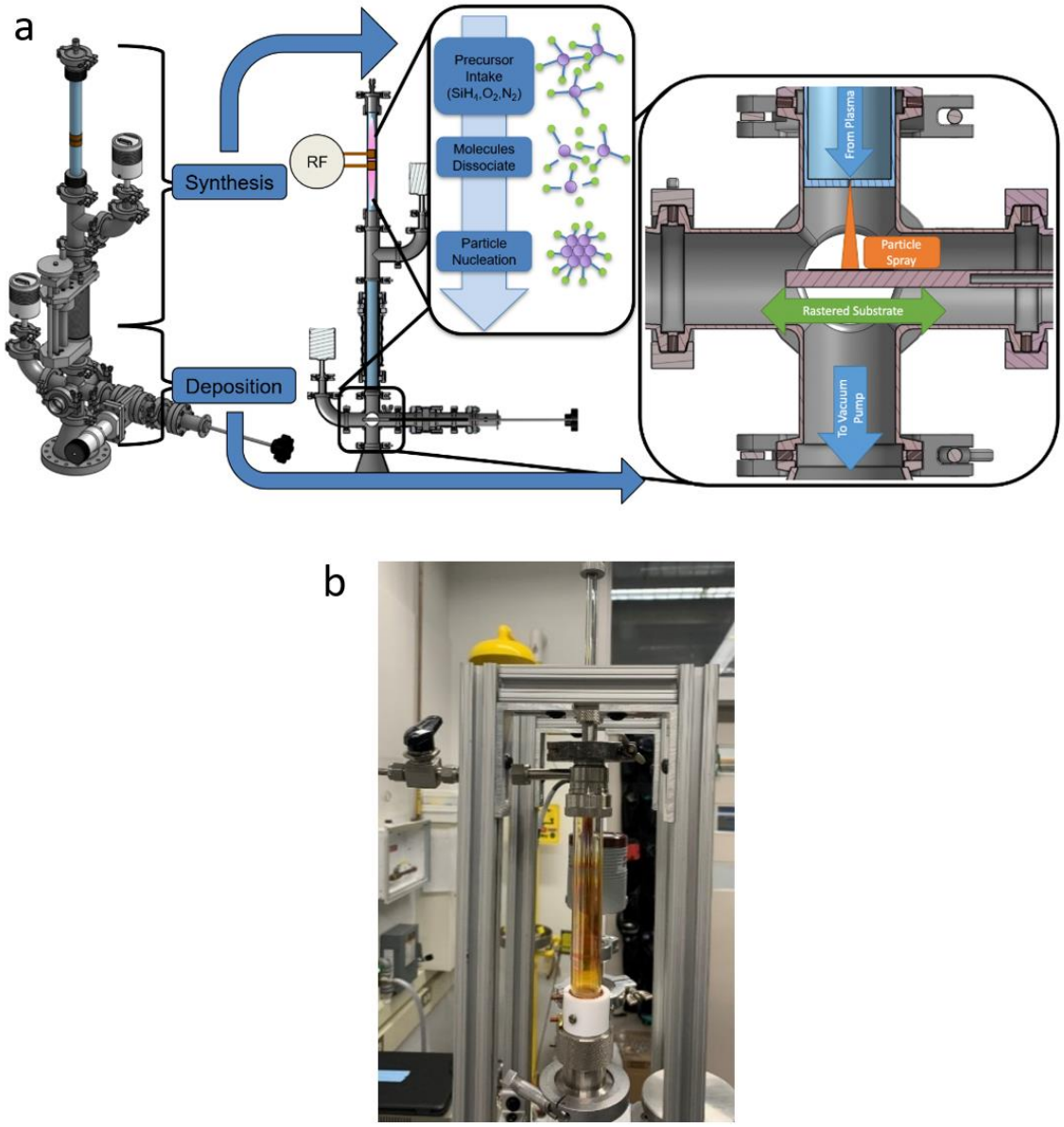

Figure 7.10. (a) Schematic of the nonthermal plasma reactor used to synthesize and deposit SiO_2 and Si_3N_4 nanoparticle films; (b) Image of the nonthermal plasma reactor.

First, TEM was used to measure the average size and shapes of the nanoparticles. The average radius of SiO_2 nanoparticles was approximately 3 nm and the average radius of Si_3N_4 nanoparticles was approximately 4 nm. **Fig. 7.11** shows characteristic TEM images of SiO_2 and Si_3N_4 nanoparticles from nonthermal plasma synthesis.

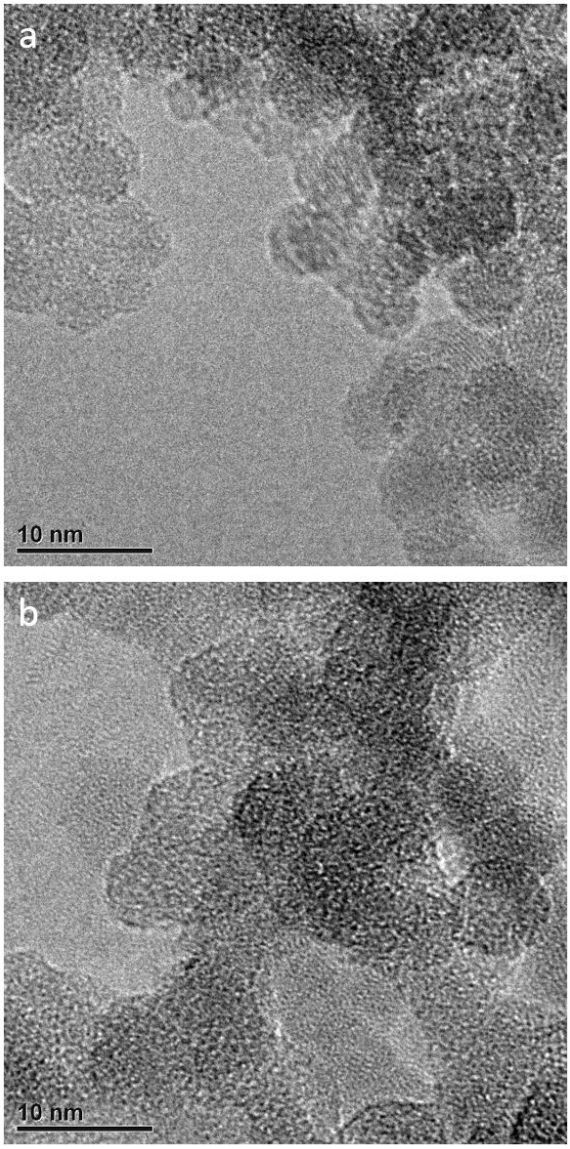

Figure 7.11. TEM images of (a) SiO_2 nanoparticles and (b) Si_3N_4 nanoparticles synthesized from a nonthermal plasma reactor.

Next, nanoparticle films were deposited on gold coated substrates; the gold layer provides a high reflectivity background in the mid-IR wavelength regime which helps improve ellipsometry and FT-IR spectroscopy measurements. The gold layers were 200 nm thick and deposited by sputter deposition onto silicon wafers with a 10 nm Ti adhesion layer. While the nonthermal plasma deposition parameters were kept constant, the film thicknesses were controlled based on the number of raster passes that the substrate made in the nonthermal

plasma reactor. SiO_2 and Si_3N_4 nanoparticle films with raster passes of 25, 50, and 75 were fabricated for characterization study. **Fig. 7.12** shows images of SiO_2 and Si_3N_4 laminate nanoparticle films on gold coated substrates deposited by nonthermal plasma synthesis. Visually, all of the samples showed high visible reflectivity, suggesting that the solar absorptivity of the nanoparticles is low.

Figure 7.12. Laminate nanoparticle films of (a) SiO_2 and (b) Si_3N_4 deposited by nonthermal plasma synthesis onto gold coated substrates. The samples are approximately 1 cm wide and 4 cm long.

For initial characterization, cross-sectional SEM was used to measure the thickness of each film. The cross-sections were created by manually scraping the surface of the nanoparticle films with a sharp diamond scribe. This method was used to create cross-sections because previous work on milling cross-sections into the nanoparticle films using Ga focused ion beam (Ga-FIB) did not produce analyzable results. As such, it was discovered that manually removing nanoparticles created clean cross sections which preserved the nanoparticle film details. **Fig. 7.13** shows characteristic SEM images of the cross-sections of SiO_2 and Si_3N_4 nanoparticle films on gold coated substrates with 25, 50, and 75 raster passes during deposition.

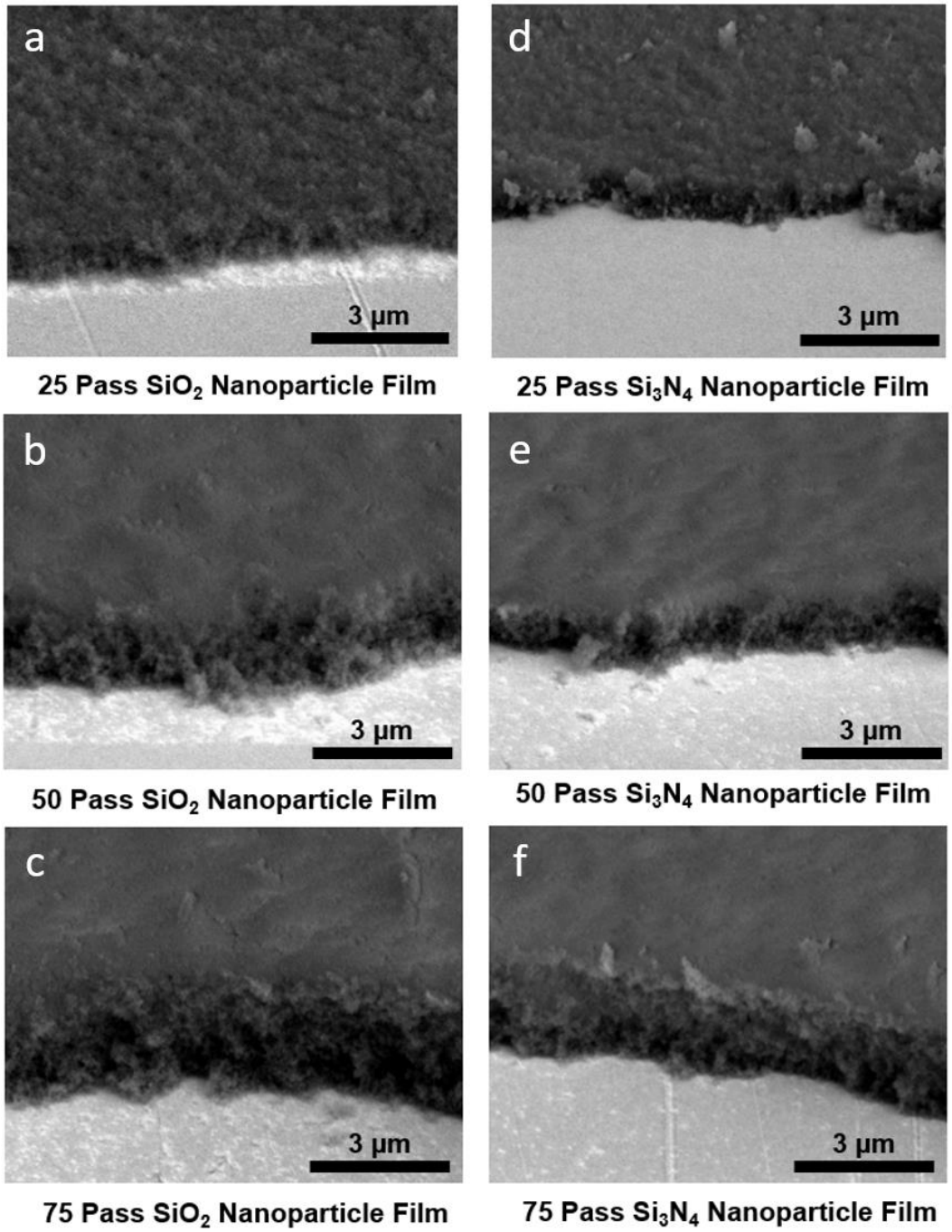

Figure 7.13. Cross-sectional SEM images of SiO_2 and Si_3N_4 nanoparticle laminate films synthesized from a nonthermal plasma reactor. The pass number refers to the number of times the substrate was moved across the deposition spray of the reactor. Note that a correction factor of 1/cos(38°) is applied in the y-axis to account for the tilt of the setup with respect to the SEM Everhart-Thornley Detector (ETD).

From the cross-sectional SEM images, we measured and found that the average thickness of the films was approximately 1.2 ± 0.1 μm, 2.2 ± 0.2 μm, and 3.0 ± 0.5 μm for the SiO_2 nanoparticle films at 25, 50, and 75 raster passes, and 1.0 ± 0.1 μm, 1.4 ± 0.1 μm, and 2.2 ± 0.2 μm for the Si_3N_4 nanoparticle films at 25, 50, and 75 raster passes. As expected, the nanoparticle film thickness increases with the number of raster passes in the reactor.

Next, we measured the spectral reflectivity of the films using FT-IR spectroscopy. **Fig. 7.14** shows the reflectivity of the SiO_2 and Si_3N_4 nanoparticle films in the mid-IR wavelength regime. As expected, the absorption response of the nanoparticle films increased with film thickness. Interestingly, we found that while the SiO_2 nanoparticles exhibited a single strong absorption response at 9 μm as expected, the Si_3N_4 nanoparticles exhibited an unusually broad absorption response with a peak at 9 μm and a peak at 11 μm, even though we only expect an absorption peak at 11 μm from the Si-N bond. The absorption peak at 9 μm suggests that the Si_3N_4 nanoparticles contain leftover impurities from the synthesis process; SiN-H bonds are the most likely reason for the absorption peak at 9 μm.

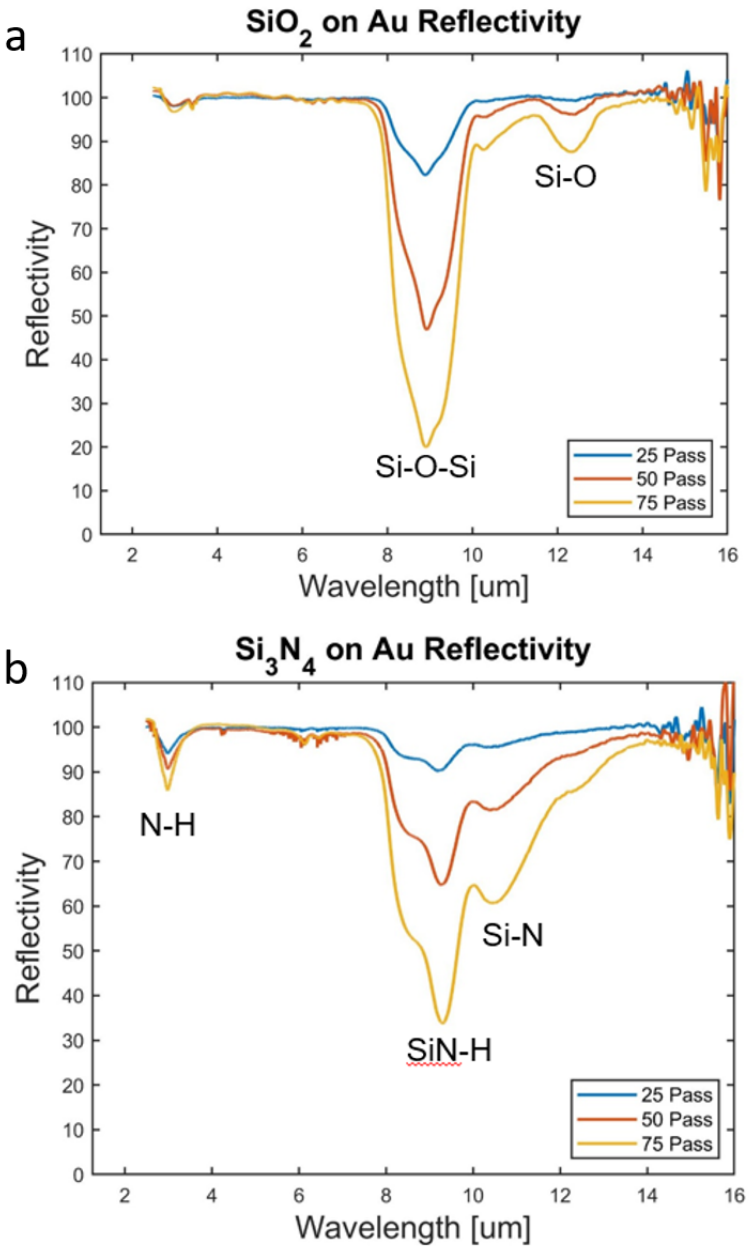

Figure 7.14. FT-IR reflectivity of (a) SiO_2 and (b) Si_3N_4 nanoparticle laminate films synthesized from a nonthermal plasma reactor on a gold coated substrate. The pass number refers to the number of times the substrate was moved across the deposition spray of the reactor.

Finally, we used infrared ellipsometry to extract the complex refractive index of the nanoparticles. Similar to the procedure discussed in Chapter 5, we used the Bruggeman effective medium approximation to model the nanoparticle films by mixing SiO_2/Si_3N_4 material with an air matrix. In other words, we coupled a Bruggeman effective medium approximation with an SiO_2/Si_3N_4 material oscillator model in the ellipsometry model, then fit the oscillator model parameters, film thickness, and fill fraction. Doing so allows us to extract the complex refractive index, thickness, and fill fraction of the nanoparticle films. The measured film thicknesses from cross-sectional SEM were used to control the bounds of the allowed film thickness in the ellipsometry fit.

From the ellipsometry fits, we found film thicknesses of 1.05 μm, 2.13 μm, and 3.45 μm for the SiO_2 nanoparticle films at 25, 50, and 75 raster passes, and 0.82 μm, 1.46 μm, and 2.50 μm for the Si_3N_4 nanoparticle films at 25, 50, and 75 raster passes. We found fill fractions of 8.1%, 8.3%, and 7.3% for the SiO_2 nanoparticle films at 25, 50, and 75 raster passes, and 9.1%, 9.5%, and 8.1% for the Si_3N_4 nanoparticle films at 25, 50, and 75 raster passes. For the complex refractive index, **Fig. 7.15** shows the extracted complex refractive index of the SiO_2 and Si_3N_4 nanoparticles. Note that the complex refractive index reported in **Fig. 7.15** shows the intrinsic bulk refractive index of the SiO_2 and Si_3N_4 material. To find the effective refractive index of the nanoparticle film, Bruggeman effective medium approximation must be used to mix the bulk refractive index of the materials with the refractive index of the air matrix at the appropriate fill fraction.

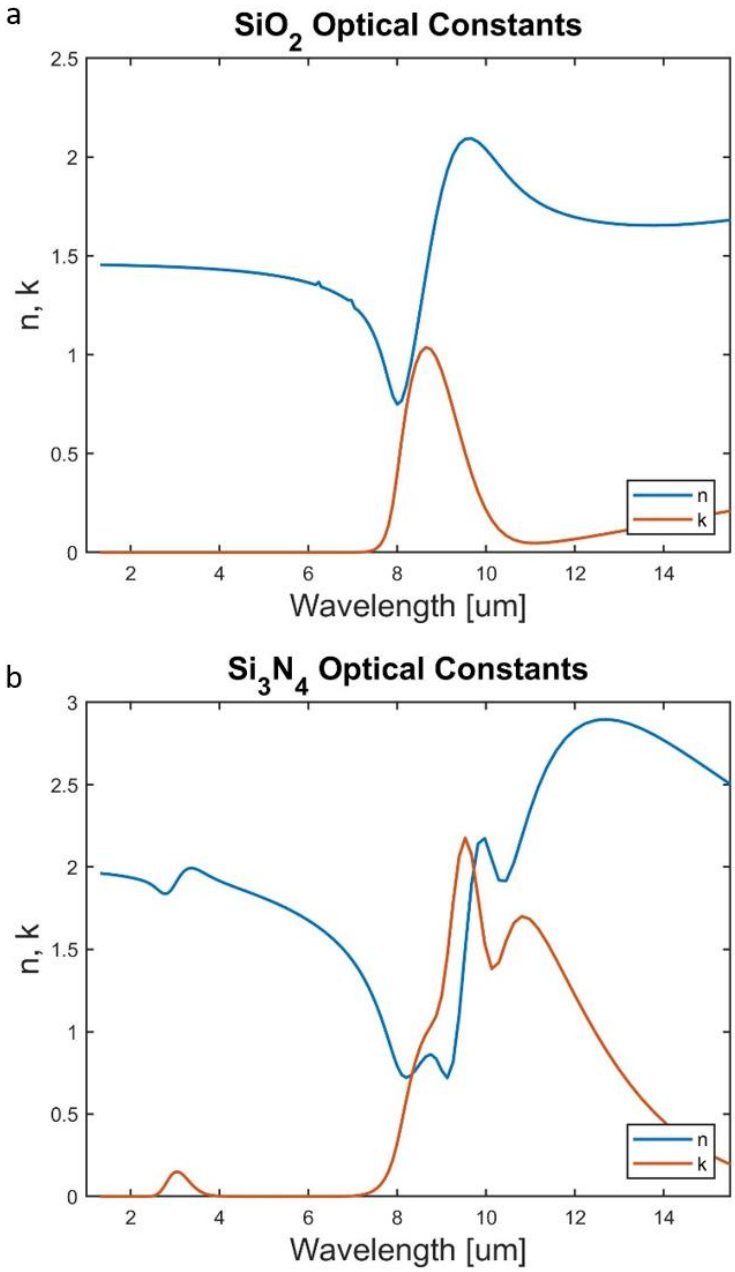

Figure 7.15. The complex refractive index of (a) SiO_2 nanoparticles and (b) Si_3N_4 nanoparticles synthesized in a nonthermal plasma reactor, extracted using ellipsometry.

Using the extracted complex refractive index of the SiO_2/ Si_3N_4 nanoparticle materials, we used ray transfer matrix method to calculate the expected spectral reflectivity of the nanoparticle films to compare the accuracy of the ellipsometry model with Bruggeman

effective medium approximation with the direct FT-IR reflectivity measurements. **Fig. 7.16** shows the calculated spectral reflectivity of the SiO_2 and Si_3N_4 nanoparticle films from ray transfer matrix method. We can see from **Fig 7.16** that the calculated reflectivity matches well with the measured FT-IR reflectivity results, suggesting that a Bruggeman effective medium approximation is an appropriate mixing model for laminate nanoparticle films.

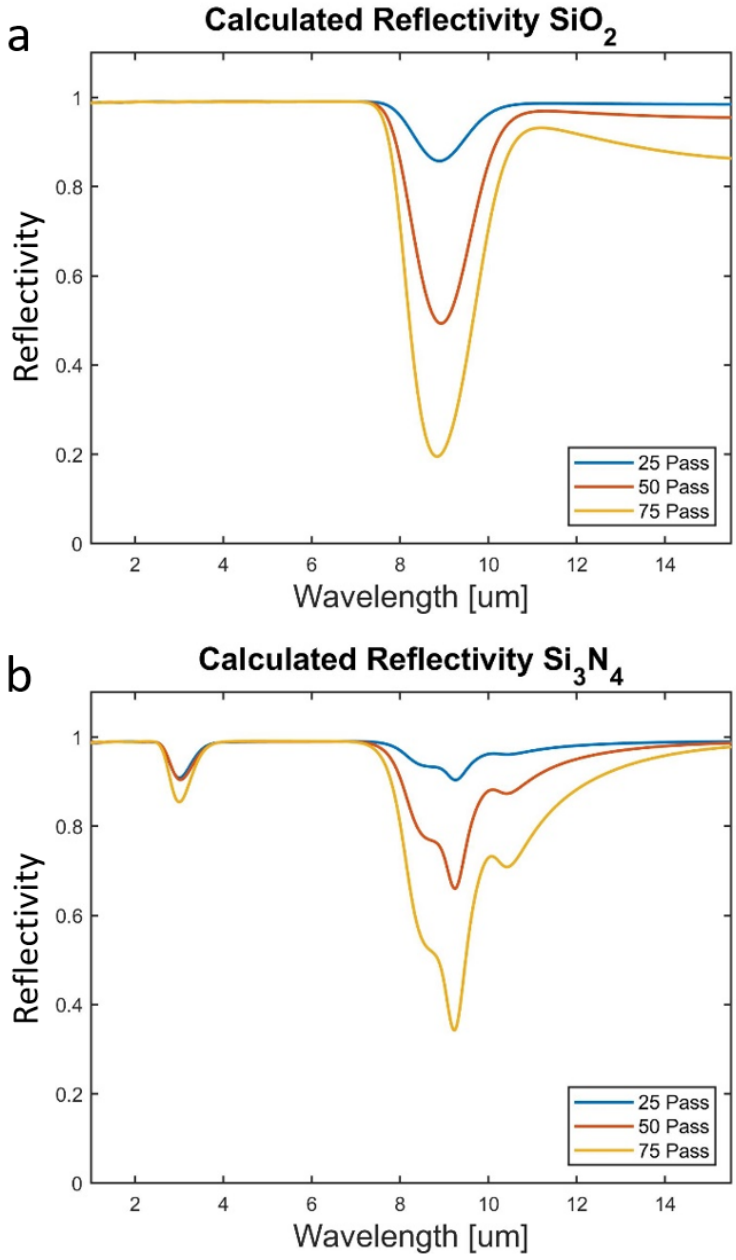

Figure 7.16. The calculated spectral reflectivity of the (a) SiO_2 and (b) Si_3N_4 nanoparticle films from ray transfer matrix method and Bruggeman effective medium approximation using the nanoparticle complex refractive index extracted by ellipsometry.

7.4 Si_3N_4 Laminate Nanoparticle Film Radiative Coolers

Using the results of the SiO_2 and Si_3N_4 nanoparticle film optical characterization, we re-optimized the two-layer laminate nanoparticle film radiative cooling designs shown in **Fig. 7.3** using the experimentally extracted complex refractive index of the SiO_2 and Si_3N_4 nanoparticles. We used Bruggeman effective medium approximation and the complex refractive index of the SiO_2 and Si_3N_4 nanoparticles with a 10% fill fraction to calculate the effective complex refractive index of the nanoparticle layers, then used ray transfer matrix method to calculate the spectral emissivity of the two-layer structure while varying thicknesses. With the spectral emissivity, we then calculated the expected cooling power of the structure. **Fig. 7.17** shows the results of the optimization process.

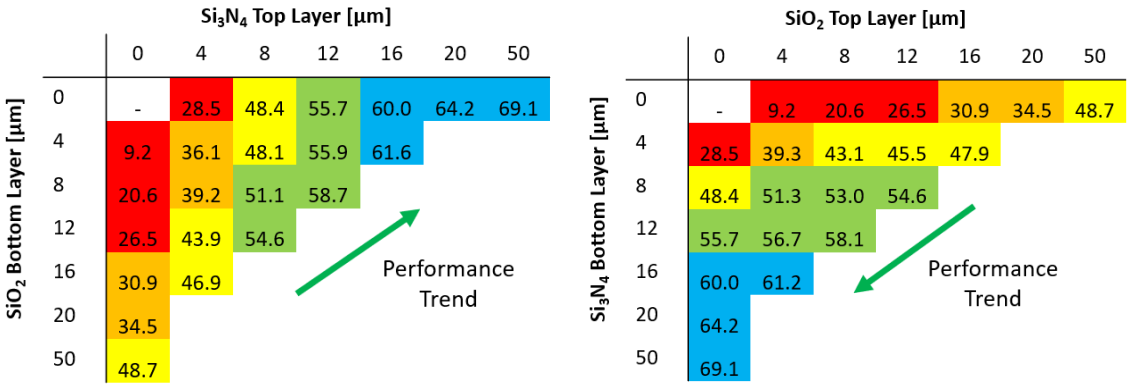

Figure 7.17. Predicted radiative cooling power of a two-layer SiO_2 and Si_3N_4 laminate nanoparticle film radiative cooling structure with varying layer thickness and order.

From **Fig. 7.17**, we see that the highest radiative cooling powers are achieved when the design becomes a single thick film of Si_3N_4 nanoparticles. This is because we discovered during the optical characterization process that while the SiO_2 nanoparticle films behave optically as expected, the Si_3N_4 nanoparticle films contain impurities leftover from the nonthermal plasma synthesis process which produce a strong absorption peak at 9 µm. Coincidentally, the original two-layer laminate nanoparticle film radiative cooling designs shown in **Fig. 7.3** use an SiO_2 nanoparticle layer to enhance emission at 9 µm and an Si_3N_4 nanoparticle layer to enhance emission at 11 µm. However, due to the impurities in the

fabricated Si_3N_4 nanoparticle film, the resulting film covers the entire emission spectrum across the atmospheric transmission window by itself without the need for an SiO_2 nanoparticle layer. As a result, the optimization process tends towards a single thick laminate film of Si_3N_4 nanoparticles as the optimal radiative cooling design.

Based on the new optimization, we fabricated very thick Si_3N_4 laminate nanoparticle films on silver substrate with 400 SiO_2 passes. We used both unprotected bare silver substrates and silver substrates with a 5 nm SiO_2 passivation layer. **Fig. 7.18** shows an image of one of these Si_3N_4 laminate nanoparticle films on silver substrate deposited from nonthermal plasma synthesis with 400 raster passes.

Figure 7.18. Image of Si_3N_4 laminate nanoparticle film on silver substrate deposited from nonthermal plasma synthesis with 400 raster passes. The sample size is approximately 1 cm by 4 cm.

Following the characterization process from Section 7.3, we used cross-sectional SEM to measure the thickness of the films. **Fig. 7.19** shows an SEM image of the cross-section of a Si_3N_4 nanoparticle films on a silver substrate with 400 raster passes during deposition. The measured thickness of the films was approximately 30 µm.

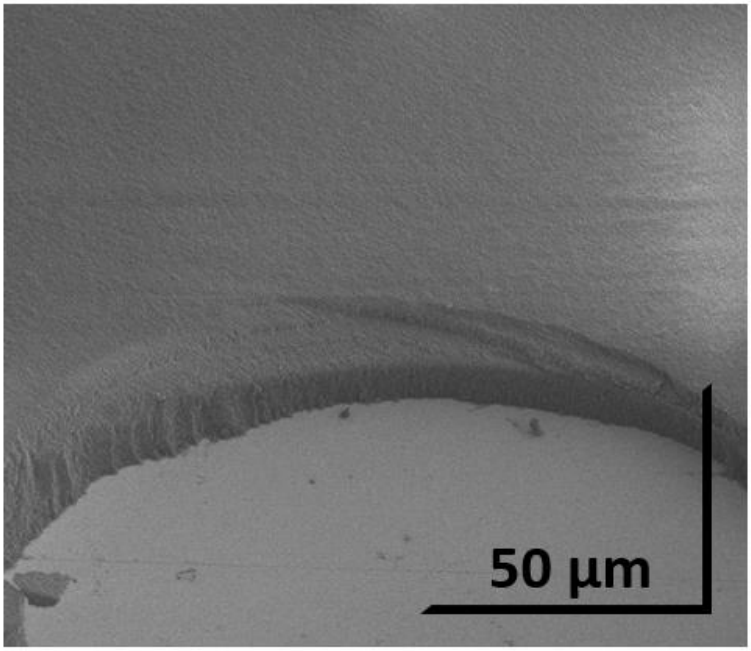

Figure 7.19. Cross-sectional SEM image of a Si_3N_4 nanoparticle laminate film synthesized from a nonthermal plasma reactor with 400 raster passes. Note that a correction factor of 1/cos(38°) is applied in the y-axis to account for the tilt of the setup with respect to the SEM Everhart-Thornley Detector (ETD).

Next, we measured the spectral reflectivity of the films using FT-IR spectroscopy. **Fig. 7.20** shows the reflectivity of 2 Si_3N_4 nanoparticle films in the mid-IR wavelength regime. One of the films was deposited on bare silver, while the other film was deposited on silver with a 5 nm SiO_2 passivation layer.

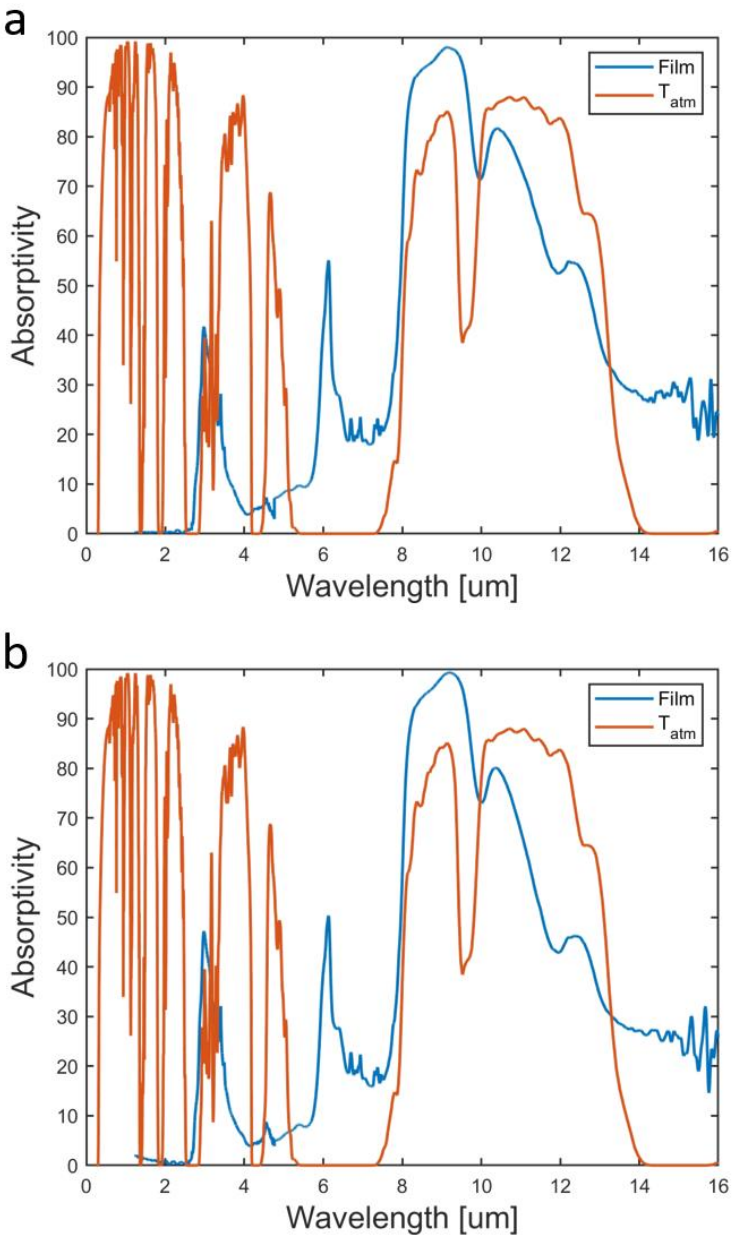

Figure 7.20. FT-IR reflectivity of Si_3N_4 laminate nanoparticle films synthesized from a nonthermal plasma reactor with 400 raster passes on a (a) bare silver substrate and (b) silver with 5 nm SiO_2 passivation layer. The atmospheric transparency window is overlaid.

We observe from **Fig. 7.20** that a single thick laminate nanoparticle film of Si_3N_4 matches well with the atmospheric transparency window. We also note that the 5 nm SiO_2 passivation

layer does not have an observable effect on the performance of the structure. This result suggests that this laminate nanoparticle film acts as a radiative cooling structure.

Finally, we used infrared ellipsometry to extract the fill fraction of the nanoparticle films. Due to the thickness of the film, the ellipsometry measurements could not be conclusively used to extract the complex refractive index or thickness of the films. As such, we used the Si_3N_4 nanoparticle material model from Section 7.3 to model the film, and we held the oscillator model parameters and the thickness of the film constant and fit only for the fill fraction using a Bruggeman effective medium approximation. The ellipsometry result suggested a nanoparticle fill fraction of 8 – 10%.

7.5 Summary and Conclusion

In this chapter, we reported on the fabrication and characterization of 4 different radiative cooling structures: 2 two-layer dense thin film structures and 2 single-layer Si_3N_4 laminate nanoparticle film structures. For the 2 two-layer dense thin film structures, our optical characterization showed that the spectral emissivity matched well with the expected spectral emissivity from our theoretical results. For the laminate nanoparticle films, our initial characterization showed that the Si_3N_4 nanoparticle films deposited from nonthermal plasma synthesis contained impurities resulting in an unexpected absorption peak at 9 μm. Combined with the natural absorption peak of Si_3N_4 at 11 μm, our re-optimization of the laminate nanoparticle film radiative cooling designs suggested that a single-layer laminate nanoparticle film of Si_3N_4 was sufficient to act as a radiative cooler without the need of an SiO_2 nanoparticle film. From the re-optimization results, we fabricated and characterized thick Si_3N_4 laminate nanoparticle films with a thickness of 30 um and fill fraction of 8 – 10%.

Finally, using the measured emissivity of each structure from the optical characterization results, we can estimate the predicted raidative cooling power of each of these structures. At 300 K, we predict a radiative cooling power of approximately 34.4 W/m^2 and 40.5 W/m^2 for the SiO_2 on Si_3N_4 and Si_3N_4 on SiO_2 dense thin film structures, respectively, and 39.6 W/m^2

and 36.0 W/m^2 for the thick Si_3N_4 laminate nanoparticle films on bare silver and passivated silver, respectively. This chapter concludes Section II: Passive Daytime Terrestrial Radiative Cooling.

SECTION III: DIRECT SPECTRALLY AND ANGULARLY RESOLVED RADIATIVE EMISSION

Chapter 8

A NEW INSTRUMENT FOR SPECTRALLY AND ANGULARLY RESOLVED RADIATIVE EMISSION MEASUREMENTS OF RADIATIVE COOLING STRUCTURES

8.1 Introduction

In Section II, we reported work on the design, fabrication, and characterization of laminate nanoparticle films for radiative cooling applications. During this process, we recognized a need for a standardized experimental method to facilitate inter-comparisons between different radiative cooling structures and performances across literature. We introduced this need in Chapter 6 with the work on comparing various radiative cooling structure performances across literature by digitizing the published spectral emissivity and calculating the predicted radiative cooling performance of each structure under the same ambient conditions. At the time, the widely reported methods for measuring the radiative cooling power of structures involved constructing a test apparatus to reduce convective and conductive effects on the sample and then measuring the temperature of the sample under ambient sunlight. By measuring the solar irradiance and surface temperature, the non-radiative heat loss coefficient Q can be extracted using the known structure emissivity. However, this method depends strongly on the test apparatus itself and does not directly measure the radiative power of the structure. We found that the experimental setup greatly influenced the final temperatures which were achievable; setups with increasing complexity utilizing vacuum chambers, radiation shields, and mirror cones report lower temperatures compared to simpler setups.

Based on the limitations of current methods, we proposed, designed, constructed, and tested an instrument for directly measuring the spectrally and angularly resolved radiative power of a radiative cooling structure. Simultaneously, the instrument measures the surface temperature of the sample. To control the ambient, the instrument reduces both thermal

convective and conductive and external radiative effects on the sample temperature and measured radiative power.

In this chapter, we report on our new instrument for direct spectrally and angularly resolved radiative emission measurements. We present a detailed overview on the instrument specifications and design considerations. We outline the operating procedure for the instrument including the alignment, start up, operation, and shut down procedure. Using this instrument, we report measurements on the spectrally and angularly resolved radiative emission of several radiative cooling structures including Si_3N_4 laminate nanoparticle films and two-layer SiO_2 and Si_3N_4 dense thin film structures at various temperatures and angles, and we discuss the results of these measurements as well as the limitations of the instrument.

8.2 Instrument Overview

In this section, we present our new instrument for simultaneous direct spectrally and angularly resolved radiative emission and surface temperature measurements. We begin by reporting the final instrument specifications in detail, then discuss the considerations which influenced the design.

8.2.1 Design Specifications

The instrument is a custom-designed cryoshroud contained within a large vacuum chamber. **Fig. 8.1** shows solid and wireframe CAD schematics of the basic design of the instrument without any attachments from different viewing angles.

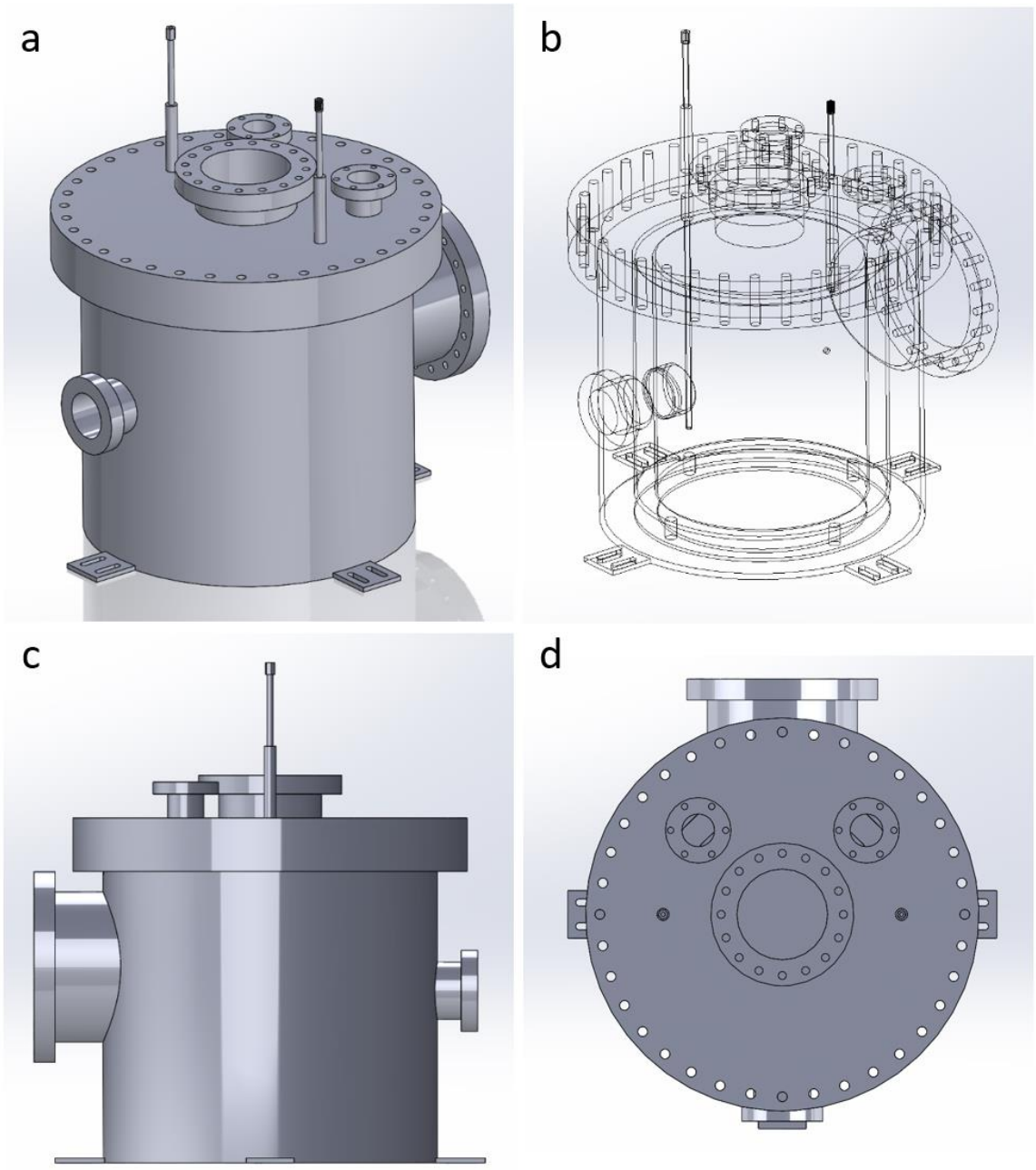

Figure 8.1. CAD schematic of the proposed instrument for simultaneous measurement of the direct radiative emission and surface temperature of a sample. The schematics shown include (a) solid schematic, (b) wireframe schematic, (c) solid schematic side view, and (d) solid schematic top view of the instrument. The instrument is a custom-design vacuum chamber with cryoshroud.

MDC Precision, LLC was commissioned for the construction of the instrument vacuum chamber. **Fig. 8.1a** is a visual schematic of the outside of the vacuum chamber. The cryoshroud itself is a hollow cylindrical tube whose walls can be filled with liquid N_2 (LN_2) to allow it to cool to temperatures around -160 °C (measured cryoshroud temperature compared to LN_2 boiling point of -196 °C). The shroud is open at the top and bottom; it is a straight cylindrical tube which runs along the height of the vacuum chamber. **Fig. 8.1b** shows the shroud which is contained entirely within the vacuum chamber. Two tubes run from the shroud walls through the top of the vacuum chamber; these tubes are cryogenic lines used to fill the cryoshroud with LN_2. The ends of the tubes are fitted with ¼-inch VCR® fittings to connect directly to a LN_2 cylinder. The vacuum chamber has an outer diameter of 14 inches (with a 16.5-inch CF flange lid), while the cryoshroud has an outer wall diameter of 11 inches, an inner wall diameter of 9 inches (1-inch hollow wall thickness), and a height of 11 inches.

Fig. 8.1a shows five separate flanges on the vacuum chamber aside from the two cryogenic tubes. These flanges include one 6-inch CF flange and two 2.75-inch CF flanges on the top of the chamber, and one 8-inch CF flange and one KF-50 vacuum flange on the sides of the chamber.

On the top of the chamber (**Fig. 8.1d**), the 6-inch CF flange is the mounting point for the motorized rotary feedthrough for the sample stage. The motorized rotary feedthrough is a vacuum feedthrough for a motorized rotary shaft that runs halfway down the height of the vacuum chamber and exactly along the center axis of the vacuum chamber and cryoshroud cylinder. At the end of the rotary shaft, the sample stage is mounted. In other words, the motorized rotary feedthrough is a motorized shaft that rotates (or tilts) the sample to the left and right; this gives us the angle-resolved directivity of the sample thermal emission. **Fig. 8.2** shows a schematic of the motorized rotary feedthrough with rotational shaft. The end of the shaft is threaded to allow mounting of various sample stages. The motor of the rotary feedthrough is connected to an external motor controller resulting in a rotational precision of approximately 0.2 ± 0.1°. This error in precision arises primarily from the physical

connection between the worm gear and worm wheel. The motor controller for the worm gear can step in intervals of approximately 0.0005° (1/1775°). The motor controller and motorized rotary feedthrough were purchased from MDC Precision, LLC. A zero-length 6-inch to 2.75-inch CF adapter is used to connect the motorized rotary feedthrough to the vacuum chamber.

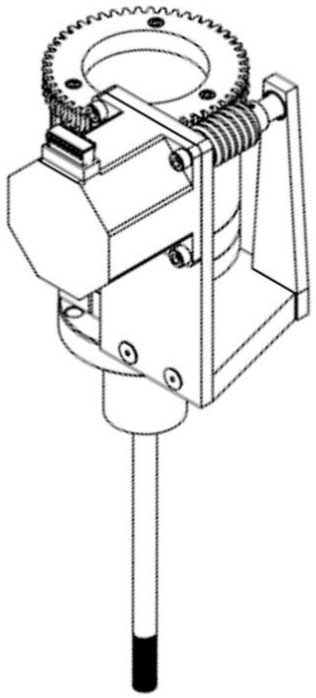

Figure 8.2. Schematic of the motorized rotary feedthrough. A sample stage (not shown here) can be mounted via the threaded end of the rotary shaft.

The sample stage is a custom-designed stage which enables tilt adjustment along the x-axis and translational adjustment along the x- and z-axes (where the y-axis is the rotary shaft axis). Thus, when combined with the rotation provided by the motorized rotary shaft, the sample stage allows xy-tilt adjustment. **Fig. 8.3** shows a CAD schematic of the sample stage. It is important to note that the surface of the sample stage lies behind the axis of the rotary shaft; once the sample is mounted onto the stage, the stage can be translated forward into eucentric position. Eucentric position is the position at which a surface can be tilted or rotated

without laterally shifting the focal point. In other words, at eucentric position, the surface of the sample lies exactly along the axis of rotation.

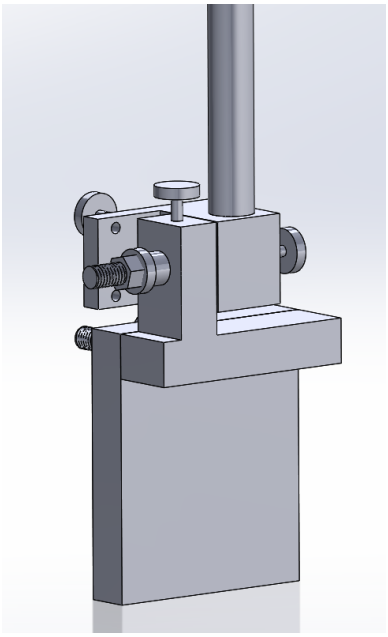

Figure 8.3. CAD schematic of the instrument sample stage. Combined with the rotary shaft, the sample stage enables xy-tilt adjustments and xz-translational adjustments.

Two 2.75-inch CF flanges are also attached to the top of the vacuum chamber (**Fig. 8.1d**). These two CF flanges are the mounting points for all necessary components which need to be connected to the vacuum chamber during operation. Two 4-way 2.75-inch CF flanges are attached to each 2.75-inch CF flange to increase the number of connections to the vacuum chamber from two to six. First, a type K thermocouple feedthrough with three miniature plugs is mounted to feed two bare wire type K thermocouples into the chamber, one to measure the temperature of the cryoshroud and one to measure the temperature of the air/vacuum. Second, a copper wire electrical feedthrough is used to connect the power source and controller for a thermoelectric heater and thermistor into the chamber. The thermoelectric heater and thermistor are mounted onto the sample stage; the thermistor measures the temperature of the sample stage (and sample), and the thermoelectric heater allows for controlled heating of the sample stage. A temperature controller and power source

are used to modulate and hold the sample stage at a specific temperature point using the thermistor as the feedback temperature monitor. The temperature controller, power source, thermistor, and thermoelectric heaters were purchased from TE Technology, Inc. Third, a KJLF® 275 Series convection gauge and KJLF® 354 Series ion gauge are mounted to measure the pressure of the vacuum chamber at pressures above and below 1×10^{-3} Torr, respectively. Fourth, an up-to-air vent valve is mounted; a gas nitrogen source and tube with a dual gas regulator are connected to the up-to-air vent valve. This allows the chamber to pump/vent with nitrogen gas. This prevents ice formation from water vapor on the cryoshroud during cooling. Finally, unused CF flanges are covered with 2.75-inch CF blanks.

On the backside side of the vacuum chamber (**Fig. 8.1c**), an 8-inch CF flange acts as the mounting point for the turbopump. The turbopump used in this system is an Agilent TV 301 Navigator. The foreline vacuum pump is an Agilent TriScroll 600 dry scroll pump.

On the front side of the vacuum chamber (**Fig. 8.1c**) is a KF-50 vacuum flange which acts as the main measurement aperture of the instrument. In order words, this is the main opening of the vacuum chamber for measuring the radiative thermal emission of a sample. A 1-inch diameter zinc selenide (ZnSe) window is mounted onto the KF-50 vacuum flange; ZnSe is used as the window because of its high transparency in the infrared wavelength regime. In order for radiative emission from the sample to escape the vacuum chamber, a 2-inch aperture is cut into the cryoshroud. This opening can be seen in **Fig. 8.1b**. The sample stage which is mounted onto the motorized rotary feedthrough shaft is aligned such as the sample faces the aperture opening of the vacuum chamber. Thus, as the sample tilts left and right, we can measure the angle-resolved outgoing radiative emission from the sample through the aperture opening of the vacuum chamber. **Fig. 8.4** shows images of the full instrument set up.

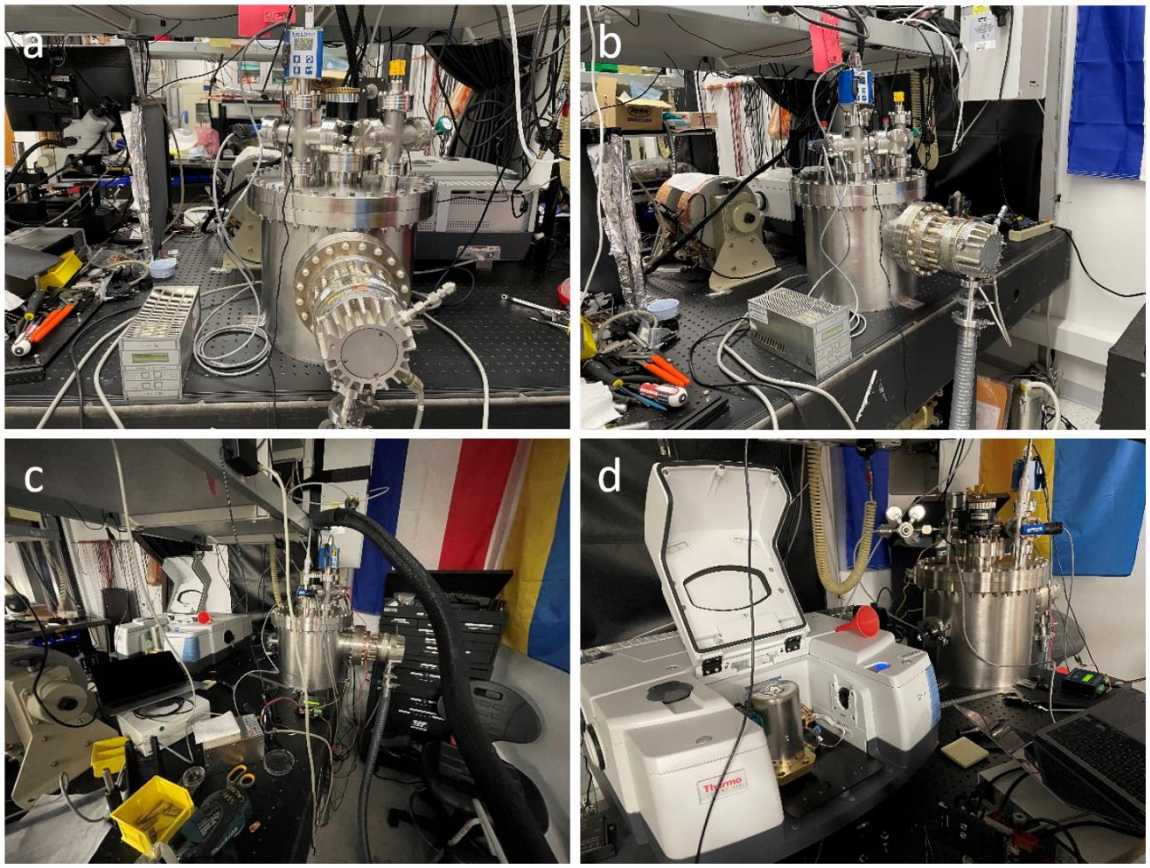

Figure 8.4. Images of the instrument setup.

In order to measure the spectral-resolved radiative emission from the sample, we collimate the outgoing radiative emission into a Nicolet^{TM} iS50 FT-IR Spectrometer from Thermo Fisher Scientific. A KBr beamsplitter is used in the FT-IR spectrometer. The FT-IR spectrometer was previously modified to accept an external collimated infrared beam as the input signal. This modification was a commercial modification provided by Thermo Fisher Scientific. To collect and collimate the radiative emission, we used a 1-inch diameter ZnSe lens with a 50 cm focal length. Gold mirrors were used to steer the beam whenever necessary.

Importantly, the infrared signal in the FT-IR spectrometer is measured using a LN_2 cooled Mercury-Cadmium-Telluride (MCT-A) detector with a spectral range of 4000 – 650 cm^{-1} from Thermo Fisher Scientific. A cryogenically cooled detector is necessary because a standard deuterated triglycine sulfate (DTGS) detector is insufficient for measuring the

emission signal strength from a thermally radiative source which has a temperature near room temperature. Furthermore, even with the MCT-A detector, the room temperature is the low temperature limit at which a radiative sample can be measured in this setup. As such, direct radiative emission measurements must be made at slightly elevated temperatures above room temperature at minimum.

To summarize, the instrument is a large vacuum chamber with a cryoshroud which surrounds the sample. A small aperture in the cryoshroud and vacuum chamber exports the thermal radiative emission out of the chamber. A Zn Se lens is used to collimate the radiative emission into an FT-IR spectrometer with an MCT-A detector. By rotating the sample using the motorized rotary shaft and continually measuring the radiative emission with the FT-IR spectrometer, we can measure the spectrally and angularly resolved radiative emission from a sample. Simultaneously, the thermoelectric heater and thermistor measure and control the sample temperature.

8.2.2 Design Considerations

The points below highlight the main design considerations which resulted in the final instrument design.

1. The main purpose of this instrument is to directly measure the spectrally and angularly resolved radiative thermal emission from a photonic structure such as a radiative cooler. To achieve this, we use a motorized rotary shaft to control the angle-resolved directivity and an FT-IR spectrometer to measure the spectral-resolved infrared emission signal. A ZnSe window allows us to export the radiative emission from a sample. An infrared focusing optic (ZnSe lens) collects and collimates the infrared emission into the FT-IR spectrometer. An MCT-A detector allows detection of radiative emission signals from thermally radiative sources at temperatures near room temperature in the mid-infrared wavelength regime. The sample stage adjusts the position of the sample so that its surface is

at eucentric position; this prevents lateral drift of the focal spot across the surface as the sample rotates.

2. The first purpose of the cryoshroud is to reduce the effect of external radiative emission on the sample. When measuring the radiative emission of a sample, we measure both the radiative emission from the sample and the environmental radiative emission reflected off the sample into the detector. While this effect is usually unnoticeable at high temperatures, it contributes significantly to the total emission signal at temperatures near room temperature. By enclosing the sample with a cryoshroud, we ensure that very little environmental thermal emission will affect our measurements.
    a. To contextualize the impact of environmental radiative emission, we use Stefan-Boltzmann Law to calculate the radiative emission from an environmental blackbody surrounding the sample. A blackbody at room temperature (27 °C) radiates approximately 460 W/m^2. Comparatively, a cryoshroud cooled with LN_2 at -160 °C radiates approximately 9 W/m^2.
3. The second purpose of the cryoshroud is to absorb radiative emission from the sample itself. In other words, the cryoshroud acts as a thermally radiative heat sink in a role similar to the cold background of space for radiative coolers. In this role, it prevents radiative emission from propagating within the vacuum chamber. As such, the environment of this chamber can be effectively described as a space environment, and a radiative cooler placed in this chamber would act similarly to a radiative cooler placed in space.
    a. Note: using Stefan-Boltzmann Law, we find that the background of space at 2.7 K radiates approximately 3×10^{-6} W/m^2.
4. Since the radiative thermal emission of a sample is directly related to the temperature of the sample, the instrument is designed to both make temperature measurements and control the temperature of the sample during radiative emission measurements. This is achieved using the thermoelectric heater, thermistor, and temperature controller. This allows us to either measure the temperature of the

sample as it radiatively cools or hold the sample at a set temperature point and measure its radiative emission at any given temperature.

5. The instrument aims to minimize environmental convective and conductive thermal effects on the sample. This is achieved naturally with the vacuum chamber and turbopump introducing a high vacuum ($< 1\times10^{-6}$ Bar) to the system. As previously discussed in Chapter 3, a high vacuum is an effective insulating layer. In particular, a high vacuum is necessary to isolate the cryoshroud from the sample.

We note that the remainder of the instrument components described in Section 8.2.1 are necessary for operating the instrument but were not considered directly when designing the instrument. This includes the up-to-air vent valve and gas nitrogen vent line, thermocouple feedthrough, convection and ion pressure gauges, etc.

8.3 Instrument Operating Procedure

This section outlines the procedure for aligning the instrument, mounting samples, starting up the instrument, and making a radiative emission measurement, and shutting down the instrument.

8.3.1 Reference Sample Preparation

Beforehand, we prepare two reference samples which are necessary for normalizing the radiative emission measurement results. The two reference samples are a gold reference and a blackbody reference. The references are also useful for aligning the instrument with the FT-IR spectrometer. The gold reference represents the minimum radiative emission signal, and the blackbody reference represents the maximum radiative emission signal.

Gold references were prepared using electron beam evaporation to deposit 200 nm of Au and 10 nm of Ti onto a Si wafer. The 10 nm Ti layer acts as an adhesion layer between the gold and silicon material. To prepare the blackbody references, carbon black was mixed into a 1:4 solution of isopropanol and water, and then the mixture was spray coated onto tape. Once

the solvent evaporated, a carbon black sample was left behind. From previous measurements, the gold references are approximately >98% reflective while the blackbody references are <2% reflective in the infrared wavelength regime.

We also prepare an alignment sample. The alignment sample is a printout of a 1 mm^2 spaced grid on a silicon wafer.

8.3.2 Alignment

For every measurement, the instrument and sample stage must be aligned with the FT-IR spectrometer and MCT-A detector. Generally, this means aligning the instrument and sample stage with the FT-IR spectrometer so that the sample surface is positioned at eucentric focus with respect to the focusing/collimating optic. This process involves aligning the focusing optic with the FT-IR spectrometer, then aligning the instrument, then aligning the sample stage, then aligning the MCT-A detector. For the alignment process, we use the collimated red alignment laser from the FT-IR spectrometer.

First, we align the ZnSe lens with the FT-IR spectrometer alignment laser following standard alignment procedures for mirrors and lenses. This ensures that the ZnSe lens now collimates a beam into the FT-IR spectrometer; the other end is a visible focused beam spot.

Next, we align the instrument by moving it into the path of the beam line such that the beam focal spot aligns with both the surface of the sample and the axis of rotation of the rotary shaft. To do this, we mount the alignment sample onto the sample stage. To mount a sample into the instrument, we detach the motorized rotary feedthrough from the chamber, mount the sample onto the sample stage, then re-attach the rotary feedthrough to the chamber. We adjust the sample stage so that the surface of the sample aligns with the center axis of the rotary shaft. Once the alignment sample is mounted, we move the instrument into the alignment beam path such that the focal spot is located on the alignment sample. From here, we make forward-backward adjustments of the instrument to minimize the beam spot size on the alignment sample. We use the reflected beam from the ZnSe window of the chamber

to align the tilt of the instrument with the beam. For the left-right lateral adjustment of the instrument, we rotate the sample stage and observe the movement of the beam focal spot with respect to the alignment sample grid. We adjust the left-right position of the instrument until the beam focal spot does not translate during sample rotation. Once this is achieved, we know that the instrument and the sample stage are aligned at eucentric position.

Next, we align the sample stage. To do this, we unmount the alignment sample and mount the gold reference. We use the gold reference to align the xy-tilt of the sample stage and to zero the motorized rotary shaft at normal incidence. The gold reference is necessary here to obverse the reflected alignment beam.

Finally, we align the MCT-A detector. To do this, we unmount the gold reference and mount the blackbody reference. The blackbody reference is necessary to observe a strong radiative emission signal in the FT-IR spectrometer. To improve the signal further, we use the thermoelectric heater to heat the blackbody reference to 50 °C. We cool the MCT-A detector with LN_2, then adjust the position and tilt of the MCT-A detector until the observed peak-to-peak signal strength is maximized. Once maximized, the MCT-A detector is aligned with the FT-IR spectrometer.

8.3.3 Start Up

The startup procedure for the instrument involves pumping down the vacuum chamber, then cooling the cryoshroud. It is important to pump the chamber down first to avoid condensation and ice formation on the cryoshroud during cooling. To pump down the chamber, we use the rough pump to pump the chamber to a pressure of 1 Torr, then start the turbopump. At a pressure of 1×10^{-3} Torr, we switch from the convection gauge to the ion gauge since the convection gauge cannot read pressures below 1×10^{-3} Torr. At full turbopump speed, the base pressure of the instrument is usually between 1×10^{-6} – 1×10^{-7} Torr.

Once a pressure of approximately 1×10^{-5} Torr is achieved, LN_2 is pumped into the cryoshroud directly from a LN_2 cylinder. **Fig. 8.5** shows a characteristic cryoshroud cooling

curve measured by a thermocouple attached to the surface of the cryoshroud. It takes approximately 20 – 25 minutes to cool the cryoshroud to a temperature of -150 °C. We note that the minimum temperature that we have observed is approximately -160 °C even when the cryoshroud is completely filled with LN_2. Once the cryoshroud is cooled to -140 – -160 °C, the instrument is ready for radiative emission measurements.

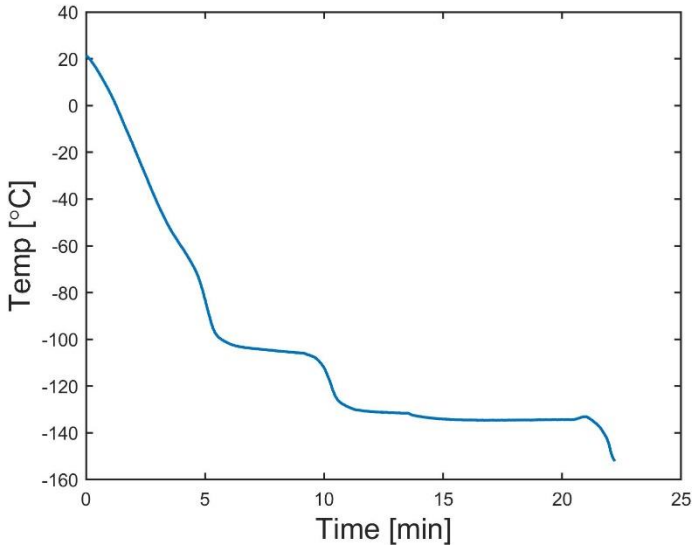

Figure 8.5. Characteristic cryoshroud cooling curve over time with LN_2, measured by a thermocouple attached to the surface of the cryoshroud.

8.3.4 Measurement

For a typical measurement, we set the optical velocity to 0.4747 or lower, the gain to 1.0, the number of scans to 100 or higher, the resolution to 2 (0.241 cm^{-1}), and the range to 4000 – 650 cm^{-1}. We do not apply any atmospheric corrections, and we set the data output format to Single Beam. To observe sufficient signal strength, we heat the sample by setting the thermoelectric heater to 30 – 50 °C.

To measure the spectrally and angularly resolved radiative emission, we make a measurement at each angle from 0 – 75°. The reason we measure up to 75° is because we find that the signal decreases at angles greater than 75° even when measuring a blackbody

reference. Since a Lambertian surface theoretically exhibits equal radiance at all angles, we know from this observation that the alignment of the sample becomes too poor at angles above 75° to make accurate measurements.

It is important to note that for each measurement, we obtain the raw signal output from the FT-IR spectrometer. This means that we must perform a normalization in order to find the resulting emissivity of a sample. As such, for each sample that we measure, we also measure at the same angles and temperatures the corresponding radiative emission for a gold reference and a blackbody reference. Then, we can perform a basic normalization to calculate the spectrally and angularly resolved emissivity of the sample:

$$\epsilon_{Sample}(\lambda, \theta, T) = \frac{E_{Sample}(\lambda, \theta, T) - E_{Au}(\lambda, \theta, T)}{E_{Blackbody}(\lambda, \theta, T) - E_{Au}(\lambda, \theta, T)} \tag{8.1}$$

Where E_{Sample} is the raw emission signal of the sample, E_{Au} is the raw emission signal of the gold reference, and $E_{Blackbody}$ is the raw emission signal of the blackbody reference. This normalization assumes that E_{Au} represents the floor of the measurement and $E_{Blackbody}$ represents the ceiling of the measurement. Thus, **Eq. 8.1** gives us the normalized direct radiative emission of a sample.

8.3.5 Shut Down

The shutdown procedure for the instrument involves warming up the cryoshroud, then venting the vacuum chamber. It is important to warm the cryoshroud to room temperature before venting the chamber to prevent condensation and ice formation on the cryoshroud. To warm the cryoshroud, we simply leave the instrument overnight until all of the LN_2 evaporates.

To vent the vacuum chamber, we turn off the turbopump and wait for the pressure to rise to 1×10^{-3} Torr. At 1×10^{-3} Torr, we switch from the ion gauge to the convection gauge since the ion gauge cannot operate safety at pressures above 1×10^{-3} Torr. Once the turbopump has fully stopped spinning, we turn the rough pump off and open the up-to-air vent valve. The

vent valve vents the chamber with gas nitrogen up to atmospheric pressure. Once at atmospheric pressure, the sample can be removed from the chamber.

8.4 Direct Radiative Emission Measurements

Using the procedure outlined in Section 8.3, we measure the spectrally and angularly resolved radiative emission of the Si_3N_4 nanoparticle film radiative coolers and the two-layer SiO_2 and Si_3N_4 dense thin film radiative coolers previously discussed in Chapter 7. We report the results of measurements made at temperatures ranging from 30 – 50 °C and angles from 0 – 75 °C.

8.4.1 Preliminary Measurements

We begin with measurements of the Si_3N_4 laminate nanoparticle film radiative cooling structures. Measurements were made at normal incidence at temperatures of 30, 40, and 50 °C. To normalize the radiative emission data according to **Eq. 8.1**, we also made measurements of the gold and blackbody reference at normal incidence and 30, 40, and 50 °C. **Fig. 8.6** shows the normalized emissivity of two Si_3N_4 laminate nanoparticle films; one of the films was deposited on bare silver, while the other film was deposited on silver with a 5 nm SiO_2 passivation layer.

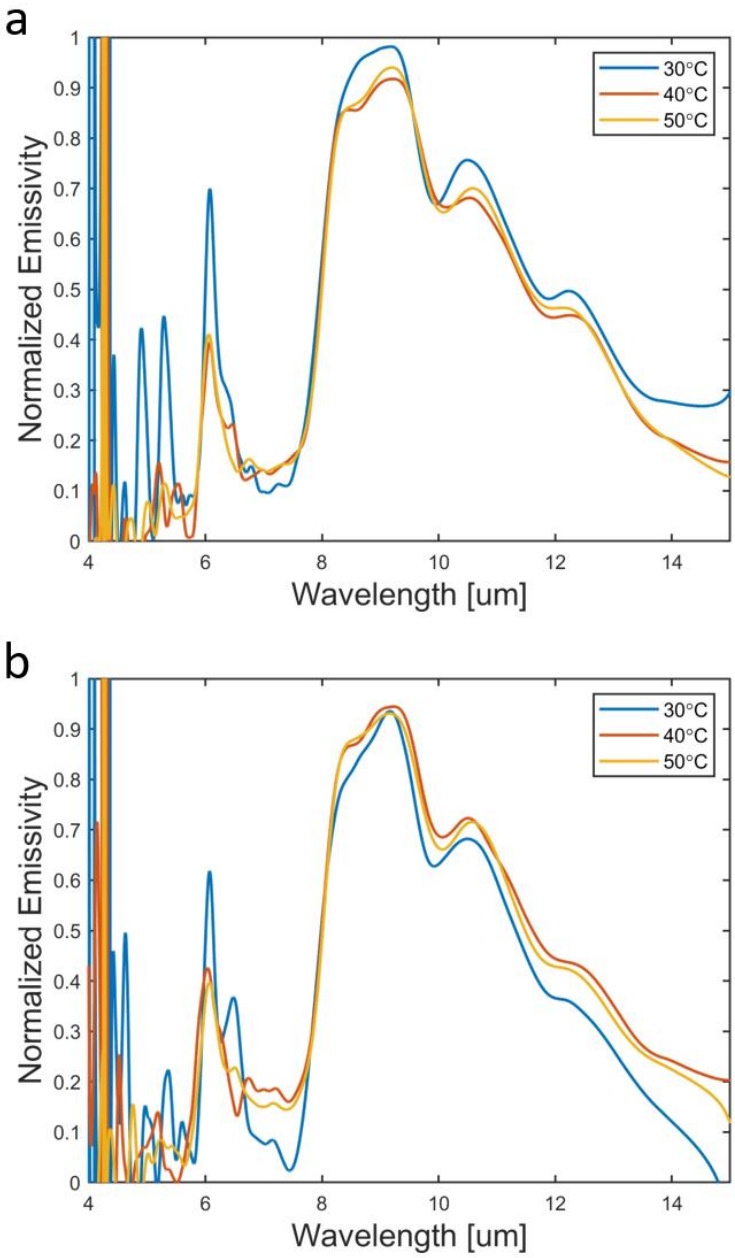

Figure 8.6. Normalized radiative emissivity of Si_3N_4 laminate nanoparticle films at normal incidence and temperatures of 30, 40, and 50 °C. The nanoparticle films were synthesized from a nonthermal plasma reactor with 400 raster passes on (a) bare silver substrate and (b) silver with 5 nm SiO_2 passivation layer.

From **Fig. 8.6**, we observe that from 8 – 14 μm, the spectral shape of the normalized emissivity extracted using our instrument matches well with the measured reflectivity of the

Si_3N_4 laminate nanoparticle films from FT-IR reflectivity (**Fig. 7.20**). This suggests that the instrument can measure the direct radiative emission of samples accurately. We note that the normalized emissivity becomes noisy below 6 μm because the MCT-A detector signal drops to nearly 0 at this wavelength range.

To test the precision of the instrument across different days, we replicated the entire measurement and compared the new measurement results with the results shown in **Fig. 8.6**. **Fig. 8.7** compares the normalized emissivity of the two Si_3N_4 laminate nanoparticle films obtained on different days at normal incidence, 30, 40, and 50 °C. The gold and blackbody references were also re-measured for the normalization.

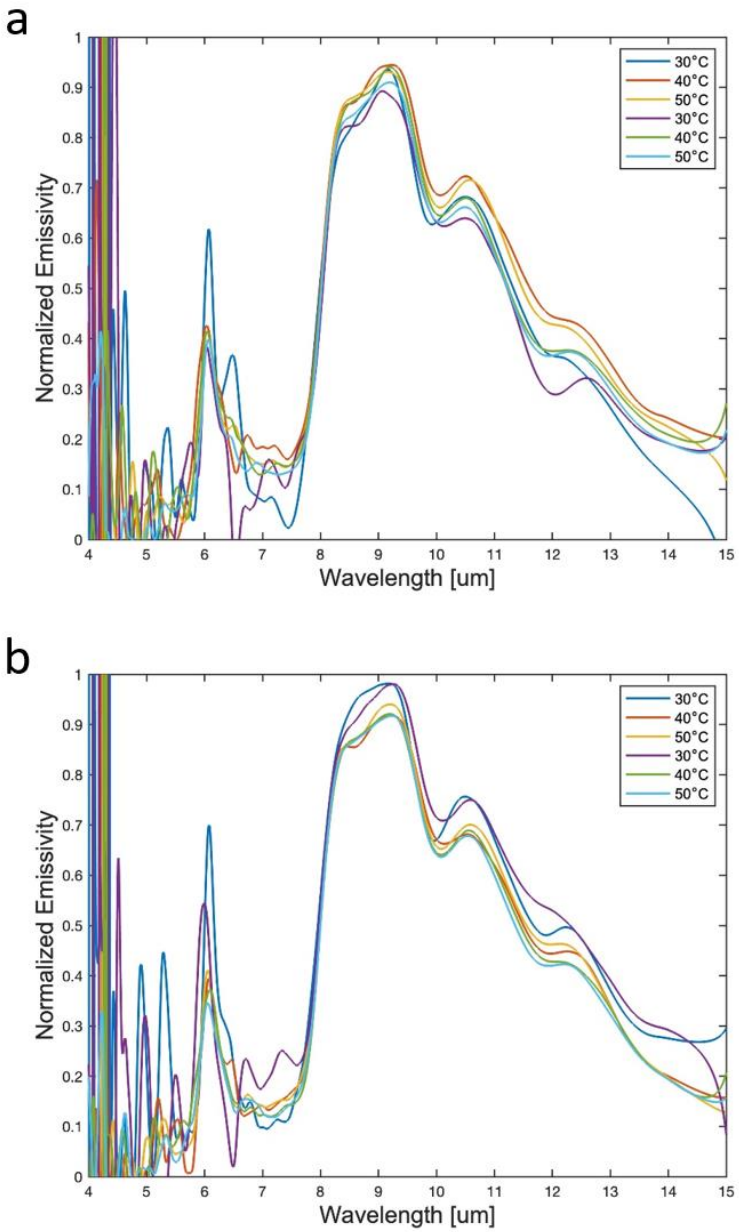

Figure 8.7. Comparison of the normalized radiative emissivity of Si_3N_4 laminate nanoparticle films, on either (a) bare silver substrate or (b) silver with 5 nm SiO_2 passivation layer, at normal incidence and temperatures of 30, 40, and 50 °C from two separate measurements made on different days.

From **Fig. 8.7**, we observe that the spectral shape of the normalized emissivity is broadly preserved. This suggests that the alignment of the instrument does not drift over time and that the instrument results are robust and reproducible. Using the results from **Fig. 8.6** and the equations discussed in Section II, we can calculate the terrestrial radiative cooling power of the Si_3N_4 laminate nanoparticle films. We find that the predicted cooling power for the nanoparticle film on passivated silver is approximately 32.6, 61.1, and 82.4 W/m^2 when the film is at 30, 40, and 50 °C, respectively.

Next, we measure the angle-resolved radiative emission of the Si_3N_4 laminate nanoparticle films. We measure the films from 0 – 75° at 50 °C with an angle resolution of 2°. For the normalization, we also measure the gold and blackbody references from 0 – 75° at 50 °C. **Fig. 8.8** shows the normalized spectrally and angularly resolved radiative emission of a Si_3N_4 laminate nanoparticle film on silver with 5 nm SiO_2 passivation layer.

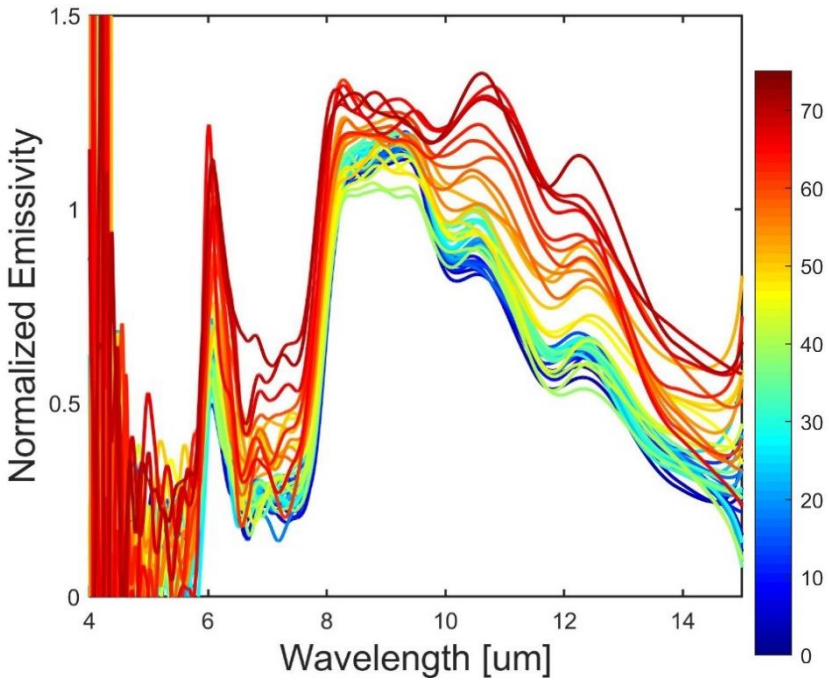

Figure 8.8. Normalized spectrally and angularly resolved radiative emission of a Si_3N_4 laminate nanoparticle film on silver with 5 nm SiO_2 passivation layer from 0 – 75° with 2° angular resolution at a temperature of 50 °C.

We note several features of the normalized emissivity from **Fig. 8.8**. First, we observe that the normalized emissivity exceeds 1 at certain wavelengths/angles. While this is not physically possible, it means experimentally that the laminate nanoparticle film measured a higher radiative emission signal at these wavelengths/angles compared to the blackbody reference. Second, we observe that as the angle increases, the spectral features broaden and flatten compared to the spectral shape at normal incidence. Combined, these observations suggest that the instrument alignment becomes less focused as the angle increases.

We also present the data in a polar plot to show the angular dependence of the radiative emission. From the characterization of nanoparticle films performed in Section II, we expect the film to be optically isotropic and Lambertian. We use the following equation to calculate the angularly resolved emissivity of the sample:

$$\epsilon_{Sample}(\theta, T) = \int_{8\ \mu m}^{14\ \mu m} \frac{E_{Sample}(\lambda, \theta, T) - E_{Au}(\lambda, \theta, T)}{E_{Blackbody}(\lambda, \theta, T) - E_{Au}(\lambda, \theta, T)} d\lambda \tag{8.2}$$

Using **Eq. 8.2**, we plot the angularly resolved emissivity of the Si_3N_4 laminate nanoparticle film on silver with 5 nm SiO_2 passivation layer in Fig. 8.8.

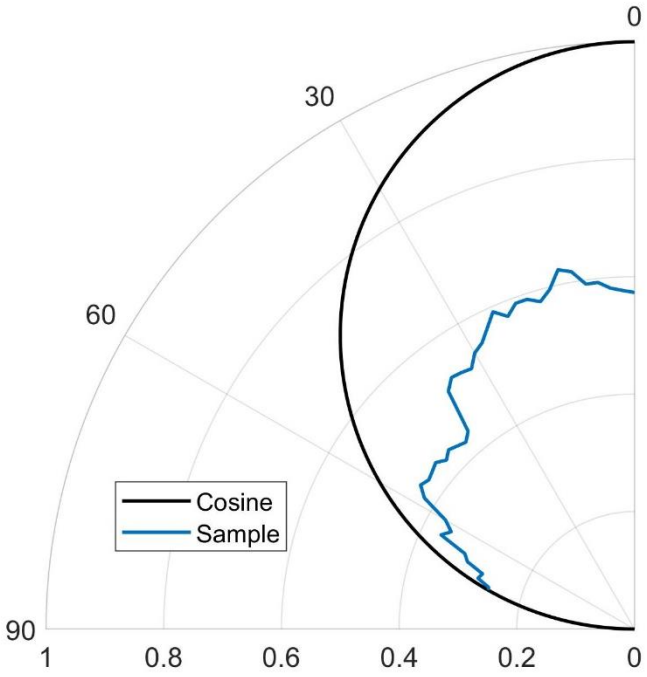

Figure 8.9. Normalized average angularly resolved radiative emission from 8 – 14 μm of a Si_3N_4 laminate nanoparticle film on silver with 5 nm SiO_2 passivation layer from 0 – 75° with 2° angular resolution at a temperature of 50 °C. Note that a cos(θ) factor is applied to the result. The Cosine curve represents the radiative intensity of a perfectly Lambertian blackbody.

We can see that in **Fig. 8.9**, the trend of the angularly resolve radiative emission of the nanoparticle film appears Lambertian. The reason the intensity of the film is less than the blackbody is because the films do not have an emissivity of 1 across the entire 8 – 14 μm wavelength regime. In other words, **Fig. 8.9** shows the angle-dependent average radiative emissivity of the nanoparticle films from 8 – 14 μm. To express the Lambertian behavior of the nanoparticle films in more detail, **Fig. 8.10** shows the angularly resolved emissivity of the Si_3N_4 laminate nanoparticle film at specific wavelengths.

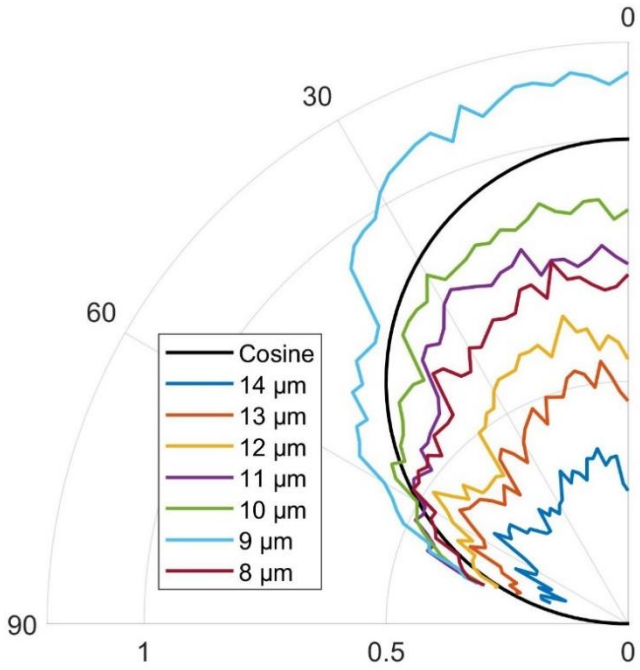

Figure 8.10. Normalized angularly resolved radiative emission at specific wavelengths of a Si_3N_4 laminate nanoparticle film on silver with 5 nm SiO_2 passivation layer from 0 – 75° with 2° angular resolution at a temperature of 50 °C. Note that a cos(θ) factor is applied to the result. The Cosine curve represents the radiative intensity of a perfectly Lambertian blackbody.

We can see from **Fig. 8.10** that the radiative emission of the nanoparticle films is strongest at 9 μm as expected. Furthermore, the radiative emission appears Lambertian since it follows the Cosine curve.

Next, we re-measure the angle-resolved radiative emission of the Si_3N_4 laminate nanoparticle films with higher angular resolution. We measure the films from 0 – 75° at 50 °C with an angle resolution of 1°. We also re-align the instrument since **Fig. 8.8** suggested that the instrument was not well-aligned at high angles. Once again, for the normalization, we must re-measure the gold and blackbody references from 0 – 75° at 50 °C. **Fig. 8.11** shows the normalized spectrally and angularly resolved radiative emission of a Si_3N_4 laminate nanoparticle film on silver with 5 nm SiO_2 passivation layer at these measurement parameters.

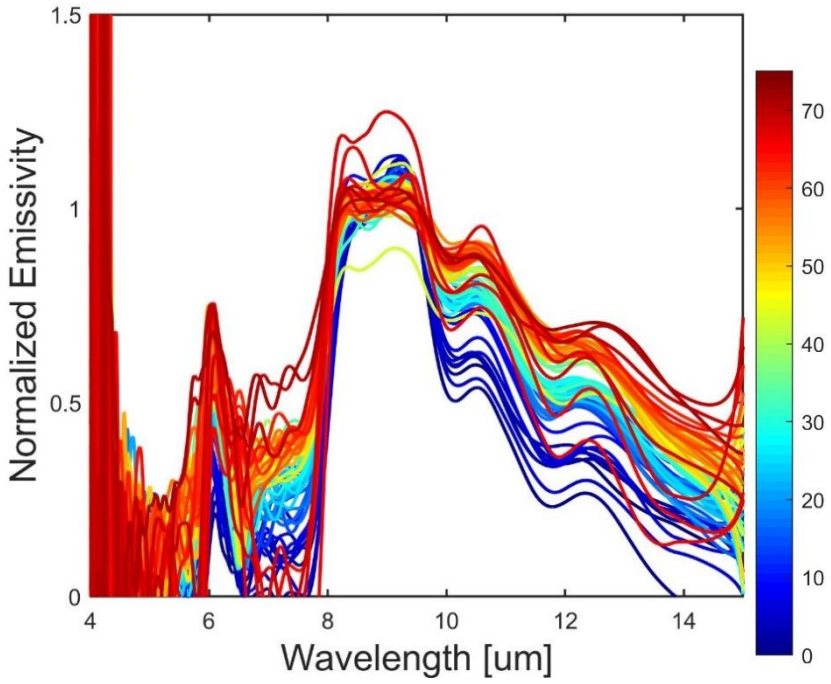

Figure 8.11. Normalized spectrally and angularly resolved radiative emission of a Si_3N_4 laminate nanoparticle film on silver with 5 nm SiO_2 passivation layer from 0 – 75° with 1° angular resolution at a temperature of 50 °C.

Comparing **Fig. 8.11** with **Fig. 8.8**, we observe that the normalized emissivity in **Fig. 8.11** is closer to 1 at most wavelengths/angles. We also observe that as the angle increases, the spectral features do not broaden and flatten as much compared to the previous measurement. These observations strongly suggest that the instrument alignment is improved compared to the previous measurement. However, these results suggest that the alignment can still be improved further.

Using **Eq. 8.2**, we calculate and plot the average angularly resolved emissivity of the measurement from 8 – 14 μm. **Fig. 8.12** shows the angularly resolved emissivity of the Si_3N_4 laminate nanoparticle film on silver with 5 nm SiO_2 passivation layer.

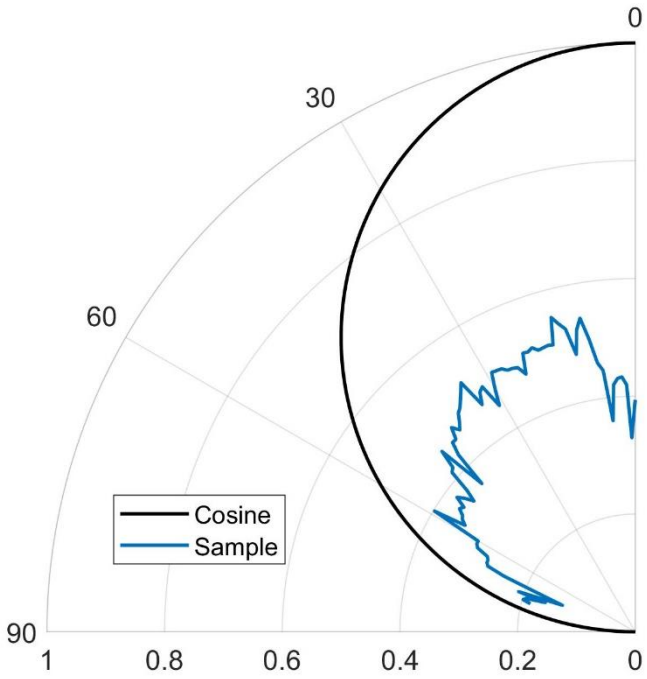

Figure 8.12. Normalized average angularly resolved radiative emission from 8 – 14 μm of a Si_3N_4 laminate nanoparticle film on silver with 5 nm SiO_2 passivation layer from 0 – 75° with 1° angular resolution at a temperature of 50 °C. Note that a cos(θ) factor is applied to the result. The Cosine curve represents the radiative intensity of a perfectly Lambertian blackbody.

We also plot the angularly resolved emissivity of the Si_3N_4 laminate nanoparticle film at specific wavelengths in **Fig. 8.13**.

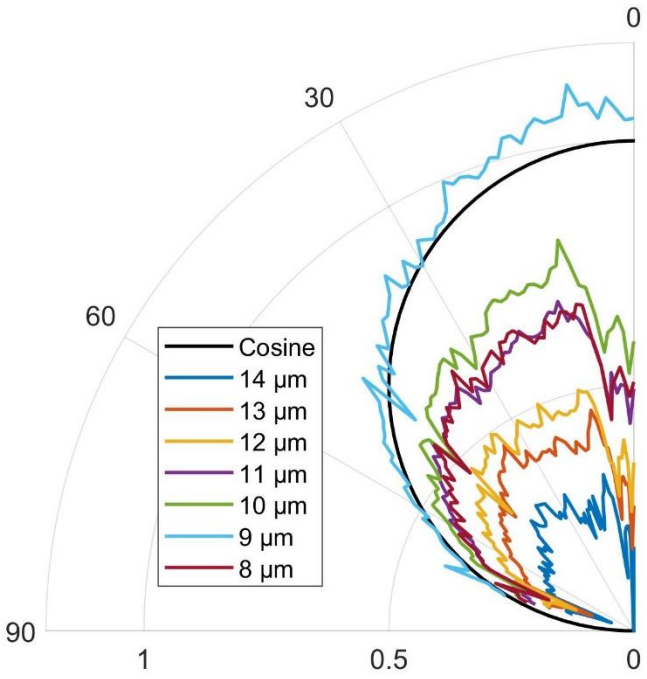

Figure 8.13. Normalized angularly resolved radiative emission at specific wavelengths of a Si_3N_4 laminate nanoparticle film on silver with 5 nm SiO_2 passivation layer from 0 – 75° with 1° angular resolution at a temperature of 50 °C. Note that a cos(θ) factor is applied to the result. The Cosine curve represents the radiative intensity of a perfectly Lambertian blackbody.

Once again, we can see from **Fig. 8.12 – 8.13** that the nanoparticle film exhibits Lambertian behavior, especially at its strongest emission peak at 9 μm. Interestingly, we notice a decrease in the intensity of the normalized radiative emission at angles near 0°. This is because we are observing the effect of the cryoshroud and aperture on the measurement.

To explain why we observe this effect, we note two observations. First, the measured blackbody radiative emission signal does not change with angle. Second, the measured gold radiative emission signal is highest at angles near 0°, and then it decreases to a low constant emission signal from approximately 7 – 75°. The blackbody radiative emission does not change with angle because the blackbody reference itself radiates at the highest possible emission strength at all wavelengths and angles; therefore, any external source of radiative thermal emission reflecting off the blackbody reference cannot overpower the intrinsic

radiative emission from the blackbody reference. Conversely, since the gold reference radiates at the lowest possible emission strength for all wavelengths and angles, it reflects all specular thermal radiative emission from the environment into the detector. From 7 – 75°, the gold reference faces the cryoshroud which has a low radiative emission compared to a room temperature ambient. This is why we observe the decrease in the measured gold radiative emission signal at these angles. However, from approximately 0 – 7°, the gold reference reflects room temperature ambient radiative emission from outside the chamber into the detector. This results in an increase in the measured gold radiative emission signal.

From **Eq. 1**, we can see that from 0 – 7°, the gold reference effectively raises the floor of the measurement, but the blackbody reference does not raise the ceiling of the measurement. As a result, the normalized radiative emission of a partially reflective sample will be lower than expected at these angles, which is the phenomenon that we observe in the measurement of the nanoparticle films in **Fig. 8.12 – 8.13**. Furthermore, we observe that this effect disappears at 9 μm because this is where the nanoparticle film behaves most like a blackbody. While this is correctable by introducing an extra term to the normalization, we leave this here as an observation of the systematic error of the instrument (To correct this, we must find and subtract out the ambient radiative thermal emission contribution to the signal. This can be done by measuring the radiative emission of a cryogenically cooled gold reference. This removes the radiative emission contribution from the gold reference and allows us to measure the total ambient radiative thermal emission reflecting into the detector.).

8.4.2 Si_3N_4 Laminate Nanoparticle Films

Following the preliminary results, we re-align the instrument and measure the spectrally and angularly resolved radiative emission of the Si_3N_4 laminate nanoparticle films from 0 – 75° with an angular resolution of 1°, and at temperatures of 30, 40, and 50 °C. As usual, we perform the same measurement on the gold and blackbody references. We increase the number of scans to 200 to improve the signal-to-noise ratio. **Fig. 8.14** shows the normalized spectrally and angularly resolved radiative emission of a Si_3N_4 laminate nanoparticle film on silver with 5 nm SiO_2 passivation layer with these measurement parameters. **Fig. 8.15** shows

the angularly resolved emissivity of the Si_3N_4 laminate nanoparticle film at specific wavelengths and across the 8 – 12 μm wavelength regime.

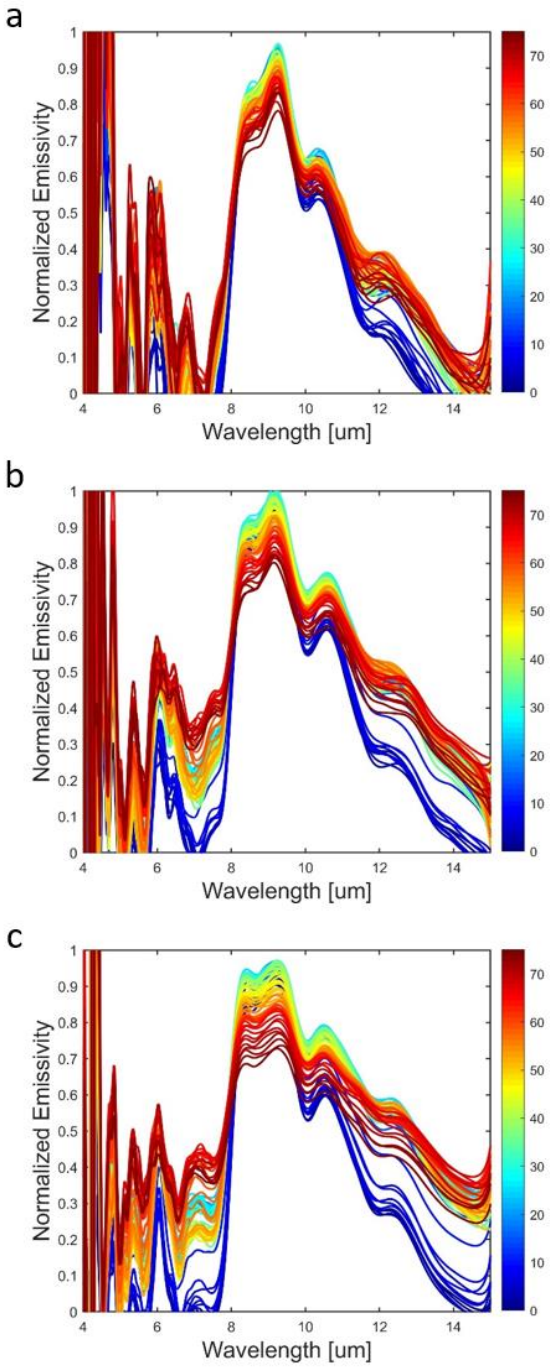

Figure 8.14. Normalized spectrally and angularly resolved radiative emission of a Si_3N_4 laminate nanoparticle film on silver with 5 nm SiO_2 passivation layer from 0 – 75° with 1° angular resolution at temperatures of (a) 30 °C, (b) 40 °C, and (c) 50 °C.

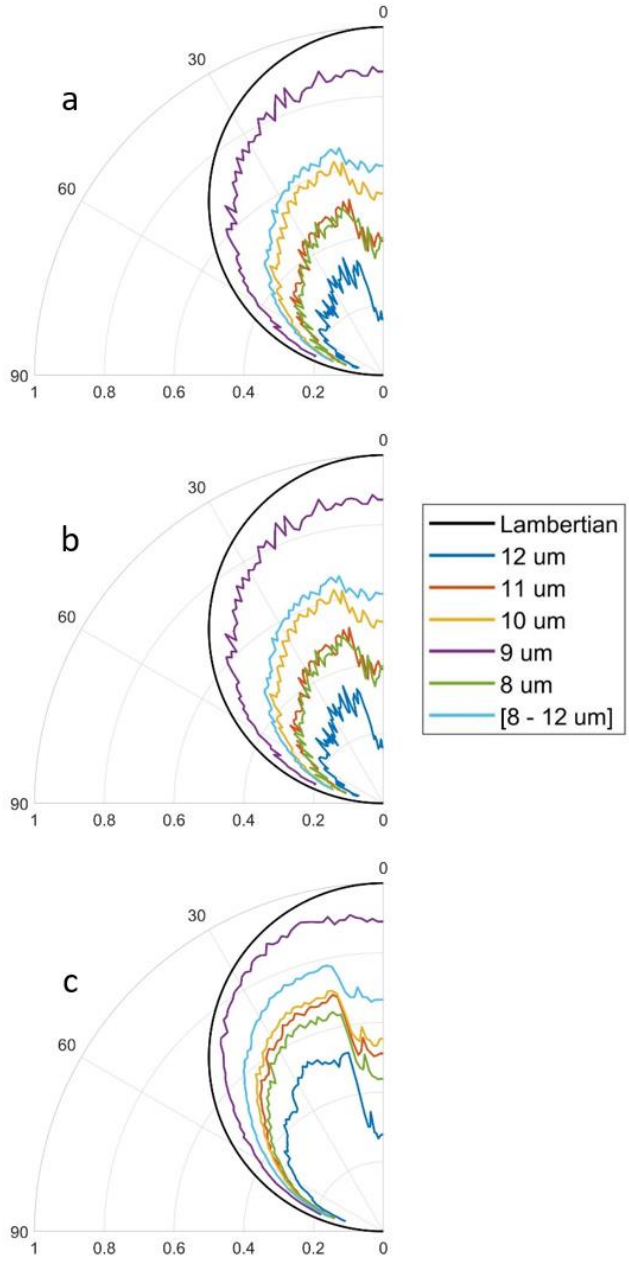

Figure 8.15. Normalized angularly resolved radiative emission of a Si_3N_4 laminate nanoparticle film on silver with 5 nm SiO_2 passivation layer from 0 – 75° with 1° angular resolution at temperatures of (a) 30 °C, (b) 40 °C, and (c) 50 °C. Shown is the radiative emission at specific wavelengths as well as the average radiative emission from 8 – 12 μm. Note that a cos(θ) factor is applied to the result. The Cosine curve represents the radiative intensity of a perfectly Lambertian blackbody.

From **Fig. 8.14**, we can see that the instrument alignment is significantly improved compared to the preliminary measurements. The instrument alignment appears improved because the normalized emissivity is below 1 for all wavelengths/angles as expected, and the spectral shape of the emissivity exhibits minimal flattening and broadening. In **Fig. 8.15**, we observe that the nanoparticle film exhibits Lambertian behavior as expected from the ellipsometry characterization of these nanoparticle films in Chapter 7. Once again, we observe the decrease in normalized radiative emission at angles near 0°. Compared to the preliminary measurements, we also observe in **Fig. 8.15** a better signal-to-noise ratio. Interestingly, we directly see the effect of sample temperature on the signal-to-noise ratio; as the temperature increases, the curves become smoother.

8.4.3 SiO_2 and Si_3N_4 Dense Laminate Thin Film

Using the same alignment and measurement setup from Section 8.4.2, we measure the spectrally and angularly resolved radiative emission of the SiO_2 and Si_3N_4 dense laminate thin film radiative cooling structures reported in Chapter 7 from 0 – 75° with an angular resolution of 1° and at temperatures of 30, 40, and 50 °C. We use the same gold and blackbody reference measurements from Section 8.4.2 to perform the normalization for these samples.

Fig. 8.16 shows the normalized spectrally and angularly resolved radiative emission of the two-layer 200 nm Si_3N_4 / 1200 nm SiO_2 dense thin film on silver substrate. **Fig. 8.17** shows the angularly resolved emissivity of the Si_3N_4 / SiO_2 dense thin film at specific wavelengths and across the 8 – 12 μm wavelength regime.

Fig. 8.18 shows the normalized spectrally and angularly resolved radiative emission of the two-layer 700 nm SiO_2 / 800 nm Si_3N_4 dense thin film on silver substrate. **Fig. 8.19** shows the angularly resolved emissivity of the SiO_2 / Si_3N_4 dense thin film at specific wavelengths and across the 8 – 12 μm wavelength regime.

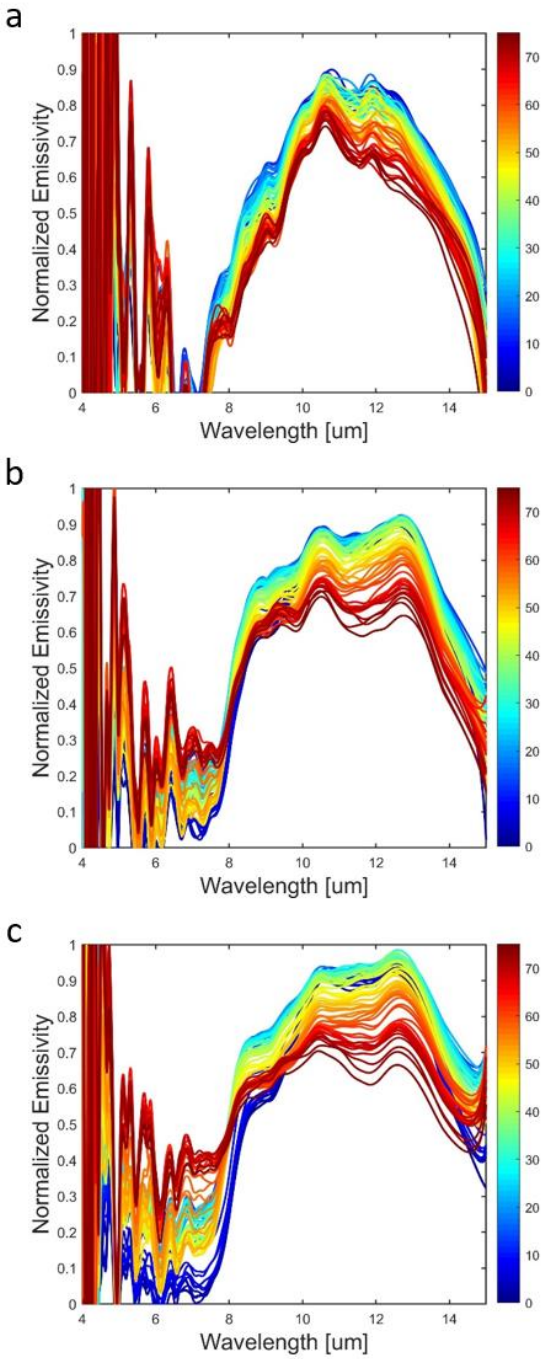

Figure 8.16. Normalized spectrally and angularly resolved radiative emission of a 200 nm Si_3N_4 / 1200 nm SiO_2 dense thin film radiative cooling structure on silver substrate from 0 – 75° with 1° angular resolution at temperatures of (a) 30 °C, (b) 40 °C, and (c) 50 °C.

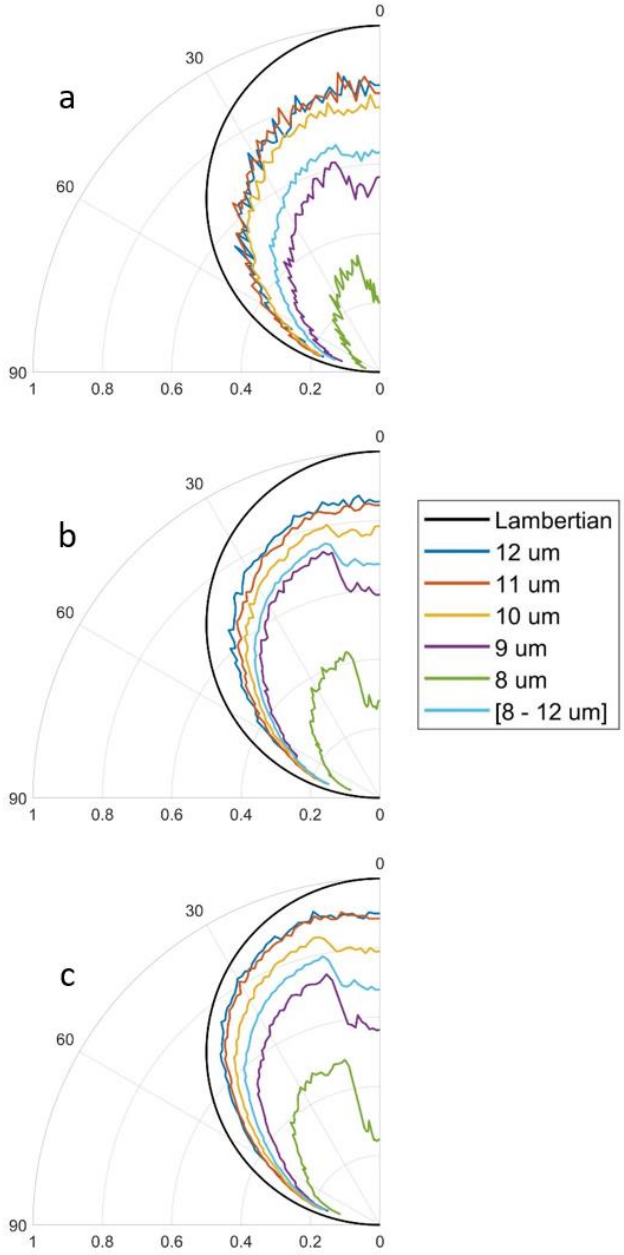

Figure 8.17. Normalized angularly resolved radiative emission of a 200 nm Si_3N_4 / 1200 nm SiO_2 dense thin film radiative cooling structure on silver substrate from 0 – 75° with 1° angular resolution at temperatures of (a) 30 °C, (b) 40 °C, and (c) 50 °C. Shown is the radiative emission at specific wavelengths as well as the average radiative emission from 8 – 12 μm. Note that a cos(θ) factor is applied to the result. The Cosine curve represents the radiative intensity of a perfectly Lambertian blackbody.

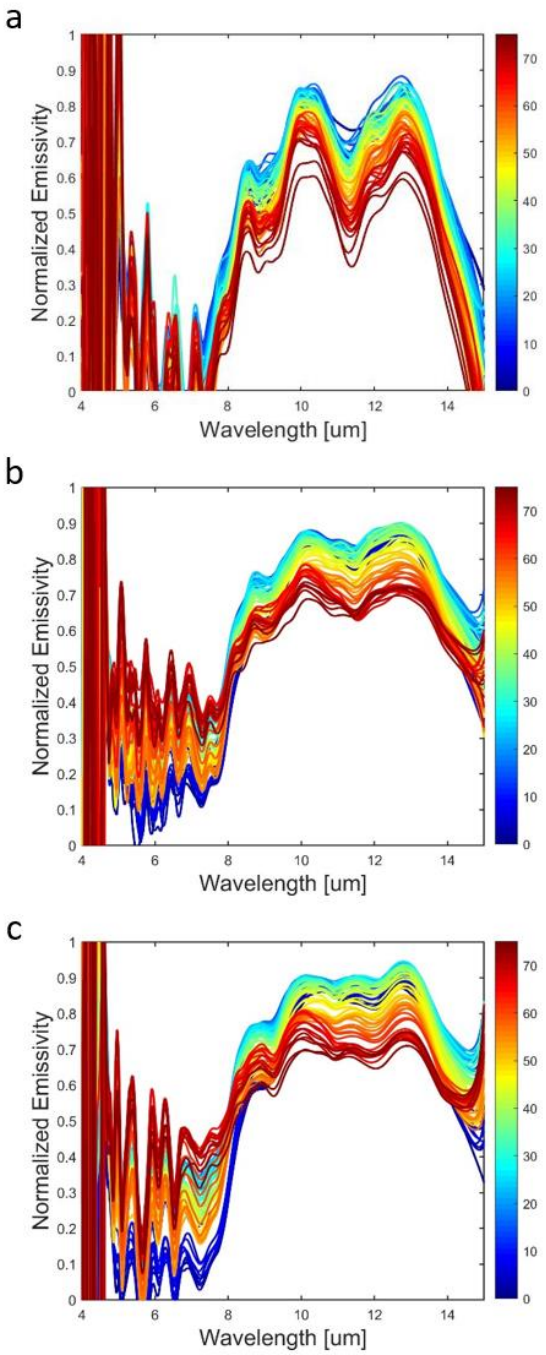

Figure 8.18. Normalized spectrally and angularly resolved radiative emission of a 700 nm SiO_2 / 800 nm Si_3N_4 dense thin film radiative cooling structure on silver substrate from 0 – 75° with 1° angular resolution at temperatures of (a) 30 °C, (b) 40 °C, and (c) 50 °C.

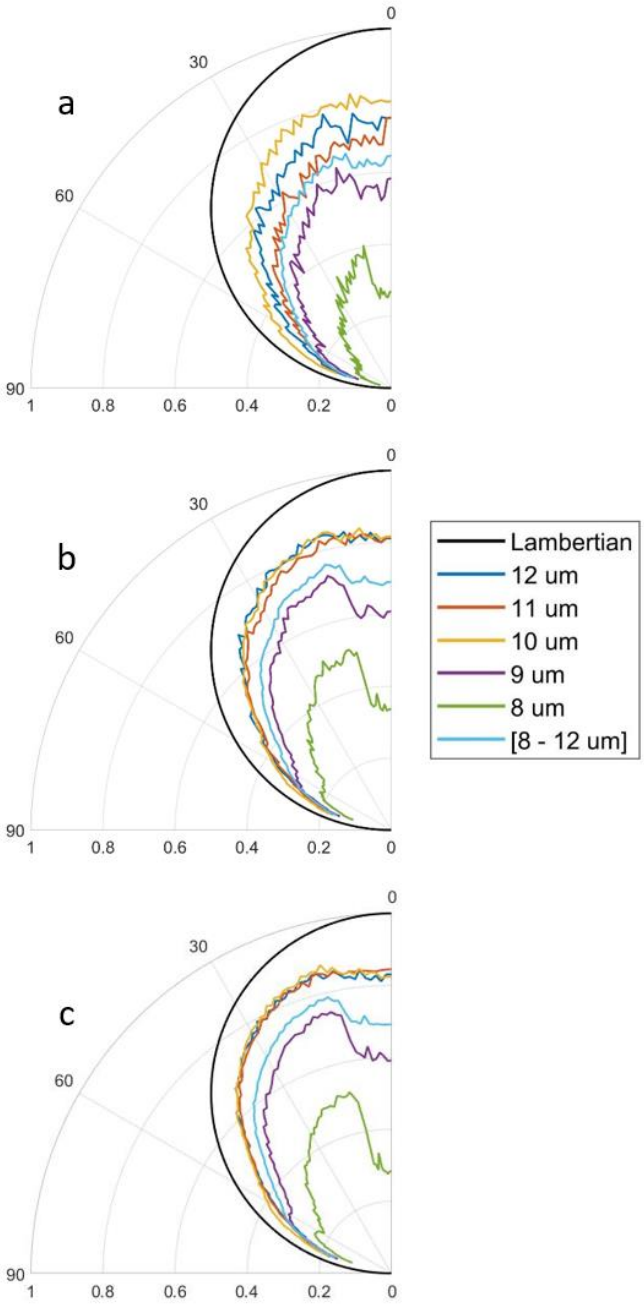

Figure 8.19. Normalized angularly resolved radiative emission of a 700 nm SiO_2 / 800 nm Si_3N_4 dense thin film radiative cooling structure on silver substrate from 0 – 75° with 1° angular resolution at temperatures of (a) 30 °C, (b) 40 °C, and (c) 50 °C. Shown is the radiative emission at specific wavelengths as well as the average radiative emission from 8 – 12 μm. Note that a cos(θ) factor is applied to the result. The Cosine curve represents the radiative intensity of a perfectly Lambertian blackbody.

From **Fig. 8.16 and 8.18**, we see that the spectral shape of the radiative emission of the two-layer dense laminate thin film structures measured by our instrument matches the spectral shape from the FT-IR reflectivity measurement of the structures (**Fig. 7.8 – 7.9**). Furthermore, **Fig. 8.17 and 8.19** show that the films exhibit Lambertian behavior as expected. Once again, we observe the decrease in normalized radiative emission at angles near 0°. We also see an increase in the signal-to-noise ratio as the sample temperature increases.

We note that the normalized spectrally and angularly resolved radiative emission for both structures at 30 °C appears different compared to 40 °C and 50 °C. We believe the cause of this phenomenon is similar to the explanation for the decrease in normalized radiative emission at angles near 0°. Essentially, the measured gold radiative emission signal is independent of temperature, while the measured blackbody radiative emission signal is strongly dependent on the temperature. Therefore, at 30 °C, the blackbody signal lowers the measurement ceiling, causing emission peaks to be accentuated in the normalization, because a small difference in the measured emission signal of the sample results in a larger difference in the normalized emissivity when the total measurement range is small. At 40 °C and 50 °C, the increase in the measurement ceiling results in an increased total measurement range which causes this effect to disappear.

Finally, we calculate the predicted terrestrial radiative cooling power of these radiative cooling structures using the equations and procedures discussed throughout Section II. **Table 8.1** lists the predicted terrestrial cooling power of each radiative cooling structure at 30, 40, and 50 °C. From these results, we can see that all the radiative cooling structures perform similarly.

Table 8.1. Calculated terrestrial radiative cooling power of various radiative cooling structures from spectrally and angularly resolved direct radiative emission measurements.

Radiative Cooling Structure	Temperature [°C]	Calculated Cooling Power [W/m^2]
Si_3N_4 Laminate Nanoparticle Film	30	20
	40	51
	50	76
200 nm Si_3N_4 / 1200 nm SiO_2 dense thin film	30	19
	40	47
	50	77
700 nm SiO_2 / 800 nm Si_3N_4 dense thin film	30	16
	40	47
	50	75

8.5 Summary and Conclusion

In this chapter, we presented a new instrument for simultaneous measurement of the spectrally and angularly resolved direct radiative emission and surface temperature of radiative cooling structures. We reported the design specifications and considerations which gave rise to the instrument reported. We discussed the operating procedure of the instrument, including the alignment process and measurement parameters. Using the instrument, we presented direct radiative emission results for the Si_3N_4 laminate nanoparticle film and the two-layer SiO_2 and Si_3N_4 dense laminate thin film radiative cooling structures. From the results, we showed that the instrument can reproducibly measure the thermal radiative emission of the structures and that the results match well with the FT-IR reflectivity measurements for these same structures. Furthermore, we showed directly that the structures exhibit Lambertian thermal emission as expected. We discussed limitations with the current instrument setup. Finally, using the direct radiative emission results, we calculated the predicted cooling power of each of these radiative cooling structures. This chapter concludes Section III: Direct Spectrally and Angularly Resolved Radiative Emission Measurements.

8.6 Supplemental Information

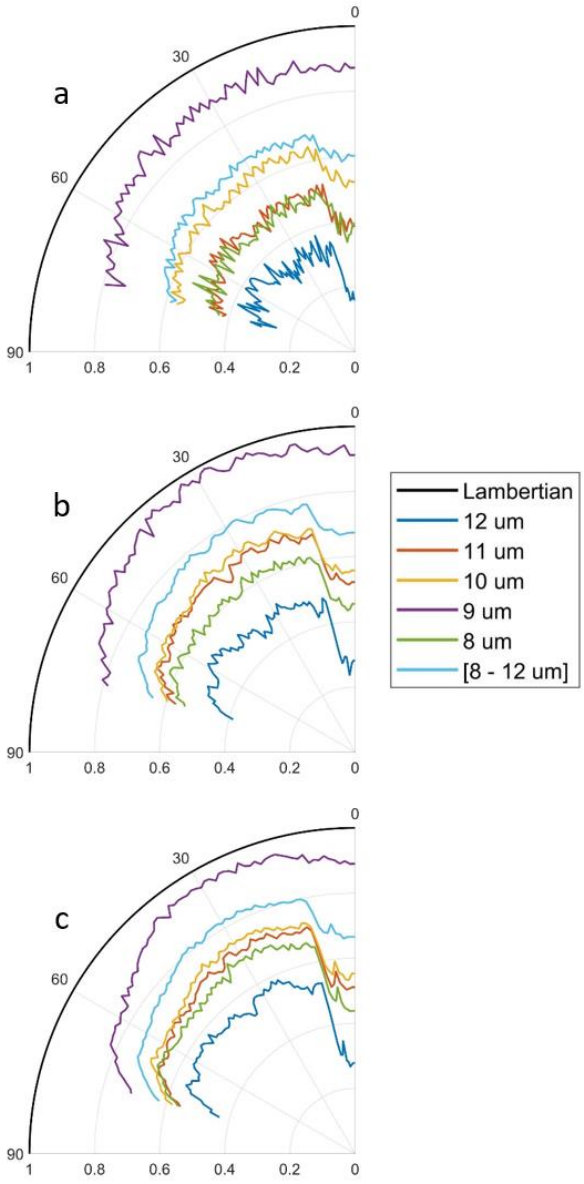

Figure S8.1. Normalized angularly resolved radiative emission of a Si_3N_4 laminate nanoparticle film on silver with 5 nm SiO_2 passivation layer from 0 – 75° with 1° angular resolution at temperatures of (a) 30 °C, (b) 40 °C, and (c) 50 °C. Shown is the radiative emission at specific wavelengths as well as the average radiative emission from 8 – 12 μm. The Cosine curve represents the radiative intensity of a perfectly Lambertian blackbody.

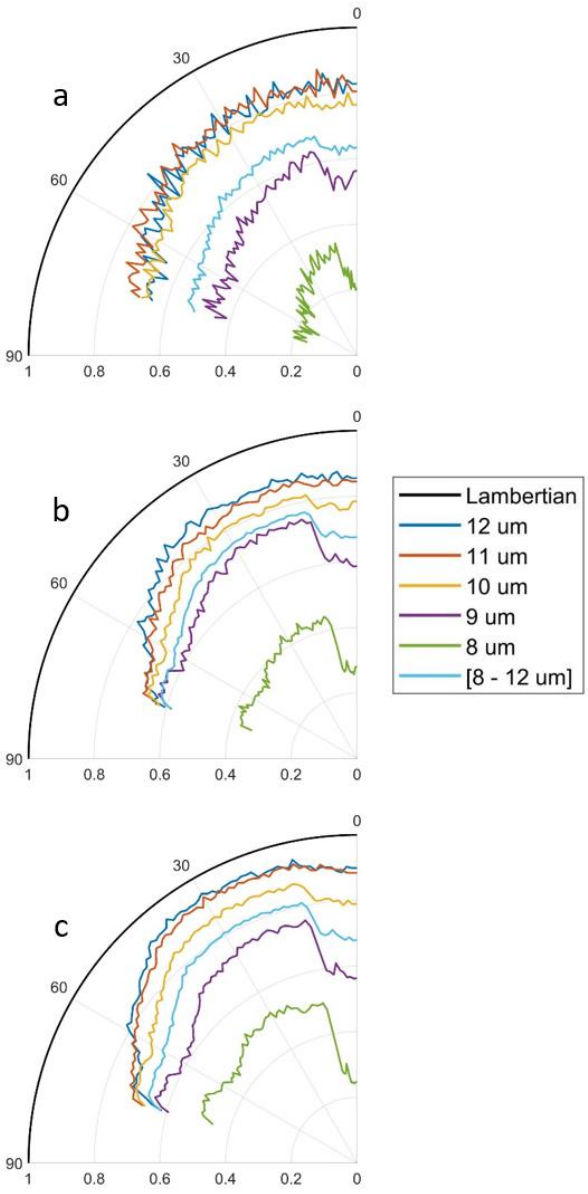

Figure S8.2. Normalized angularly resolved radiative emission of a 200 nm Si_3N_4 / 1200 nm SiO_2 dense thin film radiative cooling structure on silver substrate from 0 – 75° with 1° angular resolution at temperatures of (a) 30 °C, (b) 40 °C, and (c) 50 °C. Shown is the radiative emission at specific wavelengths as well as the average radiative emission from 8 – 12 μm. The Cosine curve represents the radiative intensity of a perfectly Lambertian blackbody.

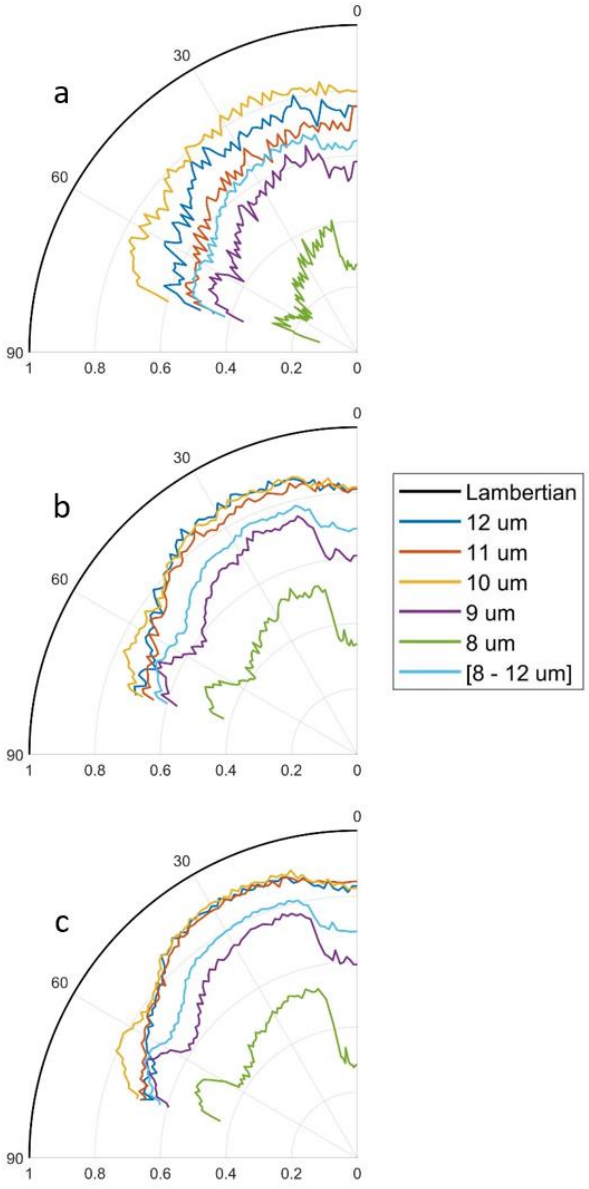

Figure S8.3. Normalized angularly resolved radiative emission of a 700 nm SiO_2 / 800 nm Si_3N_4 dense thin film radiative cooling structure on silver substrate from 0 – 75° with 1° angular resolution at temperatures of (a) 30 °C, (b) 40 °C, and (c) 50 °C. Shown is the radiative emission at specific wavelengths as well as the average radiative emission from 8 – 12 μm. The Cosine curve represents the radiative intensity of a perfectly Lambertian blackbody.

Chapter 9

CLOSING REMARKS

9.1 Summary

This thesis has presented work on exploring and advancing the use of photonics for tackling current sustainability challenges.

In Section I, we presented work on the development, fabrication, and characterization of a metal AR coated selective solar absorber designed to efficiently collect and convert solar energy into usable thermal energy. The fabricated absorber had a solar absorptivity of 49.2% and an infrared reflectivity of 11.7% with a maximum theoretical temperature of 249 °C under 1 sun intensity. We discussed the design considerations and challenges involved in building a scalable solar driven photothermal reactor for thermocatalytic reactions, and we reported work on the thermal analysis and construction of such a system. At the same time, we explored Ni-catalyzed ethylene oligomerization as an alternative low-energy direct pathway for synthesizing sustainable aviation fuels from CO_2 compared to current industrial methods. At the intersection of this work between photonics, thermal design, and thermocatalysis, we demonstrated the synthesis of hydrocarbon fuels with carbon chain lengths ranging from C_6 – C_{26} from ethylene gas, powered completely by sunlight. Under 3 sun intensity (3000 W/m^2), we reported a batch mode homogeneous Ni-catalyzed ethylene oligomerization producing C_6 – C_{26} carbon chain length 1-alkenes with an ethylene conversion efficiency of 18.5%, and a flow mode heterogeneous Ni-catalyzed ethylene oligomerization producing butenes and hexenes with an ethylene conversion efficiency of 25%. This work introduces a new selective solar absorber and solar driven photothermal reactor design, and it is one of the earliest demonstrations of solar driven ethylene oligomerization for sustainable aviation fuel synthesis.

In Section II, we presented work on the characterization of laminate nanoparticle films deposited from a nonthermal plasma reactor. Optically, we showed that laminate

nanoparticle films were accurately represented by the Bruggeman effective medium approximation. Based on this observation, we extended the use of laminate nanoparticle films as designs for efficient terrestrial daytime radiative coolers, or selective radiators which passively cool below ambient by emitting infrared thermal radiation directly into space. Exploiting the nanoparticle film properties, we designed and optimized two-layer SiO_2 and Si_3N_4 laminate nanoparticle films for radiative cooling, and we reported design parameters for nanoparticle film structures which achieve cooling powers around 70 W/m^2, competitive with other leading reports. Experimentally, we characterized and fabricated Si_3N_4 laminate nanoparticle film and two-layer SiO_2 and Si_3N_4 dense laminate thin film radiative cooling structures with cooling powers near 40 W/m^2. This work introduces a new scalable laminate nanoparticle film radiative cooling design fabricated using nonthermal plasma synthesis and competitive with leading radiative cooling reports, and it reports the fabrication and characterization of these structures.

In Section III, we presented work on the construction of a new instrument for spectrally and angularly resolved direct radiative emission measurements which facilitates cross-comparisons between radiative cooling reports. We recognized a need for a controlled ambient and measurement procedure, and we reported a new instrument to fulfill these needs. Using this instrument, we directly observed the radiative thermal emission of our Si_3N_4 laminate nanoparticle film and two-layer SiO_2 and Si_3N_4 dense laminate thin film radiative cooling structures near room temperature. Significantly, this work also presents a new instrument to aid the study of thermal emission of photonic structures outside of radiative cooling applications. The ability to measure both spectrally and angularly resolved emission means that the instrument can be used to study photonic structures which exhibit anisotropic, non-Lambertian, directed, or other interesting thermal emission properties.

9.2 Outlook

Despite the contributions reported in this thesis, many improvements and challenges remain to be addressed and explored in the future.

For the photothermal reactor, improvements can be made to its thermal performance. In the case of the selective solar absorber, work can be done to improve either the solar absorptivity or decreasing the infrared reflectivity of the design or improve the fabrication process so that the fabricated wafer optical properties match the theoretical optical properties better. For the reactor itself, much heat is currently lost to the edges due to its small-scale construction. Future improvements to the design can better thermally isolate the selective solar absorber and thermocatalytic reaction zone. Improvements can include adding another vacuum layer below the thermocatalytic zone, decreasing the distance between the selective solar absorber and the thermocatalytic reaction zone, or coupling the selective solar absorber and catalyst together in the same space. The thermal mass of the reactor can also be decreased to improve the heating rate. These improvements would increase the accessible temperature at the catalyst site, enabling higher ethylene conversion efficiency or even unlock new reactions such as hydroformylation and Fischer-Tropsch which have higher temperature requirements. Finally, future work on this project may explore coupling the photothermal reactor to a solar driven photoelectrochemical (PEC) cell in a tandem setup; in such a setup, CO_2 would be reduced to ethylene gas in the PEC cell, and then the effluent ethylene gas would be converted to hydrocarbon fuels in the photothermal reactor. This would demonstrate a completely solar driven pathway from CO_2 to sustainable aviation fuels.

For the direct radiative emission instrument, significant improvements can be made towards expediting its operation. First, the motorized rotary shaft and FT-IR spectrometer measurements can be automated to create automated batch measurements. Currently, each measurement is started manually, and the motorized rotary shaft is programmed manually for each angle. Second, a multi-axis motorized stage can be introduced to the system; this would greatly simplify the current sample mounting and alignment procedure which is done manually. Third, the use of a multi-axis stage would allow for multiple samples to be mounted inside the chamber simultaneous. By translating the stage laterally, multiple samples can be measured in a single day operation without needing to vent/pump the chamber or warm/cool the cryoshroud. Currently, the gold reference, blackbody reference,

and sample all need to be mounted and measured separately, with each involving its own vent/pump and warm/cool cycle.

Improvements can also be made to enhance the capabilities of the instrument. A bandpass filter and a solar simulator can be introduced into the instrument to stimulate a terrestrial environment. Currently, the instrument with its cryoshroud simulates a controlled space environment. By introducing a solar simulator source and a bandpass filter into the vacuum chamber, we can create a controlled daytime terrestrial environment for measuring the radiative power and equilibrium surface temperature of radiative cooling structures. In this case, the solar simulator would simulate sunlight incident on the sample and the bandpass filter would simulate the atmospheric transmission window. This was a major direction in the original instrument design, but it was ultimately faced with numerous engineering challenges which prevented it from being implemented into the current instrument setup. Particularly challenging was importing a solar source into the vacuum chamber which could provide both a spectrally accurate spectrum and an intensity of 1 sun (1000 W/m^2).

Finally, the instrument can be improved to detect radiative emission from samples at temperatures below room temperature. This is also a particularly challenging improvement because it requires the entire optical setup to be cryogenically cooled. This is because the radiative thermal emission from the ambient environment and the components of the FT-IR spectrometer itself currently overpower any radiative emission signal from samples below room temperature. If the instrument were improved such that it could detect radiative emission below room temperature and simulate a controlled daytime terrestrial environment at the same time, then one could measure the surface temperature and direct radiative emission of a radiative cooling structure from room temperature all the way down to its minimum equilibrium temperature, a feat which remains undemonstrated in literature.

BIBLIOGRAPHY

1. Liu, Z., Deng, Z., Davis, S. & Ciais, P. Monitoring global carbon emissions in 2022. *Nat. Rev. Earth Environ.* **4**, 205–206 (2023).
2. Lindsey, R. & Dahlman, L. Climate change: Global temperature. *Clim. Gov* **16**, (2020).
3. *Annual 2023 Global Climate Report*. https://www.ncei.noaa.gov/access/monitoring/monthly-report/global/202313.
4. *Understanding the Science of Ocean and Coastal Acidification*. https://www.epa.gov/ocean-acidification/understanding-science-ocean-and-coastalacidification.
5. Tarakanov, V. How carbon emissions acidify our ocean. *IAEA Bull. Online* **63**, 22–23 (2022).
6. *Paris Agreement*. https://unfccc.int/sites/default/files/english_paris_agreement.pdf (2015).
7. Armstrong McKay, D. I., et al. Exceeding 1.5 C global warming could trigger multiple climate tipping points. *Science* **377**, eabn7950 (2022).
8. Rogelj, J., et al. Scenarios towards limiting global mean temperature increase below 1.5 C. *Nat. Clim. Change* **8**, 325–332 (2018).
9. *Climate Change 2022: Mitigation of Climate Change*. https://www.ipcc.ch/report/ar6/wg3/?itid=lk_inline_enhanced-template.
10. Chen, L., et al. Strategies to achieve a carbon neutral society: a review. *Environ. Chem. Lett.* **20**, 2277–2310 (2022).

11. Farrelly, D. J., Everard, C. D., Fagan, C. C. & McDonnell, K. P. Carbon sequestration and the role of biological carbon mitigation: a review. *Renew. Sustain. Energy Rev.* **21**, 712–727 (2013).
12. Wimbadi, R. W. & Djalante, R. From decarbonization to low carbon development and transition: A systematic literature review of the conceptualization of moving toward net-zero carbon dioxide emission (1995–2019). *J. Clean. Prod.* **256**, 120307 (2020).
13. Olhoff, A. & Christensen, J. M. The Emissions Gap Report 2017: A UNEP Synthesis Report. (2017).
14. Sengupta, M., et al. The national solar radiation data base (NSRDB). *Renew. Sustain. Energy Rev.* **89**, 51–60 (2018).
15. ASTM G173-03. G173-03, Standard Tables for Reference Solar Spectral Irradiances: Direct Normal and Hemispherical on 37 Tilted Surface. (2020).
16. Gupta, R. B. *Hydrogen Fuel: Production, Transport, and Storage*. (CRC press, 2008).
17. Evangelisti, L., Vollaro, R. D. L. & Asdrubali, F. Latest advances on solar thermal collectors: A comprehensive review. *Renew. Sustain. Energy Rev.* **114**, 109318 (2019).
18. Bermel, P., Lee, J., Joannopoulos, J. D., Celanovic, I. & Soljačić, M. Selective solar absorbers. *Annu. Rev. Heat Transf.* **15**, (2012).
19. Buker, M. S. & Riffat, S. B. Building integrated solar thermal collectors–A review. *Renew. Sustain. Energy Rev.* **51**, 327–346 (2015).
20. Zhang, J., et al. Solar selective absorber for emerging sustainable applications. *Adv. Energy Sustain. Res.* **3**, 2100195 (2022).
21. Wang, Z., et al. Pathways and challenges for efficient solar-thermal desalination. *Sci. Adv.* **5**, eaax0763 (2019).

22. Li, Y., Lin, C., Huang, J., Chi, C. & Huang, B. Spectrally selective absorbers/emitters for solar steam generation and radiative cooling-enabled atmospheric water harvesting. *Glob. Chall.* **5**, 2000058 (2021).

23. Wang, H., Chang, J.-Y., Yang, Y. & Wang, L. Performance analysis of solar thermophotovoltaic conversion enhanced by selective metamaterial absorbers and emitters. *Int. J. Heat Mass Transf.* **98**, 788–798 (2016).

24. Bhatt, R., Kravchenko, I. & Gupta, M. High-efficiency solar thermophotovoltaic system using a nanostructure-based selective emitter. *Sol. Energy* **197**, 538–545 (2020).

25. Cheruvu, P., Kumar, V. P. & Barshilia, H. C. Experimental analysis and evaluation of a vacuum enclosed concentrated solar thermoelectric generator coupled with a spectrally selective absorber coating. *Int. J. Sustain. Energy* **37**, 782–798 (2018).

26. Kraemer, D., et al. High-performance flat-panel solar thermoelectric generators with high thermal concentration. *Nat. Mater.* **10**, 532–538 (2011).

27. Jin, H., Hong, H., Sui, J. & Liu, Q. Fundamental study of novel mid-and low-temperature solar thermochemical energy conversion. *Sci. China Ser. E Technol. Sci.* **52**, 1135–1152 (2009).

28. Li, W. & Hao, Y. Efficient solar power generation combining photovoltaics and mid-/low-temperature methanol thermochemistry. *Appl. Energy* **202**, 377–385 (2017).

29. Steinfeld, A. & Palumbo, R. Solar thermochemical process technology. *Encycl. Phys. Sci. Technol.* **15**, 237–56 (2001).

30. Herron, J. A., Kim, J., Upadhye, A. A., Huber, G. W. & Maravelias, C. T. A general framework for the assessment of solar fuel technologies. *Energy Environ. Sci.* **8**, 126–157 (2015).

31. Ghoussoub, M., Xia, M., Duchesne, P. N., Segal, D. & Ozin, G. Principles of photothermal gas-phase heterogeneous CO 2 catalysis. *Energy Environ. Sci.* **12**, 1122–1142 (2019).
32. Agrawal, R., Singh, N. R., Ribeiro, F. H. & Delgass, W. N. Sustainable fuel for the transportation sector. *Proc. Natl. Acad. Sci.* **104**, 4828–4833 (2007).
33. Janaun, J. & Ellis, N. Perspectives on biodiesel as a sustainable fuel. *Renew. Sustain. Energy Rev.* **14**, 1312–1320 (2010).
34. Cabrera, E. & de Sousa, J. M. M. Use of sustainable fuels in aviation—a review. *Energies* **15**, 2440 (2022).
35. Holladay, J., Abdullah, Z. & Heyne, J. Sustainable aviation fuel: Review of technical pathways. (2020).
36. Lee, D. S., et al. The contribution of global aviation to anthropogenic climate forcing for 2000 to 2018. *Atmos. Environ.* **244**, 117834 (2021).
37. Gao, J., Shiong, S. C. S. & Liu, Y. Reduction of CO2 to chemicals and Fuels: Thermocatalysis versus electrocatalysis. *Chem. Eng. J.* 145033 (2023).
38. Betz, M., Fuchs, C., Zevaco, T. A., Arnold, U. & Sauer, J. Production of hydrocarbon fuels by heterogeneously catalyzed oligomerization of ethylene: Tuning of the product distribution. *Biomass Bioenergy* **166**, 106595 (2022).
39. Zhao, B., Hu, M., Ao, X., Chen, N. & Pei, G. Radiative cooling: A review of fundamentals, materials, applications, and prospects. *Appl. Energy* **236**, 489–513 (2019).
40. Hossain, M. M. & Gu, M. Radiative cooling: principles, progress, and potentials. *Adv. Sci.* **3**, 1500360 (2016).

41. Fan, S. & Li, W. Photonics and thermodynamics concepts in radiative cooling. *Nat. Photonics* **16**, 182–190 (2022).

42. Bliss Jr, R. W. Atmospheric radiation near the surface of the ground: a summary for engineers. *Sol. Energy* **5**, 103–120 (1961).

43. *U.S. Standard Atmosphere, 1976*.

44. Catalanotti, S., et al. The radiative cooling of selective surfaces. *Sol. Energy* **17**, 83–89 (1975).

45. Bohren, C. F. & Huffman, D. R. *Absorption and Scattering of Light by Small Particles*. (John Wiley & Sons, 2008).

46. Choy, T. C. *Effective Medium Theory: Principles and Applications*. vol. 165 (Oxford University Press, 2015).

47. Sihvola, A. Homogenization principles and effect of mixing on dielectric behavior. *Photonics Nanostructures-Fundam. Appl.* **11**, 364–373 (2013).

48. Shivola, A. H. Self-consistency aspects of dielectric mixing theories. *IEEE Trans. Geosci. Remote Sens.* **27**, 403–415 (1989).

49. Chýlek, P., Srivastava, V., Pinnick, R. G. & Wang, R. Scattering of electromagnetic waves by composite spherical particles: experiment and effective medium approximations. *Appl. Opt.* **27**, 2396–2404 (1988).

50. Kortshagen, U. Nonthermal plasma synthesis of semiconductor nanocrystals. *J. Phys. Appl. Phys.* **42**, 113001 (2009).

51. Mangolini, L., Thimsen, E. & Kortshagen, U. High-yield plasma synthesis of luminescent silicon nanocrystals. *Nano Lett.* **5**, 655–659 (2005).

52. Kortshagen, U. R., et al. Nonthermal plasma synthesis of nanocrystals: fundamental principles, materials, and applications. *Chem. Rev.* **116**, 11061–11127 (2016).

53. Zhang, K., et al. A review on thermal stability and high temperature induced ageing mechanisms of solar absorber coatings. *Renew. Sustain. Energy Rev.* **67**, 1282–1299 (2017).

54. Cao, F., McEnaney, K., Chen, G. & Ren, Z. A review of cermet-based spectrally selective solar absorbers. *Energy Environ. Sci.* **7**, 1615–1627 (2014).

55. Yu, P., et al. Ultra-wideband solar absorber based on refractory titanium metal. *Renew. Energy* **158**, 227–235 (2020).

56. Thomas, N. H., Chen, Z., Fan, S. & Minnich, A. J. Semiconductor-based multilayer selective solar absorber for unconcentrated solar thermal energy conversion. *Sci. Rep.* **7**, 5362 (2017).

57. McDonald, G. E. Spectral reflectance properties of black chrome for use as a solar selective coating. *Sol. Energy* **17**, 119–122 (1975).

58. Yin, Y., Pan, Y., Hang, L., McKenzie, D. & Bilek, M. Direct current reactive sputtering Cr–Cr2O3 cermet solar selective surfaces for solar hot water applications. *Thin Solid Films* **517**, 1601–1606 (2009).

59. Barshilia, H. C., Selvakumar, N., Vignesh, G., Rajam, K. & Biswas, A. Optical properties and thermal stability of pulsed-sputter-deposited AlxOy/Al/AlxOy multilayer absorber coatings. *Sol. Energy Mater. Sol. Cells* **93**, 315–323 (2009).

60. Azad, A. K., et al. Metasurface broadband solar absorber. *Sci. Rep.* **6**, 20347 (2016).

61. Chou, J. B., et al. Enabling ideal selective solar absorption with 2D metallic dielectric photonic crystals. (2014).

62. Li, P., et al. Large-Scale Nanophotonic Solar Selective Absorbers for High-Efficiency Solar Thermal Energy Conversion. *Adv. Mater. Deerfield Beach Fla* **27**, 4585–4591 (2015).

63. Robitaille, P.-M. Kirchhoff's law of thermal emission: 150 years. *Progr Phys* **4**, 3–13 (2009).

64. Byrnes, S. J. Multilayer optical calculations. *ArXiv Prepr. ArXiv160302720* (2016).

65. Hosono, H. & Ueda, K. Transparent conductive oxides. *Springer Handb. Electron. Photonic Mater.* 1–1 (2017).

66. Raut, H. K., Ganesh, V. A., Nair, A. S. & Ramakrishna, S. Anti-reflective coatings: A critical, in-depth review. *Energy Environ. Sci.* **4**, 3779–3804 (2011).

67. Chen, W., Thoreson, M. D., Ishii, S., Kildishev, A. V. & Shalaev, V. M. Ultra-thin ultra-smooth and low-loss silver films on a germanium wetting layer. *Opt. Express* **18**, 5124–5134 (2010).

68. Jeong, E., et al. Minimizing optical loss in ultrathin Ag films based on Ge wetting layer: Insights on Ge-mediated Ag growth. *Appl. Surf. Sci.* **528**, 146989 (2020).

69. Ciesielski, A., et al. Evidence of germanium segregation in gold thin films. *Surf. Sci.* **674**, 73–78 (2018).

70. Logeeswaran, V., et al. Ultrasmooth silver thin films deposited with a germanium nucleation layer. *Nano Lett.* **9**, 178–182 (2009).

71. Fan, W. K. & Tahir, M. Recent developments in photothermal reactors with understanding on the role of light/heat for CO2 hydrogenation to fuels: A review. *Chem. Eng. J.* **427**, 131617 (2022).

72. Khan, A. A. & Tahir, M. Recent advancements in engineering approach towards design of photo-reactors for selective photocatalytic CO2 reduction to renewable fuels. *J. CO2 Util.* **29**, 205–239 (2019).

73. Song, C., et al. Photothermal conversion of CO2 with tunable selectivity using Fe-based catalysts: from oxide to carbide. *ACS Catal.* **10**, 10364–10374 (2020).

74. Chen, X., et al. MOF-templated preparation of highly dispersed Co/Al2O3 composite as the photothermal catalyst with high solar-to-fuel efficiency for CO2 methanation. *ACS Appl. Mater. Interfaces* **12**, 39304–39317 (2020).

75. Liu, L., et al. Sunlight-assisted hydrogenation of CO2 into ethanol and C2+ hydrocarbons by sodium-promoted Co@ C nanocomposites. *Appl. Catal. B Environ.* **235**, 186–196 (2018).

76. Chen, G., et al. Alumina-supported CoFe alloy catalysts derived from layered-double-hydroxide nanosheets for efficient photothermal CO2 hydrogenation to hydrocarbons. *Adv. Mater.* **30**, 1704663 (2018).

77. Kho, E. T., Jantarang, S., Zheng, Z., Scott, J. & Amal, R. Harnessing the beneficial attributes of ceria and titania in a mixed-oxide support for nickel-catalyzed photothermal CO2 methanation. *Engineering* **3**, 393–401 (2017).

78. Tahir, B., Tahir, M. & Amin, N. S. Performance analysis of monolith photoreactor for CO2 reduction with H2. *Energy Convers. Manag.* **90**, 272–281 (2015).

79. Cai, M.-J., Li, C.-R. & He, L. Enhancing photothermal CO2 catalysis by thermal insulating substrates. *Rare Met.* **39**, 881–886 (2020).

80. Meng, X., et al. Photothermal conversion of CO2 into CH4 with H2 over group VIII nanocatalysts: an alternative approach for solar fuel production. *Angew. Chem. Int. Ed.* **53**, 11478–11482 (2014).

81. Li, Y., et al. Selective light absorber-assisted single nickel atom catalysts for ambient sunlight-driven CO2 methanation. *Nat. Commun.* **10**, 2359 (2019).

82. Low, J., Zhang, L., Zhu, B., Liu, Z. & Yu, J. TiO2 photonic crystals with localized surface photothermal effect and enhanced photocatalytic CO2 reduction activity. *ACS Sustain. Chem. Eng.* **6**, 15653–15661 (2018).

83. Wang, Z., Song, H., Liu, H. & Ye, J. Coupling of solar energy and thermal energy for carbon dioxide reduction: status and prospects. *Angew. Chem. Int. Ed.* **59**, 8016–8035 (2020).

84. Tahir, M. Photocatalytic carbon dioxide reduction to fuels in continuous flow monolith photoreactor using montmorillonite dispersed Fe/TiO2 nanocatalyst. *J. Clean. Prod.* **170**, 242–250 (2018).

85. Plotkin, A. R., et al. Solar receiver steam generator design for the Ivanpah solar electric generating system. in vol. 44601 523–529 (2011).

86. Zheng, R. F. & Wegeng, R. S. *Integrated Solar Thermochemical Reaction System*. (2019).

87. COMSOL Multiphysics® v. 5.5. COMSOL AB.

88. SOLIDWORKS® 2017. SolidWorks Corporation.

89. Peckner, D. & Bernstein, I. M. *Handbook of Stainless Steels*. (1977).

90. Harvey, P. D. American Society for Metals. *Eng. Prop.* (2011).

91. ASM International. Handbook Committee. *Properties and Selection--Irons, Steels, and High-Performance Alloys*. vol. 1 (ASM International, 1990).

92. Handbook, A. M. Howard E. *Boyer Timothy Gall Eds Am. Soc. Met. Mater. Park OH* (1985).

93. *Air - Specific Heat vs. Pressure at Constant Temperature*. https://www.engineeringtoolbox.com/air-specific-heat-various-pressures-d_1535.html.

94. Databook, F. F. General Electric. (1982).

95. *Hi-MO 5m LR5-72HPH 535-555M*. https://static.longi.com/Hi_MO_5m_LR_5_72_HPH_535_555_M_0665596eac.pdf.

96. Hemighaus, G., et al. Aviation fuels: Techincal review. Chevron Products Company. (2007).

97. Maurice, L. Q., Lander, H., Edwards, T. & Harrison Iii, W. Advanced aviation fuels: a look ahead via a historical perspective. *Fuel* **80**, 747–756 (2001).

98. Kallio, P., Pásztor, A., Akhtar, M. K. & Jones, P. R. Renewable jet fuel. *Curr. Opin. Biotechnol.* **26**, 50–55 (2014).

99. Gutiérrez-Antonio, C., Gómez-Castro, F. I., de Lira-Flores, J. A. & Hernández, S. A review on the production processes of renewable jet fuel. *Renew. Sustain. Energy Rev.* **79**, 709–729 (2017).

100. Liu, G., Yan, B. & Chen, G. Technical review on jet fuel production. *Renew. Sustain. Energy Rev.* **25**, 59–70 (2013).

101. van der Westhuizen, R., et al. Comprehensive two-dimensional gas chromatography for the analysis of synthetic and crude-derived jet fuels. *J. Chromatogr. A* **1218**, 4478–4486 (2011).

102. Jalama, K., et al. A comparison of Au/Co/Al2O3 and Au/Co/SiO2 catalysts in the Fischer–Tropsch reaction. *Appl. Catal. Gen.* **395**, 1–9 (2011).

103. Lobo, P., Hagen, D. E. & Whitefield, P. D. Comparison of PM emissions from a commercial jet engine burning conventional, biomass, and Fischer–Tropsch fuels. *Environ. Sci. Technol.* **45**, 10744–10749 (2011).

104. Liu, G., Larson, E. D., Williams, R. H., Kreutz, T. G. & Guo, X. Making Fischer− Tropsch fuels and electricity from coal and biomass: performance and cost analysis. *Energy Fuels* **25**, 415–437 (2011).

105. Kang, S.-H., et al. Catalytic performance on iron-based Fischer–Tropsch catalyst in fixed-bed and bubbling fluidized-bed reactor. *Appl. Catal. B Environ.* **103**, 169–180 (2011).

106. Bezemer, G. L., et al. Cobalt particle size effects in the Fischer− Tropsch reaction studied with carbon nanofiber supported catalysts. *J. Am. Chem. Soc.* **128**, 3956–3964 (2006).

107. Hilmen, A., Schanke, D., Hanssen, K. & Holmen, A. Study of the effect of water on alumina supported cobalt Fischer–Tropsch catalysts. *Appl. Catal. Gen.* **186**, 169–188 (1999).

108. Cano, L. A., Cagnoli, M. V., Bengoa, J. F., Alvarez, A. M. & Marchetti, S. G. Effect of the activation atmosphere on the activity of Fe catalysts supported on SBA-15 in the Fischer–Tropsch Synthesis. *J. Catal.* **278**, 310–320 (2011).

109. Lopez, J. S., Dagle, R. A., Dagle, V. L., Smith, C. & Albrecht, K. O. Oligomerization of ethanol-derived propene and isobutene mixtures to transportation fuels: catalyst and process considerations. *Catal. Sci. Technol.* **9**, 1117–1131 (2019).

110. Bai, S., et al. Highly active and selective hydrogenation of CO2 to ethanol by ordered Pd–Cu nanoparticles. *J. Am. Chem. Soc.* **139**, 6827–6830 (2017).

111. Zhang, M. & Yu, Y. Dehydration of ethanol to ethylene. *Ind. Eng. Chem. Res.* **52**, 9505–9514 (2013).

112. Chen, X., et al. Electrochemical CO2-to-ethylene conversion on polyamine-incorporated Cu electrodes. *Nat. Catal.* **4**, 20–27 (2021).

113. Li, F., et al. Molecular tuning of CO2-to-ethylene conversion. *Nature* **577**, 509–513 (2020).

114. Finiels, A., Fajula, F. & Hulea, V. Nickel-based solid catalysts for ethylene oligomerization–a review. *Catal. Sci. Technol.* **4**, 2412–2426 (2014).

115. Seufitelli, G. V. & Gustafson, R. Novel Ni-SIRAL catalyst for heterogeneous ethylene oligomerization. *Ind. Eng. Chem. Res.* **61**, 4286–4299 (2022).

116. Keim, W., Kowaldt, F. H., Goddard, R. & Krüger, C. New coordination mode of (benzoylmethylene) triphenylphosphorane in a nickel oligomerization catalyst. *Chem. Informationsdienst* **9**, no-no (1978).

117. Keim, W. Oligomerization of ethylene to α-olefins: discovery and development of the shell higher olefin process (SHOP). *Angew. Chem. Int. Ed.* **52**, 12492–12496 (2013).

118. Lee, M., et al. Ni/SIRAL-30 as a heterogeneous catalyst for ethylene oligomerization. *Appl. Catal. Gen.* **562**, 87–93 (2018).

119. Boisier, G., et al. Electrochemical behavior of chemical vapor deposited protective aluminum oxide coatings on Ti6242 titanium alloy. *Electrochem. Solid-State Lett.* **11**, C55 (2008).

120. Samélor, D., et al. Amorphous alumina coatings: processing, structure and remarkable barrier properties. *J. Nanosci. Nanotechnol.* **11**, 8387–8391 (2011).

121. Avis, C. & Jang, J. High-performance solution processed oxide TFT with aluminum oxide gate dielectric fabricated by a sol–gel method. *J. Mater. Chem.* **21**, 10649–10652 (2011).

122. Amini, G., Najafpour, G. D., Rabiee, S. M. & Ghoreyshi, A. A. Synthesis and Characterization of Amorphous Nano-Alumina Powders with High Surface Area for Biodiesel Production. *Chem. Eng. Technol.* **36**, 1708–1712 (2013).

123. Kang, D., Tong, S., Yu, X. & Ge, M. Template-free synthesis of 3D hierarchical amorphous aluminum oxide microspheres with broccoli-like structure and their application in fluoride removal. *RSC Adv.* **5**, 19159–19165 (2015).

124. Li, J., Pan, Y., Xiang, C., Ge, Q. & Guo, J. Low temperature synthesis of ultrafine α-Al2O3 powder by a simple aqueous sol–gel process. *Ceram. Int.* **32**, 587–591 (2006).

125. Karim, M., et al. Synthesis of γ-alumina particles and surface characterization. *Open Colloid Sci. J.* **4**, (2011).

126. Laishram, K., Mann, R. & Malhan, N. A novel microwave combustion approach for single step synthesis of α-Al2O3 nanopowders. *Ceram. Int.* **38**, 1703–1706 (2012).

127. Sathyaseelan, B., Baskaran, I. & Sivakumar, K. Phase transition behavior of nanocrystalline Al 2 O 3 powders. *Soft Nanosci. Lett.* **2013**, (2013).

128. Ozuna, O., Hirata, G. & McKittrick, J. Pressure influenced combustion synthesis of γ- and α-Al2O3 nanocrystalline powders. *J. Phys. Condens. Matter* **16**, 2585 (2004).

129. Toniolo, J., Lima, M., Takimi, A. & Bergmann, C. Synthesis of alumina powders by the glycine–nitrate combustion process. *Mater. Res. Bull.* **40**, 561–571 (2005).

130. Sharma, A., Modi, O. & Gupta, G. K. Effect of fuel to oxidizer ratio on synthesis of Alumina powder using Solution Combustion Technique-Aluminium Nitrate & Glycine combination. *Adv Appl Sci Res* **3**, 2151–2158 (2012).

131. Su, X., Chen, S. & Zhou, Z. Synthesis and characterization of monodisperse porous α-Al2O3 nanoparticles. *Appl. Surf. Sci.* **258**, 5712–5715 (2012).

132. Sanamyan, T., Pavlacka, R., Gilde, G. & Dubinskii, M. Spectroscopic properties of Er3+-doped α-Al2O3. *Opt. Mater.* **35**, 821–826 (2013).

133. Wang, J., et al. Facile size-controlled synthesis of well-dispersed spherical amorphous alumina nanoparticles via homogeneous precipitation. *Ceram. Int.* **42**, 8545–8551 (2016).

134. Zhang, W., et al. Luminescent amorphous alumina nanoparticles in toluene solution. *J. Phys. Condens. Matter* **18**, 9937 (2006).

135. Pan, C., Shen, P. & Chen, S.-Y. Condensation, crystallization and coalescence of amorphous Al2O3 nanoparticles. *J. Cryst. Growth* **299**, 393–398 (2007).

136. Atrak, K., Ramazani, A. & Taghavi Fardood, S. Green synthesis of amorphous and gamma aluminum oxide nanoparticles by tragacanth gel and comparison of their photocatalytic activity for the degradation of organic dyes. *J. Mater. Sci. Mater. Electron.* **29**, 8347–8353 (2018).

137. Kunath-Fandrei, G., Bastow, T. J., Hall, J., Jäger, C. & Smith, M. E. Quantification of aluminum coordinations in amorphous aluminas by combined central and satellite transition magic angle spinning NMR spectroscopy. *J. Phys. Chem.* **99**, 15138–15141 (1995).

138. Lamparter, P. & Kniep, R. Structure of amorphous Al2O3. *Phys. B Condens. Matter* **234**, 405–406 (1997).

139. Gutierrez, G. & Johansson, B. Molecular dynamics study of structural properties of amorphous Al 2 O 3. *Phys. Rev. B* **65**, 104202 (2002).

140. Snijders, P., Jeurgens, L. & Sloof, W. Structural ordering of ultra-thin, amorphous aluminium-oxide films. *Surf. Sci.* **589**, 98–105 (2005).

141. Lee, S. K., Lee, S. B., Park, S. Y., Yi, Y. S. & Ahn, C. W. Structure of amorphous aluminum oxide. *Phys. Rev. Lett.* **103**, 095501 (2009).

142. Lizárraga, R., Holmström, E., Parker, S. C. & Arrouvel, C. Structural characterization of amorphous alumina and its polymorphs from first-principles XPS and NMR calculations. *Phys. Rev. B* **83**, 094201 (2011).

143. John, C., Alma, N. & Hays, G. Characterization of transitional alumina by solid-state magic angle spinning aluminium NMR. *Appl. Catal.* **6**, 341–346 (1983).

144. Levin, I. & Brandon, D. Metastable alumina polymorphs: crystal structures and transition sequences. *J. Am. Ceram. Soc.* **81**, 1995–2012 (1998).

145. Stumpf, H. C., Russell, A. S., Newsome, J. & Tucker, C. Thermal Transformations of Aluminas and Alumina Hydrates-Reaction with 44% Technical Acid. *Ind. Eng. Chem.* **42**, 1398–1403 (1950).

146. Lippens, B. & De Boer, J. Study of phase transformations during calcination of aluminum hydroxides by selected area electron diffraction. *Acta Crystallogr.* **17**, 1312–1321 (1964).

147. Morrissey, K. J., Czanderna, K. K., Carter, C. & Merrill, R. P. Growth of α-Al2O3 within a transition alumina matrix. *J. Am. Ceram. Soc.* **67**, c88–c90 (1984).

148. Lamouri, S., et al. Control of the γ-alumina to α-alumina phase transformation for an optimized alumina densification. *Bol. Soc. Esp. Cerámica Vidr.* **56**, 47–54 (2017).

149. MUNRO, M. Evaluated material properties for a sintered alpha-alumina. *J. Am. Ceram. Soc.* **80**, 1919–1928 (1997).

150. Krick, B. A., et al. Ultralow wear fluoropolymer composites: nanoscale functionality from microscale fillers. *Tribol. Int.* **95**, 245–255 (2016).

151. Bhattacharyya, S. & Behera, P. S. Synthesis and characterization of nano-sized α-alumina powder from kaolin by acid leaching process. *Appl. Clay Sci.* **146**, 286–290 (2017).

152. Maciver, D. S., Tobin, H. H. & Barth, R. Catalytic aluminas I. Surface chemistry of eta and gamma alumina. *J. Catal.* **2**, 485–497 (1963).

153. Gresback, R., Holman, Z. & Kortshagen, U. Nonthermal plasma synthesis of size-controlled, monodisperse, freestanding germanium nanocrystals. *Appl. Phys. Lett.* **91**, (2007).

154. Felbier, P., et al. Highly luminescent ZnO quantum dots made in a nonthermal plasma. *Adv. Funct. Mater.* **24**, 1988–1993 (2014).

155. Greenberg, B. L., et al. Nonequilibrium-plasma-synthesized ZnO nanocrystals with plasmon resonance tunable via Al doping and quantum confinement. *Nano Lett.* **15**, 8162–8169 (2015).

156. Thimsen, E., Kortshagen, U. R. & Aydil, E. S. Nonthermal plasma synthesis of metal sulfide nanocrystals from metalorganic vapor and elemental sulfur. *J. Phys. Appl. Phys.* **48**, 314004 (2015).

157. Alvarez Barragan, A., Ilawe, N. V., Zhong, L., Wong, B. M. & Mangolini, L. A non-thermal plasma route to plasmonic TiN nanoparticles. *J. Phys. Chem. C* **121**, 2316–2322 (2017).

158. Woodard, A., et al. On the non-thermal plasma synthesis of nickel nanoparticles. *Plasma Process. Polym.* **15**, 1700104 (2018).

159. Holman, Z. C. & Kortshagen, U. R. A flexible method for depositing dense nanocrystal thin films: impaction of germanium nanocrystals. *Nanotechnology* **21**, 335302 (2010).

160. Firth, P. & Holman, Z. C. Aerosol impaction-driven assembly system for the production of uniform nanoparticle thin films with independently tunable thickness and porosity. *ACS Appl. Nano Mater.* **1**, 4351–4357 (2018).

161. Nguyen, H. M., Tang, H.-Y., Huang, W.-F. & Lin, M.-C. Mechanisms for reactions of trimethylaluminum with molecular oxygen and water. *Comput. Theor. Chem.* **1035**, 39–43 (2014).

162. Tavakoli, A. H., et al. Amorphous alumina nanoparticles: structure, surface energy, and thermodynamic phase stability. *J. Phys. Chem. C* **117**, 17123–17130 (2013).

163. Catherine, Y. & Talebian, A. Plasma deposition of aluminum oxide films. *J. Electron. Mater.* **17**, 127–134 (1988).

164. Kuech, T., Veuhoff, E., Kuan, T., Deline, V. & Potemski, R. The influence of growth chemistry on the MOVPE growth of GaAs and AlxGa1− xAs layers and heterostructures. *J. Cryst. Growth* **77**, 257–271 (1986).

165. Kobayashi, N. & Makimoto, T. Reduced carbon contamination in OMVPE grown GaAs and AlGaAs. *Jpn. J. Appl. Phys.* **24**, L824 (1985).

166. Paparazzo, E. XPS analysis of iron aluminum oxide systems. *Appl. Surf. Sci.* **25**, 1–12 (1986).

167. Van den Brand, J., Snijders, P., Sloof, W., Terryn, H. & De Wit, J. Acid− base characterization of aluminum oxide surfaces with XPS. *J. Phys. Chem. B* **108**, 6017–6024 (2004).

168. McCafferty, E. & Wightman, J. Determination of the concentration of surface hydroxyl groups on metal oxide films by a quantitative XPS method. *Surf. Interface Anal. Int. J. Devoted Dev. Appl. Tech. Anal. Surf. Interfaces Thin Films* **26**, 549–564 (1998).

169. Van den Brand, J., Sloof, W., Terryn, H. & De Wit, J. Correlation between hydroxyl fraction and O/Al atomic ratio as determined from XPS spectra of aluminium oxide layers. *Surf. Interface Anal. Int. J. Devoted Dev. Appl. Tech. Anal. Surf. Interfaces Thin Films* **36**, 81–88 (2004).

170. Zagrajczuk, B., et al. Structural investigation of gel-derived materials from the SiO2Al2O3 system. *J. Mol. Struct.* **1167**, 23–32 (2018).

171. Boumaza, A., et al. Transition alumina phases induced by heat treatment of boehmite: an X-ray diffraction and infrared spectroscopy study. *J. Solid State Chem.* **182**, 1171–1176 (2009).

172. Liang, D. *Generalized Ellipsometry Analysis of Anisotropic Nanoporous Media: Polymer-Infiltrated Nanocolumnar and Inverse-Column Polymeric Films*. (The University of Nebraska-Lincoln, 2015).

173. Schmidt, D., Schubert, E. & Schubert, M. Generalized ellipsometry determination of non-reciprocity in chiral silicon sculptured thin films. *Phys. Status Solidi A* **205**, 748–751 (2008).

174. Chang, P.-L., Yen, F.-S., Cheng, K.-C. & Wen, H.-L. Examinations on the critical and primary crystallite sizes during θ-to α-phase transformation of ultrafine alumina powders. *Nano Lett.* **1**, 253–261 (2001).

175. Sihvola, A. Mixing rules with complex dielectric coefficients. *Subsurf. Sens. Technol. Appl.* **1**, 393–415 (2000).

176. Voshchinnikov, N. V., Videen, G. & Henning, T. Effective medium theories for irregular fluffy structures: aggregation of small particles. *Appl. Opt.* **46**, 4065–4072 (2007).

177. Pekonen, O., Kärkkäinen, K., Sihvola, A. & Nikoskinen, K. Numerical testing of dielectric mixing rules by FDTD method. *J. Electromagn. Waves Appl.* **13**, 67–87 (1999).

178. Wäckelgård, E. The experimental dielectric function of porous anodic alumina in the infrared region; a comparison with the Maxwell-Garnett model. *J. Phys. Condens. Matter* **8**, 4289 (1996).

179. Markel, V. A. Introduction to the Maxwell Garnett approximation: tutorial. *JOSA A* **33**, 1244–1256 (2016).

180. Wormeester, H., Kooij, E. S. & Poelsema, B. Effective dielectric response of nanostructured layers. *Phys. Status Solidi A* **205**, 756–763 (2008).

181. Daugherty, J. & Graves, D. Particulate temperature in radio frequency glow discharges. *J. Vac. Sci. Technol. Vac. Surf. Films* **11**, 1126–1131 (1993).

182. Mangolini, L. & Kortshagen, U. Selective nanoparticle heating: another form of nonequilibrium in dusty plasmas. *Phys. Rev. E* **79**, 026405 (2009).

183. McCallum, J., Simpson, T. & Mitchell, I. Time resolved reflectivity measurements of the amorphous-to-gamma and gamma-to-alpha phase transitions in ion-implanted Al2O3. *Nucl. Instrum. Methods Phys. Res. Sect. B Beam Interact. Mater. At.* **91**, 60–62 (1994).

184. Simpson, T. W., Wen, Q., Yu, N. & Clarke, D. R. Kinetics of the amorphous→ γ→ α transformations in aluminum oxide: effect of crystallographic orientation. *J. Am. Ceram. Soc.* **81**, 61–66 (1998).

185. Eklund, P., Sridharan, M., Singh, G. & Bøttiger, J. Thermal stability and phase transformations of γ-/amorphous-Al2O3 thin films. *Plasma Process. Polym.* **6**, S907–S911 (2009).

186. Nakamura, R., Shudo, T., Hirata, A., Ishimaru, M. & Nakajima, H. Nanovoid formation through the annealing of amorphous Al2O3 and WO3 films. *Scr. Mater.* **64**, 197–200 (2011).

187. Nakamura, R., et al. Enhancement of nanovoid formation in annealed amorphous Al2O3 including W. *J. Appl. Phys.* **110**, (2011).

188. Diouf, S. & Molinari, A. Densification mechanisms in spark plasma sintering: Effect of particle size and pressure. *Powder Technol.* **221**, 220–227 (2012).

189. Kim, B.-C., Lee, J.-H., Kim, J.-J. & Ikegami, T. Rapid rate sintering of nanocrystalline indium tin oxide ceramics: particle size effect. *Mater. Lett.* **52**, 114–119 (2002).

190. Liu, C., Shih, K., Gao, Y., Li, F. & Wei, L. Dechlorinating transformation of propachlor through nucleophilic substitution by dithionite on the surface of alumina. *J. Soils Sediments* **12**, 724–733 (2012).

191. *The Future of Cooling*. https://www.iea.org/reports/the-future-of-cooling.

192. Goetzler, W., Guernsey, M., Young, J., Fujrman, J. & Abdelaziz, A. *The Future of Air Conditioning for Buildings*. (2016).

193. Laillonne, B. The future of air-conditioning. *Enerdata Grenoble* (2019).

194. US Energy Information Administration. Residential energy consumption survey. (2015).

195. Santamouris, M. & Kolokotsa, D. Passive cooling dissipation techniques for buildings and other structures: The state of the art. *Energy Build.* **57**, 74–94 (2013).

196. Seyboth, K., Beurskens, L., Langniss, O. & Sims, R. E. Recognising the potential for renewable energy heating and cooling. *Energy Policy* **36**, 2460–2463 (2008).

197. Fensholt, R., et al. Assessment of vegetation trends in drylands from time series of earth observation data. *Remote Sens. Time Ser. Reveal. Land Surf. Dyn.* 159–182 (2015).

198. Zhai, Y., et al. Scalable-manufactured randomized glass-polymer hybrid metamaterial for daytime radiative cooling. *Science* **355**, 1062–1066 (2017).

199. Kou, J., Jurado, Z., Chen, Z., Fan, S. & Minnich, A. J. Daytime radiative cooling using near-black infrared emitters. *Acs Photonics* **4**, 626–630 (2017).

200. Raman, A. P., Anoma, M. A., Zhu, L., Rephaeli, E. & Fan, S. Passive radiative cooling below ambient air temperature under direct sunlight. *Nature* **515**, 540–544 (2014).

201. Rephaeli, E., Raman, A. & Fan, S. Ultrabroadband photonic structures to achieve high-performance daytime radiative cooling. *Nano Lett.* **13**, 1457–1461 (2013).

202. Chen, Z., Zhu, L., Raman, A. & Fan, S. Radiative cooling to deep sub-freezing temperatures through a 24-h day–night cycle. *Nat. Commun.* **7**, 13729 (2016).

203. Hossain, M. M., Jia, B. & Gu, M. A metamaterial emitter for highly efficient radiative cooling. *Adv Opt Mater* **3**, 1047–1051 (2015).

204. Zhu, L., Raman, A. & Fan, S. Color-preserving daytime radiative cooling. *Appl. Phys. Lett.* **103**, (2013).

205. Huang, Z. & Ruan, X. Nanoparticle embedded double-layer coating for daytime radiative cooling. *Int. J. Heat Mass Transf.* **104**, 890–896 (2017).

206. Zhu, L., Raman, A., Wang, K. X., Abou Anoma, M. & Fan, S. Radiative cooling of solar cells. *Optica* **1**, 32–38 (2014).

207. Ao, X., et al. Preliminary experimental study of a specular and a diffuse surface for daytime radiative cooling. *Sol. Energy Mater. Sol. Cells* **191**, 290–296 (2019).

208. Bao, H., et al. Double-layer nanoparticle-based coatings for efficient terrestrial radiative cooling. *Sol. Energy Mater. Sol. Cells* **168**, 78–84 (2017).

209. Gentle, A. R. & Smith, G. B. Radiative heat pumping from the earth using surface phonon resonant nanoparticles. *Nano Lett.* **10**, 373–379 (2010).

210. Chan, H.-Y., Riffat, S. B. & Zhu, J. Review of passive solar heating and cooling technologies. *Renew. Sustain. Energy Rev.* **14**, 781–789 (2010).

211. Kamal, M. A. An overview of passive cooling techniques in buildings: design concepts and architectural interventions. *Acta Tech. Napoc. Civ. Eng. Archit.* **55**, 84–97 (2012).

212. Kendrick, J. & Burnett, A. D. PDielec: The calculation of infrared and terahertz absorption for powdered crystals. (2016).

213. Xi, J.-Q., et al. Optical thin-film materials with low refractive index for broadband elimination of Fresnel reflection. *Nat. Photonics* **1**, 176–179 (2007).

214. Zaitsu, S., Jitsuno, T., Nakatsuka, M., Yamanaka, T. & Motokoshi, S. Optical thin films consisting of nanoscale laminated layers. *Appl. Phys. Lett.* **80**, 2442–2444 (2002).

215. Yeh, P., Yariv, A. & Hong, C.-S. Electromagnetic propagation in periodic stratified media. I. General theory. *JOSA* **67**, 423–438 (1977).

216. Molesky, S., Dewalt, C. J. & Jacob, Z. High temperature epsilon-near-zero and epsilon-near-pole metamaterial emitters for thermophotovoltaics. *Opt. Express* **21**, A96–A110 (2013).

217. Goya, G. F. Handling the particle size and distribution of Fe3O4 nanoparticles through ball milling. *Solid State Commun.* **130**, 783–787 (2004).

218. Jeon, S. & Shin, J. Ideal spectral emissivity for radiative cooling of earthbound objects. *Sci. Rep.* **10**, 13038 (2020).

219. Granqvist, C. & Hjortsberg, A. Radiative cooling to low temperatures: General considerations and application to selectively emitting SiO films. *J. Appl. Phys.* **52**, 4205–4220 (1981).

220. Wright, J. C. Accuracy of lowtran 7 and modtran in the 2.0–5.5-μm region. *Appl. Opt.* **33**, 1755–1759 (1994).

221. Wright, J. Evaluation of LOWTRAN and MODTRAN for use over high zenith angle/long path length viewing. (1991).

222. Abreu, L. & Anderson, G. The MODTRAN 2/3 report and LOWTRAN 7 model. *Contract* **19628**, 0132 (1996).

223. Launer, P. J. & Arkles, B. Infrared analysis of organosilicon compounds: spectra-structure correlations. *Silicone Compd. Regist. Rev.* **100**, 100–103 (1987).

224. Smith, A. L. Infrared spectra-structure correlations for organosilicon compounds. *Spectrochim. Acta* **16**, 87–105 (1960).

225. Anderson, D. & Smith, A. L. Analysis of silicones. *Wiley-Intersci. N. Y.* 247 (1974).

226. Bellamy, L. *The Infra-Red Spectra of Complex Molecules*. (Springer Science & Business Media, 2013).

227. Malitson, I. H. Interspecimen comparison of the refractive index of fused silica. *Josa* **55**, 1205–1209 (1965).

228. Stroud, D. The effective medium approximations: Some recent developments. *Superlattices Microstruct.* **23**, 567–573 (1998).

229. Karkkainen, K. K., Sihvola, A. H. & Nikoskinen, K. I. Effective permittivity of mixtures: numerical validation by the FDTD method. *IEEE Trans. Geosci. Remote Sens.* **38**, 1303–1308 (2000).

230. Bossa, J.-B., et al. Porosity measurements of interstellar ice mixtures using optical laser interference and extended effective medium approximations. *Astron. Astrophys.* **561**, A136 (2014).

231. Hülser, T., Schnurre, S. M., Wiggers, H. & Schulz, C. Gas-phase synthesis of nanoscale silicon as an economical route towards sustainable energy technology. *KONA Powder Part. J.* **29**, 191–207 (2011).

232. Rao, N., et al. Nanoparticle formation using a plasma expansion process. *Plasma Chem. Plasma Process.* **15**, 581–606 (1995).

233. Shigeta, M. & Murphy, A. B. Thermal plasmas for nanofabrication. *J. Phys. Appl. Phys.* **44**, 174025 (2011).

234. Donev, A., et al. Improving the density of jammed disordered packings using ellipsoids. *Science* **303**, 990–993 (2004).

235. Dullien, F. A. *Porous Media: Fluid Transport and Pore Structure*. (Academic press, 2012).

236. Varner, J. F., Eldabagh, N., Volta, D., Eldabagh, R. & Foley, J. J. WPTherml: A Python Package for the Design of Materials for Harnessing Heat. *J. Open Res. Softw.* **7**, (2019).

237. Kneizys, F. X. *Users Guide to LOWTRAN 7*. vol. 88 (Air Force Geophysics Laboratory, 1988).